Quantitative Imaging in Medicine and Surgery

September 2018. Volume 8 Number 8 Pages 724-883

AME Publishing Company

Editorial Correspondence: Mike Cheung, Science Editor. Quantitative Imaging in Medicine and Surgery. HK Office: Rm C, 16/F, Kings Wing Plaza 1, No. 3 On Kwan Street, Shatin, NT, Hong Kon. Tel: +86 20 66355775. Email: qims@amepc.org

ISSN 2223-4292

Vol 8, No 8
September 2018

qims.amegroups.com

QUANTITATIVE IMAGING IN MEDICINE AND SURGERY

Endorsed by *Nanotechnology Cancer Asia-Pacific (NCAP) Network & Macau Radiology Association*

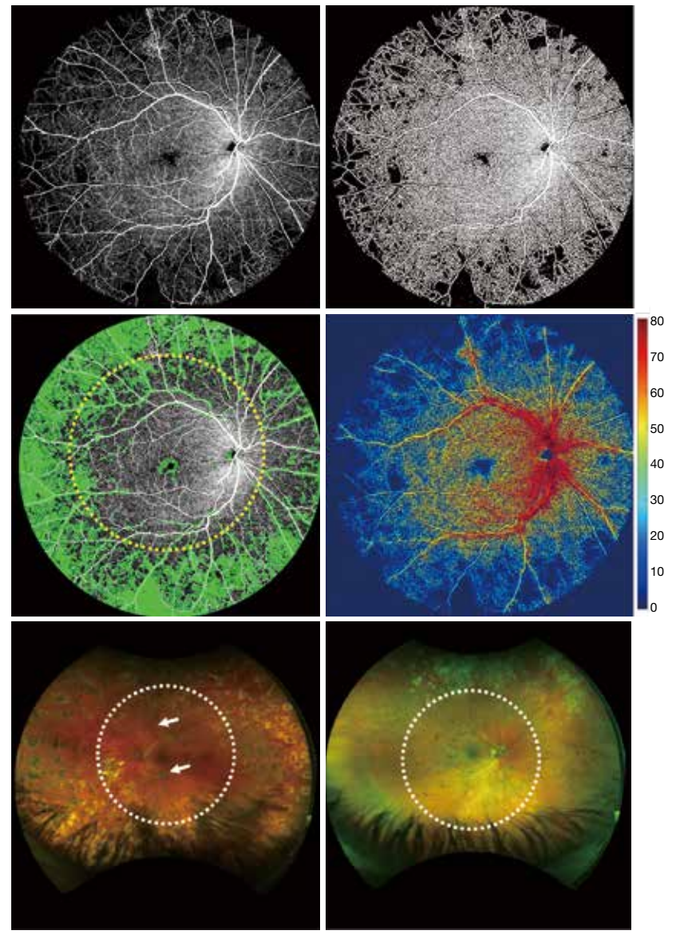

AME Publishing Company

2017 IMPACT FACTOR 2.231

Indexed in PubMed, SCIE

Aims and Scope
Quantitative Imaging in Medicine and Surgery (Print ISSN 2223-4292; Online ISSN 2223-4306; QIMS) publishes peer-reviewed original reports and reviews in medical imaging, including X-ray, ultrasound, computed tomography, magnetic resonance imaging and spectroscopy, nuclear medicine and related modalities, and their application in medicine and surgery. While focus is on clinical investigations, papers on medical physics, image processing, or biological studies which have apparent clinical relevance are also published. This journal encourages authors to look at the medical images from a quantitative angle. To grade or score imaging features is also an important way of quantification.

Editorial Correspondence
Mike Cheung
Science Editor
Quantitative Imaging in Medicine and Surgery
HK Office: Flat/RM C 16F, Kings Wing Plaza 1, No. 3 On Kwan Street, Shatin, NT, Hong Kong. Tel: +852 3615 8769. Email: qims@amepc.org

Note to NIH Grantees
Pursuant to NIH mandate, AME Publishing Company will post the accepted version of contributions authored by NIH grant-holders to PubMed Central upon acceptance. This accepted version will be made publicly available 1 month after publication. For further information, see qims.amegroups.com

Cover image
Ultra-wide OCTA image of the whole retinal layer (WRL) in gray scale of a patient and the corresponding quantification process: The original ultra-wide OCTA image; binary OCTA image that was used for vessel density and further non-perfusion area measurements. (upper part)
The OCTA image overlaid with non-perfusion area map in green color. Typical 50-degree FOV is outlined approximately with yellow dashed circle. The non-perfusion area within the outlined circle is measured with 11.83 mm^2, whereas that of the outside is 108.59 mm^2 and the vessel density map overlaid with the binary OCTA image. The color-bar indicates the degree of the vessel density in percentage. (middle part)
Optos ultra-wide color fundus image of a 31-year-old female with a diagnosis of severe PDR on her left eye and PDR on her right eye. Typical 50-degree FOV is outlined with white dashed circle line. (lower part)

For submission instructions, subscription and all other information visit qims.amegroups.com

Table of Contents

Editorial

Original Article

Review Article

Letter to the Editor

In Memoriam

Editorial

Advances in super-resolution photoacoustic imaging

Junhui Shi[1], Yuqi Tang[2], Junjie Yao[2]

[1]Caltech Optical Imaging Laboratory, Andrew and Peggy Cherng Department of Medical Engineering, Department of Electrical Engineering, California Institute of Technology, Pasadena, CA 91125, USA; [2]Photoacoustic Imaging Laboratory, Department of Biomedical Engineering, Duke University, Durham, NC 27708, USA

Correspondence to: Junjie Yao. Photoacoustic Imaging Laboratory, Department of Biomedical Engineering, Duke University, Durham, NC 27708, USA. Email: junjie.yao@duke.edu.

Submitted Sep 09, 2018. Accepted for publication Sep 17, 2018.
doi: 10.21037/qims.2018.09.14
View this article at: http://dx.doi.org/10.21037/qims.2018.09.14

Introduction

Photoacoustic (PA) imaging (PAI), or optoacoustic imaging, is a hybrid imaging modality that combines optical absorption contrast and ultrasound image formation. In PAI, the target is excited by a short laser pulse and subsequently absorbs the photon energy, leading to a transient local temperature rise. The temperature rise induces a local pressure rise that propagates as acoustic waves. As acoustic waves generally undergo less scattering and attenuation in tissue compared with light, PAI can provide high-resolution images in both the optical (quasi)ballistic and (quasi)diffusive regimes (1,2). Based on the image formation methods, PAI can be classified into two categories: photoacoustic microscopy (PAM) and photoacoustic computed tomography (PACT). PAM uses a focused excitation light beam and/or a focused single-element ultrasonic transducer for direct image formation through position scanning (1,2). PAM has a maximum imaging depth ranging from a few hundred micrometers to a few millimeters with spatial resolution ranging from sub-micrometer to sub-millimeter (2,3). PAM can be further classified into optical-resolution PAM (OR-PAM) and acoustic-resolution PAM (AR-PAM). For both OR-PAM and AR-PAM, the axial resolution is determined by the bandwidth of the ultrasonic transducer (4). OR-PAM works in the optical (quasi)ballistic regime, whereas the light is tightly focused that it can penetrate about one optical transport mean free path (~1 mm in soft tissue). Therefore, the lateral resolution of OR-PAM is mainly determined by the optical focal spot size (4-6). The optical focusing is diffraction-limited as $\lambda/2NA$, where λ is the light wavelength, and NA is the numerical aperture of objective lens. On the contrary, in AR-PAM, the laser is loosely focused to fulfill the entire acoustic focal spot, thereby penetrating a few optical transport mean free paths, i.e., in the quasi-diffusive regime. The lateral resolution of AR-PAM is thus determined by the size of acoustic focus (4,7,8), limited by acoustic diffraction. In PACT, the object is illuminated with a wide-field laser beam in the diffusive regime, and the generated acoustic waves are detected at multiple locations or by using a multi-element transducer array. The image formed by PACT is reconstructed by an inverse algorithm. The spatial resolution of PACT is fundamentally limited by acoustic diffraction, and additionally affected by the directionality and spacing of the detector elements (9).

Recently, several studies have shown that sub-diffraction imaging of biological samples can be achieved through PAI by breaking optical-diffraction limit in the (quasi) ballistic regime or acoustic-diffraction limit in the (quasi) diffusive regime, which have opened new possibilities for fundamental biological studies. Yao *et al.* developed a photoimprint PAM using the intensity-dependent photobleaching effect and acquired a melanoma cell PA image with a lateral resolution of 90 nm (10). Danielli *et al.* reported a label-free PA nanoscopy based on the optical-absorption saturation effect and acquired a mitochondria PA image with a lateral resolution of 88 nm (11). Chaigne *et al.* exploited the sample-dynamics-induced inherent temporal fluctuation in the PA signals and achieved a resolution enhancement of about 1.4 over conventional

PACT (12). Murray *et al.* broke the acoustic diffraction limit by implementing a blind speckle illumination and block-FISTA reconstruction algorithm and achieved a resolution close to the acoustic speckle size (13). Dean-Ben *et al.* also overcame the acoustic diffraction limit by incorporating rapid sequential acquisition of 3D PA images of flowing absorbing particles and further enhanced the visibility of structures under limited-view tomographic conditions (14). Conkey *et al.* optimized wavefront shaping with photoacoustic feedback and achieved up to ten times improvement in signal-to-noise ratio and five to six times sub-acoustic-diffraction resolution (15). In this concise review, we summarize and analyze the recent development in super-resolution (SR) PAI (SR-PAI) in both the optical (quasi)ballistic and (quasi)diffusive regime, as well as their representative applications. We also discuss the current challenges in SR-PAI and envision the potential breakthroughs.

Super-resolution OR-PAM in (quasi)ballistic regime

For OR-PAM of biological tissue at relatively superficial region, typically within one mean free path of optical scattering (<1 mm), the light propagation is in the optical (quasi)ballistic regime. Within this range, the light beam can be tightly focused on the target, and the lateral resolution is determined by the optical focal spot size, which is limited by optical diffraction, similar to other traditional optical imaging methods (16-18). To achieve super-resolution OR-PAM in the (quasi)ballistic regime, two strategies based on nonlinear optical mechanisms have been successfully exploited to overcome the optical diffraction limit (10,11).

The first strategy is reported by Yao *et al.*, who developed photoimprint PAM (PI-PAM) based on the intensity-dependent photobleaching effect (19). Dual-pulse excitation process was implemented in this method, and its principle is illustrated in *Figure 1A*. The first excitation generates a PA signal from the whole excitation volume, and at the same time, bleaches more absorbers in the central diffraction-limited excitation volume than those in the peripheral region, due to the inherent illumination inhomogeneity of a Gaussian beam. In the subsequent second excitation, molecules in the bleached central area have reduced absorption and generate a smaller PA signal than that from the first excitation. Although the PA signals generated from the two excitations are linear to the excitation energy, the difference between the two PA signals, which mostly represents the signal contribution from the central area of the focus, is nonlinear to the excitation energy. This mechanism of nonlinearity endows PI-PAM with both lateral and axial resolution enhancement, and the resultant imaging resolution is determined by the 'sharpened' focal spot. Compared to the diffraction-limited PAM, the lateral resolution of PI-PAM is enhanced by a factor of $\sqrt{1+b}$, where b is the power dependence of the photobleaching rate on the excitation intensity. In addition, the axial resolution of PI-PAM is improved by a factor of $1/\sqrt{2^{1(1+b)}-1}$ over conventional PAM. *Figure 1B,C* show the lateral resolution enhancement of PI-PAM over conventional OR-PAM. This imaging method can be performed on both fluorescent and nonfluorescent biological species. The major drawback of this method is the potential sample damage due to inherent photobleaching. The high frame number or excitation intensity may result in severe distortion between 'bleached' and 'unbleached' regions, thus balancing between sample distortion and SNR needs to be carefully sought. In practice, permanent photobleaching might become a concern, and photoswitchable chromophores can be introduced and cycled between bright and dark state (10,20,21). Moreover, different samples may have inconsistent resolution enhancement due to their different power dependence of photobleaching rates on the light intensity.

The second strategy attains nonlinear SR-PAM by using nonlinear thermal expansion and optical absorption saturation (11). The magnitude of PA signal is proportional to thermal expansion coefficient $\beta(T)$, which is temperature dependent. When T is in the physiological temperature range, $\beta(T)\approx\beta_1+\beta_2 T$ (22). For typical biological tissues with a nanosecond laser pulse excitation, the thermal diffusion length is around tens of nanometer (23). On the other hand, the optical excitation spot is around hundreds of nanometers, which is confined by the optical diffraction limit. Therefore, there exists the nonlinear enhancement of PA signals due to the local temperature rise within a short-pulsed optical excitation. In addition, the optical absorption coefficient saturates with increasing optical fluence (24), thereby contributing a second source of nonlinearity to the PA signals. Based on these two effects, high order nonlinear PA images can be constructed by using an optical pulse train with different energies striking on the same target. Given M optical pulses in a train, PA images with up to Nth-order

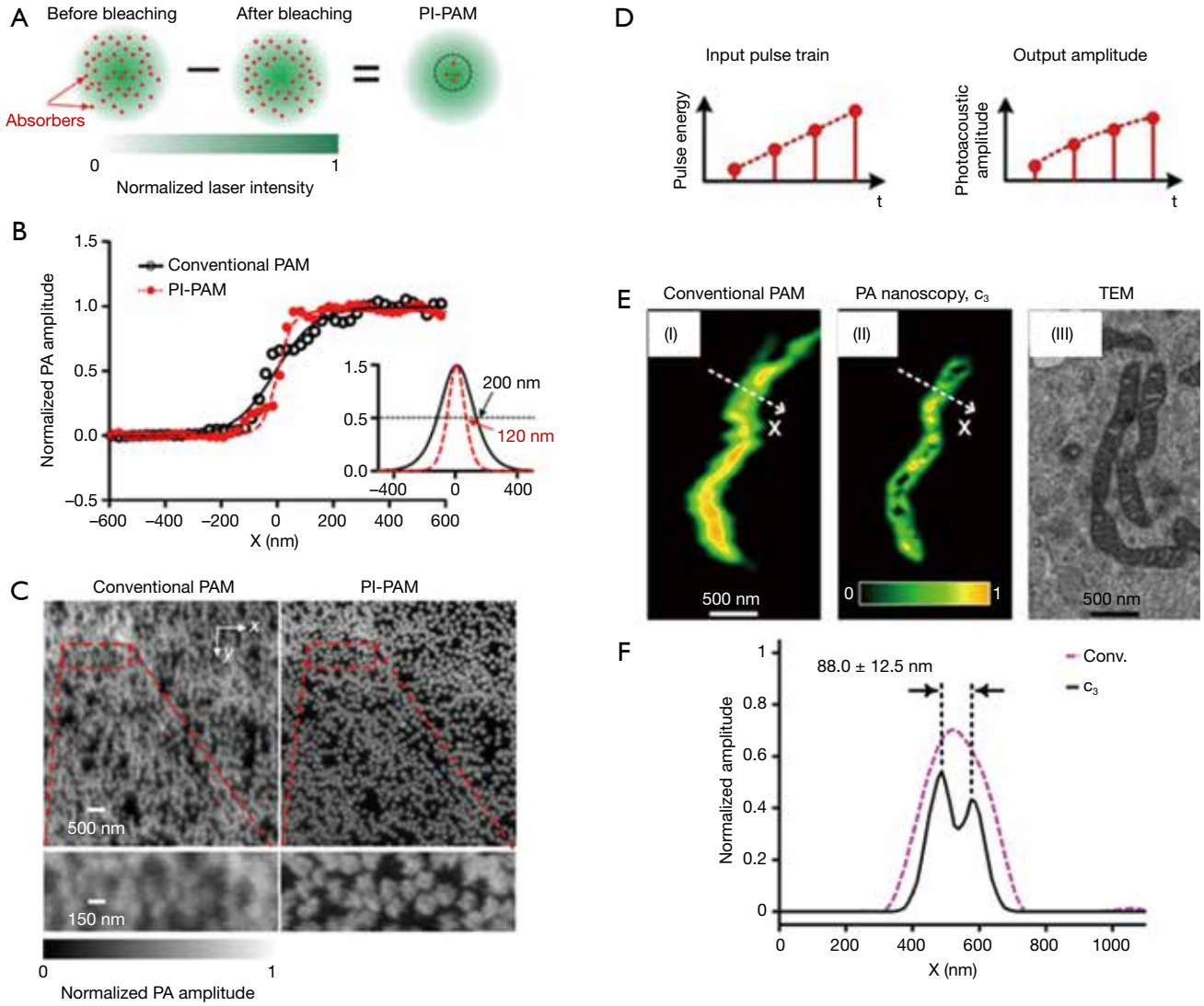

Figure 1 Two methods of nonlinear OR-PAM with sub-diffraction resolution. (A) Principle of PI-PAM; (B) the edge spread function of PI-PAM and conventional OR-PAM. The lateral resolution is improved from 200 to 120 nm; (C) comparison of images of red-dyed microspheres obtained by conventional PAM and PI-PAM, showing the improved lateral resolutions; (D) principle of nonlinear-absorption based PA-nanoscopy; (E) images of a single mitochondrion obtained by conventional PAM and PA-nanoscopy, which resolves 88-nm-apart features; (F) signal profiles along the dashed lines in (E), showing the improved resolution of PA-nanoscopy. Figure adopted with permission from (10,11). OR-PAM, optical-resolution photoacoustic microscopy; PI-PAM, photoimprint photoacoustic microscopy.

(N≤M) can be formed. The nonlinear high-order PA image narrows the lateral point spread function (PSF), thereby improves the lateral resolution by a factor of $\sqrt{N}$ over that of conventional PAM. In Danielle *et al.*'s work (11), a train of 1.6-ns laser pulses with pulse-to-pulse intensity modulation was used to embody this method. As illustrated in *Figure 1D*, at each position, four PA signals are successively excited with increasing pulse energy, then the third-order PA signals are extracted to achieve sub-diffraction resolution. In the experiment demonstration of this method, it reveals 88-nm features in a single mitochondrion (*Figure 1E,F*). The major drawbacks of this method include the long imaging time, slow pixel-by-pixel high-order fitting, and potential heating and photobleaching damage to the sample with repeated

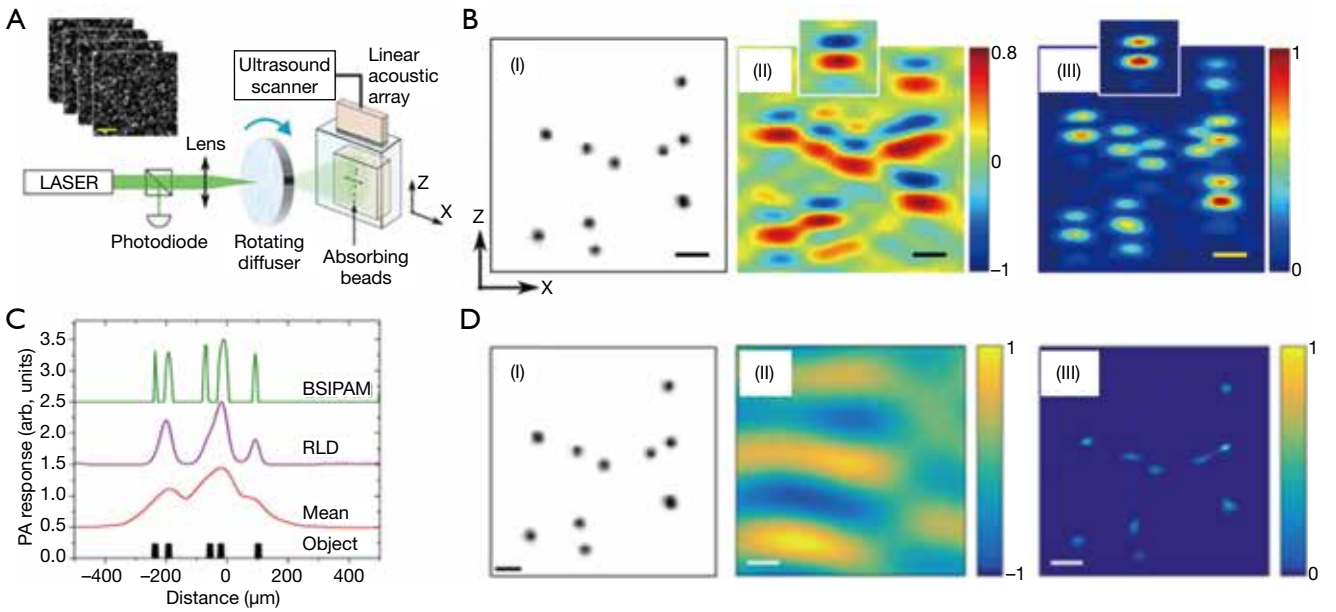

Figure 2 Sub-acoustic-diffraction PA imaging based on statistical fluctuation of PA signals and blind speckle illumination. (A) Experimental setup of fluctuation PA imaging with multiple speckle illumination. The blind-speckle illumination PAM has a similar scheme; (B) photography of sample (left), mean PA image over 100 speckle realizations (middle), and variance PA image (right). Figures adopted with permission from (25); (C) 1D demonstration with blind-speckle illumination PAM. Figures adopted with permission from (13); (D) a 2D image (right) obtained by blind-speckle illumination PAM, compared to photography of sample (left), mean PA image (middle). Figures adopted with permission from (26). PA, photoacoustic; PAM, photoacoustic microscopy.

excitation. Though no observable damages were reported on *ex vivo* cells, shorter pulses with lower energy can be used to approach the saturation intensity level with reduced photothermal damage potential (11).

Super-resolution PA imaging in (quasi)diffusive regime

For deep tissue imaging, it is challenging to focus light at depths beyond the optical mean free path (i.e., >1 mm). As light enters the (quasi)diffusive regime, the acoustic diffraction determines the lateral resolution of AR-PAM and PACT. To break the acoustic diffraction limit, several techniques have been exploited by probing the PA signal fluctuation (12,25), deconvolution with speckle structure illumination (13,26), localization of flowing absorbing particles (14,27), and improving optical focusing through wavefront shaping (15).

Originally developed for improving the resolution of conventional fluorescence microscopy, the statistical analysis of temporal signal fluctuations provides a simple way to obtain sub-diffraction optical resolution (28). Inspired by this approach, Chaigne *et al.* reported two similar methods (12,25) to achieve SR-PAI using temporal PA signal fluctuation analysis. The first method introduced multiple optical speckle illumination as the source of signal fluctuations (25). Since the speckle grain size was smaller than the acoustic focal spot size, a sub-diffraction acoustic resolution image was formed from analyzing second-order fluctuation of PA images with a number of random speckle illumination patterns. As illustrated in *Figure 2A,B*, this method achieved a resolution enhancement of about 1.4 times over conventional PACT. The second method relies on the fluctuation analysis of varying PA signals induced by flowing absorbing particles (12). With the natural motion of flowing particles, the fluctuation-analysis-based method is further simplified, and a long-coherence laser focus is no longer required for deep-tissue speckle illumination as in the first method. The second method can achieve a $\sqrt{n}$ resolution enhancement using n^{th}-order cumulant analysis. Nevertheless, the fluctuation-based methods are slow and likely to suffer from the natural motion artifacts for *in vivo*

applications, including the heart beating and breathing.

Inspired by blind speckle illumination in super-resolution fluorescence imaging, Murray *et al.* implemented this method to break the acoustic diffraction limit in PAI in scattering media (13,29). Encoded with unknown speckle illumination patterns, the generated PA image is a convolution of the system's PSF and the spatial product of speckle pattern and absorber distribution. Although the PA image reconstruction using this scheme is an ill-conditioned deconvolution process with a smooth kernel, Murray *et al.* assumed block sparsity and developed an efficient deconvolution algorithm called block-FISTA (fast iterative shrinkage-thresholding algorithm) to obtain high-resolution images. The PAT setup is similar to the fluctuation-analysis based method with speckle illumination. The experimental demonstration in *Figure 2C* clearly showed that this method has a much better resolution than the regular deconvoluted or averaged PA images. The 2D image formation (*Figure 2D*) with this method was also realized with a linear transducer array in an independent study by Hojman *et al.* (26).

Localization of sub-diffraction absorbers is the basis of stochastic super-resolution fluorescence microscopy (30,31), which has enabled *in vivo* sub-cellular biochemical research since 2006. The super-resolution localization images are constructed by superposition of a large number of isolated individual sources, which are otherwise not resolvable due to the diffraction limit. In the past two years, localization-based super-resolution ultrasound imaging has also been achieved through tracking microbubbles in deep vessels (32). Recently, two independent studies overcame the acoustic diffraction limit in PAI by localizing flowing optical absorbers (14,27). Vilov *et al.* performed a proof-of-principle experiment using microbeads flowing in microfluidic channels and imaged by a 15-MHz linear transducer array (27), while Dean-Ben *et al.* demonstrated 3D imaging of a knotted pipette filled with flowing microbeads imaged by a 4 MHz semi-spherical transducer array (14). In both studies, sparsely distributed PA point sources, i.e., microbeads, were driven through the micro-tubing or micro-channels and repeatedly captured in sequential PA images. The localization images were constructed through superposition of the central positions of point sources extracted from each PA image (*Figure 3A,B,C*). While the point sources were blurred in each conventional PA images due to acoustic diffraction limit, the localization image was able to break this limit and achieve sub-diffraction resolution (16,33). Nevertheless, the concept has only been demonstrated on simple phantoms without background signals or motion artifacts, and its applications for animal studies are expected to be more challenging due to reduced signal strength and image contrast.

Another way to achieve SR-PAI in deep tissue is to create a sub-acoustic-diffraction optical focus through optical wavefront shaping. Focusing light in highly scattering media has long been sought for deep-tissue imaging at optical resolution (34-37). Most of the reported wavefront shaping techniques rely on a guide-star inside the media to provide optical signal feedback (e.g., fluorescence, transmittance) for wavefront optimization. Similarly, Conkey *et al.* optimized optical wavefront using PA signals as the feedback (15). As illustrated in *Figure 3D*, the optical speckle pattern inside the ultrasound focal region was optimized using PA signal feedback through evolution algorithm, and finally reached sub-acoustic-diffraction optical focusing. When scanning the object with the optimized optical focusing, 2D PA images with sub-acoustic-diffraction resolution are formed. Using this method, Conkey *et al.* demonstrated a 13 μm resolution, which is much better than the conventional PAI (*Figure 3E*), but the speed for optimization and scanning was low. In future, with the advances in optical components and optimization algorithms, wavefront shaping in scattering media will be improved in its speed and robustness for SR-PAI in deep tissue.

Conclusions

In this concise review, we summarized various SR-PAI methods that have been explored to improve the resolution finer than either the optical or acoustic diffraction. *Table 1* lists these methods and compares their mechanisms, key performance, strength and weakness. The technological advances in SR-PAI have opened new possibilities for fundamental biological studies. Compared with conventional fluorescence-based super-resolution microscopy, SR-PAI is label-free and thus can minimize the possibility of introducing image artefacts during the labeling process (38). While other label-free imaging technologies such autofluorescence-based and phase-sensitive microscopy are limited to thin samples or superficial tissues (11,39,40), SR-PAI can provide functional and structural information by imaging endogenous chromophores (e.g., hemoglobin, melanin, lipids, DNA/RNA) or exogenous chromophores (e.g., nanoparticles, organic dyes, reporter gene products) at depths far beyond the optical diffusion limit (41). Mostly

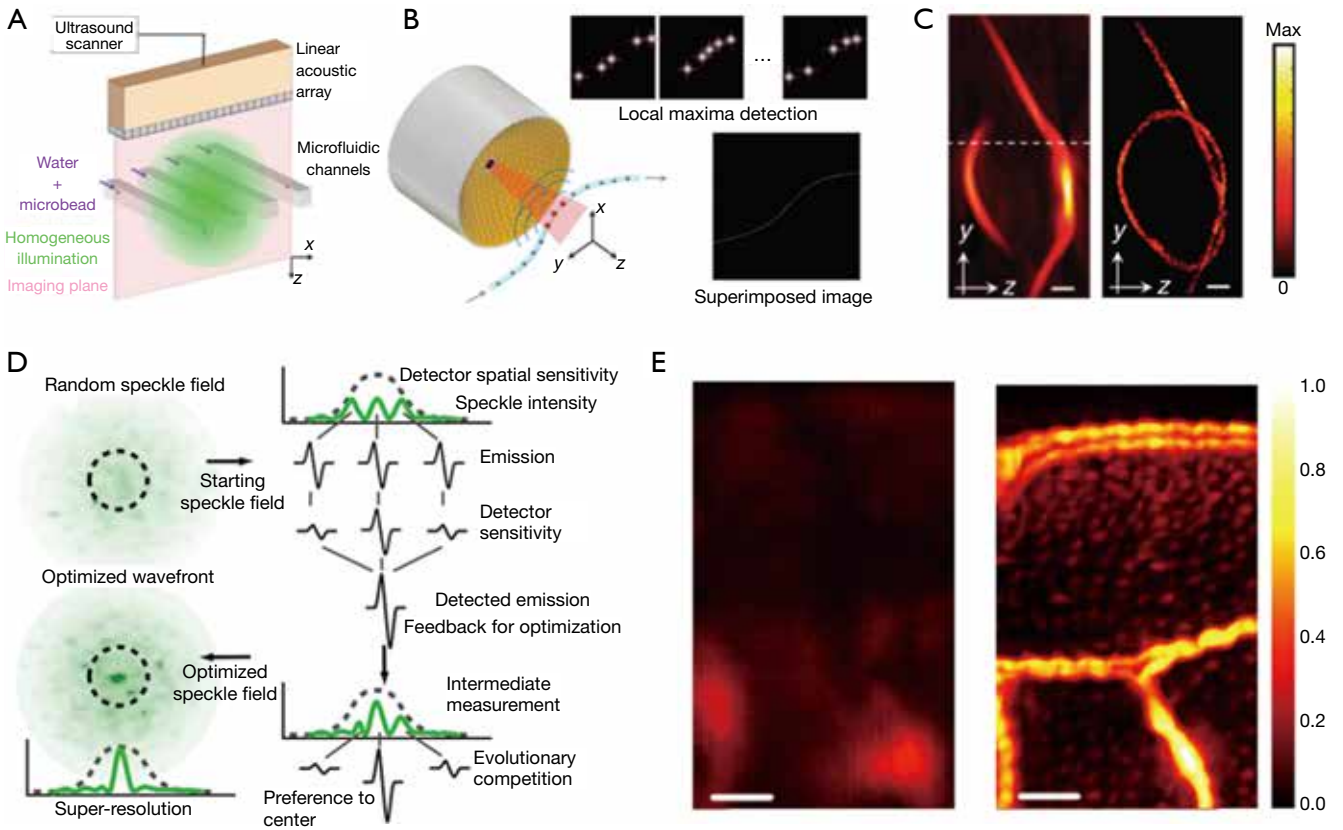

Figure 3 Sub-acoustic-diffraction PA imaging based on particle localization and wavefront shaping. (A,B) The experimental setup of localization PA imaging with a linear array (A) (27) and semi-spherical array (B) (14); (C) images of a knotted pipette tip (~220 μm in diameter) obtained by conventional PACT (left) and localization PA imaging (right). Scale bar: 600 μm. Figures adopted with permission from (14,27); (D) the principle of optical focusing in highly scattering media by wavefront shaping with PA feedback; (E) images of a sweat bee wing obtained by conventional AR-PAM (left) and PAM with optical focusing through wavefront shaping (right). Scale bar: 100 μm. Figures adopted with permission from (15). PA, photoacoustic; PACT, photoacoustic computed tomography; AR-PAM, acoustic-resolution photoacoustic microscopy.

excitingly, the novel AR-PAM and PACT technologies with finer resolutions than the acoustic diffraction can potentially benefit *in vivo* cancer diagnostics, hemodynamics studies, and neuroscience research.

Nevertheless, challenges largely remain for deep-tissue SR-PAI. Applying blind illumination for deep tissue imaging is difficult because of the large difference between the optical speckle grain dimensions and the acoustic focal spot size. Longer optical wavelengths and higher ultrasound frequency will be beneficial to overcome the difficulty in the future (26). In optical wavefront shaping, the greatest challenge is to focus the light inside the living biological tissue with fast decorrelation motions such as blood flow and breathing. The number of input modes and genetic algorithm iterations need to be decreased, at the price of focusing quality (15). To detect PA signal fluctuation induced by flowing particles, the number of characteristic images may limit the temporal resolution of the technique (12,25,42). Similarly, the time for localizing absorbing particles depends on the frame rate and the number of pixels per image. The temporal resolution can be optimized by increasing the particle density, but it is still challenging for real-time imaging (14). Future improvements in the SR-PAI methods are needed and more phantom and *in vivo* validations should be performed to strengthen these methods.

Table 1 Summary of methods used for SR-PAI

Depth regime	Imaging modality	Mechanism	Resolution		Imaging speed	Pros	Cons	Ref
			Lateral	Axial				
Ballistic	OR-PAM	Nonlinear photobleaching effect	90 nm	400 nm	Medium	Can be applied to both fluorescent and nonfluorescent samples. Capable of optical sectioning	The high frame number or excitation intensity may result in severe distortion between 'bleached' and 'unbleached' regions	(10)
		Nonlinear absorption coefficient	88 nm	–	Medium	High-order PA image leads to higher resolution. Capable of optical sectioning	Long imaging time, slow pixel-by-pixel high-order fitting, and potential heating and photobleaching damage to the sample with repeated excitation	(11)
Diffusive	AR-PAM	Deconvolution with blind speckle illumination	80 μm	–	Low	Uses blind structure illumination to achieve F imaging. Efficiently exploits dynamic temporal fluctuations	Requires sparsity of the structures The small fluctuations over a large background may be challenging under low SNR conditions	(13,26)
		Improved optical focus through wavefront shaping	30 μm	–	Low	Can create an optical focal spot five times smaller than the acoustic focal spot size in scattering medium	Feedback optimization of wavefront for each pixel is very slow	(15)
	PACT (OAT)	Photoacoustic signal fluctuation induced by flowing particles	72 μm	–	Low	Free from common photoacoustic imaging artifacts caused by band-limited acoustic detection. Potential for label-free microvessel imaging	Lacks high temporal resolution intrinsically. Requires high frame rate for fluctuation analysis	(12)
		Photoacoustic signal fluctuation with multiple speckle illumination	160 μm	–	Low	Simple experimental setup. Reveals high spatial frequencies by considering fluctuations in PA images	Requires a very large number of frames for high SNR	(25)
		Localization of flowing absorbing particles	78 μm	112 μm	Very low	Not affected by flow rate. Enhances the visibility of structures under limited-view conditions	Needs high frame rate and high particle density	(14,27)

SR-PAI, super-resolution photoacoustic imaging; OR-PAM, optical-resolution photoacoustic microscopy; AR-PAM, acoustic-resolution photoacoustic microscopy; PACT, photoacoustic computed tomography; SNR, signal-to-noise ratio.

Acknowledgements

Funding: We would like to thank the support from Duke MEDx Basic Science Pilot Grant, Duke Center for Genomic and Computational Biology Faculty Pilot Research Grant, and American Heart Association Collaborative Sciences Award 18CSA34080277 (all to J Yao).

Footnote

Conflicts of Interest: The authors have no conflicts of interest to declare.

References

1. Xia J, Yao J, Wang LV. Photoacoustic tomography: principles and advances. Electromagn Waves (Camb) 2014;147:1-22.
2. Wang LV. Multiscale photoacoustic microscopy and computed tomography. Nat Photonics 2009;3:503-9.
3. Wang LV, Hu S. Photoacoustic tomography: in vivo imaging from organelles to organs. Science 2012;335:1458-62.
4. Yao J, Wang LV. Photoacoustic microscopy. Laser Photon Rev 2013;7:758-78.
5. Hu S, Maslov K, Wang LV. Second-generation optical-resolution photoacoustic microscopy with improved sensitivity and speed. Opt Lett 2011;36:1134-6.
6. Maslov K, Zhang HF, Hu S, Wang LV. Optical-resolution photoacoustic microscopy for in vivo imaging of single capillaries. Opt Lett 2008;33:929-31.
7. Zhang HF, Maslov K, Stoica G, Wang LV. Functional photoacoustic microscopy for high-resolution and noninvasive in vivo imaging. Nat Biotechnol 2006;24:848-51.
8. Maslov K, Stoica G, Wang LV. In vivo dark-field reflection-mode photoacoustic microscopy. Opt Lett 2005;30:625-7.
9. Cox B, Laufer JG, Beard PC, Arridge SR. Quantitative spectroscopic photoacoustic imaging: a review. J Biomed Opt 2012;17:061202.
10. Yao J, Wang L, Li C, Zhang C, Wang LV. Photoimprint photoacoustic microscopy for three-dimensional label-free subdiffraction imaging. Phys Rev Lett 2014;112:014302.
11. Danielli A, Maslov KI, Garcia-Uribe A, Winkler AM, Li C, Wang L, Chen Y, Dorn GW, Wang LV. Label-free photoacoustic nanoscopy. J Biomed Opt 2014;19:086006.
12. Chaigne T, Arnal B, Vilov S, Bossy E, Katz O. Super-resolution photoacoustic imaging via flow-induced absorption fluctuations. Optica 2017;4:1397-404.
13. Murray TW, Haltmeier M, Berer T, Leiss-Holzinger E, Burgholzer P. Super-resolution photoacoustic microscopy using blind structured illumination. Optica 2017;4:17-22.
14. Dean-Ben XL, Razansky D. Localization optoacoustic tomography. Light Sci Appl 2018;7:18004.
15. Conkey DB, Caravaca-Aguirre AM, Dove JD, Ju H, Murray TW, Piestun R. Super-resolution photoacoustic imaging through a scattering wall. Nat Commun 2015;6:7902.
16. Bower AJ, Chidester B, Li J, Zhao Y, Marjanovic M, Chaney EJ, Do MN, Boppart SA. A quantitative framework for the analysis of multimodal optical microscopy images. Quant Imaging Med Surg 2017;7:24-37.
17. Kam J, Zhang Q, Lin J, Liu J, Wang RK, Rezaei K. Optical coherence tomography based microangiography findings in hydroxychloroquine toxicity. Quant Imaging Med Surg 2016;6:178-83.
18. Le N, Song S, Zhang Q, Wang RK. Robust principal component analysis in optical micro-angiography. Quant Imaging Med Surg 2017;7:654-67.
19. Jacobson K, Elson E, Koppel D, Webb W. Fluorescence photobleaching in cell biology. Nature 1982;295:283.
20. Bates M, Huang B, Dempsey GT, Zhuang X. Multicolor super-resolution imaging with photo-switchable fluorescent probes. Science 2007;317:1749-53.
21. Subach OM, Patterson GH, Ting L-M, Wang Y, Condeelis JS, Verkhusha VV. A photoswitchable orange-to-far-red fluorescent protein, PSmOrange. Nat Methods 2011;8:771-7.
22. Larina IV, Larin KV, Esenaliev RO. Real-time optoacoustic monitoring of temperature in tissues. J Phys D Appl Phys 2005;38:2633.
23. Wang LV, Wu H. Biomedical optics: principles and imaging. John Wiley & Sons; 2012.
24. Siegman AE. Lasers university science books. Mill Valley, CA 1986;37:208.
25. Chaigne T, Gateau J, Allain M, Katz O, Gigan S, Sentenac A, Bossy E. Super-resolution photoacoustic fluctuation imaging with multiple speckle illumination. Optica 2016;3:54-7.
26. Hojman E, Chaigne T, Solomon O, Gigan S, Bossy E, Eldar YC, Katz O. Photoacoustic imaging beyond the acoustic diffraction-limit with dynamic speckle illumination and sparse joint support recovery. Opt Express 2017;25:4875-86.
27. Vilov S, Arnal B, Bossy E. Overcoming the acoustic diffraction limit in photoacoustic imaging by the localization of flowing absorbers. Opt Lett 2017;42:4379-82.
28. Dertinger T, Colyer R, Iyer G, Weiss S, Enderlein J. Fast, background-free, 3D super-resolution optical fluctuation imaging (SOFI). Proc Natl Acad Sci U S A 2009;106:22287-92.
29. Mudry E, Belkebir K, Girard J, Savatier J, Le Moal E, Nicoletti C, Allain M, Sentenac A. Structured illumination microscopy using unknown speckle patterns. Nat Photonics 2012;6:312-5.
30. Betzig E, Patterson GH, Sougrat R, Lindwasser OW, Olenych S, Bonifacino JS, Davidson MW, Lippincott-Schwartz J, Hess HF. Imaging intracellular fluorescent

proteins at nanometer resolution. Science 2006;313:1642-5.
31. Rust MJ, Bates M, Zhuang X. Sub-diffraction-limit imaging by stochastic optical reconstruction microscopy (STORM). Nat Methods 2006;3:793.
32. Errico C, Pierre J, Pezet S, Desailly Y, Lenkei Z, Couture O, Tanter M. Ultrafast ultrasound localization microscopy for deep super-resolution vascular imaging. Nature 2015;527:499.
33. Fehm TF, Deán-Ben XL, Ford SJ, Razansky D. In vivo whole-body optoacoustic scanner with real-time volumetric imaging capacity. Optica 2016;3:1153-9.
34. Vellekoop IM, Mosk A. Focusing coherent light through opaque strongly scattering media. Opt Lett 2007;32:2309-11.
35. Yaqoob Z, Psaltis D, Feld MS, Yang C. Optical phase conjugation for turbidity suppression in biological samples. Nat Photonics 2008;2:110.
36. Vellekoop IM, Lagendijk A, Mosk A. Exploiting disorder for perfect focusing. Nat Photonics 2010;4:320.
37. Bertolotti J, van Putten EG, Blum C, Lagendijk A, Vos WL, Mosk AP. Non-invasive imaging through opaque scattering layers. Nature 2012;491:232.
38. Huang B, Bates M, Zhuang X. Super-resolution fluorescence microscopy. Annu Rev Biochem 2009;78:993-1016.
39. Bierwagen J, Testa I, Fölling J, Wenzel D, Jakobs S, Eggeling C, Hell SW. Far-field autofluorescence nanoscopy. Nano Lett 2010;10:4249-52.
40. Cotte Y, Toy F, Jourdain P, Pavillon N, Boss D, Magistretti P, Marquet P, Depeursinge C. Marker-free phase nanoscopy. Nat Photonics 2013;7:113.
41. Beard P. Biomedical photoacoustic imaging. Interface Focus 2011;1:602-31.
42. Gateau J, Chaigne T, Katz O, Gigan S, Bossy E. Improving visibility in photoacoustic imaging using dynamic speckle illumination. Opt Lett 2013;38:5188-91.

Cite this article as: Shi J, Tang Y, Yao J. Advances in super-resolution photoacoustic imaging. Quant Imaging Med Surg 2018;8(8):724-732. doi: 10.21037/qims.2018.09.14

Original Article

Responsive alginate-cisplatin nanogels for selective imaging and combined chemo/radio therapy of proliferating macrophages

Suk Ho Hong[1], Yan Li[1], Joo Beom Eom[2], Yongdoo Choi[1]

[1]Biomarker Branch, National Cancer Center, Goyang-si, Gyeonggi-do, Korea; [2]Medical Photonics Research Center, Korea Photonics Technology Institute (KOPTI), Gwangju, Korea

Correspondence to: Yongdoo Choi. Biomarker Branch, National Cancer Center, Goyang-si, Gyeonggi-do 10408, Korea. Email: ydchoi@ncc.re.kr; Joo Beom Eom. Medical Photonics Research Center, Korea Photonics Technology Institute (KOPTI), Gwangju 61007, Korea. Email: jbeom@kopti.re.kr.

Background: Atherosclerosis is a major global health concern. Targeting macrophages is hypothesized as an alternative treatment for atherosclerosis.

Methods: We synthesized alginate-based cisplatin-loaded nanogels (TANgel) as a pH-responsive drug-releasing theranostic nanoplatform for macrophage cells. Carboxylic acid groups of alginic acid were modified with iminodiacetic acid (IDA) to enhance chelation of platinum ions. The near infrared (NIR) fluorophore ATTO655 was conjugated to the modified alginic acid. Cisplatin was used as an antiproliferation drug and as a crosslinking agent between alginate molecules to form TANgel. Release behavior of cisplatin from TANgel was analyzed under different pH conditions. Cellular uptake and therapeutic efficacy of TANgel were tested in the macrophage cell line J774A.1 and normal human cell lines such as HDMVECn.

Results: The nanogel had a narrow size distribution of approximately 100 nm. The nanogel showed highly pH-responsive drug release behavior. All incorporated cisplatin was released at pH 5 within 48 h, while less than 15% was released at pH 7.4. The nanogel was preferentially taken up by J774A.1 cells compared to normal human cells, enabling selective NIR fluorescence imaging and chemotherapy of macrophage cells. In addition, the nanogel formulation lowered the therapeutic concentration of the drug with and without low dose radiation therapy (RT) compared to the free drug form.

Conclusions: This nanogel system may have potential utility for selective NIR fluorescence imaging and combined chemo/radio therapy of proliferating macrophage cells in atherosclerotic regions, allowing for reduction of systemic toxicity.

Keywords: Alginic acid; atherosclerosis; cisplatin; combination therapy; macrophage; theranostic

Submitted Aug 29, 2018. Accepted for publication Sep 06, 2018.
doi: 10.21037/qims.2018.09.01
View this article at: http://dx.doi.org/10.21037/qims.2018.09.01

Introduction

Atherosclerosis is a disease where lipids and fibrous elements accumulate in arteries and is the underlying cause of more than 50% of deaths in the westernized world (1). The early stages of atherosclerosis are marked by subendothelial accumulation of cholesterol-engorged macrophages, later joined by smooth muscle cells and necrotic debris leading to plaque formation (1,2). As macrophages play a pivotal role in development of atherosclerosis as well as atheroma plaque destabilization and rupture, which in turn leads frequently to thrombo-occlusive complications including strokes and myocardial infarction, macrophages may be a valuable therapeutic target. Indeed, previous studies support targeting macrophages as a promising strategy for atherosclerosis treatment (2).

Recent studies have shown that the majority of macrophages in atherosclerotic lesions originate from

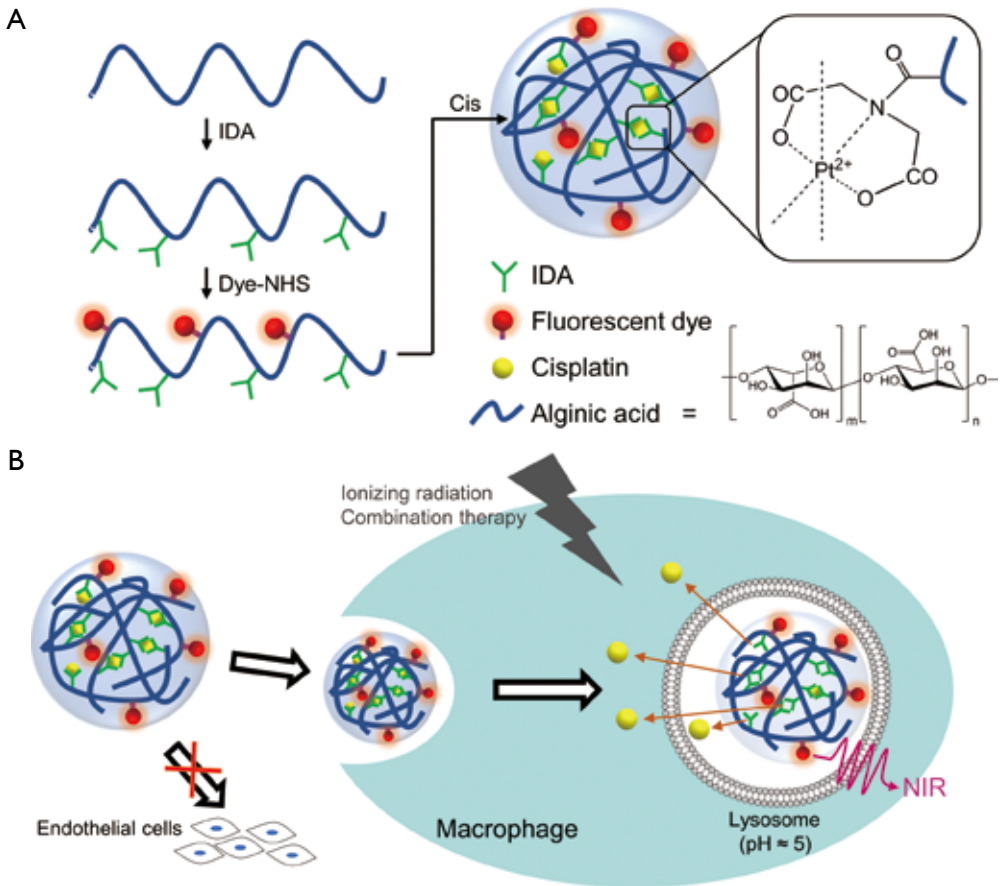

Figure 1 Synthesis and mechanism of action of theranostic alginate-based cisplatin-loaded nanogel (TANgel). (A) Synthesis steps of alginate derivative and TANgel. On the right side, the chelation of platinum to polymer is explained. (B) Schematic diagram of TANgel taken up selectively by macrophages and releasing cisplatin and fluorescence, enabling selective imaging and combined chemo/radio therapy. IDA, iminodiacetic acid.

local proliferation rather than inflammatory monocyte recruitment from the bloodstream (3). This suggests that use of antiproliferation agents may be an effective and novel approach to treat atherosclerosis. Antitumor drugs such as doxorubicin (4) and photodynamic therapy (5) are examples of antiproliferation treatments. However, development of theranostic agents which can selectively target and treat proliferating macrophages in atherosclerotic regions is an ongoing challenge.

Cisplatin is a widely used platinum-based drug included in many standard regimens for cancer treatment, sometimes in combination with radiotherapy. Cisplatin acts on cells by crosslinking DNA, resulting in DNA damage. Cisplatin also has radiosensitizing properties. The tendency of cisplatin to form crosslinks with carboxyl or sulfhydryl groups in proteins or specific nitrogen atoms in DNA has led to use in incorporation in polymers (6) and other carriers to overcome drug resistance and drug side effects such as nephrotoxicity (7,8). Alginic acid is a polymer obtained from seaweed known for being inexpensive, nontoxic, and biocompatible (9). Alginate gelates in the presence of cations such as Ca^{2+} (9). However, we demonstrated that it does not readily gelate with Pt^{2+} for nanogel synthesis.

In this study, we synthesized theranostic alginate-based nanogels (TANgel) as a pH-responsive drug-releasing theranostic nanoplatform for macrophage cells (*Figure 1*). Initially, carboxylic acid groups of alginate were modified with iminodiacetic acid (IDA) to enhance chelation with platinum ions (10,11). Near infrared (NIR) fluorophore ATTO655 was conjugated to the modified alginic acid. Then, cisplatin, which functions as an antiproliferation drug, was used to crosslink alginate molecules to form TANgel (*Figure 1A*). This was the first synthesis of TANgel. We hypothesized that TANgel would be stable

in blood circulation, minimizing systemic toxicity of cisplatin. As atherosclerotic plaques have leaky vascular structure resulting in enhanced permeability (12,13), TANgel can accumulate in leaky regions and be actively taken up by macrophage cells. In macrophages, release of cisplatin may be triggered at lysosomal pH (pH 4.5–5.5) because of pH-dependent decreased affinity of IDA (as well as carboxylic acids of alginic acid) for metal ions (14). The sites at which this occurs would then be detected through NIR fluorescence imaging. In addition, combined treatment with radiation therapy (RT) may further reduce the therapeutic concentration of the drug with regard to reducing macrophage proliferation (*Figure 1B*). Therefore, TANgel may be useful for selective imaging and combined chemo/radio therapy of proliferating macrophage cells in atherosclerotic regions with reduced systemic toxicity.

Methods

Materials

IDA, sodium alginate (MW =190 kDa), 1-ethyl-3-(3-dimethylaminopropyl)carbodiimide (EDC), ethylenediamine, ATTO655-NHS ester, cisplatin [*cis*-diamminedichloridoplatinum (II)], and *o*-phenylenediamine (OPDA) were purchased from Sigma-Aldrich (St. Louis, MO, USA). Dialysis membrane (MWCO =10 kDa) was purchased from Repligen (Waltham, MA, USA) and dialysis tubing (MWCO =12 kDa) was purchased from Thermo Fisher Scientific (Waltham, MA, USA).

Synthesis of IDA-modified alginic acid (Alg-IDA)

IDA was attached to the alginic acid backbone by utilizing EDC. Sodium alginate (200 mg) was dissolved in 10 mL of deionized (DI) water. Five milliliters of EDC aqueous solution (200 mM) was added and the mixture was adjusted to pH 6 by addition of 0.1 M hydrochloric acid. After stirring for 45 min, IDA (200 mg) was dissolved in 4 mL of sodium hydroxide solution (0.1 M), and the solution was added to the mixture in a dropwise manner. The mixture was re-adjusted to pH 6 and stirred for 3 h. Following stirring, the mixture was dialyzed (MWCO =15 kDa) in 1 mM hydrochloric acid for 2 days, in 1 mM hydrochloric acid +1% sodium chloride solution for 1 day, then in DI water for 1 day. Finally, the product was freeze-dried and stored. To synthesize the Alg-IDA-dye conjugate, one-tenth of the IDA solution was combined with equimolar ethylenediamine (11 mg). Two and one-half milliliters of the resulting product was concentrated to a volume of 0.5 mL using a centrifugal filter, to which 2 mL phosphate buffer (pH 8.5) and 1 µmol ATTO655-NHS ester was added. The mixture was shaken for 1 h, then dialyzed (MWCO = 10 kDa) in DI water for 2 days. The product was freeze-dried for storage.

Preparation of TANgel

Cisplatin was dissolved in DI water at 5 mg/mL and preheated to 90 ℃ for dissolution. Alg-IDA and Alg-IDA-dye, at a mass ratio of 9:1, were dissolved in water to a final concentration of 2 mg/mL. Then 0.2 mL of cisplatin solution was mixed with 0.8 mL of Alg-IDA/Alg-IDA-dye solution, and the mixture was incubated at 95 ℃ for 1 h. Following incubation, the mixture was cooled on ice for 15 min. The mixture was then dialyzed (MWCO =2 kDa) in DI water for 4 h.

Characterizations

UV-Vis absorption spectra of free dye, Alg-IDA-dye, and TANgel were obtained using a UV-Vis spectrophotometer DU730 (Beckman Coulter, USA). Fluorescence spectra of the solutions (λ_{ex} =655 and 710 nm) were obtained on a multifunctional microplate reader (Safire 2, Tecan, Switzerland). Scanning electron microscope (SEM) images of nanoparticles were obtained using a JEM-7800F field emission SEM (JEOL, Japan). EDS data was obtained using an X-max (Oxford Instruments, UK) analyzer attached to a JEM-F200 (JEOL) transmission electronic microscope (TEM) in scanning TEM mode. Dynamic light scattering (DLS) and zeta potential analysis were performed on a Zetasizer Nano-ZS (Malvern Instruments, UK). Inductively coupled plasma mass spectrometry (ICP-MS) measurement was performed on a NexION 300 (PerkinElmer, USA). Cisplatin equivalent concentration was determined using ICP-MS results and the freeze-dried mass of TANgel. Fluorescence photographs were taken with *in vitro* imaging system (IVIS) Lumina XR (Caliper Life Science, USA).

In vitro drug release test

Release of cisplatin from TANgel was analyzed at different pH conditions. TANgel solution (625 µg/250 µL) was transferred to dialysis microtubes (MWCO =12 kDa) and immersed in 40 mL of phosphate buffer solutions (0.1 M)

at pH 7.4 or pH 5 and shaken gently. At each time point 1.5 mL of buffer solution was collected and 1.5 mL of fresh buffer was added back. The amount of cisplatin in each sample was determined with a modified version of the OPDA assay (15). Total cisplatin released was calculated cumulatively. Experiments were performed in triplicate.

Cell culture

A Murine macrophage cell line (J774A.1), a human primary dermal microvascular endothelial cell line (HDMVECn), a human primary dermal fibroblast cell line (HDF), and a human primary coronary artery smooth muscle cell line (HCASMC) were acquired from ATCC (American Type Culture Collection, Manassas, VA, USA). J774A.1 and HDF cells were maintained in Dulbecco's Modified Eagle Medium (DMEM; Thermo Fisher Scientific) supplemented with 10% fetal bovine serum (FBS) and 1% antibiotic and antimycotic (Thermo Fisher Scientific). HDMVECn and HCASMC cells were maintained in vascular cell basal medium plus microvascular endothelial growth kit (ATCC). Cells were incubated in a humidified incubation chamber containing 5% CO_2.

Cell uptake assay

J774A.1 and HDMVECn cells were plated in an 8-well Lab-Tek II chambered glass (Thermo Fisher Scientific) at a density of 5×10^4 cells/well, and incubated for 24 h to allow cell attachment. TANgel solution was diluted with the appropriate cell culture medium to achieve a concentration of 2 μM Cis equivalent. The existing culture medium was replaced with 200 μL of fresh medium containing TANgel, and cells were incubated for 24 h. Untreated control cells were incubated with cell culture medium without TANgel for 24 h. All cells were washed 3 times with fresh culture medium and stained with 50 nM Lysotracker Red DND-99 (Thermo Fisher Scientific). Fluorescence images of the cells (λ_{ex} =633 nm, λ_{em} =652–747 nm for TANgel; λ_{ex} =561 nm, λ_{em} =579–633 nm for Lysotracker) were obtained using confocal laser scanning microscopy (LSM 780, Carl Zeiss, Germany). All fluorescence images for TANgel were taken using identical settings for comparison.

Cytotoxicity assay

J774A.1 cells were seeded in a 96-well plate at a density of 5×10^3 cells/well. HDMVECn, HDF and HCASMC cells were seeded in a 96-well plate at a density of 1×10^4 cells/well. All cells were incubated for 24 h to allow cell attachment. TANgel and free Cis were diluted in cell culture medium to obtain equivalent concentrations of 0.1, 0.2, 0.5, 1 and 2 μM Cis for J774A.1 experiments, and concentrations of 1 and 2.5 μM Cis for HDMVECn, HDF, and HCASMC experiments. The existing culture medium was replaced with 100 μL of the appropriate media. Cells were incubated for 24 h then washed and the media in each well exchanged with fresh drug-free cell culture medium. To evaluate the effect of TANgel on chemo/radio therapy, J774A.1 cells were treated with TANgel or free Cis in DMEM described above for 24 h. Following treatment, the culture media were exchanged with fresh drug-free media. Cells were then irradiated with ionizing radiation. Radiation treatments were performed using a XenX irradiator platform (Xstrahl, UK) to deliver a total X-ray dose of 3 Gy.

Following radiation, cells were incubated for 72 h, and cell viability was analyzed using a CCK-8 assay kit (Dojindo Laboratories, Japan). Absorbance of each sample was measured at 450 nm using a microplate reader. Untreated control cells were used as a reference for 100% viable cells, and their medium served as the background. Data are expressed as mean ± SD of 6 data samples.

Live cell proliferation assay

The effect of TANgel or free Cis with or without radiation treatment on the rate of cell proliferation was evaluated. Cells were seeded in 96-well plates at a density of 5,000 cells/well and incubated overnight for cell attachment. Cells were treated with TANgel or free Cis (0.2 or 2 μM, respectively) for 24 h. Culture media was replaced, and cells were irradiated with ionizing radiation and were analyzed every 2 h for 72 h using an IncuCyte ZOOM live cell analysis device (Essen BioScience, Ann Arbor, MI, USA). All experiments were carried out in triplicate. Data are expressed as mean ± SD of 4 data samples.

Statistical analysis

Statistical analysis was performed using Student's *t*-test.

Results

To enhance cisplatin-binding performance of the alginic acid backbone, we attached IDA to carboxylic acids of alginate using carbodiimide. Success of the reaction was confirmed

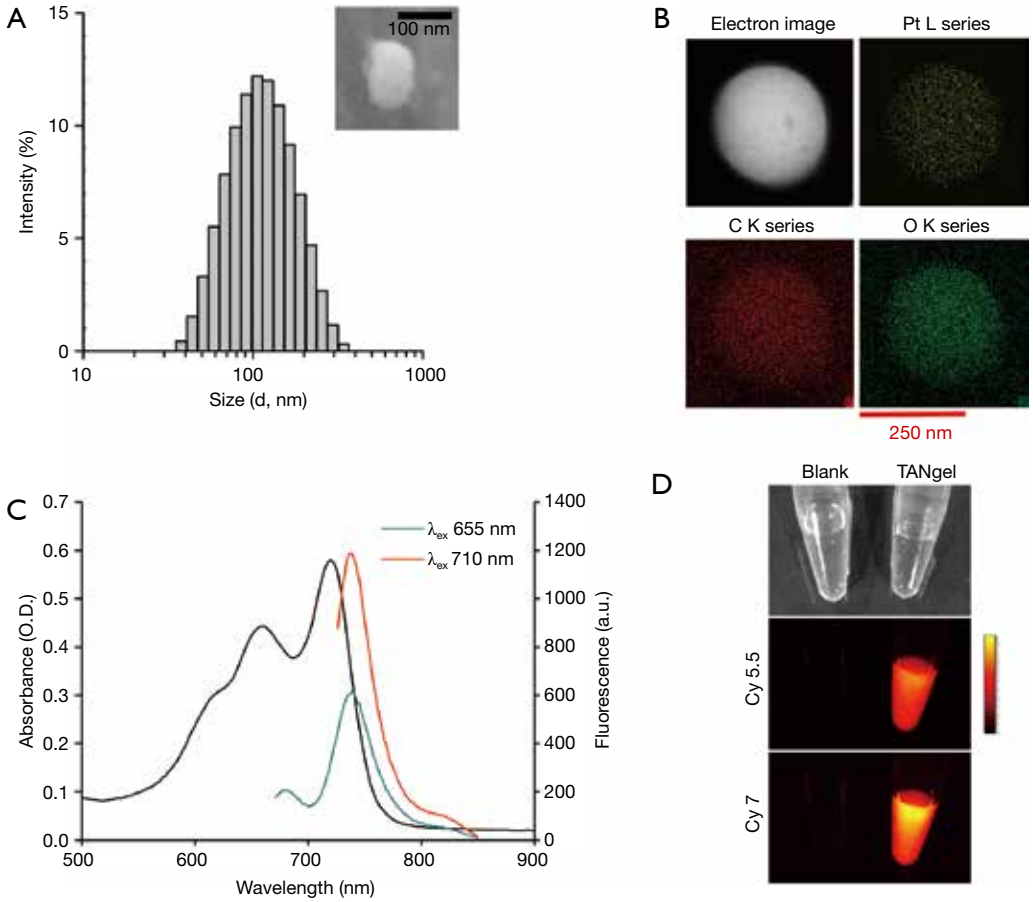

Figure 2 Characterization of TANgel. (A) Hydrodynamic size distribution and SEM image (inset) of TANgel. (B) EDS map for elements Pt, C, and O of TANgel. (C) UV-Vis absorption spectrum and fluorescence spectra upon excitation at two wavelengths (655 and 710 nm) of TANgel. (D) Photographic image and fluorescence images in two different channels (Cy 5.5: λ_{ex} =630–650 nm, λ_{em} =690–730 nm, Cy 7: λ_{ex} = 710–730 nm, λ_{em} =770–810 nm) of a blank solution (phosphate buffered saline) and TANgel solution. TANgel, theranostic alginate-based nanogels; SEM, scanning electron microscope.

by identification of Alg-IDA by ^{1}H-NMR (*Figure S1*). To allow for imaging, Alg-IDA was further functionalized with amine groups via ethylenediamine, to which fluorescent dye molecules were attached by NHS ester reaction. After obtaining fluorescent alginate molecules (Alg-IDA-dye), nanogel synthesis was carried out by mixing cisplatin with Alg-IDA and Alg-IDA-dye, and heating the mixture at 95 °C for 1 h. The optimal ratio and concentrations of Alg-IDA species and cisplatin were determined in a preliminary experiment (data not shown). After formation, TANgel was characterized through multiple means. DLS measurements gave hydrodynamic sizes of 99.3 nm with a polydispersity index (PDI) of 0.177 and zeta potential of −28.8 mV (*Figure 2A*). To determine cisplatin loading, TANgel was evaluated by ICP-MS, with a result of 8.96±0.21 wt% of Pt content, which translates to a cisplatin loading efficiency of (13.78±0.32)%. Note that the Pt content agrees with the value obtained from energy-dispersive X-ray spectroscopy (EDS) which gave 13.99 wt% of Pt. EDS mapping also showed Pt atoms evenly distributed throughout the nanogel particle (*Figure 2B*). In UV-Vis absorbance and fluorescence spectra, new absorption and emission peaks emerged in the region of 710 and 740 nm, respectively (*Figure 2C*). NIR fluorescence imaging showed that the fluorescence from TANgel could be detected through a longer-wavelength channel where free dye molecules showed no emission (*Figure 2D*, *Figure S2*).

Analysis of dispersion stability of TANgel (*Figure S3*) showed that the solution remained stable for at least 7 days under ambient conditions. DLS measurement of the sample

at day 7 showed no notable changes to the hydrodynamic size distribution of the nanogels (*Figure S3B*). Likewise, nanogels suspended in physiological solution were stable for at least 10 days (*Figure S4*). We also evaluated the effect of exchanging medium with buffer solutions at pH 7.4 and pH 5, and demonstrated little change in size distribution of TANgel after 48 h (*Figure S5*).

Drug release profile was determined by placing TANgel solutions in dialysis tubes and shaking in phosphate buffer solutions at pH 7.4 or pH 5 (*Figure 3*). Cisplatin released much faster at pH 5, as expected, with all incorporated cisplatin released within 48 h. At pH 7.4, less than 15% was released within 48 h.

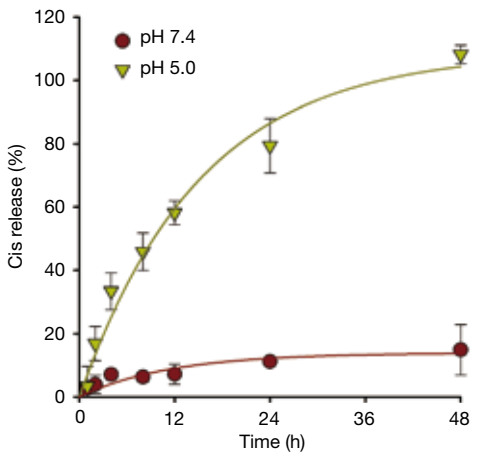

Figure 3 Cisplatin (Cis) release profile of TANgel at pH 7.4 and pH 5.0. TANgel, theranostic alginate-based nanogels.

We evaluated intracellular uptake of TANgel and its localization *in vitro*. As atherosclerosis is characterized by plaque build-up and macrophage accumulation in arteries, the J774A.1 macrophage cell line was chosen to model atherosclerosis. To model normal cells the HDMVECn human vascular endothelial cell line was used. Both cell types were treated with TANgel for 24 h. Cells were washed and NIR fluorescence images obtained (*Figure 4*). Although J774A.1 cells clearly displayed fluorescence signals from TANgel, HDMVECn cells did not display any significant fluorescence from TANgel. Also, in J774A.1 cells TANgel fluorescence was mainly coincident with fluorescence from Lysotracker, indicating that when TANgel is taken up by macrophage cells they are localized in lysosomes. As lysosomes have an acidic environment, TANgel can be expected to release cisplatin reliably because of its pH-responsiveness.

To test the potential of combination therapy on macrophage cells, *in vitro* toxicity was assessed (*Figure 5*). J774A.1 cells were treated with free cisplatin or TANgel over a concentration range of 0.1–2 μM. Half of the cells were subjected to RT (3 Gy). Cell viability was assayed after 3 days to evaluate DNA damage resulting from radiation and chemotherapy. Results showed that while TANgel showed similar toxicity in concentrations of 0.5 μM and above, at lower concentrations it was more effective at

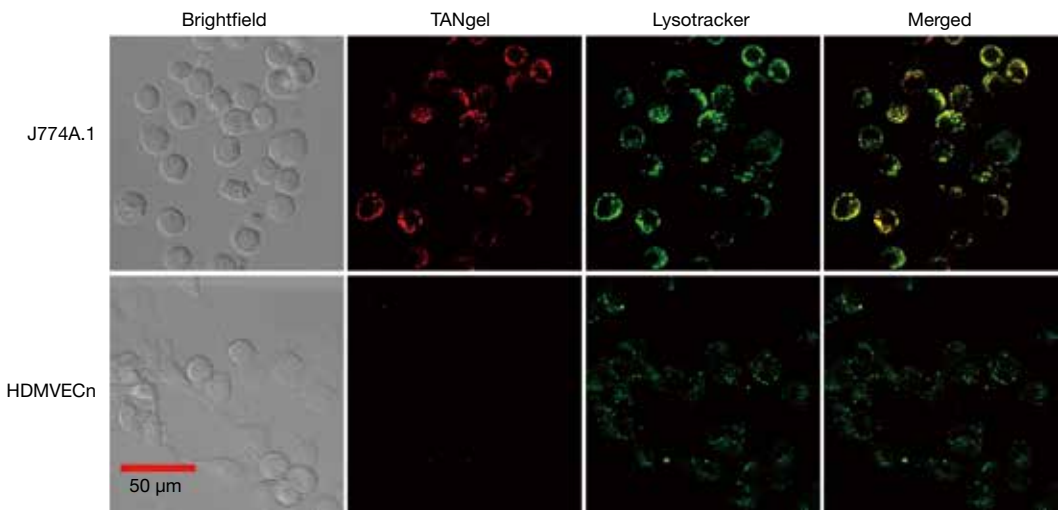

Figure 4 Cellular uptake of TANgel as observed by fluorescence. Confocal microscopy images of J774A.1 and HDMVECn cells were obtained after 24 h of treatment with TANgel followed by washing. Cells were costained with Lysotracker. TANgel, theranostic alginate-based nanogels.

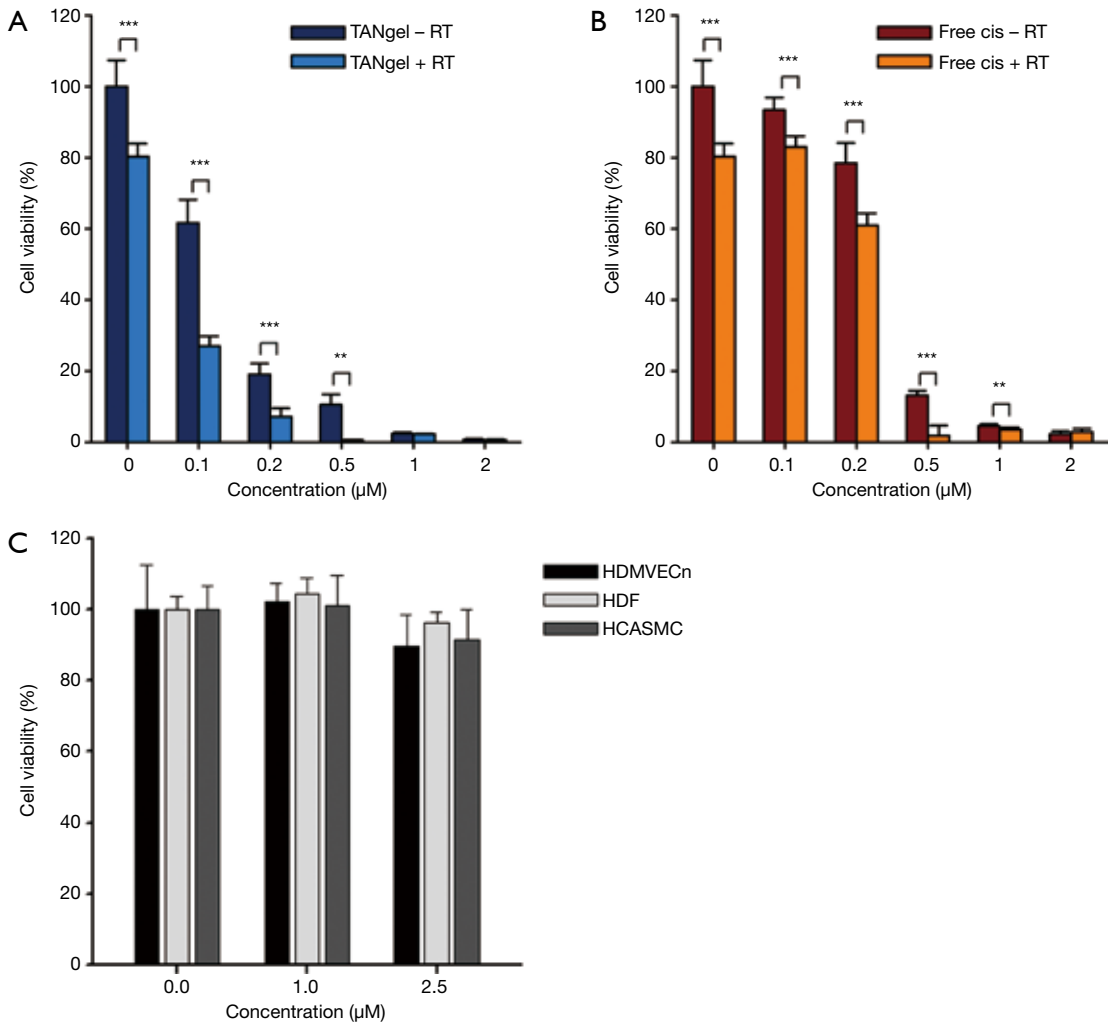

Figure 5 Viability of J774A.1 cells treated with (A) TANgel or (B) free Cis at various Cis equivalent concentrations, with or without radiotherapy (RT, 3 Gy). **, P<0.01, ***, P<0.001. (C) Viability of normal cell lines (HDMVECn, HDF, and HCASMC) treated with TANgel at various Cis equivalent concentrations. TANgel, theranostic alginate-based nanogels.

inhibiting cell viability, both with and without RT. Indeed, the IC_{50} of TANgel was calculated at 0.12 μM (cisplatin equivalent), lower than free cisplatin, which had an IC_{50} of 0.21 μM. This difference may be explained by the high uptake rate of TANgel and polymer ligands serving as protection against platinum drug detoxification by thiol residues and other chemical reactions. As a measure to increase the reliability of cytotoxicity data, J774A.1 cells were treated in a live cell analysis system (*Figure 6*). The results were similar to those seen using the more traditional assay above, including the result demonstrating higher treatment efficiency of TANgel at 0.2 μM.

To test selectivity of TANgel treatment, normal cell lines were treated with TANgel over a concentration range of 0–2.5 μM. In addition to HDMVECn, two different suitable primary human cell lines were used: HDF dermal fibroblasts and HCASMC coronary artery smooth muscle cells. Results showed no toxicity at 1 and 2.5 μM as the difference in cell viability compared to the control group was not statistically significant (P=0.128, 0.171, and 0.157, respectively). This result, combined with the selectivity of radiotherapy, signifies that collateral damage to other normal tissues can be minimized, during treatment with TANgel.

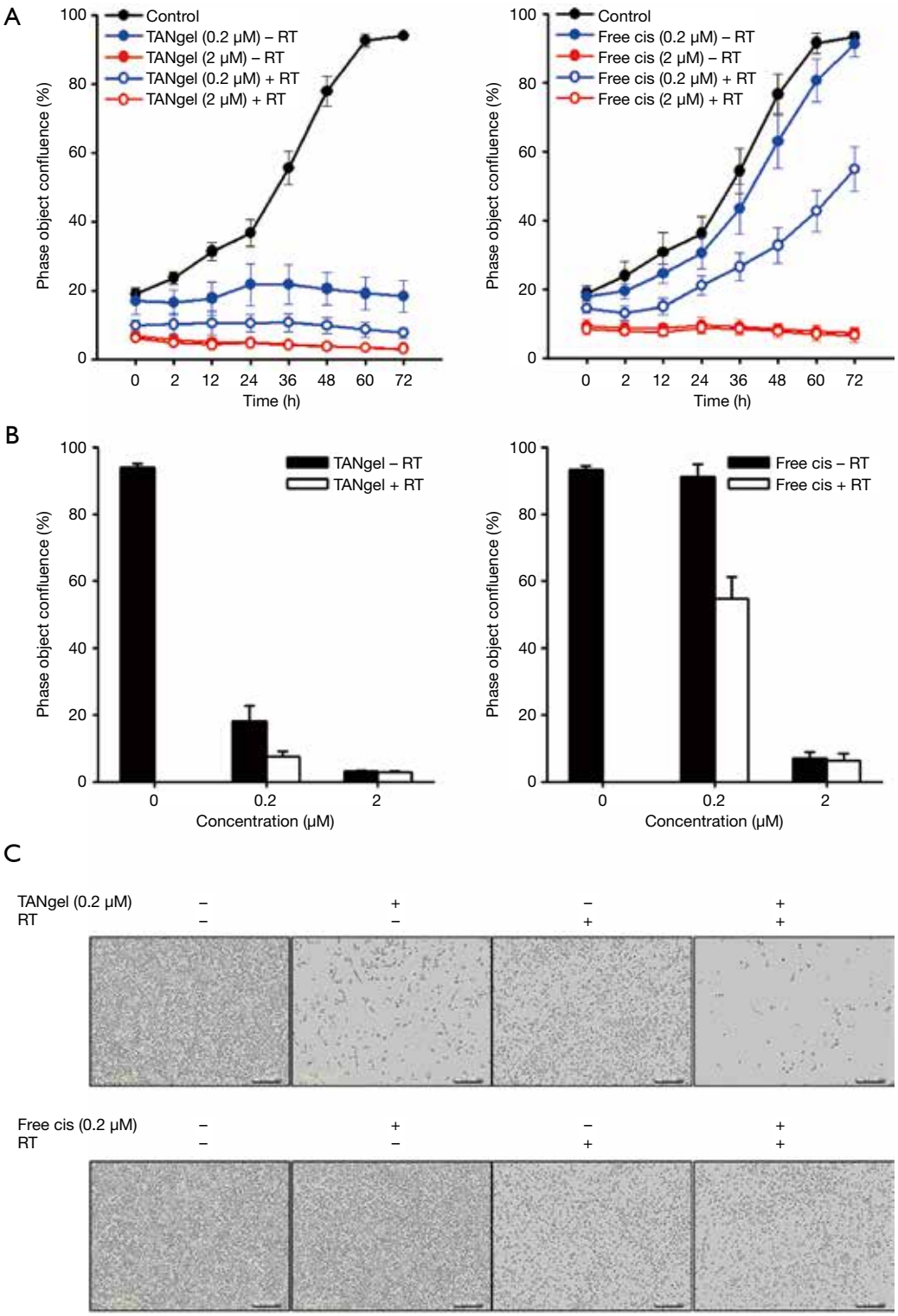

Figure 6 Effects of TANgel or free Cis at equivalent concentrations with or without radiation treatment on J774A.1 cell growth and morphology. (A) Growth measured using live cell imaging system. Cell growth was monitored for up to 72 h after TANgel or free Cis treatment with or without radiotherapy (RT). (B) Cell confluence assessed after 72 h in culture using live cell imaging system. (C) Cell morphology imaged after 72 h in culture using live cell imaging system. TANgel, theranostic alginate-based nanogels.

Discussion

Macrophages play a pivotal role in development of atherosclerosis. Proteases secreted from macrophages degrade the extracellular matrix in the lesions, leading to plaque rupture which can cause thromboembolic stroke or myocardial infarction. These characteristics highlight why development of theranostic agents which can selectively image and treat proliferating macrophages in the atherosclerotic region has great therapeutic potential.

We proposed cisplatin-loaded TANgel as a pH-responsive drug-releasing nanotheranostic for NIR fluorescence imaging and combined chemo/radio therapy of proliferating macrophages. Cisplatin was selected as an antiproliferation drug to treat macrophages and as a crosslinking agent of polymer backbones, enabling simple preparation of nanogels. As shown in *Figure 2A* and *Figure S3*, spherical shaped nanogels with a hydrodynamic size of 99.3 nm were formed, and TANgel was well dispersed in aqueous solutions without significant changes in hydrodynamic size for at least 7 d. This result suggests that cisplatin crosslinked efficiently, supporting the three-dimensional structure of TANgel.

As the alginate backbone is rich in carboxylic acid groups, alginate-based nanogels are likely to be pH-responsive. In a recent example, a doxorubicin-loaded alginate nanogel was prepared by mixing doxorubicin with alginate to take advantage of the electrostatic interaction between the molecules, followed by cross-linking with calcium ions. The release rate of doxorubicin from the nanogel was faster at pH 5.0 than at pH 7.4; however, a sizable amount of drug (~40%) was released after 24 h at pH 7.4 (16). In the current study, we showed that approximately 80% of incorporated cisplatin was released from TANgel at pH 5 within 24 h, while less than 12% was released at pH 7.4 within 24 h. We hypothesize that this results from use of an additional chelating moiety with pH-sensitivity and use of platinum ions in lieu of calcium ions. The difference in pH sensitivity supported the hypothesis that cisplatin will be preferentially released from TANgel in the acidic environment of intracellular lysosomes, but not at normal physiological pH (*Figure 1B*). Indeed, good therapeutic efficacy was obtained in TANgel-treated macrophages while no cytotoxicity was observed with up to 2.5 μM cisplatin equivalent treatment of various normal cells. This shows the potential utility of TANgel as a highly efficient pH-responsive drug delivery system for treatment of disease.

Recently, NIR fluorescence imaging has emerged as a promising technique for real-time visualization of sentinel lymph nodes, tumor tissue, and vital structures during intraoperative procedures, allowing for accurate guidance during surgery. Interestingly, the conjugated NIR dye ATTO655 in TANgel has additional excitation and emission wavelengths at a much longer NIR wavelength range compared to free ATTO655 dye. We speculate that this is due to J-aggregation of dye molecules inside TANgel (17). This shift in both the peak absorption and emission wavelength allowed us to take fluorescence images in the longer NIR wavelength region, where TANgel exhibited strong emission but the original dye molecules did not (*Figure 2D* and *Figure S2*). As TANgel was preferentially taken up by macrophage cells compared to normal vascular endothelial cells (*Figure 4*), TANgel may be useful in selective NIR fluorescence imaging of macrophage cells in atherosclerotic lesions.

In this article, we presented a theranostic nanoplatform in which the crosslinker doubles as a chemotherapy drug and a radiosensitizer. Synthesis of this theranostic nanoplatform was accomplished using a dramatically simplified novel approach. Synthesis of this nanogel is simple and proceeds under mild conditions. Our product, TANgel, was shown to have a good size distribution, stability, excellent pH-responsiveness, selective uptake, and interesting imaging properties owing to the shift in peak wavelengths. Simple components, practically consisting of only alginate derivative and cisplatin, would be beneficial for clinical use. In the future, additional drugs can be loaded onto this nanogel to target other ailments.

Acknowledgements

Funding: This work was supported by the National Research Foundation of Korea (NRF) (grants NRF-2015M2A2A6A01044298), and also from the project titled "Development of marine material based near infrared fluorophore complex and diagnostic imaging instruments [2018]" funded by the Ministry of Oceans and Fisheries, Korea.

Footnote

Conflicts of Interest: The authors have no conflicts of interest to declare.

References

1. Lusis AJ. Atherosclerosis. Nature 2000;407:233-41.

2. Wilson HM, Barker RN, Erwig LP. Macrophages: promising targets for the treatment of atherosclerosis. Curr Vasc Pharmacol 2009;7:234-43.
3. Robbins CS, Hilgendorf I, Weber GF, Theurl I, Iwamoto Y, Figueiredo JL, Gorbatov R, Sukhova GK, Gerhardt LM, Smyth D, Zavitz CC, Shikatani EA, Parsons M, van Rooijen N, Lin HY, Husain M, Libby P, Nahrendorf M, Weissleder R, Swirski FK. Local proliferation dominates lesional macrophage accumulation in atherosclerosis. Nat Med 2013;19:1166-72.
4. Park D, Cho Y, Goh SH, Choi Y. Hyaluronic acid-polypyrrole nanoparticles as pH-responsive theranostics. Chem Commun (Camb) 2014;50:15014-7.
5. Kim H, Kim Y, Kim IH, Kim K, Choi Y. ROS-responsive activatable photosensitizing agent for imaging and photodynamic therapy of activated macrophages. Theranostics 2013;4:1-11.
6. Zhang W, Tung CH. Cisplatin Cross-Linked Multifunctional Nanodrugplexes for Combination Therapy. ACS Appl Mater Interfaces 2017;9:8547-55.
7. Pabla N, Dong Z. Cisplatin nephrotoxicity: mechanisms and renoprotective strategies. Kidney Int 2008;73:994-1007.
8. Ma Pa, Xiao H, Li C, Dai Y, Cheng Z, Hou Z, Lin J. Inorganic nanocarriers for platinum drug delivery. Mater Today 2015;18:554-64.
9. Lee KY, Mooney DJ. Alginate: properties and biomedical applications. Prog Polym Sci 2012;37:106-26.
10. Yuchi A, Sato T, Morimoto Y, Mizuno H, Wada H. Adsorption mechanism of trivalent metal ions on chelating resins containing iminodiacetic Acid groups with reference to selectivity. Anal Chem 1997;69:2941-4.
11. Ohta S, Hiramoto S, Amano Y, Sato M, Suzuki Y, Shinohara M, Emoto S, Yamaguchi H, Ishigami H, Sakai Y, Kitayama J, Ito T. Production of Cisplatin-Incorporating Hyaluronan Nanogels via Chelating Ligand-Metal Coordination. Bioconjug Chem 2016;27:504-8.
12. Mause SF, Weber C. Intrusion through the fragile back door: immature plaque microvessels as entry portals for leukocytes and erythrocytes in atherosclerosis. J Am Coll Cardiol 2009;53:1528-31.
13. Lobatto ME, Fuster V, Fayad ZA, Mulder WJ. Perspectives and opportunities for nanomedicine in the management of atherosclerosis. Nat Rev Drug Discov 2011;10:835-52.
14. Chaberek Jr S, Martell AE. Stability of metal chelates. I. iminodiacetic and iminodipropionic acids. J Am Chem Soc 1952;74:5052-6.
15. Basotra M, Singh SK, Gulati M. Development and validation of a simple and sensitive spectrometric method for estimation of cisplatin hydrochloride in tablet dosage forms: application to dissolution studies. ISRN Anal Chem 2013;2013:936254.
16. Xue Y, Xia X, Yu B, Luo X, Cai N, Long S, Yu F. A green and facile method for the preparation of a pH-responsive alginate nanogel for subcellular delivery of doxorubicin. RSC Adv 2015;5:73416-23.
17. Würthner F, Kaiser TE, Saha-Möller CR. J-aggregates: from serendipitous discovery to supramolecular engineering of functional dye materials. Angew Chem Int Ed Engl 2011;50:3376-410.

Cite this article as: Hong SH, Li Y, Eom JB, Choi Y. Responsive alginate-cisplatin nanogels for selective imaging and combined chemo/radio therapy of proliferating acrophages. Quant Imaging Med Surg 2018;8(8):733-742. doi: 10.21037/qims.2018.09.01

Supplementary

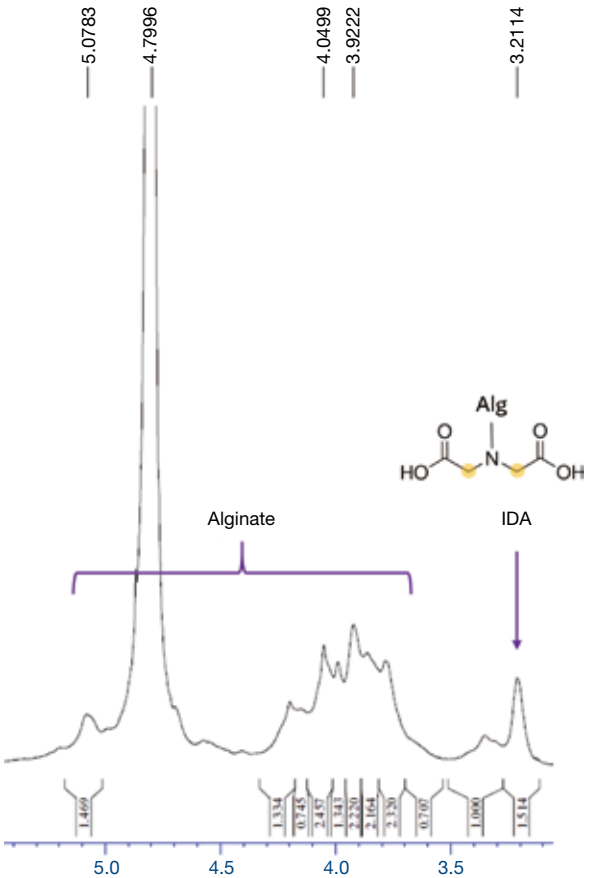

Figure S1 Proton nuclear magnetic resonance (NMR) spectrum of Alg-IDA in D_2O. NMR measurement was carried out on Avance 600 (Bruker, Germany) with operating frequency of 600 MHz. IDA, iminodiacetic acid.

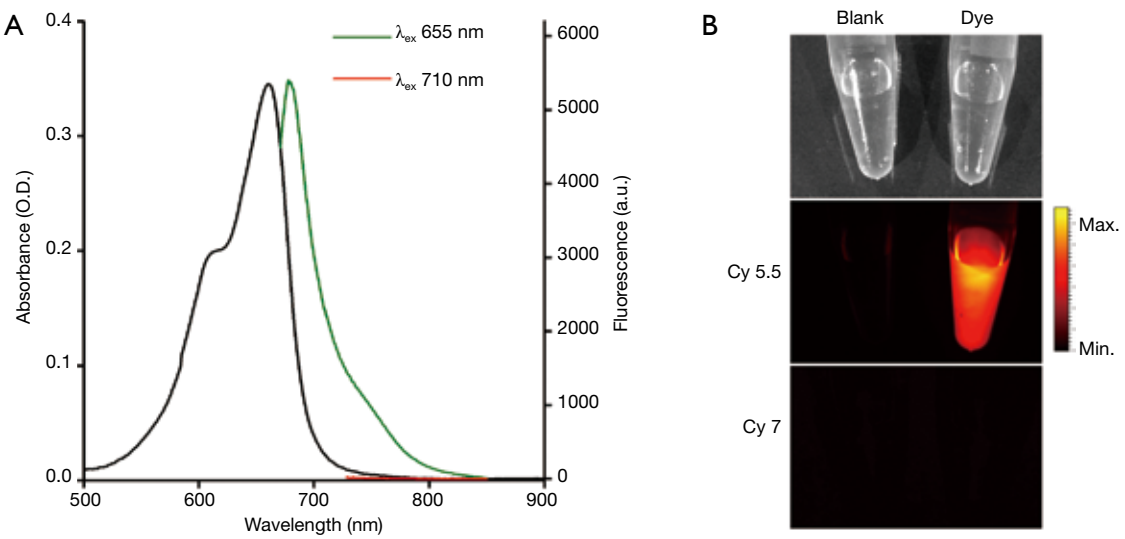

Figure S2 Optical properties of free ATTO655 dye. (A) UV-Vis absorption spectrum and fluorescence spectra of free ATTO655 dye upon excitation on two wavelengths (655 and 710 nm). (B) Photographic image and fluorescence images in two different channels (Cy 5.5: λ_{ex} =630–650 nm, λ_{em} =690–730 nm, Cy 7: λ_{ex} =710–730 nm, λ_{em} =770–810 nm) of a blank solution (phosphate buffered saline) and free ATTO655-NH2 solution. No fluorescence signal was observed in Cy 7 channel.

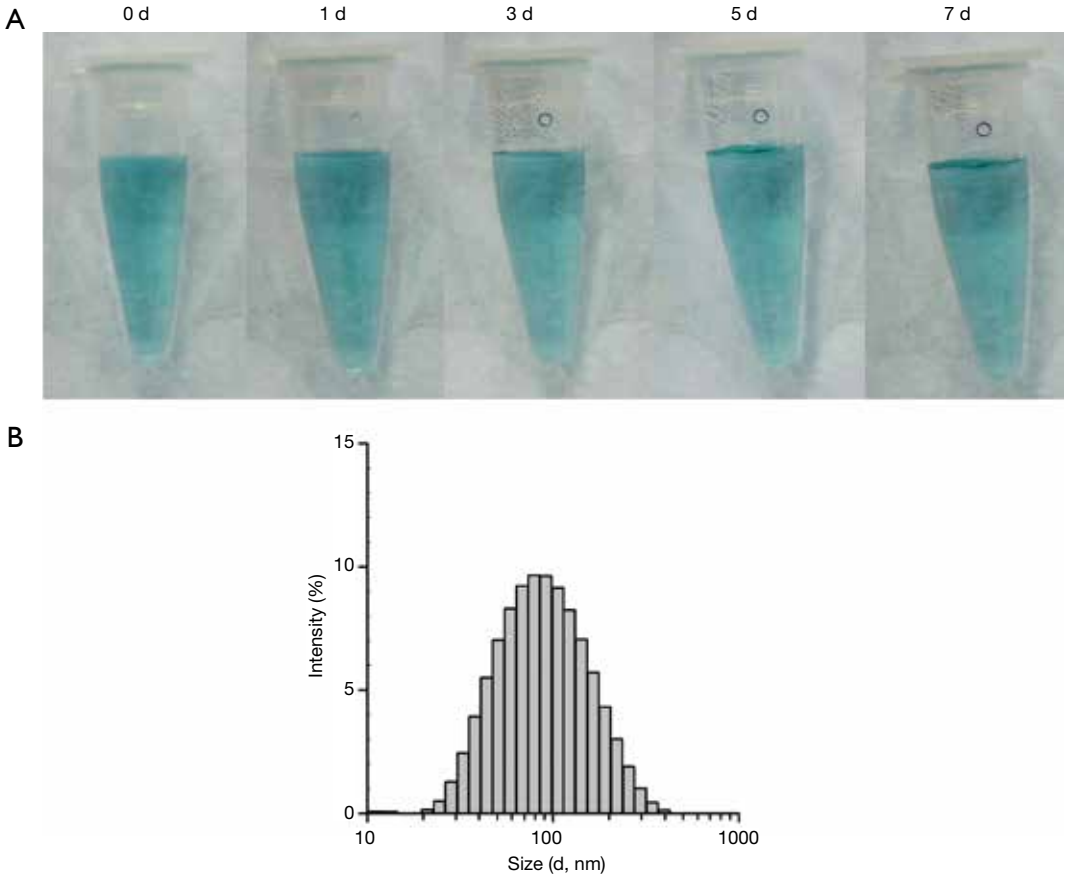

Figure S3 Stability of TANgel in deionized water. (A) Photographs of TANgel solution over time after synthesis. (B) Hydrodynamic size distribution of TANgel solution after 7 days. TANgel, theranostic alginate-based nanogels.

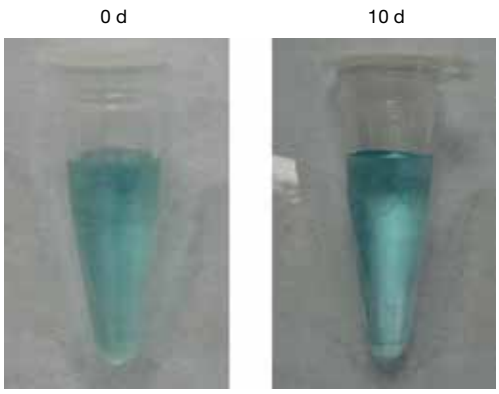

Figure S4 Stability of TANgel at physiological pH condition. Photographs of TANgel dispersed in phosphate buffered saline (pH 7.4, 0.5×) over time. TANgel, theranostic alginate-based nanogels.

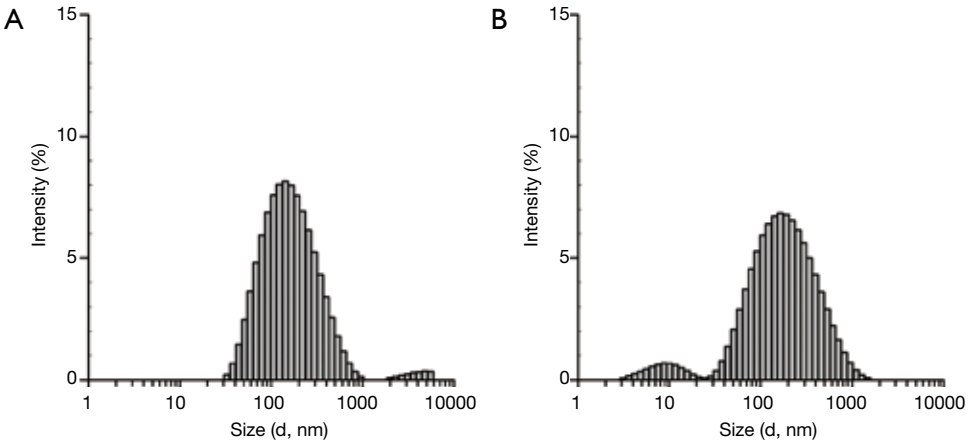

Figure S5 Hydrodynamic size distribution of TANgel solution after 48 h of dialysis at (A) pH 7.4 and (B) pH 5. TANgel, theranostic alginate-based nanogels.

Original Article

Ultra-wide optical coherence tomography angiography in diabetic retinopathy

Qinqin Zhang[1], Kasra A. Rezaei[2], Steven S. Saraf[2], Zhongdi Chu[1], Fupeng Wang[1], Ruikang K. Wang[1,2]

[1]Department of Bioengineering, University of Washington, Seattle, Washington, USA; [2]Department of Ophthalmology, University of Washington Eye Institute, Seattle, Washington, USA

Correspondence to: Ruikang K. Wang, PhD. Department of Bioengineering, University of Washington, Seattle, WA 98195, USA. Email: wangrk@uw.edu.

Background: To implement an ultra-wide optical coherence tomography angiography imaging (UW-OCTA) modality in eyes with diabetic retinopathy (DR) with the aim of quantifying the burden of microvascular disease at baseline and subsequent clinic visits.

Methods: UW-OCTA was implemented on a 1,060 nm swept source (SS) OCTA engine running at 100 kHz A-line rate with a motion tracking mechanism. A montage scanning protocol was used to capture a 100-degree field of view (FOV) using a 4×4 grid of sixteen total individual 6×6 mm^2 scans. Typical OCTA images with a FOV of 3×3, 6×6 and 12×12 mm^2 were obtained for comparison. DR patients were scanned at baseline and follow-up. They were treated at the clinician's discretion. Vessel density and non-perfusion area maps were calculated based on the UW-OCTA images.

Results: Three proliferative DR patients were included in the study. UW-OCTA images provided more detailed visualization of vascular networks compared to 50-degree fluorescein angiography (FA) and showed higher burden of pathology in the retinal periphery that was not captured by typical OCTA. Neovascularization complexes were clearly detected in the two patients with active PDR. Vessel density and non-perfusion maps were used to measure progressive capillary non-perfusion and regression of neovascularization between visits.

Conclusions: UW-OCTA provides approximately 100-degree OCTA images of the fundus comparable to that of wide-angle fundus photography, and may be more applicable in conditions such as DR which affect the peripheral retina in contrast to standard OCTA.

Keywords: Diabetic retinopathy (DR); field of view (FOV); non-perfusion; optical coherence tomography angiography (OCTA); swept source OCTA; vessel density

Submitted Sep 04, 2018. Accepted for publication Sep 12, 2018.
doi: 10.21037/qims.2018.09.02
View this article at: http://dx.doi.org/10.21037/qims.2018.09.02

Introduction

Diabetic retinopathy (DR) is the leading cause of blindness in the United States for patients aged 20–64 years (1). It is characterized by microaneurysms (MAs), capillary non-perfusion, and ischemia within the retina (2-5) that may lead to several complications, such as diabetic macular edema (DME), diabetic macular ischemia, and neovascularization of the retina (6-10). Capillary non-perfusion impairs the delivery of nutrients to the neuroglial tissues in the retina, resulting in hypoxia and the expression of vascular endothelial growth factor (VEGF). VEGF promotes both angiogenic responses and vascular permeability (11,12). Currently, retinal capillary non-perfusion is readily demonstrated by fluorescein angiography (FA). Midperipheral capillary non-perfusion has been shown to be the most common type in early stage DR and the extent of capillary non-perfusion is more pronounced in eyes with retinal and optic disc neovascularization (13,14). Therefore, it is crucial to detect midperipheral or far peripheral

capillary non-perfusion in DR patients, especially in the early stages of the disease.

FA, a dye-based angiography, is widely recognized as an essential tool in evaluating the severity of DR (15). Traditional fundus cameras capture FA images from the posterior pole, covering a 20–50 degree field which is important for macular diseases such as age-related macular degeneration. The introduction of widefield imaging systems, including color fundus photography and FA, has proven to be of higher utility in diseases such as DR that have significant effects on the peripheral retina (16-18). Compared to the traditional fundus images, widefield FA imaging devices enable imaging of up to 200 degrees of the posterior pole in a single scan. However, despite its clinical usefulness, FA and widefield FA are invasive procedures requiring the intravenous injection of fluorescein which has documented risks of nausea, vomiting, itching, anaphylaxis, and in rare cases, can cause death (19).

Optical coherence tomography (OCT) is a non-invasive imaging modality that can rapidly render three-dimensional images of retinal microanatomy. It has become an important tool in the management of DR, especially with the advent of anti-VEGF therapy for the treatment of DME (20). Optical coherence tomography angiography (OCTA) (21-25) is a further step in OCT technology that allows assessment of the microvasculature by detecting functional blood flow. It has become increasingly important as a non-invasive, functional imaging modality in conditions affecting the retinal and choroidal vasculature (26-29). The basis of OCTA is to isolate and exhibit only tissues with variable backscattering of light. By repeating an OCT scan multiple times at the same location, post-processing methods are applied to isolate only tissues that produce variable backscattering of light such as those produced by the continual flux of red blood cells through the retinal vasculature (30,31). Given current OCT system speed, the tolerance of the human eye to maintain its position for approximately 5 seconds limits the field of view (FOV) obtainable by OCTA, which requires rapid acquisition of images in a small window of time. Typically, 3×3 and 6×6 mm^2 are the most common FOVs of spectral domain (SD) OCTA with an imaging speed of approximately 70 kHz. Larger FOVs of up to 9×9 and 12×12 mm^2 can be achieved in a single scan by utilizing a faster swept source (SS) OCTA system (100 kHz). However, with larger scan areas, there is a correspondingly decreased resolution of the fine retinal vasculature. To maintain the high resolution of the vasculature, a montage protocol can be used to cover a larger FOV, performing multiple individual scans of the fundus and merging them into a larger image. Zhang *et al.* showed that montaged SD-OCTA images could be used to cover a larger FOV of approximately 50 degrees while maintaining a high vascular resolution (32). The described method is comparable to traditional fundus imaging, but still it is not ideal for conditions such as DR that predominately affect the more peripheral retina.

In this study, we implemented a montage protocol that utilizes SS-OCTA to achieve ultra-wide images that are more applicable in DR patients. The more rapid acquisition time of SS-OCTA makes this method possible and practical in the clinical setting.

Methods

Clinical and imaging data were collected prospectively from patients receiving care at the eye institute at the University of Washington, Seattle, WA, between January 2016 and October 2017. This study was approved by the Institutional Review Board of the University of Washington and informed consent was obtained from all subjects. This study followed the tenets of the Declaration of Helsinki and was conducted in compliance with the Health Insurance Portability and Accountability Act.

All patients underwent imaging with a 100 kHz Plex® Elite 9000 SS-OCTA (Carl Zeiss Meditec Inc., USA) machine that operates at a central wavelength of 1,060 nm with a bandwidth of 100 nm, an A-scan depth of 3.0 mm in tissue, a full-width at half maximal (FWHM) axial resolution of approximately 5 µm in tissue, and a lateral resolution at the retinal surface estimated at 12 µm. FastTrac™ motion correction software was used while the images were acquired, which enabled the montage scanning protocol to achieve an unprecedented FOV. The montage was comprised of a 4×4 grid of sixteen total individual 6×6 mm^2 FOV scans. Two repeated B-scans were acquired as a cluster scan at each position over the slow axis. In total, 500 clusters were stepped in the slow axis. In each B-scan, 500 A-lines were sampled over the fast axis direction. The high-density sampling of the 6×6 mm^2 scans resulted in 12 µm spacing, rendering the retinal microvasculature at high resolution and allowing for quantitative analysis. The complex optical microangiography (OMAG^c) algorithm was used to obtain OCTA images, by utilizing the variations in both the intensity and phase information between sequential B-scans at the same location to generate flow signal (30). The 4×4 grid was imaged in a standardized manner by

changing the fixation target to guide the OCT probe. Twenty percent overlap between adjacent cubes was allowed in order to guide the rendering of the montage image. In addition, traditional single scan images were obtained, including 3×3, 6×6 and 12×12 mm^2, to allow comparison with the ultra-wide montage image.

Retinal layers were segmented using a validated semi-automated segmentation algorithm (33). Three retinal layers were segmented in all patients: a vitreous retinal layer (VRL) that is a slab covering approximately 100 microns above the inner limiting membrane (ILM), a superficial retinal layer (SRL) extending from the ILM to the inner plexiform layer (IPL), and a deep retinal layer (DRL) covering a slab from the outer border of the IPL to the outer border of the outer plexiform layer (OPL) (32). Maximum projection was applied on the segmented volumes to generate the en face angiograms. The different layers were color coded as follows: purple in VRL, red in SRL, and green in DRL. An automated montage algorithm was then applied to generate the final ultra-wide angiograms.

Vessel density and flow impairment areas indicating capillary non-perfusion were calculated on the en face angiograms using our previously described method (34).

A non-perfusion flow impairment map was created in all patients to highlight voids where capillaries were not detected but excluding areas of less than or equal to 0.03 mm^2. In addition, the foveal avascular zone and optic disc were excluded in the analysis. Comparisons between the composite ultra-wide FOV and common FOVs in detecting flow impairment area were conducted. In addition, vessel density changes were detected between clinical visits.

Results

Starting from January 2016, 50 patients comprising a total of 60 study eyes with either non-proliferative DR (NPDR) or proliferative diabetic retinopathy (PDR), were enrolled in our study and underwent OCTA imaging. Twelve study eyes were excluded due to severe cataract or motion artifacts. Thirty patients, contributing 20 study eyes, underwent ultra-wide FOV scans. Of these, 3 patients, contributing four study eyes in total, underwent the montage UW-OCTA scan, in addition to the single scan images of all three FOVs (3×3, 6×6 and 12×12 mm^2). These three cases are described in this report. Of note, one of the three patients (patient #3) had an adverse reaction to traditional FA imaging and refused further invasive studies. She was subsequently followed with SS-OCTA scans on her routine clinical visits in order to monitor progression.

Patient #1: PDR (non-high risk) in a 33-year-old man

A 33-year-old man presented with best-corrected visual acuity (BCVA) of 20/20 in the right eye and was diagnosed with non-high risk PDR. Both color fundus photography and traditional FA images demonstrated intraretinal hemorrhages and MAs in the macula (*Figure 1A,B*). Typical 3×3 mm^2 (*Figure 1C*) and 6×6 mm^2 (*Figure 1D*) OCTA images showed only details of the central macula and did not provide a FOV comparable to traditional fundus imaging, but did provide greater detail of the capillary networks in the macula. A 12×12 mm^2 (*Figure 1E*) OCTA image encompassed the macula and a portion of the retina outside of the arcades, but with lower resolution of the capillary networks compared to the smaller FOV scans. The UW-OCTA image (*Figure 1F*), with approximately 100 degrees FOV, demonstrated the widest field view with vascular detail comparable to the smaller FOV scans. The UW-OCTA demonstrated non-perfusion areas (dark signal), and neovascularization in the VRL (purple color) that were not visualized on traditional FA or the smaller field OCTA scans.

Quantification methods previously described (34) were applied to the UW-OCTA image to quantify the areas of non-perfusion as well as vessel density (*Figure 2*). Flow impairment was found to be more concentrated in the retinal periphery rather than the macula (area shaded green in *Figure 2C*) with less dense capillary circulation in the same distribution (*Figure 2D*). To provide quantitative measures, we measured the non-perfusion areas with typical 50-degree FA FOV (yellow dashed circle in *Figure 2C*), and compared that to the outside region within 100-degree OCTA. The total area of non-perfusion was 11.83 mm^2 within 50-degree FOV, whereas that of the outside 50-degree but within 100-degree FOV, was 108.59 mm^2.

Patient #2 inactive PDR in a 54-year-old man

A 54-year-old man presented with best-corrected visual acuity (BCVA) of 20/20 in his left eye that was stable compared to 1 year ago. Panretinal photocoagulation (PRP) had been performed in the left eye 20 years ago with scars demonstrated on both the typical 50-degree color fundus photograph (*Figure 3A*) and FA (*Figure 3B*) images. The UW-OCTA images at baseline and his subsequent follow up 1 year later are shown in *Figure 3C,D,E* and *Figure 3F,G,H,*

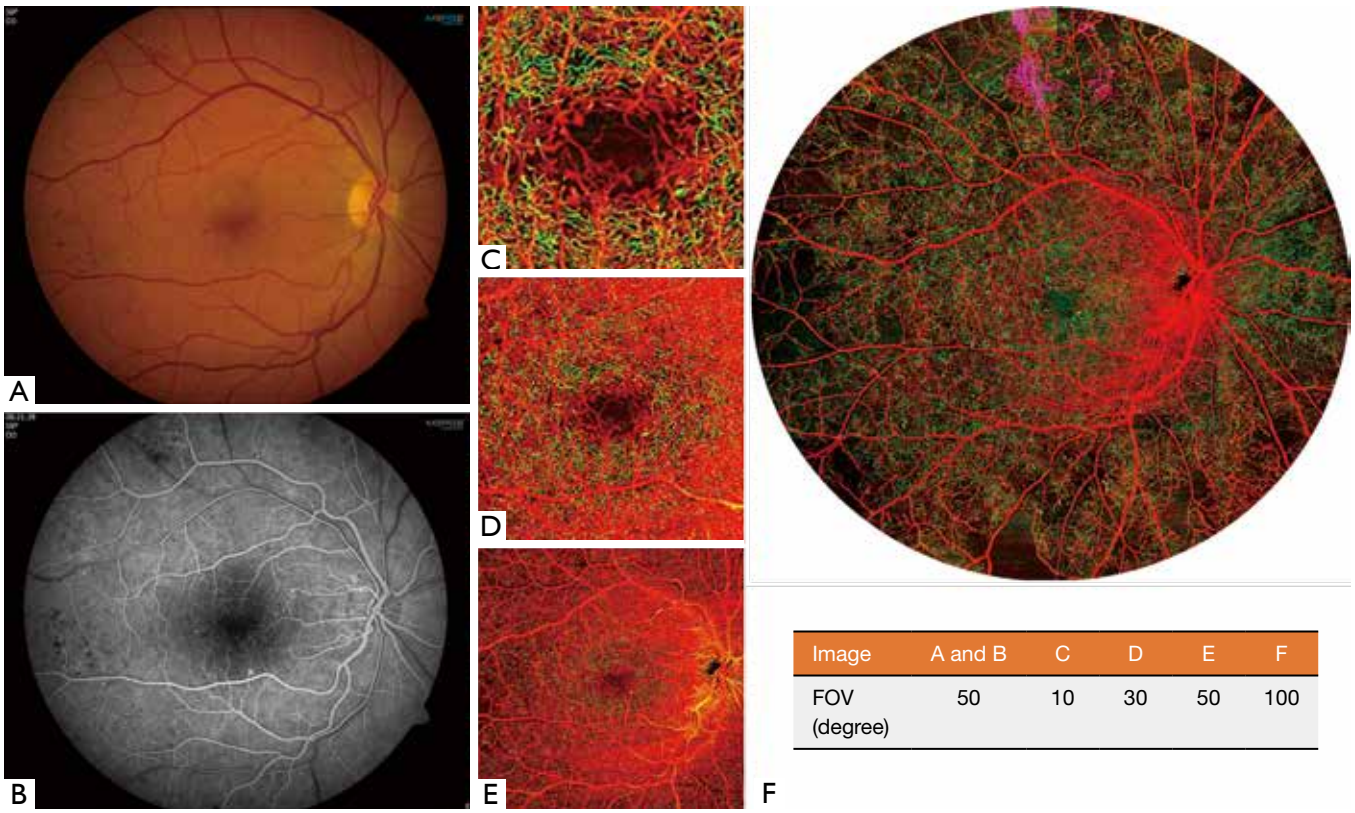

Image	A and B	C	D	E	F
FOV (degree)	50	10	30	50	100

Figure 1 The clinical images and OCTA images with different field of views (FOVs) of a 33-year-old man (patient #1) with a diagnosis of non-high risk PDR in his right eye. (A) 50-degree color fundus image; (B) 50-degree early phase of FA image; (C,D,E) typical OCTA color-coded images with a FOV of 3×3, 6×6, and 12×12 mm^2 scans, respectively; (F) the ultra-wide OCTA color-coded image with a FOV of approximately 100 degrees. Red indicates superficial retinal layer (SRL); Green indicates deep retinal layer (DRL); Purple indicates the vitreous retinal layer (VRL) to demonstrate neovascularization consistent with PDR. The FOVs of each image are listed in the table.

respectively. A 50-degree circle is overlaid onto the UW-OCTA images demonstrating the additional information gained by widefield OCTA compared to traditional fundus camera images. Quantitative measures of non-perfusion area in *Figure 3D* and *Figure 3G* within typical 50-degree FOV were 9.68 mm^2 for the first visit and 10.38 mm^2 for the second visit, respectively. However, these values were 67.36 mm^2 for the first visit and 69.88 mm^2 for the second visit in the region bounded by 50-degree and 100-degree outlines. The vessel density maps in *Figure 3E,H* showed that there is no appreciable difference in the 1-year follow-up interval (on average 24.42% *vs.* 24.77%), suggesting stable or minimal progressive capillary perfusion loss.

Patient #3 High-risk PDR in a 31-year-old woman

A 31-year-old woman presented with best-corrected visual acuity (BCVA) of 20/20 in her right eye and 20/60 in her left eye. At her initial consultation, the patient had a severe allergic reaction to the fluorescein dye and fainted. She did not consent to further FA studies. However, Optos widefield color fundus images were captured on both right and left eyes (*Figure 4*). Her baseline UW-OCTA showed extensive neovascularization of the disc (NVD) and retina elsewhere (NVE) in the left eye (*Figure 5A*). Intravitreal bevacizumab and panretinal photocoagulation laser treatments were performed in the left eye. One month later, the UW-OCTA was repeated (*Figure 5B*). Comparison of Optos photograph (*Figure 4A*) to UW-OCTA (*Figure 5*) demonstrates the response to treatment more dramatically in the color-coded UW-OCTA, showing regression of the NVD and NVE. The non-perfusion map (*Figure 5C,D*) reflects the regression of neovascularization in the VRL, exposing a larger area of underlying non-perfusion in the

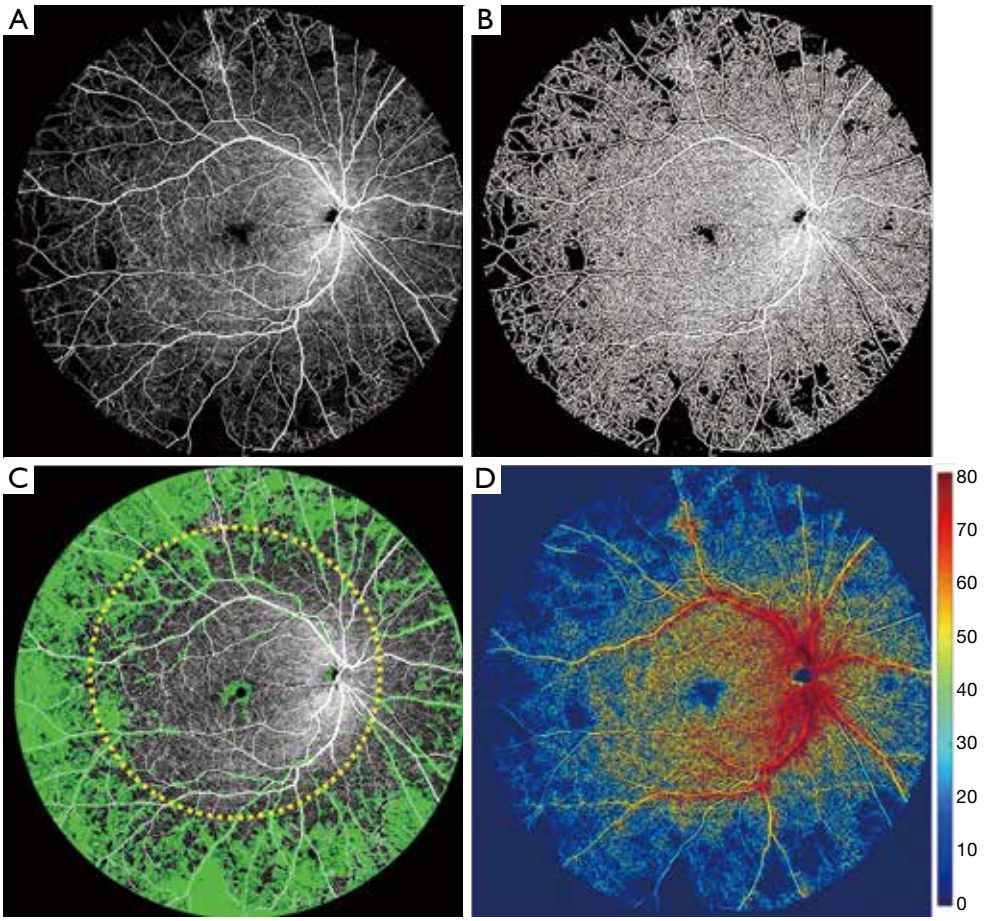

Figure 2 Ultra-wide OCTA image of the whole retinal layer (WRL) in gray scale of patient #1 and the corresponding quantification process. (A) The original ultra-wide OCTA image; (B) binary OCTA image that was used for vessel density and further non-perfusion area measurements; (C) the OCTA image overlaid with non-perfusion area map in green color. Typical 50-degree FOV is outlined approximately with yellow dashed circle. The non-perfusion area within the outlined circle is measured with 11.83 mm^2, whereas that of the outside is 108.59 mm^2. (D) The vessel density map overlaid with the binary OCTA image. The color-bar indicates the degree of the vessel density in percentage.

retinal circulation. Quantitative measures of total non-perfusion area in *Figure 5C,D* within typical 50-degree FOV were 32.31 mm^2 for the first visit and 49.02 mm^2 for the second visit, respectively. The non-perfusion in the area bounded by the 50-degree and 100-degree lines was 122.37 mm^2 at the first visit, and 135.84 mm^2 for the second visit. The vessel density maps in *Figure 5E,F* showed that there is also a decrease in the vessel density measurement by the second visit (30.26% to 22.02% on average) consistent with the regression of NVD and NVE.

Figure 6 shows images of the patient's right eye. Again, the NVD and NVE are more readily appreciable on the UW-OCTA images compared to the Optos image. With one month of observation, the NVE has progressed in the UW-OCTA image (*Figure 6A vs. Figure 6D*) and on the vessel density map [*Figure 6C* (27.52% in average) *vs. Figure 6F* (24.69% in average)]. Non-perfusion area (*Figure 6B vs. Figure 6E*) has also progressed within the 50-degree FOV (30.28 to 35.91 mm^2), but more so outside of the 50-degree region (84.71 to 97.77 mm^2).

Discussion

In this study, we utilized SS-OCTA in a novel protocol to render UW-OCTA images in patients with PDR. As we showed in our previous study, the maximum composited

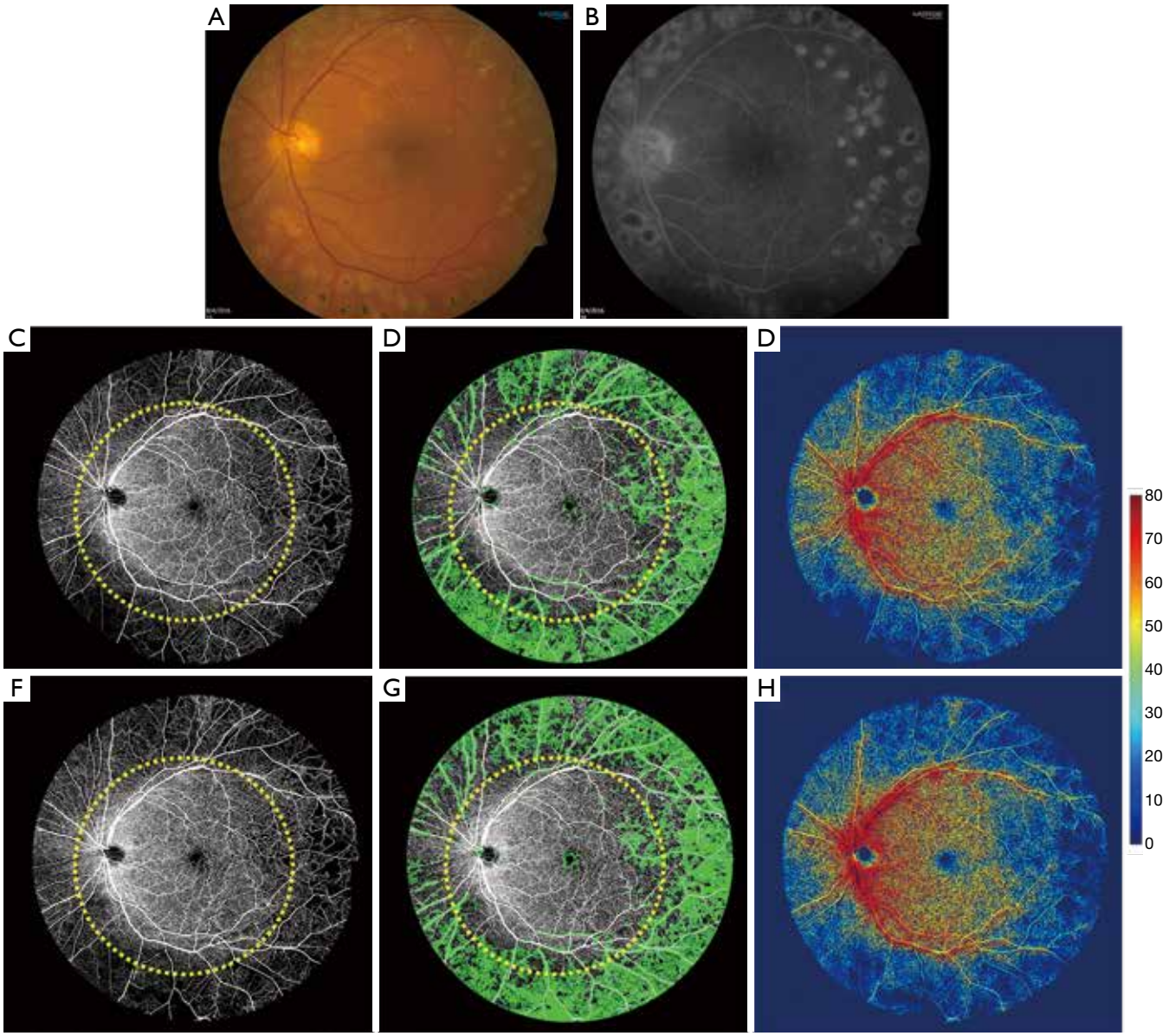

Figure 3 Clinical images and ultra-wide OCTA images of a 54-year-old man (patient #2) with a diagnosis of inactive PDR on his left eye. The clinical images were taken in his first visit. (A) 50-degree color fundus image; (B) 50-degree late phase of FA image; (C,F) the original ultra-wide OCTA images at his baseline and 1-year follow-up visit; (D,G) the non-perfusion map in green color of his first and follow-up visit; (E,H) vessel-density map overlaid with binary map of the two different visits. The yellow circle overlaid on OCTA images is a 50-degree circle to identify the typical clinical FOV.

FOV on patients we obtained from the SD-OCTA prototype with an A-line rate of 68 kHz can be extended to 50 degrees with high vascular resolution (contributed by the dense sampling of the single cube, 2.4×2.4 mm^2 with 245 A-line × 245 B-scan), comparable to the standard clinical images. In this study, the faster speed of SS-OCTA (up to 100 kHz) and its modified tracking system allowed us to extend the FOV even wider to approximately 100 degrees with less imaging time. The application of this methodology is of special interest in cases such as DR and other retinal conditions predominately affecting the peripheral retina, such as sickle cell retinopathy, retinal vasculitis, or ocular

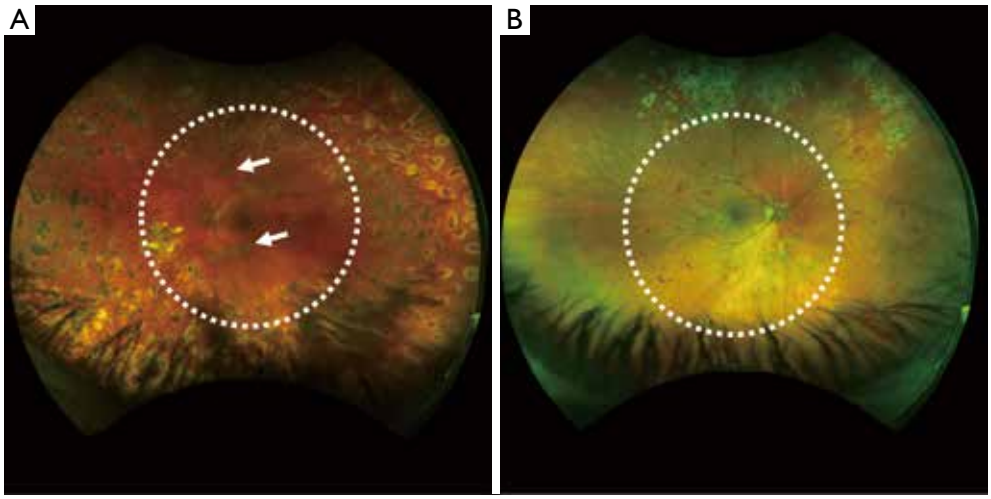

Figure 4 Optos ultra-wide color fundus image of a 31-year-old female (patient #3) with a diagnosis of (A) severe PDR on her left eye and (B) PDR on her right eye. Typical 50-degree FOV is outlined with white dashed circle line.

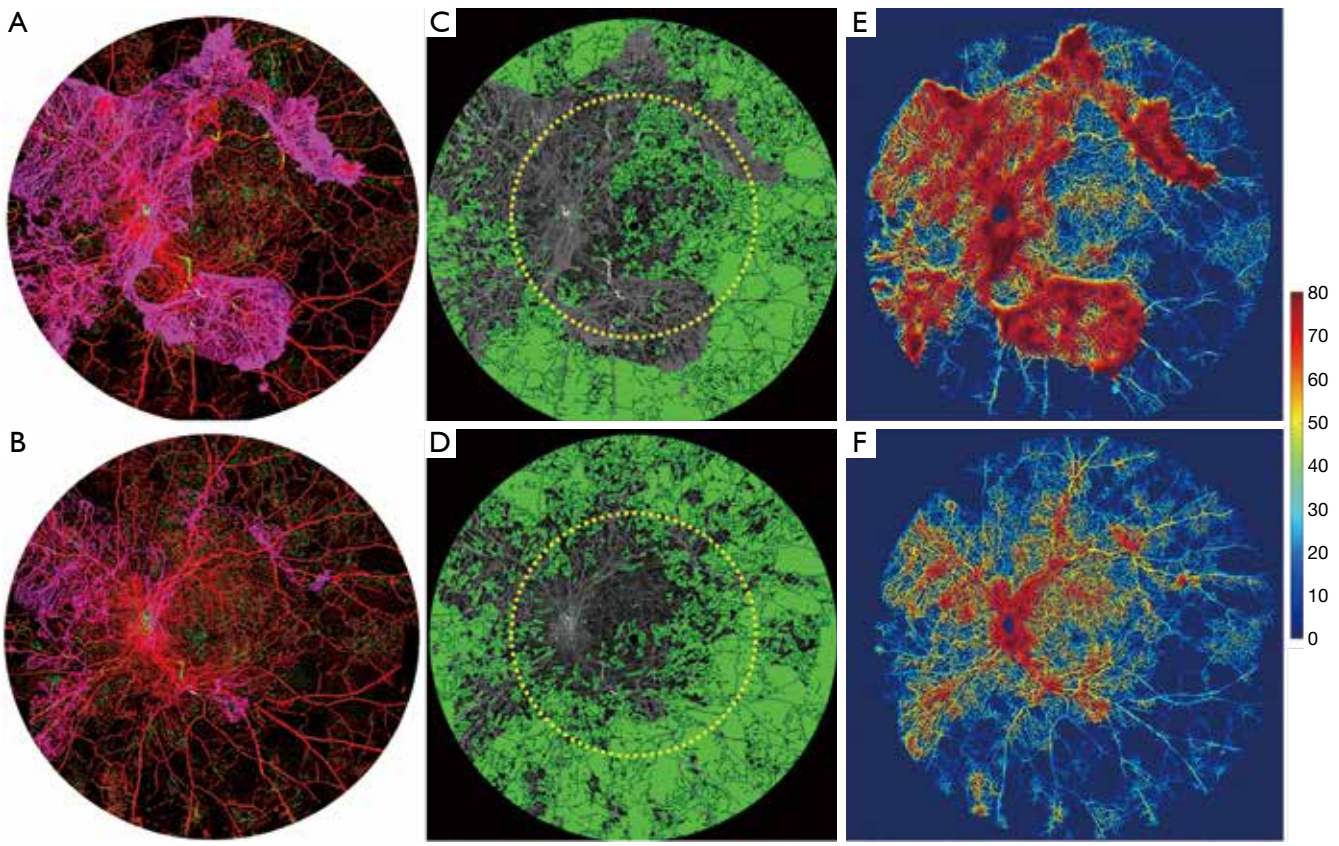

Figure 5 Ultra-wide OCTA image of a 31-year-old woman (patient #3) with a diagnosis of severe PDR on her left eye. (A,B) Ultra-wide color-coded OCTA images at the first visit and 1-month follow-up visit after intravitreal bevacizumab and panretinal photocoagulation; (C,D) the non-perfusion map in green color of his first and second visit; (E,F) vessel density map of her first and second visit. The yellow circle overlaid on OCTA images is a 50-degree circle to identify the typical clinical FOV. On (A) and (E), red indicates superficial retinal layer (SRL); green indicates deep retinal layer (DRL); purple indicates the vitreous retinal layer (VRL) to demonstrate the neovascularization.

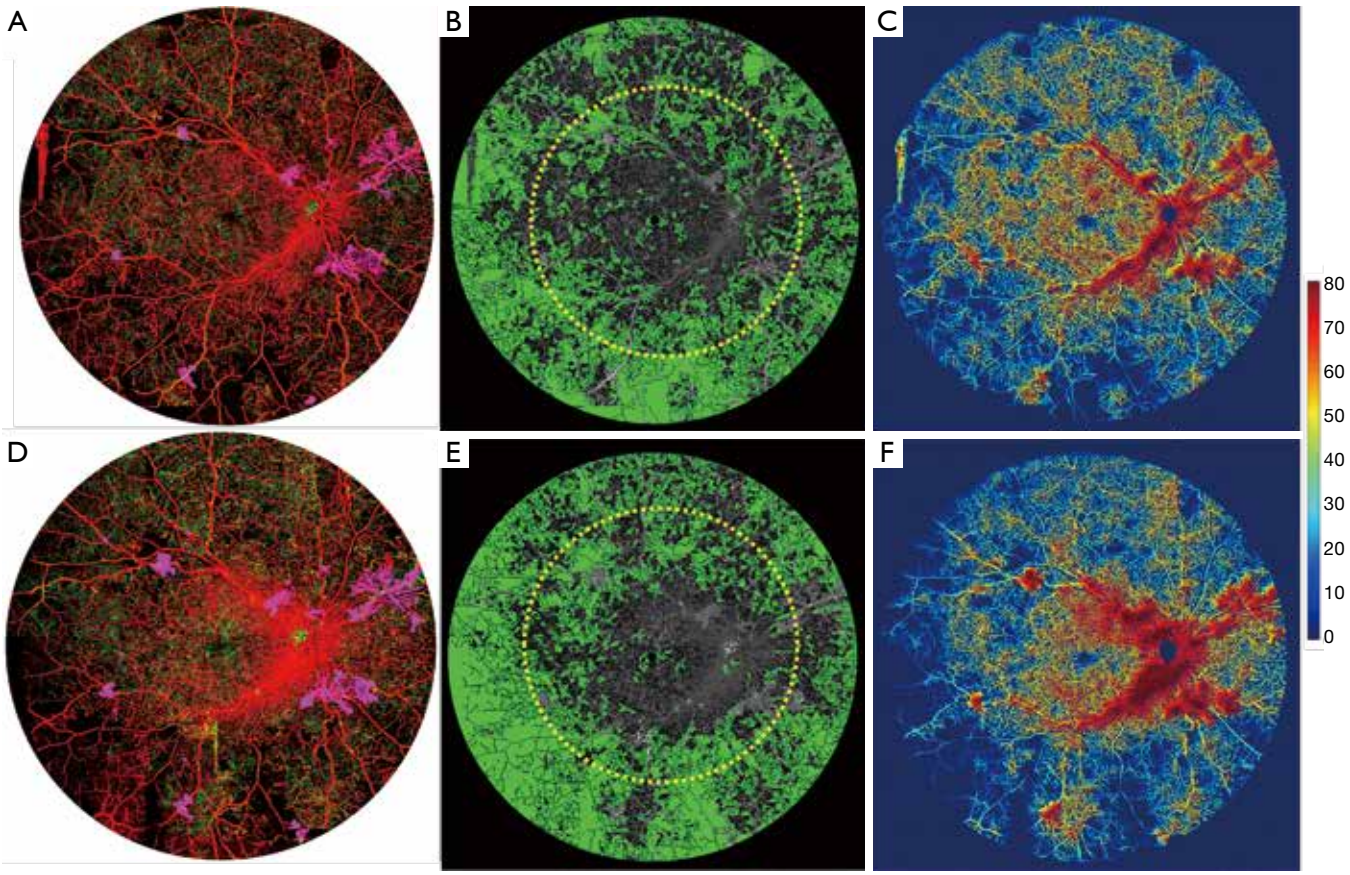

Figure 6 Ultra-wide OCTA image of a 31-year-old woman (patient #3) with a diagnosis of PDR in her right eye. (A,D) Ultra-wide color-coded OCTA images of the first visit and one-month follow-up visit; (B,E) the non-perfusion map in green color of his first and second visit; (C,F) Vessel-density map at her baseline and 1 month follow-up visit. The yellow circle overlaid on OCTA images is a 50-degree circle to identify the typical clinical FOV. On (A) and (D), red indicates superficial retinal layer (SRL); Green indicates deep retinal layer (DRL); Purple indicates the vitreous retinal layer (VRL) to demonstrate the neovascularization.

ischemic syndrome.

The three reported cases demonstrate the ability of UW-OCTA to provide valuable clinical information in grading retinopathy, monitoring stability, or monitoring treatment response.

In the case of patient #1, it is clear that OCTA renders a higher level of capillary network detail compared to conventional FA. Furthermore, the wider FOV of UW-OCTA captured NVE missing in the 50-degree image obtained by traditional FA and the smaller FOV OCTA scans (*Figure 1C,D,E*). In the case of patient #2, the patient had a history of inactive PDR. UW-OCTA showed no active NVD or NVE and capillary density remained stable at 1-year follow-up, corresponding to the assessment of clinical stability. In the case of patient #3, we presented a case of adverse reaction to fluorescein dye that was effectively followed with the less invasive UW-OCTA. In this case, we are able to monitor the response of NVD and NVE to intravitreal anti-VEGF injections and PRP without invasive fluorescein dye testing. It can also be concluded that regression of NVD and NVE after treatment is more easily appreciated with UW-OCTA compared to Optos fundus photography. UW-OCTA may be of significant value in such clinical contexts wherein the number of necessary injections to achieve control requires frequent re-imaging, such as when more providers are opting to treat PDR with anti-VEGF injections rather than PRP (35,36). In the fellow eye, quantification indices on the vessel-density map show worsening NVE in the right eye after 1-month observation. In addition, progressive non-perfusion was measured on

the non-perfusion map. All three cases demonstrate that the burden of microangiopathy in DR is more heavily concentrated outside of the central 50 degrees that are captured by conventional photography methods.

There are limitations in our methodology. First, the acquisition time of UW-OCTA imaging is relatively long compared to standard OCTA imaging, which takes approximately 5 seconds per scan. Each UW-OCTA takes around 20 minutes to perform for both eyes, which may make acquisition difficult in patients who have low vision and cannot maintain fixation. On the other hand, acquisition time and difficulty may be comparable or better when compared to standard FA, which requires significant set-up time, placement of intravenous access, and at least 10 minutes of image capture time, exposing the patient to significant flash photography. Second, we provide quantification of retinal capillary perfusion using a vessel-density map. Although this may allow trending of microvascular disease between visits, there have not been studies to establish the clinical significance of vessel density changes. Most of our understanding and clinical approach to DR are from clinical findings such as MAs, retinal hemorrhages, and signs of neovascularization, which have been described in the ETDRS study. Further study is needed to understand the clinical utility of vessel density changes now that advancements in technology make trending this metric possible.

In summary, we have described an ultra-wide OCTA imaging protocol for DR patients, which can provide up to 100 degrees of high vascular resolution by utilizing SS-OCTA. The UW-OCTA images capture both the entire macula and retinal periphery in DR patients, which has widespread application in early disease screening, assessing treatment response, and assessing stability.

Acknowledgements

Funding: Research supported by grants from Carl Zeiss Meditec, Inc. (Dublin, CA), the National Eye Institute (R01EY024158, R01EY028753), an unrestricted grant from the Research to Prevent Blindness, Inc., New York, NY, and the Washington Research Foundation. The funding organization had no role in the design or conduct of this research.

Footnote

Conflicts of Interest: Dr. Wang disclosed intellectual property owned by the Oregon Health and Science University and the University of Washington related to OCT angiography, and licensed to commercial entities, which are related to the technology and analysis methods described in parts of this manuscript. Dr. Wang received an innovative research award from Research to Prevent Blindness. He is a consultant to Carl Zeiss Meditec, and Insight Photonic Solutions.

Ethical Statement: This study was approved by the Institutional Review Board of the University of Washington and informed consent was obtained from all subjects. This study followed the tenets of the Declaration of Helsinki and was conducted in compliance with the Health Insurance Portability and Accountability Act.

References

1. Klein R, Klein BE, Moss SE, Davis MD, DeMets DL. The Wisconsin epidemiologic study of diabetic retinopathy. III.Prevalence and risk of diabetic retinopathy when age at diagnosis is 30 or more years. Arch Ophthalmol 1984;102:527-532.
2. Adhi M, Brewer E, Waheed NK, Duker JS. Analysis of morphological features and vascular layers of choroid in diabetic retinopathy usingspectral-domain optical coherence tomography. JAMA Ophthalmol 2013;131:1267-74.
3. Hwang TS, Gao SS, Liu L, Lauer AK, Bailey ST, Flaxel CJ, Wilson DJ, Huang D, Jia Y. Automated quantification of capillary nonperfusion using optical coherence tomography angiography in diabetic retinopathy. JAMA Ophthalmol 2016;134:367-73.
4. Hwang TS, Jia Y, Gao SS, Bailey ST, Lauer AK, Flaxel CJ, Wilson DJ, Huang D. Optical coherence tomography angiography features of diabetic retinopathy. Retina 2015;35:2371-6.
5. Ishibazawa A, Nagaoka T, Takahashi A, Omae T, Tani T, Sogawa K, Yokota H, Yoshida A. Optical coherence tomography angiography in diabetic retinopathy: a prospective pilot study. Am J Ophthalmol 2015;160:35-44.e1.
6. Diabetic Retinopathy Clinical Research Network, Elman MJ, Aiello LP, Beck RW, Bressler NM, Bressler SB, Edwards AR, Ferris FL 3rd, Friedman SM, Glassman AR, Miller KM, Scott IU, Stockdale CR, Sun JK. Randomized trial evaluating ranibizumab plus prompt or deferred laser or triamcinolone plus prompt laser for diabetic macular edema. Ophthalmology 2010;117:1064-1077.e35.

7. Agemy SA, Scripsema NK, Shah CM, Chui T, Garcia PM, Lee JG, Gentile RC, Hsiao YS, Zhou Q, Ko T, Rosen RB. Retinal vascular perfusion density mapping using optical coherence tomography angiography in normals and diabetic retinopathy patients. Retina 2015;35:2353-63.
8. Conrath J, Giorgi R, Raccah D, Ridings B. Foveal avascular zone in diabetic retinopathy: quantitative vs qualitative assessment. Eye (Lond) 2005;19:322-6.
9. ETDRS Research Group. Classification of diabetic retinopathy from fluoresceinangiograms. Early treatment diabetic retinopathy study report number 11. Ophthalmology 1991;98:807-22.
10. ETDRS Research Group. Photocoagulation for diabetic macular edema. Early treatment diabetic retinopathy study report number 1. Arch Ophthalmol 1985;103:1796-806.
11. Aiello LP, Avery RL, Arrigg PG, Keyt BA, Jampel HD, Shah ST, Pasquale LR, Thieme H, Iwamoto MA, Park JE, Nguyen HV, Aiello LM, Ferrara N, King GL. Vascular endothelial growth factor in ocular fluid of patients with diabetic retinopathy and other retinal disorders. N Engl J Med 1994;331:1480-7.
12. Antonetti DA, Klein R, Gardner TW. Diabetic retinopathy. N Engl J Med 2012;366:1227-1239.
13. Niki T, Muraoka K, Shimizu K. Distribution of capillary nonperfusion in early-stage diabetic retinopathy. Ophthalmology 1984;91:1431-9.
14. Shimizu K, Kobayashi Y, Muraoka K. Midperipheral fundus involvement in diabetic retinopathy. Ophthalmology 1981;88:601-12.
15. Classification of diabetic retinopathy from fluorescein angiograms. ETDRS report number 11. Early Treatment Diabetic Retinopathy Study Research Group. Ophthalmology 1991;98:807-822.
16. Wessel MM, Aaker GD, Parlitsis G, Cho M, D'Amico DJ, Kiss S. Ultra-wide-field angiography improves the detection and classification of diabetic retinopathy. Retina 2012;32:785-91.
17. Silva PS, Cavallerano JD, Sun JK, Soliman AZ, Aiello LM, Aiello LP. Peripheral lesions identified by mydriatic ultrawide field imaging: distribution and potential impact on diabetic retinopathy severity. Ophthalmology 2013;120:2587-95.
18. Tan CS, Sadda SR, Hariprasad SM. Ultra-wide retinal imaging in the management of diabetic eye diseases. Ophthalmic Surg Lasers Imaging Retina 2014;45:363-6.
19. Yannuzzi LA, Rohrer KT, Tindel LJ, Sobel RS, Costanza MA, Shields W, Zang E. Fluorescein angiography complication survey. Ophthalmology 1986;93:611-7.
20. American Academy of Ophthalmology: American Academy of Ophthalmology Retina and Vitreous Panel. Preferred Practice Pattern® guidelines. Diabetic retinopathy. San Francisco, CA: American Academy of Ophthalmology; 2014.
21. Deegan AJ, Wang W, Men SJ, Li YD, Song SZ, Xu JJ, Wang RK. Optical Coherence Tomography Angiography Monitors Human Cutaneous Wound Healing Over Time. Quant Imaging Med Surg 2018;8:135-50.
22. Chen CL, Bojikian KD, Zhang QQ, Gupta D, Wen JC, Xin C, Mudumbai RC, Kono R, Johnstone MA, Chen PP, Wang RK. Optic disc perfusion in normal eyes and eyes with glaucoma using optical coherence tomography-based microangiography. Quant Imaging Med Surg 2016;6:125-33.
23. Chen CL, and Wang RK. Optical Coherence Tomography Based Angiography. Biomedical Optics Express 2017;8:1056-82.
24. Kashani AH, Chen CL, Gahm JK, Zheng F, Richter GM, Rosenfeld PJ, Shi Y, Wang RK. Optical coherence tomography angiography: A comprehensive review of current methods and clinical applications. Progress in Retinal and Eye Research 2017;60:66-100.
25. Zhang A, Zhang QQ, Chen CL, Wang RK. Methods and Algorithms for Optical Coherence Tomography Based Angiography: A Review and Comparison. J Biomed Opt 2015;20:100901.
26. Thorell MR, Zhang QQ, Huang Y, An L, Durbin MK, Laron M, Sharma U, Stetson PF, Gregori G, Wang RK, and Rosenfeld PJ. Swept-Source OCT Angiography of Macular Telangiectasia Type 2. Ophthalmic Surg. Lasers Imaging Retina 2014;45:369-80.
27. Kim DY, Fingler J, Zawadzki RJ, Park SS, Morse LS, Schwartz DM, Fraser SE, Werner JS. Optical imaging of the chorioretinal vasculature in the living human eye. Proc Natl Acad Sci U S A 2013;110:14354-9.
28. Zhang Q, Wang RK, Chen CL, Legarreta AD, Durbin MK, An L, Sharma U, Stetson PF, Legarreta JE, Roisman L, Gregori G, Rosenfeld PJ. Swept source OCT angiography of neovascular MacTel2. Retina 2015;35:2285-99.
29. Roisman L, Zhang Q, Wang RK, Gregori G, Zhang A, Chen CL, Durbin MK, An L, Stetson PF, Robbins G, Miller A, Zheng F, Rosenfeld PJ. Optical Coherence Tomography Angiography of Asymptomatic Neovascularization in Intermediate Age-Related Macular Degeneration. Ophthalmology 2016;123:1309-19.
30. Wang RK, An L, Francis P, Wilson DJ. Depth-resolved

imaging of capillary networks in retina and choroid using ultrahigh sensitive optical microangiography. Opt Lett 2010;35:1467-9.
31. Wang RK. Optical Microangiography: A Label Free 3D Imaging Technology to Visualize and Quantify Blood Circulations within Tissue Beds in vivo. IEEE J Sel Top Quantum Electron 2010;16:545-54.
32. Zhang Q, Lee CS, Chao J, Chen CL, Zhang T, Sharma U, Zhang A, Liu J, Rezaei K, Pepple KL, Munsen R, Kinyoun J, Johnstone MA, Van Gelder RN, Wang RK. Wide-field optical coherence tomography based microangiography for retinal imaging. Sci Rep 2016;6:22017.
33. Yin X, Chao JR, Wang RK. User-guided segmentation for volumetric retinal optical coherence tomography images. J Biomed Opt 2014;19:086020.
34. Chu Z, Lin J, Gao C, Xin C, Zhang Q, Chen C, Roisman L, Gregori G, Rosenfeld PJ, Wang RK. Quantitative assessment of the retinal microvasculature using optical coherence tomography angiography. J Biomed Opt 2016;21:66008.
35. Hutton DW, Stein JD, Bressler NM, Jampol LM, Browning D, Glassman AR; Diabetic Retinopathy Clinical Research Network. Cost-effectiveness of intravitreous ranibizumab compared with panretinal photocoagulation for proliferative diabetic retinopathy:secondary analysis from a Diabetic Retinopathy Clinical Research Network randomized clinical trial. JAMA Ophthalmol 2017;135:576-84.
36. Writing Committee for the Diabetic Retinopathy Clinical Research Network, Gross JG, Glassman AR, Jampol LM, Inusah S, Aiello LP, Antoszyk AN, Baker CW, Berger BB, Bressler NM, Browning D, Elman MJ, Ferris FL 3rd, Friedman SM, Marcus DM, Melia M, Stockdale CR, Sun JK, Beck RW. Panretinal photocoagulation vs. intravitreous ranibizumab for proliferative diabetic retinopathy: A randomized clinical trial. JAMA 2015;314:2137-46.

Cite this article as: Zhang Q, Rezaei KA, Saraf SS, Chu Z, Wang F, Wang RK. Ultra-wide optical coherence tomography angiography in diabetic retinopathy. Quant Imaging Med Surg 2018;8(8):743-753. doi: 10.21037/qims.2018.09.02

Original Article

Monitoring reperfused myocardial infarction with delayed left ventricular systolic dysfunction in rabbits by longitudinal imaging

Yuanbo Feng[1#], Bianca Hemmeryckx[2#], Liesbeth Frederix[2], Marleen Lox[2], Jun Wu[3], Ward Heggermont[2], Hua Rong Lu[4], David Gallacher[4], Raymond Oyen[1], H. Roger Lijnen[2], Yicheng Ni[1]

[1]Radiology, Department of Imaging and Pathology, KU Leuven, Leuven, Belgium; [2]Center for Molecular and Vascular Biology, Department of Cardiovascular Sciences, KU Leuven, Leuven, Belgium; [3]Ultrasound Diagnostic department, the second affiliated hospital of Dalian Medical University, Dalian 116000, China; [4]Translational Sciences, Safety Pharmacology Research, Janssen Research & Development, Janssen Pharmaceutical NV, Beerse, Belgium

[#]These authors contributed equally to this work.

Correspondence to: Yicheng Ni, MD, PhD. Theragnostic Laboratory, Department of Imaging & Pathology, Biomedical Sciences Group, KU Leuven, Radiology Section, University Hospitals, Herestraat 49, 3000 Leuven, Belgium. Email: yicheng.ni@kuleuven.be.

Background: An experimental imaging platform for longitudinal monitoring and evaluation of cardiac morphology-function changes has been long desired. We sought to establish such a platform by using a rabbit model of reperfused myocardial infarction (MI) that develops chronic left ventricle systolic dysfunction (LVSD) within 7 weeks.

Methods: Fifty-five New Zeeland white (NZW) rabbits received sham-operated or 60-min left circumflex coronary artery (LCx) ligation followed by reperfusion. Cardiac magnetic resonance imaging (cMRI), transthoracic echocardiography (echo), and blood samples were collected at baseline, in acute (48 hours or 1 week) and chronic (7 weeks) stage subsequent to MI for *in vivo* assessment of infarct size, cardiac morphology, LV function, and myocardial enzymes. Seven weeks post MI, animals were sacrificed and heart tissues were processed for histopathological staining.

Results: The success rate of surgical operation was 87.27%. The animal mortality rates were 12.7% and 3.6% both in acute and chronic stage separately. Serum levels of the myocardial enzyme cardiac Troponin T (cTnT) were significantly increased in MI rabbits as compared with sham animals after 4 hours of operation ($P<0.05$). According to cardiac morphology and function changes, 4 groups could be distinguished: sham rabbits (n=12), and MI rabbits with no (MI_NO_LVSD; n=10), moderate (MI_M_LVSD; n=9) and severe (MI_S_LVSD; n=15) LVSD. No significant differences in cardiac function or wall thickening between sham and MI_NO_LVSD rabbits were observed at both stages using both cMRI and echo methods. cMRI data showed that MI_M_LVSD rabbits exhibited a reduction of ejection fraction (EF) and an increase in end-systolic volume (ESV) at the acute phase, while at the chronic stage these parameters did not change further. Moreover, in MI_S_LVSD animals, these observations were more striking at the acute stage followed by a further decline in EF and increase in ESV at the chronic stage. Lateral wall thickening determined by cMRI was significantly decreased in MI_M_LVSD versus MI_NO_LVSD animals at both stages ($P<0.05$). As for MI_S_LVSD versus MI_M_LVSD rabbits, the thickening of anterior, inferior and lateral walls was significantly more decreased at both stages ($P<0.05$). Echo confirmed the findings of cMRI. Furthermore, these *in vivo* outcomes including those from vivid cine cMRI could be supported by exactly matched *ex vivo* histomorphological evidences.

Conclusions: Our findings indicate that chronic LVSD developed over time after surgery-induced MI in rabbits can be longitudinally evaluated using non-invasive imaging techniques and confirmed by the entire-heart-slice histomorphology. This experimental LVSD platform in rabbits may interest researchers in the field of experimental cardiology and help strengthen drug development and translational research for the

management of cardiovascular diseases.

Keywords: Rabbits; 3T cardiac magnetic resonance imaging (3T cMRI); echocardiography (Echo); myocardial infarction (MI); systolic dysfunction

Submitted Sep 02, 2018. Accepted for publication Sep 11, 2018.
doi: 10.21037/qims.2018.09.05
View this article at: http://dx.doi.org/10.21037/qims.2018.09.05

Introduction

Myocardial infarction (MI) is the leading cause of morbidity, mortality, and disability worldwide and remains one of the greatest challenges in biomedical research (1). The evaluation of cardiac dysfunction after MI is essential for the prediction and diagnosis of heart failure (HF). The common fundamental defect in cardiac dysfunction after MI is a gradually decreased ability of the heart to provide sufficient cardiac output to support the normal functions of organs due to impaired ejection of the left ventricle and blood perfusion to tissues. Severe left ventricle systolic dysfunction (LVSD) will lead to irreversible congestive HF. Therefore, LVSD is most frequently studied to elucidate the physiological and pathophysiological mechanisms of HF and to develop new diagnostic and therapeutic approaches for HF after MI (2-5). Several factors such as infarct size, LV remodeling, stunned or hibernating myocardium, and mechanical complications, may influence the appearance of LVSD after MI (6-8). Among these factors, ventricular remodeling is the most important (8). The process of ventricular remodeling refers to alterations in ventricular architecture, associated with an increased volume and an altered chamber configuration, which are driven by a combination of pathologic hypertrophy and apoptosis of myocytes, myofibroblast proliferation, and interstitial fibrosis (9). Ventricular remodeling is directly implicated in post-infarction development of ventricular dilation, a process that can influence LV function and survival outcomes (10). Multiple imaging approaches have been used to better understand the structural and molecular changes that underlie the progression of LV remodeling from myocardial injury to MI and, ultimately, to congestive HF. Advances in cardiovascular imaging have come at a rapid pace over the last several years (11). Cardiac magnetic resonance imaging (cMRI) and speckle-tracking imaging with ultrasound echocardiography (Echo) have been widely used to monitor LV remodeling after MI. These techniques can (I) provide specific quantitation of cardiac function, accurate chamber volumes and structure, myocardial viability and coronary perfusion in both acute and chronic settings and, (II) exclude mechanical complications (11-14), though often lacking gold standard histopathology proofs.

In translational cardiology, development of appropriate animal models for non-invasive evaluation of cardiac function is important to understand mechanisms of cardiac remodeling, and to provide new therapeutic strategies. Surgical complete coronary ligation to induce irreversible myocardium damage and subsequent remodeling has been extensively used and described (15-17), but often with high mortality due to severe ventricular tachycardia and ventricular fibrillation in the acute phase (18-20). While small animal MI models in rats and mice (19,21) display marked differences compared to the human heart (22), larger animals such as the dog, sheep and swine are very labor intensive and expensive (23,24). We experienced that the rabbit coronary occlusion/reperfusion model meets the requirements of the ideal experimental model (25). A medium sized rabbit heart has many similarities to the human heart in terms of cardiovascular anatomy, ventricular performance, cardiac metabolism, electrophysiology, coronary artery distribution, and collateralization after an acute event. In addition, with the lower phylogenetic scale, longer life span, strain-specific characteristics and low cost, the rabbit is a suitable species for cardiac research (13,25,26). Technically, the dimension of a rabbit heart is large enough to study with clinical imaging scanners and small enough to just fit in a standard glass slide for entire-heart-slice histomorphologic studies, both of great translational significance.

In the clinic, approximately 40% of MI patients suffer from LVSD (8). However, a good animal model of LVSD has not been proposed thus far. Most experiments have focused on acute or subacute MI over hours and days, but not on a MI model that systematically progresses to chronic LVSD. In this study, we established a rabbit model of reperfused MI that evolves to chronic LVSD

over the time course of 7 weeks, and developed an imaging platform for longitudinal monitoring and evaluation of cardiac morphology and contractile function. This experimental platform combines *in vivo* cardiac MRI and echocardiography with postmortem immunohistochemical analysis.

Methods

Experimental protocol

All animal procedures were approved by the Ethical Committee of the KU Leuven. Fifty-five New Zeeland white male rabbits (3–4 kg) were obtained from the Animal Center of KU Leuven (Heverlee, Belgium). Animals were randomized into two groups: one group was subjected to open-chest surgery without manipulation of the heart (sham group), while the other group received induction of MI (MI group). To monitor cardiac function, cMRI and echocardiography were performed at baseline, 48 h (cMRI only), 1 week (echo only) and 7 weeks post MI on each animal. After 7 weeks, rabbits were killed for further multiple histological processions.

MI model

All surgical procedures were performed in a sterile manner in the animal operating suites. The rabbit model of acute reperfused MI was previously described in details (13). Briefly, rabbits were sedated, endotracheally intubated and mechanically ventilated. After intravenous (iv) access was established, rabbits received 40 mg/kg/h sodium pentobarbital to maintain anesthesia. After disinfection of the chest, skin and subcutaneous tissues were cut open by layers along the left sternal border. Subsequently, the 4th and 5th intercostal space cartilages were cut and the pericardium was opened to expose the left circumflex artery branch (LCx). The LCx was ligated by a detachable knot using 2-0 silk at 2 mm below the left atrial appendage, of which the pullable end was left outside the thorax after closure of the thoracic cavity by layered sutures. Reperfusion was induced by pulling the exteriorized end of the suture in a closed-chest condition after 1 h of coronary occlusion. Similar procedures were applied for sham-operated animals, except for the LCx ligation. In the event of sustained ventricular fibrillation during coronary occlusion or reperfusion, animals were given 2% XYLOCAINE (1 mg/kg iv; lidocain, Eurovet Animal Health B.V.). After reperfusion, animals were allowed to recover on a warming blanket and were ventilated further until their own respiration took over.

Serum cardiac troponin T (cTnT) measurements

To determine the optimal time point of peak cTnT concentrations, serum samples at different time points post MI (baseline, 30 min, 1, 2, 4, 8 and 24 h) from a rabbit were collected from the ear vein without anesthesia. Serum cTnT levels were evaluated using a routine laboratory assay.

Cardiac magnetic resonance imaging

Using a 16-channel phased array knee coil, cMRI was performed on the anesthetized rabbit at a 3.0T clinical Siemens MRI scanner (Trio, Siemens, Erlangen, Germany) with a maximum gradient capability of 45 mT/m, triggered by ECG and gated by respiration using a small animal monitoring and gating system (SA Instruments, Inc. Stony Brook, NY, USA). The two ECG electrodes were attached to the shaved thorax skin with an apical pulse and to the left leg. The respiration sensor was attached to abdomen of the rabbit, which was placed supinely in a holder and gas-anesthetized with 2% isoflurane in the mixture of 20% oxygen and 80% room air, through a mask connected via a tube to a ventilation instrument (Harvard Apparatus, Holliston, MA, USA). All images were acquired during free breathing of the animal. Eight short-axial slices of the heart were collected with a slice thickness of 3.0 mm without gap to cover the entire LV. Turbo spin echo sequence of black blood imaging was applied for cardiac morphology with the parameters: TR of 621–750 ms, TE of 15–74 ms, FOV of 240×195 mm^2, FA of 180°, and in-plane resolution of 0.9×0.9 mm^2. The cine-MRI images were acquired on gradient echo in the short-axis, vertical long-axis and horizontal long-axis planes for displaying cardiac contraction. Each cine-MRI consisted of 25 frames/cycle, and the scan parameters: TR of 23 ms, TE of 3.7 ms, FOV of 240× 195 mm^2, FA of 12° and spatial resolution of 1.3×0.9 mm^2. The delayed contrast enhancement (CE) images were acquired by a 3D segmented k-space inversion recovery turbo fast low angle shot sequence 20 minutes after an iv bolus injection of meglumine gadoterate (Gd-DOTA, Dotarem®, Guerbet, France) at 0.2 mmol/kg with parameters: TR of 396 ms, TE of 1.54 ms, TI of 360 ms, FOV of 240×180 mm^2, FA of 15° and in-plane resolution of 1.1×0.8 mm^2.

Analysis of cMRI

cMRI images were read using an off-line workstation with dedicated software (SyngoMR A30, Siemens). The assessment and quantification of MI size and global LV function in CE and Cine-MRI images were made using the software SEGMENT (Medviso AB, Lund, Sweden). The endocardial and epicardial borders were manually traced in the end-diastolic and end-systolic short-axis Cine images. Papillary muscles were included in the myocardium. Global LV functions including end-diastolic volume (EDV), end-systolic volume (ESV), stroke volume (SV), ejection fraction (EF), cardiac output (CO) and mass were measured according to standard methods (4). Regional LV function was also assessed by measuring wall thickening from end-diastolic phase to end-systolic phase in six clockwise sectors on the mid-ventricle section of Cine images.

Transthoracic echocardiography

Transthoracic echocardiographic examinations were performed on anesthetized rabbits using a 10S transducer (4.4–10 Mhz) (GE Healthcare, Machelen, Belgium) on a Vivid 7 ultrasound machine (GE Healthcare). LV internal diameter at end-diastolic (LVIDd) and end-systolic phase (LVIDs), muscle thickness in diastole (IVSd) and in systole (IVSs) and LV posterior wall thickness in end-diastole (LVPWd) and end-systole (LVPWs) were measured at three levels: at the level of the mitral valve (mv), papillary muscle (pm) and apex (ap). In addition, the long axis diameter in end-diastole (LAXd) and systole (LAXs) was obtained. EDV [EDV = (LVIDd_mv^2 + LVIDd_pm^2 + LVIDd_ap^2) ×LAXd×Π/18] and ESV [ESV = (LVIDs_mv^2 + LVIDs_pm^2 + LVIDs_ap^2) ×LAXs×Π/18], EF {EF = [(EDV – EDV)/EDV] ×100}, and SV (SV = EDV – ESV) were calculated (27). The measurements for all parameters at 1 and 7 weeks post-surgery are reported as a percentage of the baseline measurement for each animal. Subsequently, an average per group was calculated for each parameter.

Histomorphology

After *in vivo* data acquisition, rabbits were euthanized with an overdose of sodium pentobarbital. The isolated heart and left lung were photographed, and then fixed with 10% formalin for 24 h. The fixed heart was cut into 3 mm short-axis sections, which were paraffin-embedded and cut into 5 µm slices. The heart slices were mounted entirely on standard glass slides, followed by hematoxylin-eosin (HE) and Masson Trichrome (MT) staining for necrosis and chronic fibrosis evaluation. Myocardial macrophage infiltration was evaluated by RAM-11 staining, using a mouse monoclonal anti-rabbit macrophage clone (1/50; M0633; DAKO, Leuven, Belgium) in Tris-NaCl-blocking buffer (TNB) (Perkin Elmer, Boston, USA). RAM-11 signals were subsequently detected with the Tyramide Signal Amplification kit (Perkin Elmer). In addition, the dissected lung was photographed and a small portion of fixed pulmonary tissue was paraffin-embedded and cut into 5 µm slices for HE staining to observe the presence or absence of HF-induced pulmonary congestion.

Statistical analysis

Data are shown as means ± SD for the number of animals studied. Differences between all groups were analyzed using the parametric one-way ANOVA. If a statistical difference was detected ($P<0.05$), the difference between the individual groups was determined using the Tukey's multiple comparison test. Correlation analyses between serum cTnT levels and LV infarct sizes and between EF measurements of MRI and Echo were performed using the non-parametric Pearson correlation test. All statistical analyses were performed with GraphPad Prism 6 software (GraphPad, La Jolla, CA, USA).

Results

General characteristics of the rabbits

In 48 out of 55 rabbits, surgery was successful (87.3%). Mortality rate was 12.7% (7/55) or 3.6% (2/55) for the acute or chronic stage respectively. Four groups were distinguished: sham (n=12), MI_NO_LVSD (n=10), MI_M (moderate)_LVSD (n=9), and MI_S (severe)_LVSD (n=15). LVSD and severe LVSD developed in 71% (24/34) and 44% (15/34) respectively of MI animals after 7 weeks.

Body weight was not significantly different between the groups at the start, at 1 and 7 weeks post-surgery (*Table 1*). Serum cTnT levels were the highest in MI_S_LVSD rabbits and were significantly different from that of sham, MI_NO_LVSD and MI_M_LVSD animals (*Table 1*). Serum cTnT levels correlated positively with LV infarct size at the acute stage ($r=0.89$; $P<0.0001$), while they were negatively correlated with EF ($r=0.95$; $P<0.01$).

Table 1 General characteristics of rabbits with no (MI_NO_LVSD), moderate (MI_M_LVSD) or severe left ventricle systolic dysfunction (MI_S_LVSD) after sham-operation or with reperfused myocardial infarction (MI)

General outcomes	Sham	MI_NO_LVSD	MI_M_LVSD	MI_S_LVSD
N	12	10	9	15
Body weight				
Baseline	3.5±0.41	3.5±0.27	3.6±0.21	3.6±0.50
1 week post MI	3.8±0.47	3.8±0.33	3.8±0.36	3.9±0.47
7 weeks post MI	4.1±0.48	4.1±0.28	4.1±0.34	4.2±0.46
CTnT (μg/L) 4 hours post MI	ND	0.21±0.20	0.56±0.18•†	1.0±0.33•†‡
Infarct size (%LV)				
48 hours (cMRI)	ND	10±6.0	38±4.1•†	48±3.3•†‡
7 weeks (cMRI)	ND	7.9±5.1	30±5.9•†a	46±2.9•†‡
7 weeks (histology)	ND	7.2±3.9	26±6.4•†a	44±3.4•†‡

Data are expressed as means ± SD of n rabbits. •, P<0.05 versus sham rabbits; †, P<0.05 versus MI_NO_LVSD rabbits; ‡, P<0.05 versus MI_M_LVSD animals; [a], P<0.05 versus 48 hours post MI surgery according to the one-way ANOVA test followed by the Tukey's multiple comparison test. cTnT, serum cardiac Troponin T; ND, not detectable.

Cardiac MRI

MI sizes were less than 20% of the LV in MI_No_LVSD, 20–42% of the LV in MI_M_LVSD and 43–54% of the LV in MI_S_LVSD (*Table 1*). Chronic MI sizes by cMRI were smaller than acute MI sizes, and were better correlated with MI sizes determined by histology (r=0.93 versus r=0.86, respectively). As shown in *Figure 1*, longitudinal evaluation by *in vivo* CE-MRI of mid-ventricular slices at 48 hrs and at 7 weeks post MI (*Figure 1A,B,C,D,E,F,G,H*) revealed that the hyper-enhanced MI region in the MI_S_LVSD animals extended to the anterior, lateral and posterior wall at the acute stage (*Figure 1D*). This range persisted, however the wall became thinner 7 weeks (*Figure 1H*) post-surgery for MI_S_LVSD rabbits in comparison to the other groups. The corresponding cine images for the MI_S_LVSD (*Figure 1L,P*) rabbits indicated that the LV dilated and wall motion decreased, as can be demonstrated vividly by the videos of cine cMRI (*Figure S1*).

For global cardiac functions as shown in *Figure 2*, cMRI parameters did not show significant differences (either as raw data or expressed as % change of baseline) between sham and MI_NO_LVSD animals at either acute (48 hrs) or chronic (7 weeks) post MI stages. MI_M_LVSD rabbits at the acute and chronic stage showed an unrecovered reduction in cardiac function (EF decreased from 57% to 43% and to 44%, respectively) and functional changes (%EF decreased by 25% and 23%, respectively). In MI_S_LVSD rabbits this reduction was more pronounced (EF decreased from 58% to 36% and to 28%, respectively; %EF decreased by 36% and 49%, respectively). MI size was significantly correlated with EF for all groups (r=0.95, P<0.01). In contrast to sham rabbits, EDV and ESV in MI_M_LVSD animals increased by 10% and 45% respectively at the acute stage and by 20% and 60% respectively at the chronic stage; in MI_S_LVSD rabbits EDV and ESV were increased by 17% and 70% respectively at the acute stage and by 27% and 130% respectively at the chronic stage (*Figure 2*). SV in MI_M_LVSD rabbits decreased by 17% and 11% at the acute and chronic stage, respectively; the decrease of SV in MI_S_LVSD animals was more pronounced (25% and 36% at the acute and chronic stage respectively, suggesting decompensation of the heart), in comparison to the sham group.

For regional cardiac function measured by six segments, there were no significant changes of LV wall thickening between sham and MI_NO_LVSD animals at both experimental stages (*Table 2*). Wall thickening significantly decreased to about 44% and 42% at the acute and chronic stage, respectively (P<0.05 for each) in only two cardiac segments (inferolateral and anterolateral) of MI_M_LVSD rabbits. But, wall thickening significantly decreased (25–38% at the acute stage; 25–41% at the chronic stage; P<0.05 for each) in up to four cardiac segments (anterior, inferior, inferolateral and anterolateral) of MI_S_LVSD rabbits, as compared to other groups (*Table 2*).

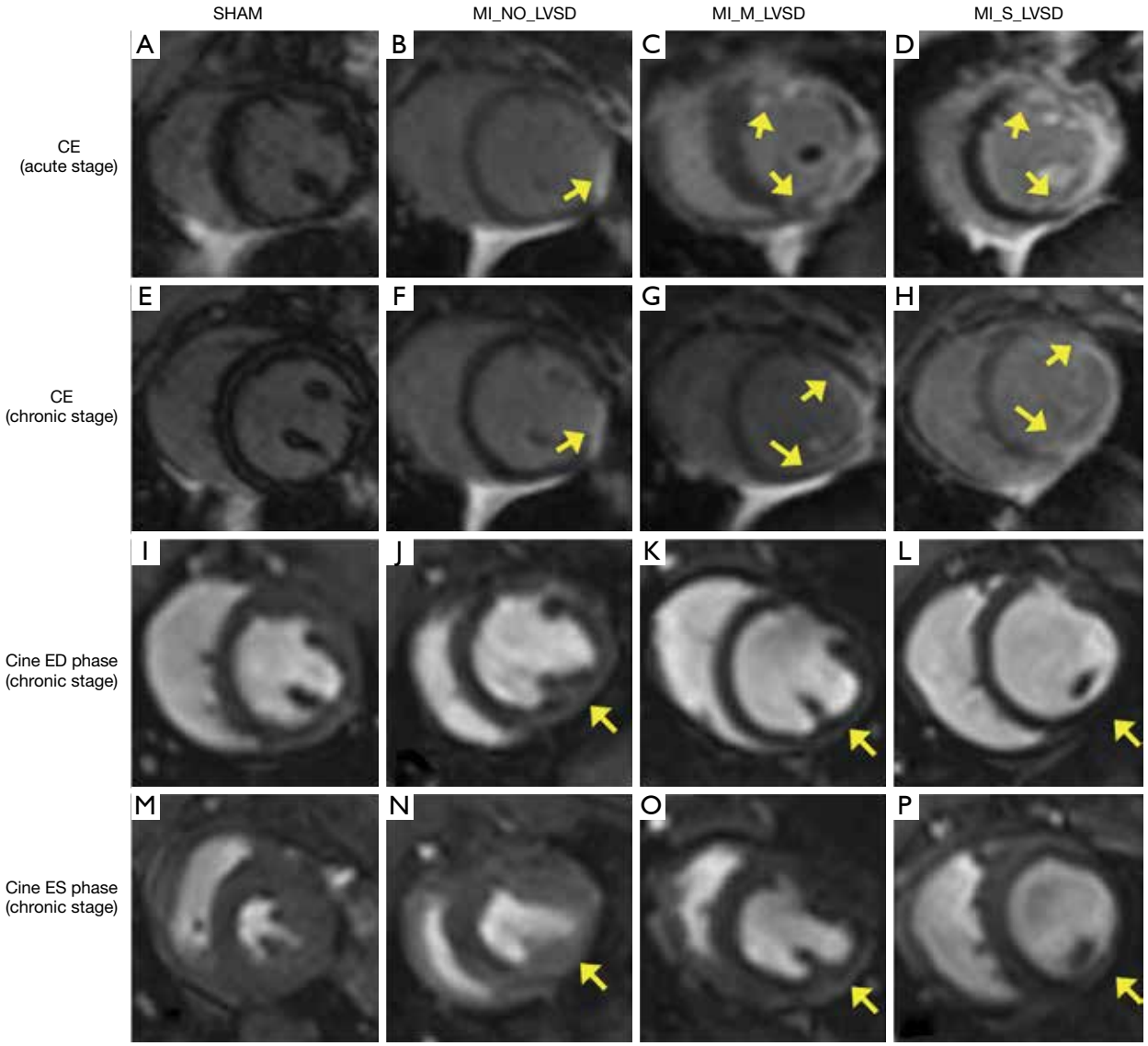

Figure 1 Longitudinal evaluation of cardiac remodeling by *in vivo* cardiac magnetic resonance imaging (cMRI) after the induction of a reperfused myocardial infarction (MI) in rabbits. Serial images of the mid-ventricle slices obtained by contrast enhanced (CE) cMRI are shown at 48 hours (acute stage) and seven weeks (chronic stage) post MI of sham (A,E), MI_NO_LVSD (B,F), MI_M_LVSD (C,G) and MI_S_LVSD (D,H) rabbits. The infarct areas, depicted as hyper-enhanced regions on the CE cMRI images (yellow arrows), extended to the anterior, lateral and posterior wall at 48 hours post MI (D) for MI_S_LVSD rabbits as compared to the other groups. At the chronic stage, the infarct area became thinner and evenly enhanced for MI_S_LVSD rabbits (H), but not for MI_M_LVSD animals (G). The corresponding cine cMRI images at end-diastolic (ED) (I,J,K,L) and end-systolic (ES) phase (M,N,O,P) were taken 7 weeks post MI. Hypokinesis or dyskinesia of the lateral wall was observed for MI_M_LVSD (K,L,M,N,O) and MI_S_LVSD (L,M,N,O,P) rabbits, respectively, with increasing LV diameters displayed.

Echocardiography

Echocardiographic analysis revealed that rabbits with the largest LV infarct size (MI_S_LVSD group) developed a severe cardiac dysfunction 1 and 7 weeks post MI, as indicated by a significant EF reduction as compared to the other groups (*Table 3*). Acutely, hearts of these rabbits showed a significant increase in ESV as compared to MI_

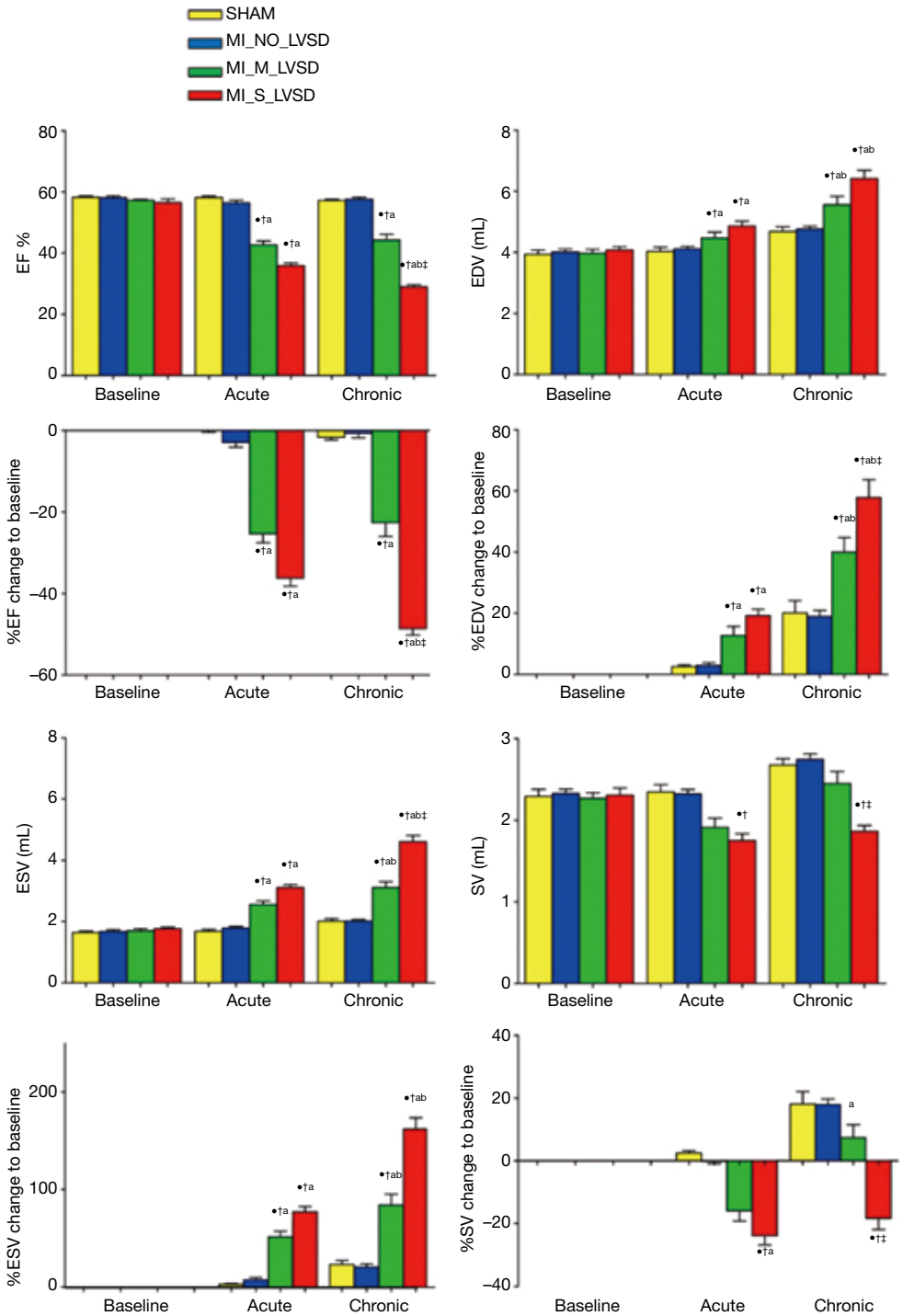

Figure 2 Bar charts of cardiac functions evaluated by *in vivo* cine cMRI after the induction of a reperfused MI in rabbits. Data are presented as means ± SD for sham (n=12), MI_NO_LVSD (n=10), MI_M_LVSD (n=9) and MI_S_LVSD (n=15) rabbits. Global functional parameters in panels A-D and % changes of parameters to baseline in panels E-H are shown for baseline, 48 hours (acute stage) and 7 weeks (chronic stage) post MI surgery, respectively. •P<0.05 versus sham; †, P<0.05 versus MI_NO_LVSD; ‡, P<0.05 versus MI_M_LVSD; [a], P<0.05 versus baseline and [b], P<0.05 versus the acute stage according to the parametric one way ANOVA statistical test and Tukey's multiple comparison test. EF, ejection fraction; EDV, end-diastolic volume; ESV, end-systolic volume; SV, stroke volume.

Table 2 Longitudinal evaluation of left ventricular wall thickening by cMRI in rabbits with no (MI_NO_LVSD), moderate (MI_M_LVSD) or severe left ventricle systolic dysfunction (MI_S_LVSD) after sham-surgery or with reperfused MI

Wall thickening (%)	Anterior	Anteroseptal	Inferoseptal	Inferior	Inferolateral	Anterolateral
Sham						
48 hours post MI	66±4.8	66±4.3	67±4.0	67±5.6	72±6.8	74±6.8
7 weeks post MI	68±5.2	68±8.5	69±6.9	70±5.3	74±7.7	74±6.5
MI_NO_LVSD						
48 hours post MI	66±7.2	65±4.5	66±7.7	66±8.4	69±7.0	70±7.6
7 weeks post MI	68±7.6	66±5.2	68±6.8	68±6.2	72±6.6	74±8.2
MI_M_LVSD						
48 hours post MI	55±4.2	62±3.9	63±3.3	54±4.3	45±5.4$^{•†}$	43±5.9$^{•†}$
7 weeks post MI	59±4.6	66±3.6	67±4.3	54±4.6	45±6.6$^{•†}$	42±6.9$^{•†}$
MI_S_LVSD						
48 hours post MI	38±6.0$^{•†‡}$	65±4.3	65±3.8	33±4.9$^{•†‡}$	26±5.5$^{•†‡}$	25±4.2$^{•†‡}$
7 weeks post MI	41±7.2$^{•†‡}$	69±5.6	69±5.4	33±5.7$^{•†‡}$	26±6.2$^{•†‡}$	25±5.1$^{•†‡}$

Data are expressed as means ± SD of 9–15 rabbits. $^{•}$, P<0.05 versus sham rabbits; †, P<0.05 versus MI_NO_LVSD rabbits; ‡, P<0.05 versus MI_M_LVSD animals according to the one-way ANOVA test followed by the Tukey's multiple comparison test.

NO_LVSD rabbits, while EDV was not different. This resulted in a significant reduction of the SV in rabbits with severe LVSD versus the other three groups (*Table 3*). At the chronic stage both EDV and ESV were increased and EF significantly reduced in MI_S_LVSD rabbits as compared to the other animals. A strong positive correlation was found between EF determined by echocardiography and by cMRI at both time points, but the correlation was even stronger at 7 weeks as compared to 1 week post MI surgery (*Figure 3*).

For MI_S_LVSD rabbits LVID in both phases was also significantly enhanced as compared to the other groups (*Table 3*). In addition, these animals had significant thinning of the posterior wall at the papillary muscle level in the chronic phase as compared to the other groups; however, this change was more pronounced in the end-systolic phase as compared to the end-diastolic phase (*Table 3*).

Figure 4 illustrates the echocardiographic changes as shown in *Table 3*. For sham-operated and MI_NO_LVSD animals, LV volume and wall thickness did not change over time. Hypokinesis and akinesis of the posterior wall was observed for rabbits with a large infarct area (MI_M_LVSD and MI_S_LVSD) at the acute stage. At the chronic stage hypokinesis and akinesis was more severe for the MI_S_LVSD group. MI_S_LVSD rabbits showed the highest dilation of the heart and extreme thinning of the posterior wall in the end-diastolic (*Figure 4W*) and end-systolic phase (*Figure 4X*) as compared to the other groups at the chronic stage.

Postmortem histomorphology

Postmortem heart sections of the four animal groups revealed ventricular remodeling to different degrees among three MI groups (*Figure 5*). The most extensive infarct lesion was present in MI_S_LVSD animals (whitish region in *Figure 5D*). The infarct lesion was substantially smaller for animals with moderate (*Figure 5C*) or no LVSD (*Figure 5B*) relative to no infarct in sham animal (*Figure 5A*). The LV cavity was dilated, the thickness of lateral wall was decreased and the papillary muscles were atrophied in rabbits with MI_S_LVSD (*Figure 5D*) relative to the other groups. The transverse heart slices (*Figure 5A,B,C,D*), size of the infarct lesion, dilation of the LV cavity and lateral wall thickness corresponded well in-between the macroscopic views of the HE (*Figure 5E,F,G,H*), MT (*Figure 5I,J,K,L*) and RAM-11 (*Figure 5M,N,O,P*) stained heart sections. The isolated wet lung lobes gradually turned dark red from sham animals to rabbits with MI_S_LVSD due to a different degree of pulmonary congestion (*Figure 5Q,R,S,T*), confirming our findings in the heart.

Table 3 Longitudinal evaluation of changes in cardiac function by *in vivo* echocardiography

% of baseline	Sham	MI_NO_LVSD	MI_M_LVSD	MI_S_LVSD
N	12	10	9	15
EDV (mL)				
1 week post MI	−1.1±15	−4.8±14	6.6±10	−5.8±13
7 weeks post MI	3.4±22	−2.9±15	2.8±22	35±30$^{•†‡ab}$
ESV (mL)				
1 week post MI	−1.1±14	−7.5±17	6.5±16	24±27†
7 weeks post MI	2.4±28	−8.5±19	15±27†	79±34$^{•†‡ab}$
SV (mL)				
1 week post MI	−0.65±22	0.26±28	7.7±16	−30±12$^{•†a}$
7 weeks post MI	5.0±20	5.0±27	−5.8±26	−2.4±25^{b}
EF (%)				
1 week post MI	−0.29±9.8	4.3±19	1.0±11	−25±13$^{•†‡a}$
7 weeks post MI	2.1±10	7.2±18	−8.8±14†	−28±8.2$^{•†‡a}$
LVIDd (mm)				
1 week post MI	−0.11±6.5	−1.5±6.3	6.7±7.6	0.79±8.3
7 weeks post MI	−0.32±9.6	−3.3±9.5	−1.6±7.6	18±10$^{•†‡b}$
LVIDs (mm)				
1 week post MI	0.35±11	−2.4±11	1.8±12	12±16
7 weeks post MI	−4.8±15	−7.1±9.8	−3.0±12	30±11$^{•†‡ab}$
LVPWd (mm)				
1 week post MI	4.7±22	7.5±33	39±52	40±47^{a}
7 weeks post MI	1.0±26	−3.7±24	32±26	−5.0±34^{‡b}
LVPWs (mm)				
1 week post MI	0.40±18	18±31	25±32	13±32
7 weeks post MI	8.8±18	19±43	25±27	−19±32^{†‡b}

Data are expressed as means ± SD of n rabbits. LVID and LVPW parameters were measured at the level of the papillary muscle level. $^{•}$, P<0.05 versus sham rabbits; †, P<0.05 versus MI_NO_LVSD rabbits; ‡, P<0.05 versus MI_M_LVSD animals; ^{a}, P<0.05 versus baseline; ^{b}, P<0.05 versus 1 week post MI according to the one-way ANOVA test followed by the Tukey's multiple comparison test. LVIDd, left ventricle internal diameter measured in the end-diastolic phase; LVIDs, left ventricle internal diameter measured in the end-systolic phase; LVPWd, LV posterior wall thickness at the end-diastolic; LVPWs, LV posterior wall thickness at the end-systolic phase; EDV, end-diastolic volume; ESV, end-systolic volume; SV, stroke volume; EF, ejection fraction.

Microscopically (*Figure 6*), MI_NO_LVSD hearts had more fibrosis (*Figure 6F*) and more adipocyte (*Figure 6B,F,J*) and macrophage (*Figure 6J*) infiltration as compared to the heart of sham animals (*Figure 6A,E,I*). Heart sections of MI_M_LVSD rabbits showed most severe infiltration of inflammatory macrophages (*Figure 6K*) and interstitial collagen deposition (*Figure 6C,G*) and moderate presence of adipocytes (*Figure 6C,G,K*). Hearts of rabbits with MI_S_LVSD were characterized by excessive presence of adipocytes (*Figure 6D,H,L*), enriched fibrotic collagen (*Figure 6H*) and less macrophage infiltration (*Figure 6L*), resulting in post-MI scar formation. In addition, microscopically, lung sections (*Figure 6M,N,O,P*) demonstrated that the capillaries in the alveolar walls were congested with

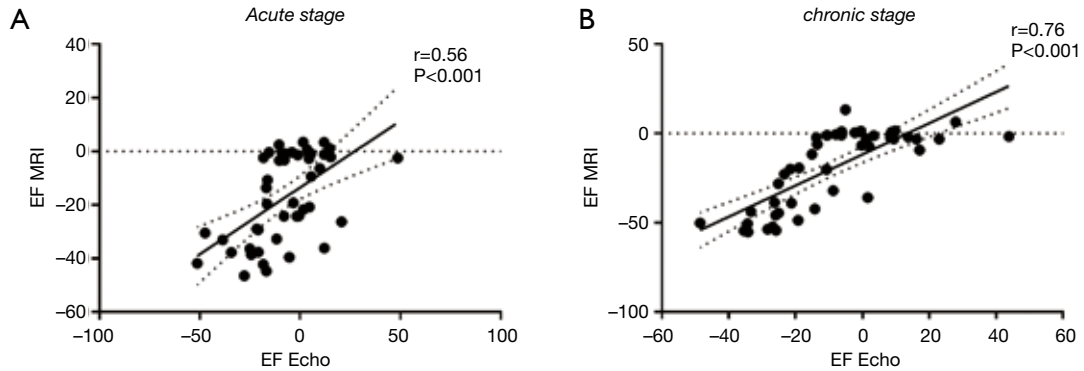

Figure 3 Correlation between ejection fraction (EF) measurements obtained by cardiac magnetic resonance imaging (cMRI) and echocardiography (Echo) at 48 hours (cMRI) or 1 week (Echo; acute stage) (A) and 7 weeks (chronic stage) post myocardial infarction (MI) induction (B). Statistically significant differences were determined using the non-parametric Pearson correlation test.

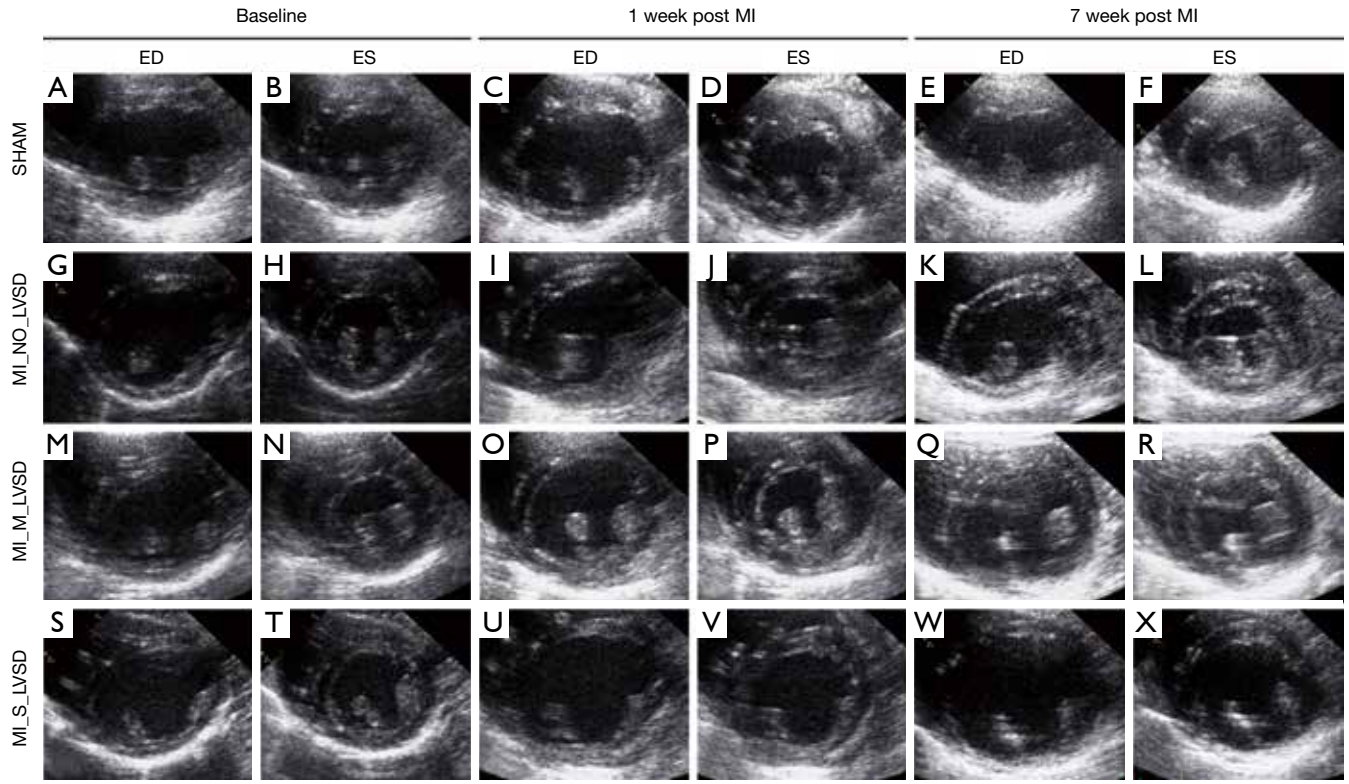

Figure 4 Longitudinal evaluation of cardiac function by *in vivo* echocardiography after the induction of a reperfused MI in rabbits. All images are echocardiographic short axis images at the level of the papillary muscle at the end-diastolic (ED) and end-systolic (ES) phase obtained from sham rabbits and reperfused MI-induced rabbits with no (MI_NO_LVSD), moderate (MI_M_LVSD) or severe (MI_S_LVSD) left ventricle systolic dysfunction.

red blood cells in MI versus sham rabbits, with the highest degree of congestion in the lung of rabbits with MI_S_LVSD.

Discussion

In this study we report, for the first time, an occlusion/reperfusion rabbit model that evolved from the acute MI

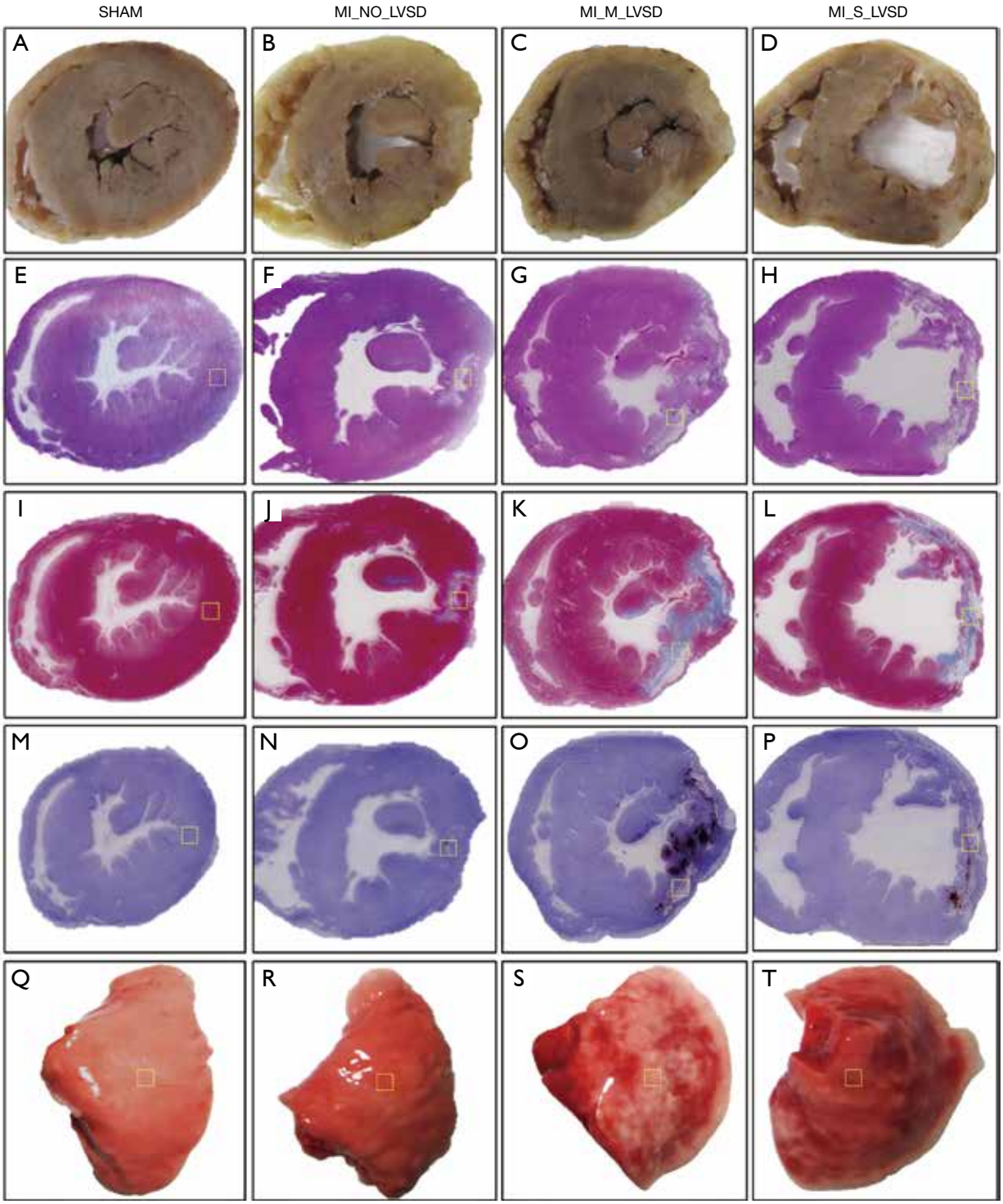

Figure 5 Post-mortem macroscopic views of the mid-ventricle sections from the sham and induced-MI rabbits with no (MI_NO_LVSD), moderate (MI_M_LVSD) and severe (MI_S_LVSD) left ventricle systolic dysfunction at 7 weeks post-surgery. All groups are shown either as gross sections (A-D) or as corresponding views stained with haematoxylin & eosin (HE, E-H), Masson Trichrome (MT, I-L) and RAM-11 (M-P). Images of the wet lungs are also shown as the different degrees of blood congestion (Q-T). The dashed yellow squares denote the areas that have been microscopically focused in *Figure 6* (E-T).

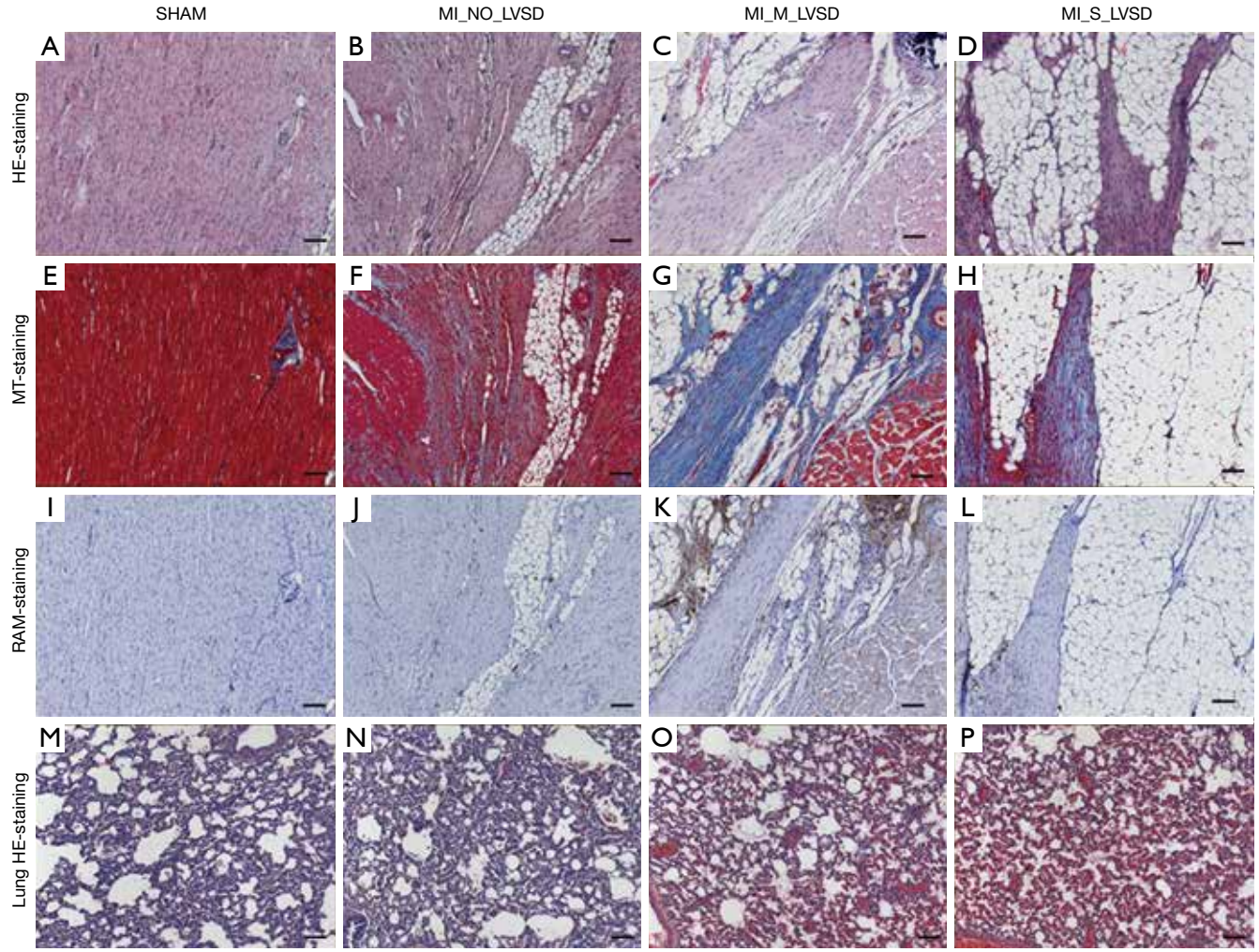

Figure 6 Microscopic views of mid-ventricle myocardial and lung sections with different histochemical stainings obtained from sham (A,E,I,M) and induced reperfused MI rabbits with no (MI_NO_LVSD, B,F,J,N), moderate (MI_M_LVSD, C,G,K,O) and severe (MI_S_LVSD, D,H,L,P) left ventricle systolic dysfunction are shown to illustrate the different degrees in fibrosis (collagen synthesis), adipocytes and macrophage infiltration via haematoxylin and eosin (HE; A-D), Masson Trichrome (MT; E-H) and RAM-11 (I-L) stainings. HE-stained lung sections of all groups (M-P) indicate different levels of red blood cell accumulation in the alveoli. Magnification: ×100. Scale bar: 100 μm.

into chronic stage with four different groups (sham, MI_NO_LVSD, MI_M_LVSD, and MI_S_LVSD) by using a combination of cMRI, echocardiography, serum biomarker cTnT test and histomorphology. The highest degree of LV remodeling was observed with the largest infarct size in MI_S_LVSD models at 1 and 7 weeks post MI surgery. EF measured by cMRI in these chronic MI_S_LVSD rabbits was less than 35%, which is consistent with clinical results (28,29). This change was accompanied by a severe dilation of the heart as evidenced by an increase of EDV and ESV by 50% and 150%, respectively after 7 weeks post MI. Among all MI models, 44% displayed severe LVSD, which is close to the clinical finding that 40% of MI patients suffer from LVSD following MI (7,8). The different degrees of chronic LVSD could be distinguished from sham and MI_NO_LVSD rabbits via imaging and histology.

The different symptoms and/or signs with HF are often subjective, and the threshold for diagnosis may vary widely among clinicians. However, the presence and degree of LVSD can be measured objectively by cardiac imaging techniques. To induce a rabbit model of LVSD is technically challenging and only rarely reported with

a less advanced imaging methods (30). In our study, we induced acute MI with ST-segment elevation by abrupt surgical occlusion of the LCx artery for 1 hour followed by coronary reperfusion. As a result, the myocardium distal to the occlusion becomes irreversibly necrotic instead of reversibly ischemic due to the prolonged ischemia (>30 minutes). Unrelieved ischemia causes permanent damage to the myocardium previously supplied by the occluded LCx artery. Moreover, the destroyed myocardium is replaced by fibrous scar tissue in the MI area and non-MI myocardium may develop hypertrophy over time. Because scar tissue does not contribute to myocardial contractility, global LV contractile function becomes impaired when the scar is large, resulting in progressive chronic LVSD. To establish a successful LVSD model, we had to induce the largest possible MI size in order to significantly impair cardiac function. This however bears risks: animals may die during or shortly after surgery due to a too large MI, severe arrhythmia, postoperative infection, etc. To avoid these risks: (I) the LCx was accurately ligated to ensure successful surgery and to reduce animal mortality; (II) the entire surgery was performed under a sterile environment to avoid infection; and (III) xylocaine was applied to prevent/stop arrhythmias during the LCx ligation-reperfusion stage. Finally, ventilation was properly maintained and each animal was kept at an optimal oxygenation level until it completely woke up. These conditions are based on our previous studies in which rabbit MI models were utilized (4,13,25,26).

So far most of the animal experiments on MI have focused on acute or subacute MI over hours and days, but the follow-up by cMRI and echocardiography over months have not been reported. Using a non-invasive imaging platform, MI from acute through chronic stage has been systematically investigated in this study. MI sizes after surgery were determined by delayed contrast-enhanced cMRI *in vivo*, and cardiac contractility was evaluated both by cine cMRI and echocardiography at the acute and chronic stages. We found that cardiac contractile function strongly correlated with MI sizes. According to cardiac function measurements, serum troponin T level analysis and histology, we distinguished four different groups after surgery: sham, MI_NO_LVSD, MI_M_LVSD and MI_S_LVSD rabbits. Acute serum levels of cardiac troponin T, a marker for myocardial injury used in the diagnosis of acute MI (31), correlated well with infarct sizes. EF, the most common parameter of global cardiac performance in clinical practice, is more influenced by the degree of LV remodeling than by any other factors (6). Therefore, we focused on EF changes for evaluation of global cardiac function and remodeling. At present, echocardiography remains the predominant clinically applicable non-invasive test of choice, based on a broader availability. The 2D echocardiography is well established and has emerged as an important non-invasive clinical tool for the assessment of LV systolic and diastolic function after MI (30,32). However, non-invasive 2D echocardiography on small animals is challenging. Although echocardiography on rabbits has been reported, most studies focused on the complete occlusion coronary artery model (30,32-34). Only one study reported the regional function in a rabbit ischemia-reperfusion model, but the authors used open chest invasive echocardiography (35). In our study, we longitudinally evaluated global LV function using non-invasive echocardiography in a rabbit ischemia-reperfusion model. We showed high-quality 2D cardiac images of rabbits with different MI sizes, which correlated well with cMRI at both acute and chronic stages.

Postmortem histology confirmed the different degrees of LV remodeling in the 3 MI groups. All animals with a large extended transmural infarction belonged to the MI group with severe LVSD, while the MI_M_LVSD rabbits showed smaller infarct areas without transmurality. This may explain why some rabbits with initially a high reduction in EF and a large infarct size at the acute stage, do not develop severe LVSD in the end. At 7 weeks post MI, the LV architecture changed in the infarcted regions, resulting in different degrees of fibrosis or collagen deposition, as well as adipocyte and macrophage infiltration as characterized using H&E and RAM-11 stainings. We found the largest quantities of macrophages mixed with fibrotic collagen and normal myocytes in the moderate LVSD heart, while the MI region in the severe LVSD heart was replaced by scar tissue enriched with adipose cells and fibrotic collagen, but with less macrophages. Larger transmural infarcts were associated with more infiltrating adipocytes, more collagen deposition/fibrosis and fewer macrophages as compared to smaller non-transmural infarcts as the MI transitioned from acute into chronic stage. In the severe LVSD heart, a large amount of adipose cells and fibrotic collagen predominantly formed the infarct scar region during the remodeling process, which resulted in elongation and thinning of the infarcted LV. These changes provoked a progressive decline in ventricular performance. In turn, the LV chamber became enlarged and the shape of the heart shifted from an elliptical to a more spherical chamber configuration. No

statistically significant differences were seen in septal wall thickness between the four groups, which may indicate that cardiomyocyte size may not have been affected. The reason may be that seven weeks post MI in rabbits are not long enough to induce the compensatory hypertrophy of normal myocardium. To confirm the different degrees of ventricular damage in our model, we analyzed postmortem wet lungs as indirect evidence. A bigger LV infarct size resulted in LV dysfunction, and ultimately led to accumulation of red blood cells in the capillaries of the pulmonary alveoli. The MI_S_LVSD group did indeed show the highest level of blood congestion as evidenced by both macro- and microscopic findings. This is the first study to report such findings in the rabbit.

MI induced by left anterior descending (LAD) coronary artery ligation results in more uniform infarct sizes, but the mortality is more than 50% due to severe ventricular tachycardia during and after the MI induction (22). In our study, we show that ligation of the LCx in rabbits reduced the mortality rate to 12.7% and 3.6% at the acute and chronic stage, respectively. Although we always ligated the LCx at the same location (2 mm below the left atria), the infarct extent is quite variable. This may be due to the anatomy of the rabbit coronary artery system. This not only differs between species, but may also vary significantly within a single species. In our study, different infarct sizes were obtained, which in turn developed into different degrees of LV dysfunction, thus more closely resembling structural and functional characteristics of the dysfunction in human patients. Combined with the advanced clinical cardiac imaging techniques (36-40), this experimental LVSD platform in rabbits can be easily applied in clinically relevant imaging studies on translational cardiology and can help strengthen drug development and clinical research for the management of cardiovascular diseases. Recently, this platform has already been successfully applied in ongoing cardiac animal experiments (41,42).

There exist certain limitations in this study. The mortality could become higher at the acute stage if the infarct area was made too big. To reduce the mortality we choose LCx instead of LAD ligation, it was difficult to control the progress of MI, thus not all MIs turned transmural and further became cases of S_LVSD. The plasma concentrations of N terminal pro B type natriuretic peptide (NT-proBNP) after MI provide an alternative method of assessing cardiac function, but we could not detect NT-proBNP in our rabbit LVSD models, the reasons might be that the kit is not sensitive to rabbit serum, or seven weeks post MI are not long enough for NT-proBNP detection.

Conclusions

Our study provides a rabbit model with different degrees of chronic LVSD, which could be distinguished from sham and MI_NO_LVSD rabbits via *in vivo* cMRI, echocardiography and postmortem histology. Our model matches the pathophysiology of systolic dysfunction after MI in human patients and is highly reproducible and cost-effective. It may also be useful for the preclinical testing of treatments targeting myocardial damage following MI and satisfy the needs in preclinical or translational cardiac imaging research.

Acknowledgements

We thank Christine Vranckx, Inge Vorsters for expert technical assistance, and Jie Yu for making histological preparations. We are grateful to Prof. Paul Herijgers and Mieke Ginckels for access to the surgery rooms and the Vivid 7 ultrasound machine.

Funding: This work was supported by a grant from the 'Agentschap voor Innovatie door Wetenschap en Technologie Onderzoek & Ontwikkeling' (ICD 668894), awarded to the groups of Prof. Ni and Prof. Lijnen and to Dr. Lu and Dr. Gallacher from Janssen Pharmaceutical NV.

Footnote

Conflicts of Interest: The authors have no conflict of interest to declare.

Ethical Statement: All animal procedures were approved by the Ethical Committee of the KU Leuven.

References

1. Sanchis-Gomar F, Perez-Quilis C, Leischik R, Lucia A. Epidemiology of coronary heart disease and acute coronary syndrome. Ann Transl Med 2016;4:256.
2. Raya TE, Gay RG, Lancaster L, Aguirre M, Moffett C, Goldman S. Serial changes in left ventricular relaxation and chamber stiffness after large myocardial infarction in rats. Circulation 1988;77:1424-31.
3. Raya TE, Gay RG, Aguirre M, Goldman S. Importance of venodilatation in prevention of left ventricular

dilatation after chronic large myocardial infarction in rats: a comparison of captopril and hydralazine. Circ Res 1989;64:330-337.
4. Feng Y, Chen F, Yin T, Xia Q, Liu Y, Huang G, Zhang J, Oyen R, Ni Y. Pharmacologic Effects of Cannabidiol on Acute Reperfused Myocardial Infarction in Rabbits: Evaluated With 3.0T Cardiac Magnetic Resonance Imaging and Histopathology. J Cardiovasc Pharmacol 2015;66:354-363.
5. Monnet E, Chachques JC. Animal models of heart failure: what is new? Ann Thorac Surg 2005;79:1445-53.
6. Zornoff LA, Paiva SA, Duarte DR, Spadaro J. Ventricular remodeling after myocardial infarction: concepts and clinical implications. Arq Bras Cardiol 2009;92:150-64.
7. Cleland JG, Torabi A, Khan NK. Epidemiology and management of heart failure and left ventricular systolic dysfunction in the aftermath of a myocardial infarction. Heart 2005;91 Suppl 2:ii7-13; discussion ii31, ii43-18.
8. Minicucci MF, Azevedo PS, Polegato BF, Paiva SA, Zornoff LA. Heart failure after myocardial infarction: clinical implications and treatment. Clin Cardiol 2011;34:410-4.
9. Konstam MA, Kramer DG, Patel AR, Maron MS, Udelson JE. Left ventricular remodeling in heart failure: current concepts in clinical significance and assessment. JACC Cardiovasc Imaging 2011;4:98-108.
10. Sutton MG, Sharpe N. Left ventricular remodeling after myocardial infarction: pathophysiology and therapy. Circulation 2000;101:2981-8.
11. Flachskampf FA, Schmid M, Rost C, Achenbach S, DeMaria AN, Daniel WG. Cardiac imaging after myocardial infarction. Eur Heart J 2011;32:272-83.
12. Weaver JC, Ramsay DD, Rees D, Binnekamp MF, Prasan AM, McCrohon JA. Dynamic Changes in ST Segment Resolution After Myocardial Infarction and the Association with Microvascular Injury on Cardiac Magnetic Resonance Imaging. Heart Lung Circ 2011;20:111-8.
13. Feng Y, Xie Y, Wang H, Chen F, Ye Y, Jin L, Marchal G, Ni Y. A modified rabbit model of reperfused myocardial infarction for cardiac MR imaging research. Int J Cardiovasc Imaging 2009;25:289-98.
14. Symons R, Claus P, Marchi A, Dresselaers T, Bogaert J. Quantitative and qualitative assessment of acute myocardial injury by CMR at multiple time points after acute myocardial infarction. Int J Cardiol 2018;259:43-6.
15. Houser SR, Margulies KB, Murphy AM, Spinale FG, Francis GS, Prabhu SD, Rockman HA, Kass DA, Molkentin JD, Sussman MA, Koch WJ, American Heart Association Council on Basic Cardiovascular Sciences CoCC, Council on Functional G, Translational B. Animal models of heart failure: a scientific statement from the American Heart Association. Circ Res 2012;111:131-50.
16. Gupta S, Sen S. Animal models for heart failure. Methods Mol Med 2006;129:97-114.
17. Kuster DW, Merkus D, Kremer A, van Ijcken WF, de Beer VJ, Verhoeven AJ, Duncker DJ. Left ventricular remodeling in swine after myocardial infarction: a transcriptional genomics approach. Basic Res Cardiol 2011;106:1269-81.
18. Gao XM, Dart AM, Dewar E, Jennings G, Du XJ. Serial echocardiographic assessment of left ventricular dimensions and function after myocardial infarction in mice. Cardiovasc Res 2000;45:330-8.
19. Saleh MG, Sharp SK, Alhamud A, Spottiswoode BS, van der Kouwe AJW, Davies NH, Franz T, Meintjes EM. Long-Term Left Ventricular Remodelling in Rat Model of Nonreperfused Myocardial Infarction: Sequential MR Imaging Using a 3T Clinical Scanner. J Biomed Biotechnol 2012;2012:504037.
20. Iwanaga K, Takano H, Ohtsuka M, Hasegawa H, Zou Y, Qin Y, Odaka K, Hiroshima K, Tadokoro H, Komuro I. Effects of G-CSF on cardiac remodeling after acute myocardial infarction in swine. Biochem Biophys Res Commun 2004;325:1353-9.
21. Nahrendorf M, Hiller KH, Hu K, Ertl G, Haase A, Bauer WR. Cardiac magnetic resonance imaging in small animal models of human heart failure. Med Image Anal 2003;7:369-75.
22. Klocke R, Tian W, Kuhlmann MT, Nikol S. Surgical animal models of heart failure related to coronary heart disease. Cardiovasc Res 2007;74:29-38.
23. Dubi S, Arbel Y. Large animal models for diastolic dysfunction and diastolic heart failure-a review of the literature. Cardiovasc Pathol 2010;19:147-52.
24. Geens JH, Trenson S, Rega FR, Verbeken EK, Meyns BP. Ovine models for chronic heart failure. Int J Artif Organs 2009;32:496-506.
25. Feng Y, Bogaert J, Oyen R, Ni Y. An overview on development and application of an experimental platform for quantitative cardiac imaging research in rabbit models of myocardial infarction. Quant Imaging Med Surg 2014;4:358-75.
26. Feng Y, Chen F, Ma Z, Dekeyzer F, Yu J, Xie Y, Cona MM, Oyen R, Ni Y. Towards stratifying ischemic components by cardiac MRI and multifunctional stainings in a rabbit model of myocardial infarction. Theranostics 2013;4:24-35.

27. Stypmann J, Engelen MA, Troatz C, Rothenburger M, Eckardt L, Tiemann K. Echocardiographic assessment of global left ventricular function in mice. Lab Anim 2009;43:127-37.
28. Yancy CW, Jessup M, Bozkurt B, Butler J, Casey DE, Drazner MH, Fonarow GC, Geraci SA, Horwich T, Januzzi JL, Johnson MR, Kasper EK, Levy WC, Masoudi FA, McBride PE, McMurray JJV, Mitchell JE, Peterson PN, Riegel B, Sam F, Stevenson LW, Tang WHW, Tsai EJ, Wilkoff BL, Anderson JL, Jacobs AK, Halperin JL, Albert NM, Bozkurt B, Brindis RG, Creager MA, Curtis LH, DeMets D, Guyton RA, Hochman JS, Kovacs RJ, Kushner FG, Ohman EM, Pressler SJ, Sellke FW, Shen WK, Stevenson WG, Yancy CW. 2013 ACCF/AHA Guideline for the Management of Heart Failure: Executive Summary A Report of the American College of Cardiology Foundation/American Heart Association Task Force on Practice Guidelines. Circulation 2013;128:1810-52.
29. Verma A, Meris A, Skali H, Ghali JK, Arnold JMO, Bourgoun M, Velazquez EJ, McMurray JJV, Kober L, Pfeffer MA, Califf RM, Solomon SD. Prognostic Implications of Left Ventricular Mass and Geometry Following Myocardial Infarction The VALIANT (VALsartan In Acute myocardial iNfarcTion) Echocardiographic Study. JACC Cardiovasc Imaging 2008;1:582-591.
30. Pennock GD, Yun DD, Agarwal PG, Spooner PH, Goldman S. Echocardiographic changes after myocardial infarction in a model of left ventricular diastolic dysfunction. Am J Physiol 1997;273:H2018-29.
31. Christenson E, Christenson RH. Characteristics of cardiac troponin measurements. Coron Artery Dis 2013;24:698-704.
32. Edwards R, Yousef Z, Rakhit R, Wright M, Rosenthal E, Redwood S, Marber M. A model of closed chest regional myocardial infarction in the rabbit: a clinically relevant in vivo assay system of post-infarction remodelling. Basic Res Cardiol 2002;97:374-83.
33. Wang YT, Popovic ZB, Efimov IR, Cheng YN. Longitudinal Study of Cardiac Remodelling in Rabbits Following Infarction. Can J Cardiol 2012;28:230-8.
34. Wu H, Li L, Niu P, Huang X, Liu J, Zhang F, Shen W, Tan W, Wu Y, Huo Y. The Structure-function remodeling in rabbit hearts of myocardial infarction. Physiol Rep 2017;5.
35. Liu YJ, Leng XP, Du GQ, Wang XD, Tian JW, Ren M. Two-dimensional longitudinal strains and torsion analysis to assess the protective effects of ischemic postconditioning on myocardial function: a speckle tracking echocardiography study in rabbits. Ultrasonics 2015;56:344-53.
36. Al Musa T, Uddin A, Swoboda PP, Garg P, Fairbairn TA, Dobson LE, Steadman CD, Singh A, Erhayiem B, Plein S, McCann GP, Greenwood JP. Myocardial strain and symptom severity in severe aortic stenosis: insights from cardiovascular magnetic resonance. Quant Imaging Med Surg 2017;7:38-47.
37. Gupta S, Li H, Keshavamurthy JH, Sharma GK, Polimenakos AC. Case-based approach to demonstrate utility of cardiac magnetic resonance imaging (MRI) for planning biventricular repair with inconclusive echo: illustration of two cases. Quant Imaging Med Surg 2017;7:732-5.
38. Lau JM, Zheng J. Disease-specific cardiovascular positron emission tomography/magnetic resonance imaging: a brief review of the current literature. Quant Imaging Med Surg 2016;6:297-307.
39. Likhite D, Suksaranjit P, Adluru G, Wilson B, DiBella E. Estimating extraction fraction and blood flow by combining first-pass myocardial perfusion and T1 mapping results. Quant Imaging Med Surg 2017;7:480-95.
40. Nemes A, Dezsi L, Domsik P, Kalapos A, Forster T, Vecsei L. Left ventricular deformation abnormalities in a patient with calpainopathy-a case from the three-dimensional speckle-tracking echocardiographic MAGYAR-Path Study. Quant Imaging Med Surg 2017;7:685-90.
41. Hemmeryckx B, Feng Y, Frederix L, Lox M, Trenson S, Vreeken R, Lu HR, Gallacher D, Ni YC, Lijnen HR. Evaluation of cardiac arrhythmic risks using a rabbit model of left ventricular systolic dysfunction. Eur J Pharmacol 2018;832:145-55.
42. Hemmeryckx B, Feng Y, Frederix L, Lox M, Trenson S, Vreeken R, Lu HR, Gallacher D, Ni YC, Lijnen HR. Prolonged High-Fat Diet Feeding of WHHLMI Rabbits does Not Aggravate Metabolic or Cardiac Dysfunction. J diab Obes 2018;5:10-7.

Cite this article as: Feng Y, Hemmeryckx B, Frederix L, Lox M, Wu J, Heggermont W, Lu HR, Gallacher D, Oyen R, Lijnen HR, Ni Y. Accurate estimation of choriocapillaris flow deficits beyond normal intercapillary spacing with swept source OCT angiography. Quant Imaging Med Surg 2018;8(8):754-769. doi: 10.21037/qims.2018.09.05

Supplementary

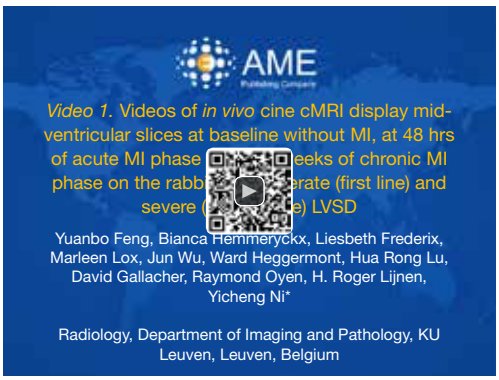

Figure S1 Videos of *in vivo* cine cMRI display mid-ventricular slices at baseline without MI, at 48 hrs of acute MI phase and at 7 weeks of chronic MI phase on the rabbits of moderate (first line) and severe (second line) LVSD. The arrow indicates the decreased lateral wall motion with different degrees (43). cMRI, cardiac magnetic resonance imaging; MI, myocardial infarction; LVSD, left ventricle systolic dysfunction.

Available online: http://www.asvide.com/article/view/27474

References

43. Feng Y, Hemmeryckx B, Frederix L, et al. Videos of in vivo cine cMRI display mid-ventricular slices at baseline without MI, at 48 hrs of acute MI phase and at 7 weeks of chronic MI phase on the rabbits of moderate (first line) and severe (second line) LVSD. Asvide 2018;5:788. Available online: http://www.asvide.com/article/view/27474

Original Article

SPIO-loaded nanostructured lipid carriers as liver-targeted molecular T2-weighted MRI contrast agent

Xiuliang Zhu[1#], Xueying Deng[2#], Chenying Lu[1#], Ying Chen[1], Liyong Jie[1], Qian Zhang[1], Wei Li[3], Zuhua Wang[4], Yongzhong Du[3], Risheng Yu[1]

[1]Department of Radiology, The Second Affiliated Hospital, Zhejiang University School of Medicine, Hangzhou 310009, China; [2]Department of Radiology, Zhejiang Cancer Hospital, Hangzhou 310022, China; [3]Institute of Pharmaceutics, College of Pharmaceutical Sciences, Zhejiang University, Hangzhou 310058, China; [4]College of Pharmaceutical Sciences, Guiyang College of Traditional Chinese Medicine, Guiyang 550002, China

[#]These authors contributed equally to this work.

Correspondence to: Risheng Yu. Department of Radiology, The Second Affiliated Hospital, Zhejiang University School of Medicine, 88# Jiefang Road, Hangzhou 310009, China. Email: risheng-yu@zju.edu.cn; Yongzhong Du. Institute of Pharmaceutics, College of Pharmaceutical Sciences, Zhejiang University, 866 Yu-Hang-Tang Road, Hangzhou 310058, China. Email: duyongzhong@zju.edu.cn; Zuhua Wang. College of Pharmaceutical Sciences, Guiyang College of Traditional Chinese Medicine, Guiyang 550002, China. Email: wangrui551601@163.com.

Background: Superparamagnetic iron oxide (SPIO) acts as a negative contrast agent in magnetic resonance imaging (MRI), and is widely used in clinical applications, including the diagnosis of hepatic diseases. Hepatocyte-targeted magnetic resonance contrast agents (MRCAs) can provide useful information for evaluating hepatic diseases. We prepared targeted magnetic nanostructured lipid carriers (MNLCs) to enhance the hepatocytes targeting efficiency.

Methods: *In vitro* characterizations of MNLCs were determined by transmission electron microscopy (TEM). The cytotoxicity assay of the MNLCs was measured by methyl tetrazolium (MTT) method. The uptaken study was measured by confocal microscopy, flow cytometry and MRI *in vitro*. The enhanced liver-targeting efficiency of MNLCs was measured by fluorescence imaging and MRI *in vivo*.

Results: Gal-NLC-SPIO was prepared successfully. The cytotoxicity assay of the MNLCs demonstrated that the MNLC had relatively low cytotoxicity and high biocompatibility for LO2 cells. More importantly, we confirmed that Gal-NLC-SPIO had greater uptake by LO2 cells than Gal-NLC-SPIO/PEG and free Gal *in vitro*. A liver distribution study of MNLCs in normal mice demonstrated that the fluorescent signal values to livers of the Gal-NLC-SPIO were significantly stronger than those of NLC-SPIO and Gal-NLC-SPIO/PEG. The liver targeting efficiency of Gal-NLC-SPIO was confirmed both *in vitro* and *in vivo*.

Conclusions: We successfully developed liver-targeting MNLCs, which showed accurate hepatocytes targeting, and thus have the potential to be a new MRI contrast agent to help the diagnosis of liver diseases.

Keywords: Superparamagnetic iron oxide (SPIO); magnetic resonance imaging (MRI); solid lipid nanoparticle galactose (SLN galactose); liver-targeted

Submitted Aug 13, 2018. Accepted for publication Sep 07, 2018.
doi: 10.21037/qims.2018.09.03
View this article at: http://dx.doi.org/10.21037/qims.2018.09.03

Introduction

Magnetic resonance imaging (MRI), because of its high spatial, high temporal resolution, non-ionizing radiation and multiparameter imaging, is widely used in clinical diagnosis and research as a non-invasive and effective imaging technique, especially for early cancer diagnosis (1,2). In order to provide more detailed abnormality images and to distinguish diagnostic interest regions from background

tissues, magnetic resonance contrast agents (MRCAs) are widely utilized (3-5). MRCAs are used to alter the water molecules' relaxation times and subsequently to the increase tissue contrast on relaxation-weighted imaging sequences (6). Furthermore, hepatocyte-targeted MRCAs can used to evaluate hepatic diseases, such as hepatic tumor and hepatitis, because hepatic diseases can reduce the hepatocyte-targeted imaging agent uptaken into hepatocytes. Therefore, hepatic diseases can be better evaluated *in vivo* by using hepatocyte-targeted MRCAs (7), of which there are two types. One type, T1 MRCA typically incudes gadolinium (Gd) complexes and manganese (Mn) oxide nanoparticles, also called positive MRCAs, which present hyperintensity in T1-weighted images (8,9). The classic examples of T2 MRCAs include superparamagnetic iron oxide nanoparticles (SPIO), also called negative MRCAs, which present hypointensity in T2-weighted images (10,11). The potential use of SPIO as MRI probes has been widely studied with regard to their suitable magnetic properties, good biocompatibility and non-toxicity. Their outlook is promising because SPIO can display magnetic behavior in the presence of the magnetic field, and so can be productively applied *in vivo* and *in vitro* (10-12).

Drug targeted delivery systems are widely found in nanomedicine, and can be used to prolong, localize, and target specific designated tissue parts of the body (13-18), and they are consist of active targeted drug delivery (e.g., targeted to hepatic tumor or normal liver) and passive targeted drug delivery (e.g., engulfed by reticuloendothelial system, RES) (15-18). Contrast agent targeted delivery systems, like drug targeted delivery systems, are becoming more popular used for targeting diagnosis of disease (18).

Lipid based nanoparticles, with poorly water-soluble and low toxicity, have been used as amphiphilic nanocarriers in recent years (19-23). The nanostructured lipid carrier (NLC) is a novel nanoparticle delivery system, composed of a solid lipid and an oil phase, which enables a higher drug loading capacity and stability when compared to solid lipid nanoparticles (SLNs) (21-23). This is possible because the NLC's strong hydrophobic surface, after intravenous injection into the body, soon to be swallowed by RES, and into the liver and spleen by passive targeting (24,25).

In addition, for the purpose of specifically targeting tumor tissue, NLCs can be modified with antibodies or ligand (26-28). Mammalian hepatocytes have large numbers of high-affinity and cell-surface receptors (asialoglycoprotein receptor, ASGPR) which can bind to asialoglycoproteins and can specifically recognize ligands with terminal galactose residues. Each liver cell has more than 5×10^5 receptors in a normal liver, but the number and function of the receptors declines from hepatitis, cirrhosis, liver cancer and other liver diseases. Galactose (Gal) is a hepatocyte-specific ligand of ASGPR and the liver targeting group, which has potential to induce and improve cell adhesion and the performance of liver extracellular matrix scaffold (27,28).

In this study, galactose-conjugated nanostructured lipid carriers (Gal-NLCs) were prepared as a hepatocyte-targeting imaging probe to deliver magnetic SPIO nanoparticles (i.e., SPIO loaded Gal-NLC, Gal-NLC-SPIO), which could passively and actively target the liver due to active targeting modification with galactose in the nano-carrier (*Figure 1*). Then, the targeting ability of nanoparticles to normal liver cells and hepatoma cells was further investigated, while the diagnostic efficiency of hepatocellular carcinoma *in vivo* and *in vitro* was also evaluated.

Methods

Cell culture

RAW264.7 cells (mouse macrophage cell line), LO2 cells (human hepatic cell line) and HepG2 cells (human hepatocellular carcinoma cell line) were investigated in this study. The cells were maintained in DMEM at 37 ℃ in a humidified atmosphere of 5% CO_2. All the mediums contained fetal bovine serum (FBS) [10% (v/v)], and 1% streptomycin/penicillin.

Synthesis of Gal-ODA

The Gal-ODA conjugate was synthesized by the acylation between the carboxyl group of lactobionic acid (LA) derived from the lactose and amino group of ODA. LA was coupled with ODA using 1-ethyl-3-(3-dimethyl aminopropyl) carbodiimide hydrochloride (EDC) as the coupling agent. Briefly, 1 g of LA, 0.5 g of ODA and 1.76 g of EDC were dissolved in 50 mL of ethanol solution in a water bath at 60 ℃ for 24 h. The final products were further purified and followed by lyophilization, and the Gal-ODA was finally extracted.

Preparation of magnetic nanostructured lipid carriers (MNLC)

Galactose-conjugated MNLC (NLC-SPIO, Gal-NLC-SPIO and Gal-NLC-SPIO/PEG) was prepared using the

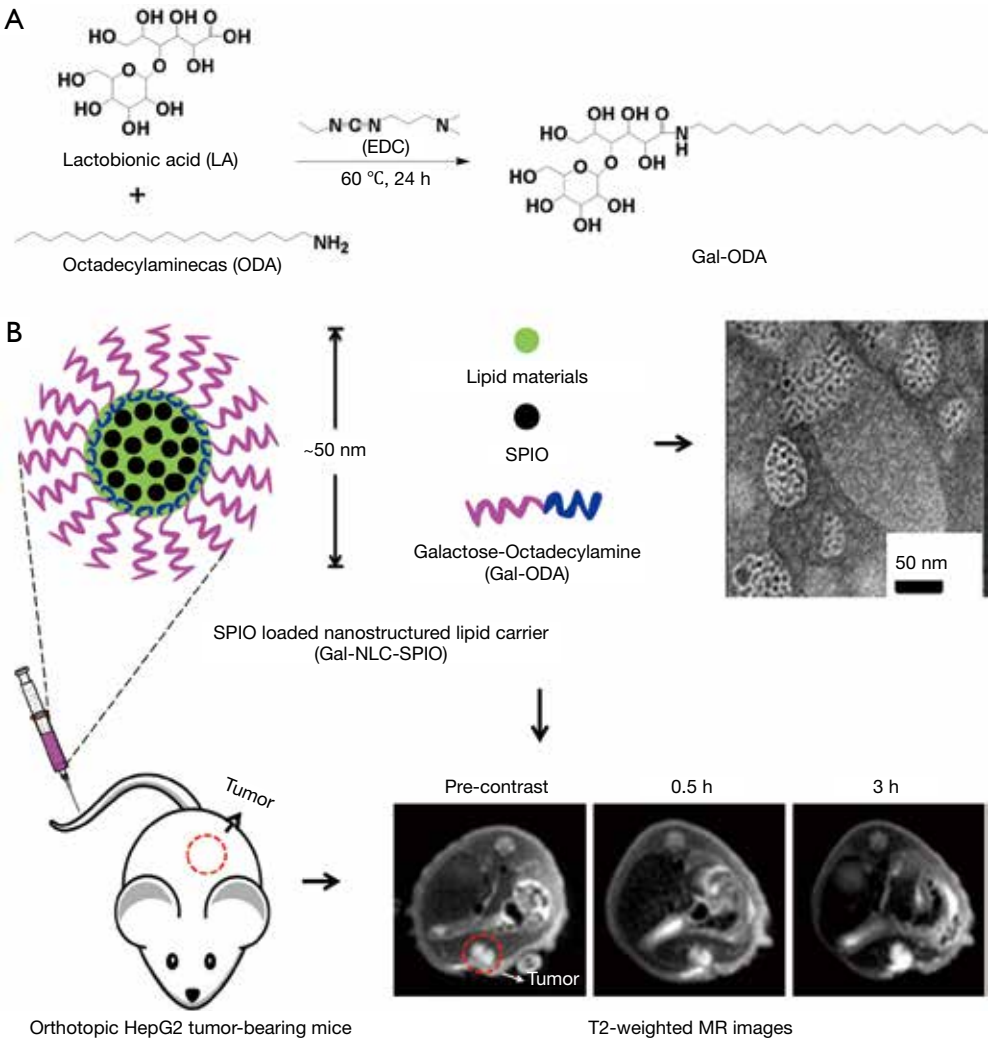

Figure 1 Schematic illustration of the Gal-NLC-SPIO nanoparticles. (A) Synthetic scheme of Gal-ODA; (B) fabrication procedure of Gal-NLC-SPIO nanoparticles and further liver molecular MRI imaging. Gal-NLC, galactose-conjugated nanostructured lipid carrier; SPIO, superparamagnetic iron oxide.

solvent diffusion method. Briefly, Fe_3O_4 dispersion (1 mL) was added into 0.1% Poloxamer 188 (47 mL) in deionized water solution using a probe sonicator (600 W, Sonicator JY92-II DN, China) working 2 s following stopping 3 s to form a dispersion of magnetic nanoparticles. Oleic acid in ethanol solution (1 mL, 5 mg/mL) was added and followed by sonication for 5 minutes to stabilize the nanoparticles. Subsequently, 32 mg of monostearin, 32 mg of monostearin +3 mg of Gal-ODA, and 32 mg of monostearin +3 mg of Gal-ODA +3 mg of polyethylene glycol monostearate, were respectively dissolved in ethanol solution (2 mL, 70 ℃), and immediately added into the Fe_3O_4 nanoparticles in an ultrasound water bath (70 ℃) for 10 min to obtain the magnetic nanoparticles of NLC-SPIO, Gal-NLC-SPIO and Gal-NLC-SPIO/PEG.

Physicochemical characteristics of MNLC

^{1}H nuclear magnetic resonance (NMR) spectra were used to analyse the synthesized Gal-ODA. LA, ODA and Gal-ODA were dissolved in D_2O, and measured by NMR spectra. The average diameter and zeta potential of the MNLC were measured with a zetasizer (3000HS, Malvern Instruments Ltd, UK). Morphological examination of the MNLC was performed via transmission electron microscopy (TEM) (JEOL JEM-1230, Japan). Each sample was dropped onto a

copper grid and stained with phosphotungstic acid (2%, w/v) for viewing.

Cytotoxicity assay in vitro

In order to study the cytotoxicity of MNLC, the methyl tetrazolium (MTT) assay was used on the test cells. Three kinds of cells were each briefly seeded onto their own 96-well culture plate at a density of 10,000 cells per well in 200 μL of complete medium. After cultured at 37 ℃ for 24 h, the cells were exposed to a series of concentrations of magnetic nanoparticles for another 48 h. At the end of incubation, cells were incubated with 20 μL MTT solution (5 mg/mL) in each well for a further 4 h at 37 ℃. Finally, the cells were dissolved by dimethyl sulfoxide (DMSO, 100 μL) and the absorbance values were measured at 570 nm using a microplate reader (Bio-Rad, Model 680, USA). All the experiments were performed 3 times. Cell viability was calculated using an MTT assay.

Cellular uptake test of MNLC

The fluorescein isothiocyanate-octadecylamine (FITC-ODA) was prepared according to our previous study (29). As described above, the FITC-labeled MNLC were prepared using FITC-ODA (5 mg) instead of monostearin.

LO2, HepG2 and RAW264.7 cells were seeded onto coverslips in a 24-well plate for 24 h, respectively. Cells were then incubated with FITC labeled MNLC in growth medium for 30 min. The cells were then washed 3 times, and the coverslips were observed under a confocal microscope (LSM-510META, ZEISS, Germany). The quantitative analysis of cellular uptake was further evaluated via a flow-cytometer (FC500MCL, Beckman Coulter, USA).

In vitro MR imaging of MNLC

A 3.0 T clinical MR scanner (GE, Discovery 750, USA) was used for an *in vitro* MR imaging experiment. LO2 and HepG2 cells were incubated with MNLC for 3 h, and then collected in 1.5 mL microcentrifuge tubes by centrifugation. The cells were mixed with agarose gel (0.5%, 200 mL), and T2-weight MR images were obtained using an MR scanner.

In vivo MR imaging studies

Male BALB/C+nu/F1 nude mice were provided by the Zhejiang Medical Animal Centre. All the animal studies were conducted in accordance with the National Institutes of Health (NIH, USA) guidelines for the care and use of laboratory animals and with the approval of the Scientific Investigation Board of Zhejiang University.

Nude mice were implanted with HepG2 cells to establish orthotopic liver cancer models. The abdominal cavity was cut to reveal normal liver tissues, and the wound was then sutured using biodegradable stitches after injecting HepG2 cells (~5×10^6 cells in 20 μL of serum-free DMEM) into the liver parenchyma. About 2 weeks later, mice bearing HepG2 tumors of approximately 2 mm^3 were randomized into 3 groups (n=5 per group), and taken for MR imaging. T2-weighted MR images were obtained before MNLC (200 μL, 100 μg/mL) was injected through each mouse's tail vein. The mice were then imaged again at predetermined times (0, 1, 3 h) after the injection.

Histological analysis

The mice were sacrificed after MR examination, and the livers were collected for histological analysis. The fresh tissues were fixed with 10% paraformaldehyde, and embedded in paraffin. The sections were stained using haematoxylin-eosin (H&E), and examined under a light microscope for histological analysis. The accumulation of iron in the tissues was observed by Prussian blue staining. The microscopic images were observed by a Leica fluorescence microscope.

Statistical analysis

The data were expressed as the mean (standard error) of three separate experiments. Differences between the groups were assessed with Student's *t*-test, and P values less than 0.05 were considered statistically significant.

Results

Structure confirmation of Gal-ODA

The reaction scheme of Gal-ODA is shown in *Figure 1*. The chemical structure of LA, ODA and Gal-ODA were determined by ^{1}H NMR spectra (*Figure S1)*. The ^{1}H NMR chemical shift of the proton of carboxyl group for LA (about 12.5) was displaced to about 7.5, equal to the chemical shift of the proton of amide group for Gal-ODA. These results indicate that Gal-ODA was synthesized successfully.

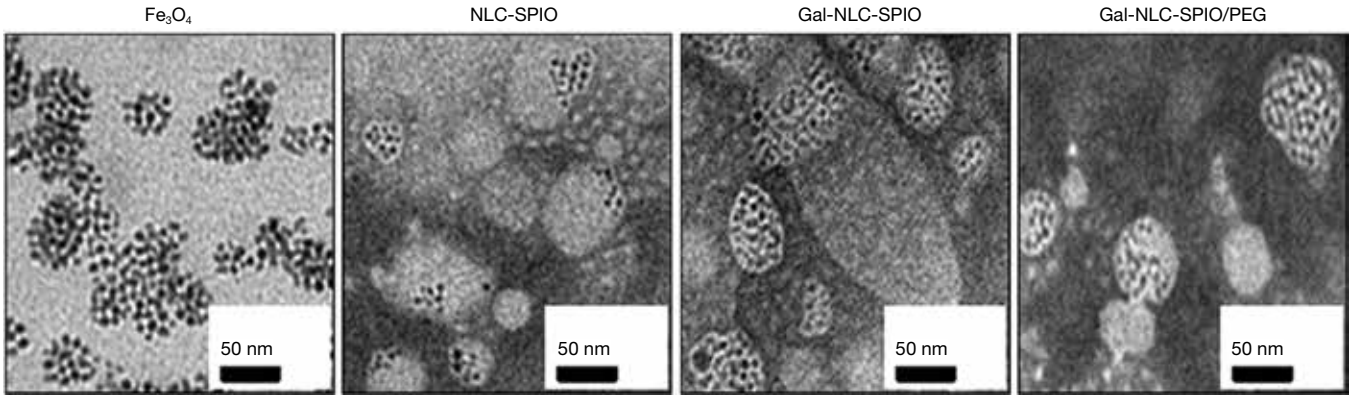

Figure 2 Preparation and characteristics. TEM images of Fe_3O_4, NLC-SPIO, Gal-NLC-SPIO and Gal-NLC-SPIO/PEG nanoparticles (×100,000, bar =50 nm). TEM, transmission electron microscopy; Gal-NLC, galactose-conjugated nanostructured lipid carrier; SPIO, superparamagnetic iron oxide.

Preparation and physicochemical characteristics of MNLC

The solvent diffusion method was utilized to prepare Gal-NLC-SPIO, NLC-SPIO and Gal-NLC-SPIO/PEG. The morphology and size of MNLC were characterized by zetasizer and TEM. Particle diameter and zeta potential of Gal-NLC-SPIO, NLC-SPIO and Gal-NLC-SPIO/PEG are shown in *Table S1*. The results indicate that 3 magnetic lipid nanoparticles are uniformly distributed (PI <0.3) and have negative charges, with the particle sizes being similar. TEM photographs of Fe_3O_4, Gal-NLC-SPIO, NLC-SPIO and Gal-NLC-SPIO/PEG are shown in *Figure 2*. The photographs demonstrate the successful entrapment of SPIO into Gal-NLC-SPIO, NLC-SPIO and Gal-NLC-SPIO/PEG, with particle size of approximately 50 nm. The results were similar to that from the zetasizer.

In vitro cytotoxicity

The cytotoxicities of Gal-NLC-SPIO, NLC-SPIO and Gal-NLC-SPIO/PEG were tested by both MTT and cell viability assays. Using LO2, HepG2, and RAW264.7 cell lines as model cells, the results in *Figure S2* illustrate that cell viability was still higher than 80% even when the concentration of Fe_3O_4 rose to 100 $\mu g \cdot mL^{-1}$ (nanoparticles was 1 $mg \cdot mL^{-1}$). This is evidence to the fact that the MNLC had a relatively high biocompatibility and low cytotoxicity for both normal cells and tumor cells.

Uptake of MNLC by cells

In order to study the targeting efficiency of Gal-NLC-SPIO toward LO2 cells, cellular competitive uptake of rhodamine isothiocyanate (RITC), labeled MNLC on LO2/HepG2 cells co-cultured systems, and the targeting efficiency was detected via confocal microscopy (*Figure 3*).

Line 3 in *Figure 3B* shows an obvious difference in the cellular uptake of Gal-NLC-SPIO on the LO2/HepG2 cells co-cultured systems, characterized by more efficient cellular uptake of Gal-NLC-SPIO on LO2 cells compared with HepG2 cells. However, NLC-SPIO and Gal-NLC-SPIO/PEG showed minor uptake on the LO2/HepG2 cells co-cultured systems (line 1 and 2 in *Figure 3B*).

The results of cellular competitive uptake confirmed the specific binding of the Gal-NLC-SPIO to LO2 cells, on account of the presence of an abundant ASGPR on the LO2 cell surface (26-28). The results of qualitative and quantitative cellular uptake for FITC labeled Gal-NLC-SPIO, NLC-SPIO and Gal-NLC-SPIO/PEG were presented (*Figure 4*) after the MNLC were incubated with LO2, HepG2 and RAW264.7 cells for 1 h and 12 h, respectively. The results demonstrated that the SPIO could be internalized into cells mediated by the MNLC. The uptake of the Gal-NLC-SPIO, NLC-SPIO and Gal-NLC-SPIO/PEG by LO2, HepG2 and RAW264.7 cells were time dependent. The SPIO accumulation in RAW264.7 cells by NLC-SPIO was faster than in Gal-NLC-SPIO and Gal-NLC-SPIO/PEG. The SPIO accumulation in LO2 cells by Gal-NLC-SPIO was faster than in NLC-SPIO and Gal-NLC-SPIO/PEG, while there was no significant difference among the magnetic NLCs in HepG2 cells. The cellular uptake data confirmed the specific and strong targeting abilities of the NLC-SPIO to RAW264.7 cells and the Gal-NLC-SPIO to LO2 cells.

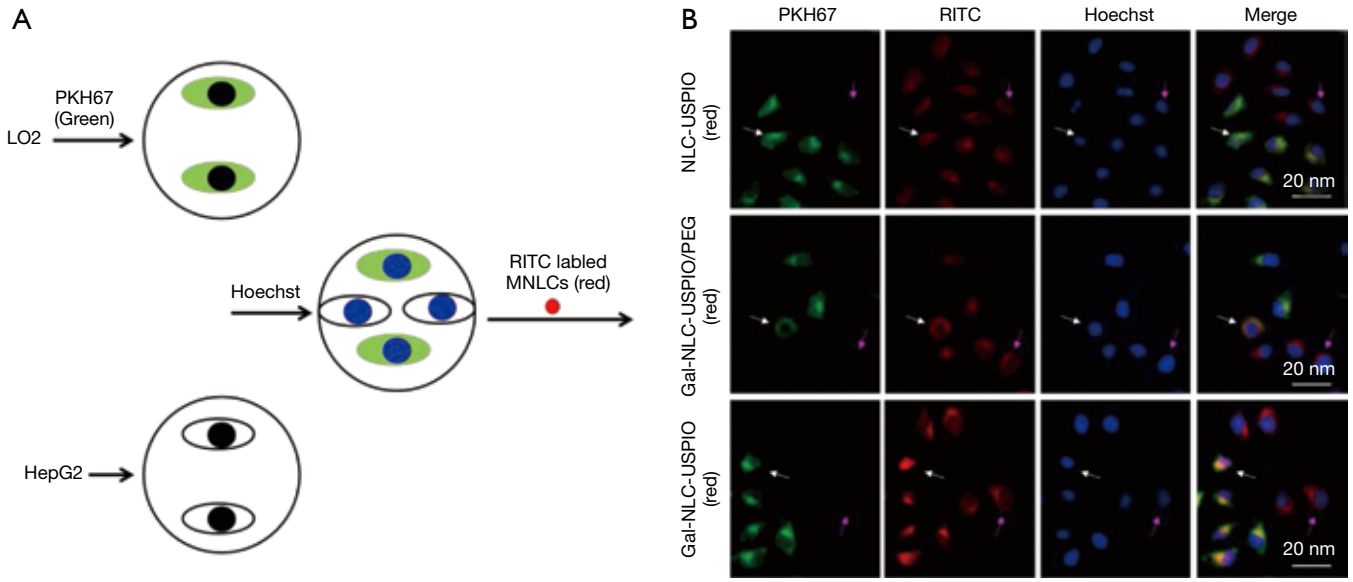

Figure 3 Cellular competitive uptake studies. (A) Schematic diagram of cellular competitive uptake of Gal-NLC-SPIO, NLC-SPIO and Gal-NLC-SPIO/PEG; (B) confocal microscopy images of RITC labeled MNLC for 1 h. LO2 cells (the cytoplasmic membrane labeled with PKH67 fluorescent linker, green) co-cultured with HepG2 cells were incubated with RITC-Gal-NLC-SPIO, RITC-NLC-SPIO and RITC-Gal-NLC-SPIO/PEG (red). The nucleus were all stained with Hoechst 33342. The white arrow stands for LO2 cells, the pink arrow stands for HepG2 cells. (PKH67/FITC, excitation wavelengths 488 nm, emission wavelengths 500–540 nm; RITC, excitation wavelengths 561 nm, emission wavelengths 580–620 nm). Gal-NLC, galactose-conjugated nanostructured lipid carrier; SPIO, superparamagnetic iron oxide; RITC, rhodamine isothiocyanate; MNLC, magnetic nanostructured lipid carrier.

Liver distribution of MNLC in vivo

Liver distribution is an important prerequisite for the diagnosis of liver disease. To further research whether MNLC could target the liver *in vivo*, DiR was loaded in MNLC and used as a fluorescent probe for *in vivo* imaging. After injection of DiR loaded MNLC, accumulation of DiR fluorescence in the liver was time dependent and the fluorescent signal intensity increased gradually. The fluorescence intensity of liver injected by Gal-NLC-SPIO/DiR was stronger than in NLC-SPIO/DiR and Gal-NLC-SPIO/PEG/DiR, as shown in *Figure 5A*. The results in *Figure 5B* also demonstrate that the fluorescent signal values of the Gal-NLC-SPIO to livers were significantly stronger than those of NLC-SPIO and Gal-NLC-SPIO/PEG in livers at every time point, suggesting that Gal-NLC-SPIO has specific targeting ability to liver tissue and has great potential as an MRI contrast agent.

In vitro MR imaging of MNLC

Having magnetic properties is a significant parameter for a MRI contrast agent. In *Figure 5C*, the T2-weighted MRI of Gal-NLC-SPIO shows obvious color change with a variation of Fe_3O_4 concentration. It was found that Gal-NLC-SPIO exhibited good superparamagnetic properties of negative contrast enhancement. The relaxation rate, R2 =1/T2, linearly proportional to the Fe concentration, is also shown in *Figure 5C*. It was indicated in the experiment that Gal-NLC-SPIO exhibited good contrast effect.

T2-weighted images of Gal-NLC-SPIO, NLC-SPIO and Gal-NLC-SPIO/PEG, incubated with HepG2 and LO2 cells for 1 h, along with their signal intensity, are shown in *Figure 5D*. The most apparent decrease in signal density can be seen in the Gal-NLC-SPIO incubated with LO2 cells (*Figure 5E)*, and the Gal-NLC-SPIO/LO2 cells showed significant differences in contrast to the other groups ($P<0.01$). This may be attributed to the specific targeting ability of Gal-NLC-SPIO nanoparticles to LO2 cells, leading to the overexpression of cell surface receptors and for the receptor-mediated endocytosis to enhance the uptake into hepatocytes (30).

In vivo MRI of MNLC and pathology studies

Orthotopic implantation hepatoma models were used for

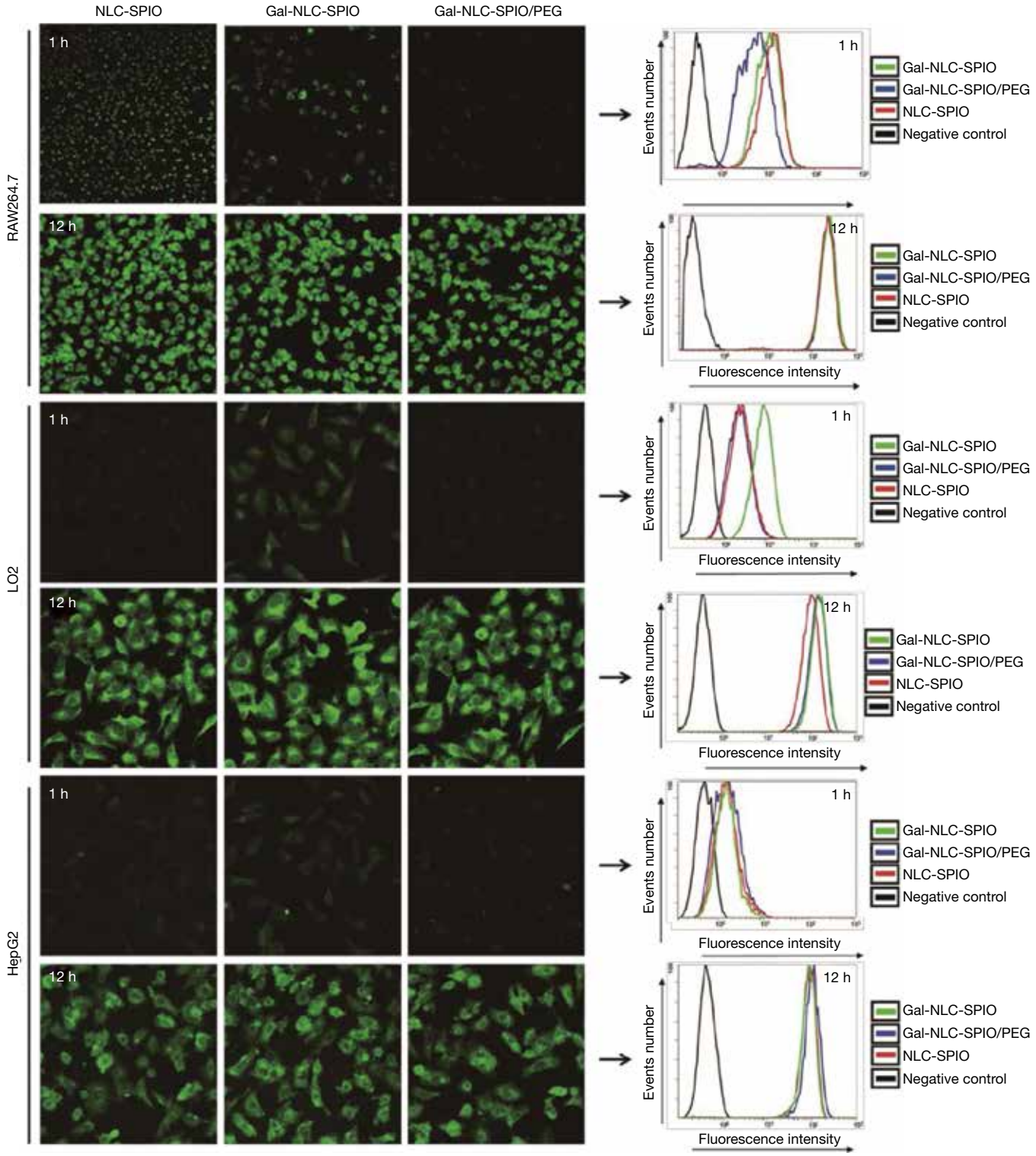

Figure 4 *In vitro* cellular uptake of MNLC in different cell lines. Fluorescence images observed by confocal microscopy and fluorescence intensity inside cells measured by flow cytometry of LO2, HepG2 and RAW264.7 cells incubated with FITC-Gal-NLC-SPIO, FITC-NLC-SPIO and FITC-Gal-NLC-SPIO/PEG for 1 h and 12 h, respectively. MNLC, magnetic nanostructured lipid carrier; Gal-NLC, galactose-conjugated nanostructured lipid carrier; SPIO, superparamagnetic iron oxide.

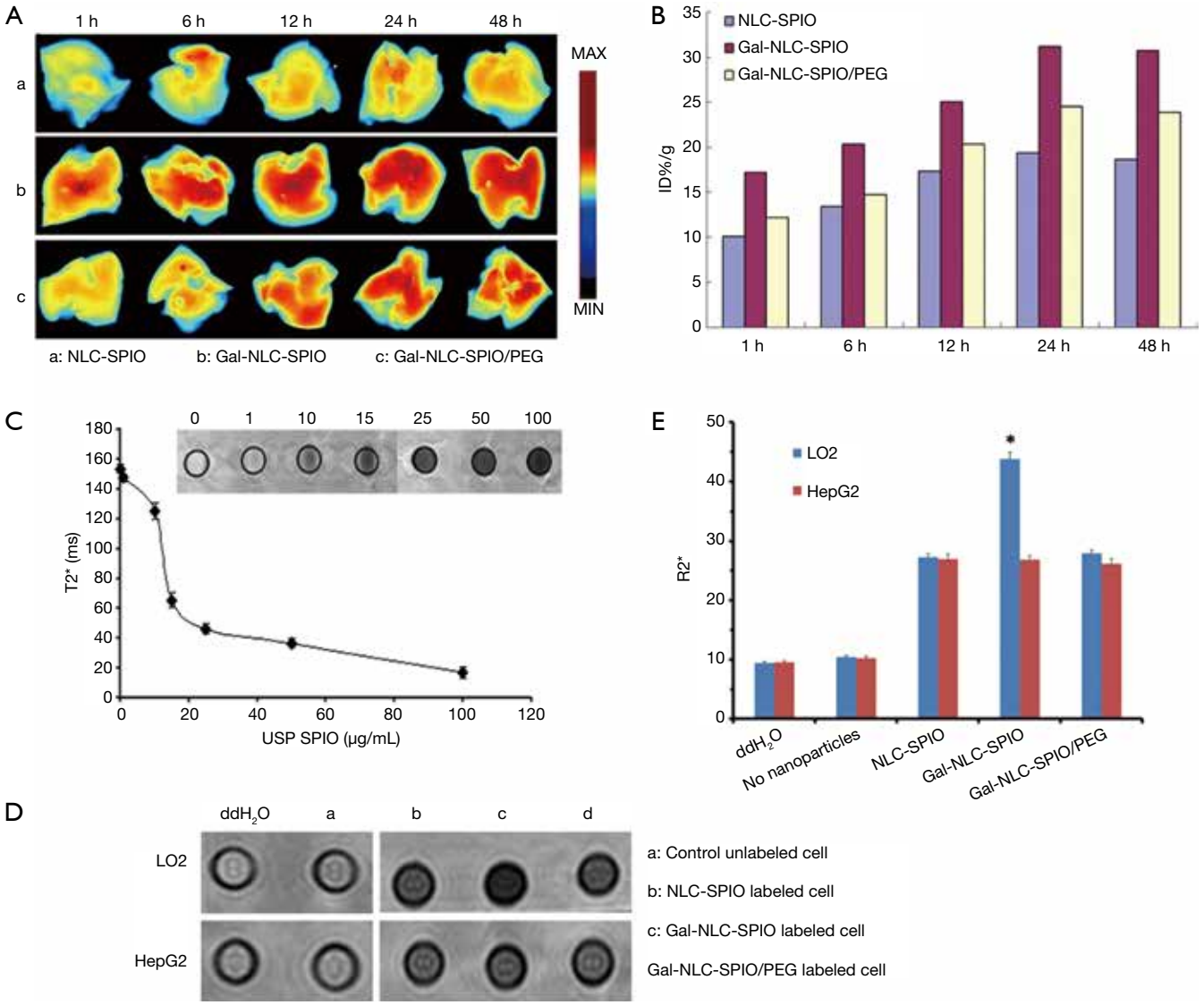

Figure 5 Bioimaging studies in orthotopic models. *In vivo* fluorescence imaging (A) and fluorescent semi-quantitative analysis (B) of normal nude mice liver after intravenous injection of DiR labled NLC-SPIO, Gal-NLC-SPIO and Gal-NLC-SPIO/PEG at different times. MR imaging of magnetic NLCs *in vitro*. (C) T2-weighted images of Gal-NLC-SPIO at different iron concentrations and the chart of T2* values of Gal-NLC-SPIO changing with iron concentrations. (D) LO2 cells or HepG2 cells were incubated with three different kinds of magnetic NLCs for 1 h, and then scanned with MRI. (E) R2* values of LO2 cells or HepG2 cells in different groups were measured (*P<0.01). Gal-NLC, galactose-conjugated nanostructured lipid carrier; SPIO, superparamagnetic iron oxide.

in vivo MRI studies. T2-weighted images of tumor models were obtained before and after intravenous injection of Gal-NLC-SPIO, NLC-SPIO and Gal-NLC-SPIO/PEG, respectively (*Figure 6A*), and the contrast-to-noise ratio (CNR) of T2-weighted MR signal intensity of the tumors are shown in *Figure 6B*. The results produced several significant observations: the liver images of the post-injection of three MNLCs for 0.5 and 3 h became darkened obviously in contrast with that of pre-injection of MNLC, the CNR of T2-weighted images intensity of livers were obviously decreased (P<0.05), and no significant difference was observed in the CNR of the T2-weighted images intensity of tumors between pre-injection and post-injection of MNLC (P>0.05). Thus, the CNR of the tumor-liver was

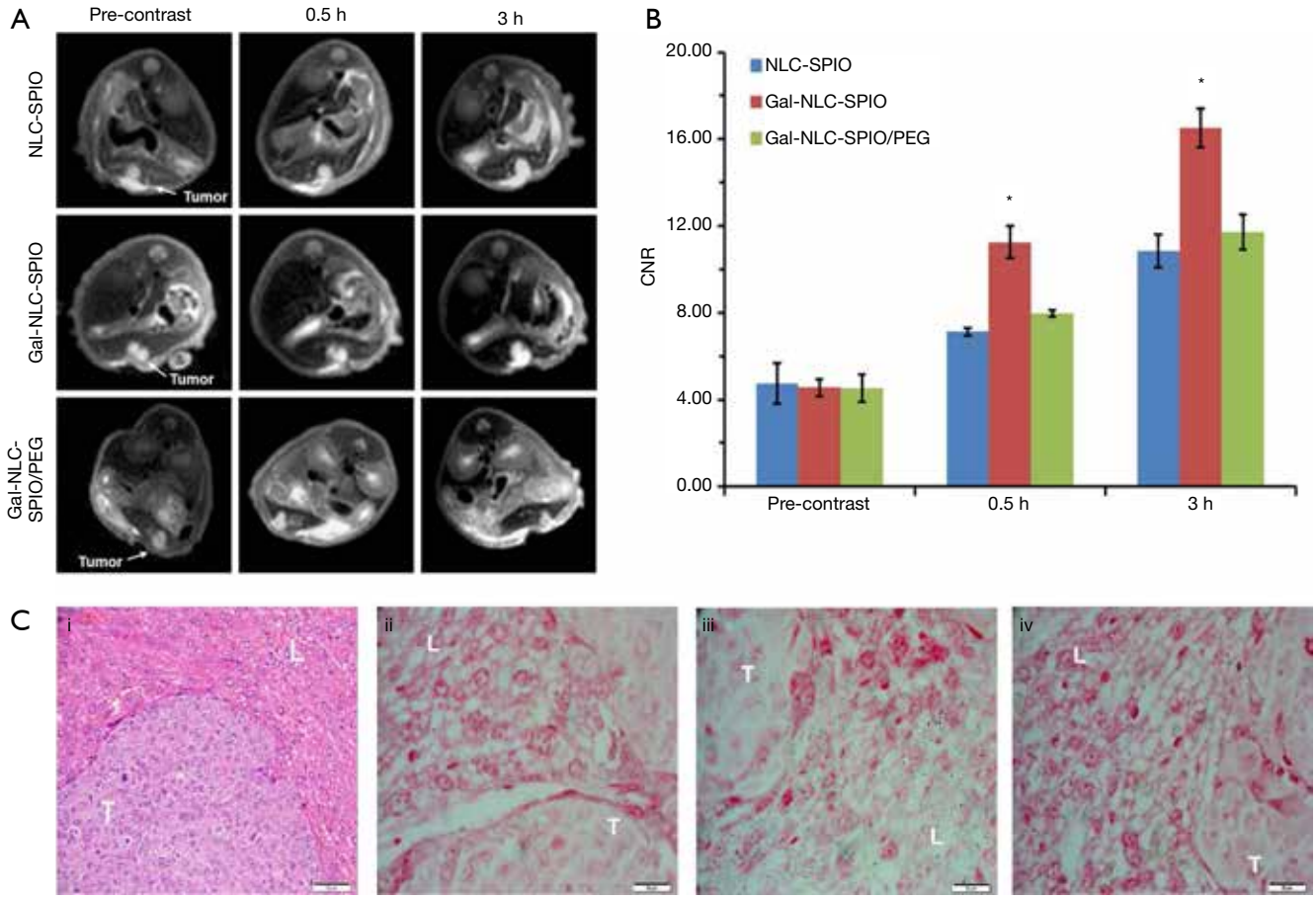

Figure 6 MR imaging and biodistribution studies. (A) T2-weighted single shot fast spin echo images of nude mice bearing HepG2 orthotopic implantation tumor before contrast and at 0.5 and 3 h postinjection of three kinds of MNLC, respectively. The pink arrow stands for tumors. (B) Comparison of CNR of tumor-liver of the three group nude mice at different time points before and after contrast. (C) Microscopic view of HE stained tumor tissue section from nude mice bearing HepG2 tumor (i, magnification: ×400); Prussian blue-stained tumor-liver tissue section of nude mice treated with NLC-SPIO (ii), Gal-NLC-SPIO (iii) and Gal-NLC-SPIO/PEG (iv), respectively (ii, iii and iv, magnification: ×1,000). "L" stands for the normal liver, "T" stands for the tumor. MNLC, magnetic nanostructured lipid carrier; CNR, contrast-to-noise ratio; Gal-NLC, galactose-conjugated nanostructured lipid carrier; SPIO, superparamagnetic iron oxide.

significantly increased after the injection of the Gal-SLN-SPIO compared with those of NLC-SPIO and Gal-NLC-SPIO/PEG ($P<0.05$), indicating that the Gal-SLN-SPIO shows active targeting ability to normal liver tissues.

The accumulation of iron in tumor tissues and normal liver tissues were further verified. As shown in the first image in *Figure 6C*, the tumor cells were larger and pleomorphic with bigger nucleus and abundant cytoplasm, which indicates that the establishment of orthotopic implantation hepatoma models were successful. More iron could be detected in the liver tissues of the Gal-NLC-SPIO injected group (the third image in *Figure 6C*) than that of the NLC-SPIO and Gal-NLC-SPIO/PEG injected groups (the second and forth images in *Figure 6C*). These results indicate that Gal-NLC-SPIO has the more effective targeting ability to liver tissues in contrast to NLC-SPIO or Gal-NLC-SPIO/PEG. This can be primarily attested by the fact that Gal-NLC-SPIO successfully inherited the ability to specifically target LO2 liver cells.

Discussion

ASGPR is a specific endocytotic receptor of mammalian hepatocytes, which has a predetermined selectivity for

oligosaccharide or oligosaccharide protein of galactose residues from the end of the molecule in the circulation. Therefore, galactose-modified MNLCs can be applied as a hepatocyte-targeted nano-drug delivery system. Because it has significant clinical value for evaluation of liver disease, it is important to determine if this delivery system is effective and safe. In this study, the novel liver-targeted MRI contrast agents Gal-NLC-SPIO exhibited very low acute toxicity and reasonably good biocompatibility. The results suggest that SPIO loading does not affect the biosafety of the MNLCs. Moreover, the study also found that Gal-NLC-SPIO uptake by LO2 cells was significantly higher and easier than Gal-NLC-SPIO/PEG and free Gal *in vitro* due to the specific interaction between and ASGPR on hepatocytes. Interestingly, Gal-NLC-SPIO uptake by HepG2 cells is relatively rare (*Figures 3-6*), this can be attributed to: (I) the narrow size distribution and biocompatible of Gal-NLC-SPIO (*Figure 2*); (II) and the targeted modification with galactose ligand, which enabled it to specifically internalize into LO2 cells and greatly enhance the hepatocyte targeting by the EPR effect and selective binding of ASGPR (*Figure 3*). However, ASGPR expression of hepatocytes remained at a very low level in disease states, thus resulting in the relatively weak targeting capabilities of Gal-NLC-SPIO in HepG2 cells. Due to the significant difference of Gal-NLC-SPIO in cellular internalization and MRI between LO2 and HepG2 cells, it is possible that Gal-NLC-SPIO shows promise as a novel MRI contrast agent for diagnosis of liver disease.

In this study, Gal-ODA graft was synthesized successfully, and formed MNLC in aqueous solution for the delivery of SPIO. The Gal-NLC-SPIO nanoparticles were effectively consolidated in the liver tissue, due to the targeting peptide Gal-enhanced endocytosis of the nanoparticles. The results of *in vitro* and *in vivo* studies indicated that Gal-NLC-SPIO has a better targeting ability to liver compared with NLC-SPIO and Gal-NLC-SPIO/PEG. Our research shows that, with the mediation of targeting peptide Gal, the Gal-NLC-SPIO has potential for liver-targeting molecular imaging. Therefore, Gal-NLC-SPIO is especially promising as a liver-targeted molecular MRI contrast agent for further clinical utilization.

Acknowledgements

Funding: The authors thank the Nature Science Foundation of Zhejiang province under Contract LY18H180003, and the National Natural Science Foundation of China under Contract 81571662, 81171334, and 81760643, for their great support on this project.

Footnote

Conflicts of Interest: The authors have no conflicts of interest to declare.

References

1. Gong M, Yang H, Zhang S, Yang Y, Zhang D, Li ZH, Zou lg. Targeting T1 and T2 dual modality enhanced magnetic resonance imaging of tumor vascular endothelial cells based on peptides-conjugated manganese ferrite nanomicelles. Int J Nanomedicine 2016;11:4051-63.
2. Terreno E, Castelli DD, Viale A, Aime S. Challenges for molecular magnetic resonance imaging. Chem Rev 2010;110:3019-42.
3. Xie J, Liu G, Eden HS, Ai H, Chen XY. Surface-engineered magnetic nanoparticle platforms for cancer imaging and therapy. Acc Chem Res 2011;44:883-92.
4. Major JL, Meade TJ. Bioresponsive, cell-Penetrating, and multimeric MR contrast agents. Acc Chem Res 2009;42:893-903.
5. Wáng YX, Idee JM. A comprehensive literatures update of clinical researches of superparamagnetic resonance iron oxide nanoparticles for magnetic resonance imaging. Quant Imaging Med Surg 2017;7:88-122.
6. Hasserodt J, Kolanowski JL, Touti F. Magnetogenesis in water induced by a chemical analyte. Angew Chem Int Ed Engl 2014;53:60-73.
7. Lu J, Ma S, Sun J, Xia C, Liu C, Wang Z, Zhao X, Gao F, Gong Q, Song B, Shuai X, Ai H, Gu Z. Manganese ferrite nanoparticle micellar nanocomposites aivs MRI contrast agent for ler imaging. Biomaterials 2009;30:2919-28.
8. Lee SH, Kim BH, Na HB, Hyeon T. Paramagnetic inorganic nanoparticles as T1 MRI contrast agents. Wiley Interdiscip Rev Nanomed Nanobiotechnol 2014;6:196-209.
9. Na HB, Song IC, Hyeon T. Inorganic nanoparticles for MRI contrast agents. Adv Mater 2009;21:2133-148.
10. Wu W, Wu ZH, Yu TY, Jiang CZ, Kim WS. Recent progress on magnetic iron oxide nanoparticles: synthesis, surface functional strategies and biomedical applications. Sci Technol Adv Mater 2015;16:023501.
11. Ghazani AA, Pectasides M, Sharma A, Castro CM, Mino-Kenudson M, Lee H, Shepard JA, Weissleder R. Molecular characterization of scant lung tumor cells using iron-oxide nanoparticles and micro-nuclear magnetic resonance.

Nanomedicine 2014;10:661-8.
12. Li J, He Y, Sun WJ, Luo Y, Cai HD, Pan YQ, Shen MW, Xia JD, Shi XY. Hyaluronic acid-modified hydrothermally synthesized iron oxide nanoparticles for targeted tumor MR imaging. Biomaterials 2014;35:3666-77.
13. De Jong WH, Borm PJ. Drug delivery and nanoparticles: applications and hazards. Int J Nanomedicine 2008;3:133-49.
14. Binnemars-Postma K, Storm G, Prakash J. Nanomedicine Strategies to Target Tumor-Associated Macrophages. Int J Mol Sci 2017;18:E979.
15. Ngambenjawong C, Cieslewicz M, Schellinger JG, Pun SH. Synthesis and evaluation of multivalent M2pep peptides for targeting alternatively activated M2 macrophages. J Control Release 2016;224:103-11.
16. Du YZ, Cai LL, Liu P, You J, Yuan H, Hu FQ. Tumor cells-specific targeting delivery achieved by A54 peptide functionalized polymeric micelles. Biomaterials 2012;33:8858-67.
17. Chaudhary S, Garg T, Murthy RSR, Goyal GAK. Development, optimization and evaluation of long chain nanolipid carrier for hepatic delivery of silymarin through lymphatic transport pathway. Int J Pharm 2015;485:108-21.
18. Situ JQ, Wang XJ, Zhu XL, Xu XL, Kang XQ, Hu JB, Lu CY, Ying XY, Yu RS, You J, Du YZ. Multifunctional SPIO/DOX-loaded A54 Homing Peptide Functionalized Dextran-g-PLGA Micelles for Tumor Therapy and MR Imaging. Sci Rep 2016;6:35910.
19. Shidhaye SS, Vaidya R, Sutar S, Patwardhan A, Kadam VJ. Solid lipid nanoparticles and nanostructured lipid carriers--innovative generations of solid lipid carriers. Curr Drug Deliv 2008;5:324-31.
20. Yingchoncharoen P, Kalinowski DS, Richardson DR. Lipid-Based Drug Delivery Systems in Cancer Therapy: What Is Available and What Is Yet to Come. Pharmacol Rev 2016;68:701-87.
21. Beloqui A, Solinis MA, Rodriguez-Gascon A, Almeida AJ, Preat V. Nanostructured lipid carriers: Promising drug delivery systems for future clinics. Nanomedicine 2016;12:143-61.
22. Khan S, Baboota S, Ali J, Khan S, Narang RS, Narang JK. Nanostructured lipid carriers: an emerging platform for improving oral bioavailability of lipophilic drugs. Int J Pharm Investig 2015;5:182-91.
23. Iqbal MA, Md S, Sahni JK, Baboota S, Dang S, Ali J. Nanostructured lipid carriers system: recent advances in drug delivery. J Drug Target 2012;20:813-30.
24. Lu W, He LC, Wang CH, Li YH, Zhang SQ. The use of solid lipid nanoparticles to target a lipophilic molecule to the liver after intravenous administration to mice. Int J Biol Macromol 2008;43:320-4.
25. Maeda H, Nakamura H, Fang J. The EPR effect for macromolecular drug delivery to solid tumors: Improvement of tumor uptake, lowering of systemic toxicity, and distinct tumor imaging in vivo. Adv Drug Deliv Rev 2013;65:71-9.
26. Lee CM, Jeong HJ, Kim SL, Kim EM, Kim DW, Lim ST, Jang KY, Jeong YY, Nah JW, Sohn MH. SPION-loaded chitosan-linoleic acid nanoparticles to target hepatocytes. Int J Pharm 2009;371:163-9.
27. Wang W, Zhao XL, Hu HY, Chen DW, Gu JC, Deng YH, Sun J. Galactosylated solid lipid nanoparticles with cucurbitacin B improves the liver targetability. Drug delivery 2010;17:114-22.
28. Craparo EF, Sardo C, Serio R, Zizzo MG, Bondi ML, Giammona GG. Galactosylated polymeric carriers for liver targeting of sorafenib. Int J Pharm 2014;466:172-80.
29. Yuan H, Miao J, Du YZ, You J, Hu FQ, Zeng S. Cellular uptake of solid lipid nanoparticles and cytotoxicity of encapsulated paclitaxel in A549 cancer cells. Int J Pharm 2008;348:137-45.
30. Lian J, Zhang S, Wang J, Fang K, Zhang Y, Hao Y. Novel galactosylated SLN for hepatocyte-selective targeting of floxuridinyl diacetate. J Drug Target 2008;16:250-6.

Cite this article as: Zhu X, Deng X, Lu C, Chen Y, Jie L, Zhang Q, Li W, Wang Z, Du Y, Yu R. SPIO-loaded nanostructured lipid carriers as liver-targeted molecular T2-weighted MRI contrast agent. Quant Imaging Med Surg 2018;8(8):770-780. doi: 10.21037/qims.2018.09.03

Supplementary

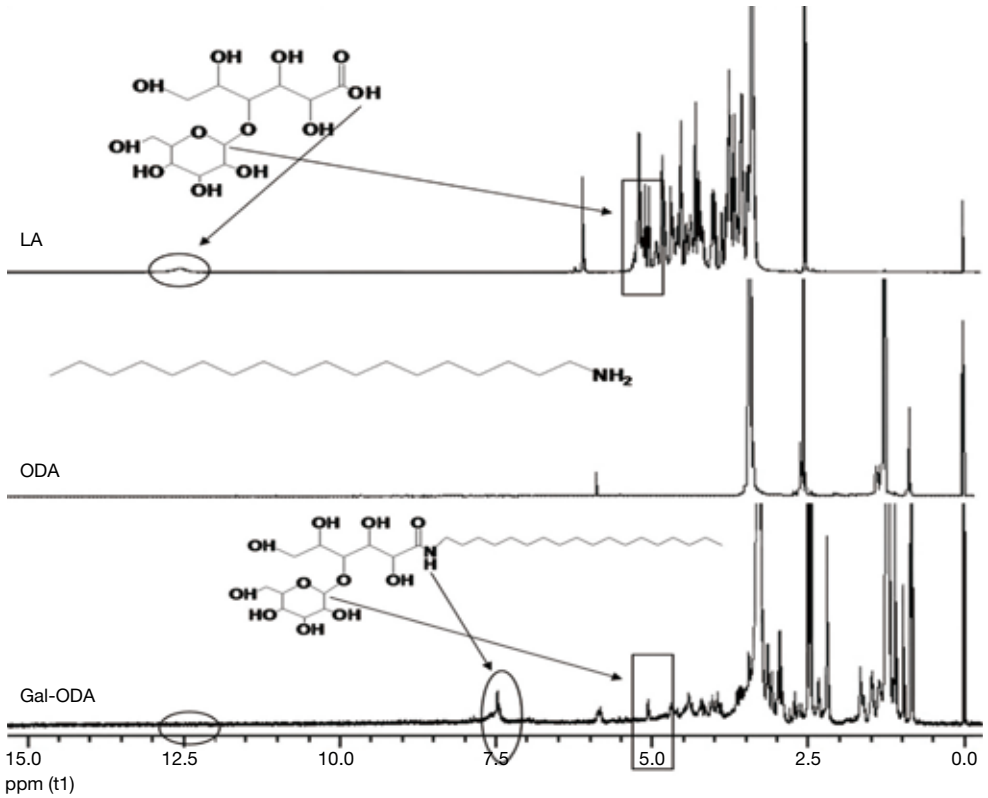

Figure S1 ^{1}H NMR spectra of LA, ODA and Gal-ODA.

Table S1 Particle diameter and zeta potential of NLC-SPIO, Gal-NLC-SPIO and Gal-NLC-SPIO/PEG. Data represent the mean ± standard deviation (n=3)

Sample	Diameter (nm)	PI (–)	Zeta potential (mV)
NLC-SPIO	52.60±5.74	0.24±0.09	–28.45±1.20
Gal-NLC-SPIO	53.47±3.39	0.24±0.08	–30.68±1.10
Gal-NLC-SPIO/PEG	55.87±5.81	0.19±0.05	–33.72±1.28

Gal-NLC, galactose-conjugated nanostructured lipid carrier; SPIO, superparamagnetic iron oxide.

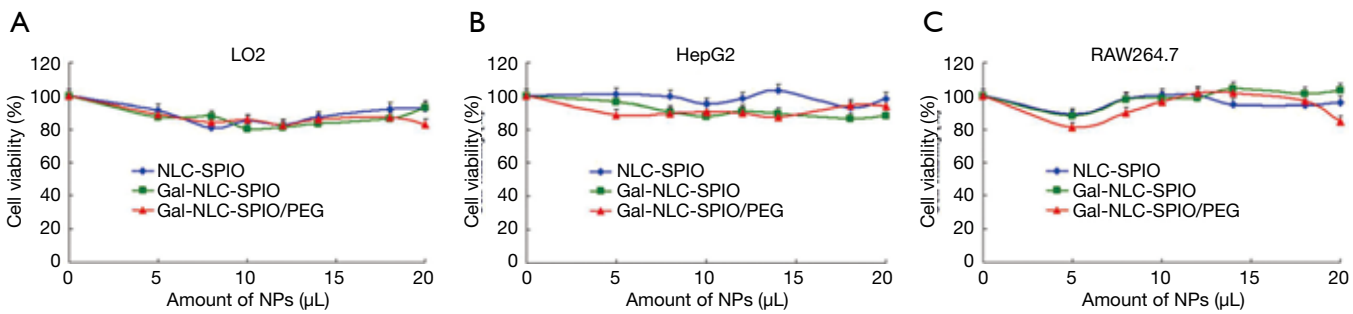

Figure S2 *In vitro* cytotoxicity of NLC-SPIO, Gal-NLC-SPIO and Gal-NLC-SPIO/PEG against LO2 (A), HepG2 (B) and RAW264.7 (C) cells, respectively. Data represent the mean ± standard deviation (n=3). Gal-NLC, galactose-conjugated nanostructured lipid carrier; SPIO, superparamagnetic iron oxide.

Original Article

Sonographic appearance of fluid in peripheral joints and bursae of healthy asymptomatic Chinese population

Liyun Wang, Xi Xiang, Yuanjiao Tang, Yujia Yang, Li Qiu

Department of Ultrasound, West China Hospital of Sichuan University, Chengdu 610041, China

Correspondence to: Li Qiu. Department of Ultrasound, West China Hospital of Sichuan University, No.37 Guo Xue Xiang, Chengdu 610041, China. Email: wsqiuli@126.com.

Background: High frequency ultrasound is often used to measure the thickness of fluid in peripheral joints and bursae of healthy asymptomatic populations. Two major steps critical to this procedure are obtaining the detection rates and analyzing the relevant factors.

Methods: Healthy Chinese adult volunteers with no history of arthritis, past trauma or surgery and joint pain were enrolled in this study. Ultrasonography was performed on the bilateral shoulders, elbows, wrists, metacarpophalangeal joints (MCP) 1–5, proximal interphalangeal joints (PIP) 1–5, distal interphalangeal joints (DIP) 2–5, suprapatellar knees, ankles, metatarsophalangeal joints (MTP) 1–5, subacromial and subdeltoid bursae, deep infrapatellar bursae, retrocalcaneal bursae and long biceps tendons in B mode. Average size of fluid thickness and detection rate were calculated and correlated with demographic parameters. Mean + 1.64 SD was defined as the upper limit of the 95% reference range.

Results: One hundred and fifty-two volunteers (71 males and 81 females) with mean age of 48.0± 14.1 years were enrolled. Both the highest detection rate and the thickest fluid were found in the suprapatellar knee (82.9%, 3.7±1.7 mm). There was no significant difference between the left and right side of the same structure in the detection rate and the fluid thickness. Females had a higher detection rate and fluid thickness than males in most examined structures, especially in the upper-limb joints. The greatest number of examined structures was found to be affected by age, and all of the correlations were positive (r from 0.118 to 0.510, $P<0.05$). Positive correlations were found in the long biceps tendon and MTP1 between detection rate and body mass index (BMI) (r=0.251 and 0.123, respectively, $P<0.05$), and in the long biceps tendon between effusion thickness and BMI (r=0.228, $P<0.05$). The upper limits of the 95% reference range for peripheral joints and bursae were determined.

Conclusions: Fluid in certain peripheral joints of healthy asymptomatic populations can be associated with gender, age or BMI. This study provided reference values for future comparisons with pathological conditions among Chinese populations.

Keywords: Healthy volunteers; effusion; ultrasound; joints

Submitted May 21, 2018. Accepted for publication Sep 10, 2018.
doi: 10.21037/qims.2018.09.10
View this article at: http://dx.doi.org/10.21037/qims.2018.09.10

Introduction

High frequency ultrasound has been increasingly used in musculoskeletal diseases, such as rheumatoid arthritis, for diagnostic purposes and to evaluate disease activity or drug response (1-4). Although MRI can detect lesions of minor joint structures, such as triangular fibrocartilage complex (TFCC) tears (5), high resolution ultrasound has become an important complement to musculoskeletal imaging beyond MRI. Ultrasound manifestation of inflammatory joints may include bone erosion, synovial hyperplasia, synovial vascularization and synovial fluid (2,3,6). Synovial fluid can

also be found in certain joints under normal conditions, and can be visualized on sonography (7-9).

Assessing the ultrasound appearance of peripheral joints, bursae and tendon sheaths in a healthy asymptomatic population may provide insights into interpreting ultrasound exams in pathologic cases. It is important for clinicians to differentiate between effusion—the excess fluid in joints—and physiologic fluid accumulation, as the latter does not need clinical intervention. Therefore, in this study, we aimed to (I) use ultrasound to measure the thickness of fluid in peripheral joints, bursae and tendon sheaths in regards to situation, gender, age and BMI (US); (II) calculate the upper limit of the 95% reference range, in order to better understand both normal and pathologic conditions of joints and bursae fluids.

Methods

The study was approved by the local Ethics Committee. Informed consent was obtained from the volunteers for the acquisition, analysis and reporting of imaging data at the time of their examinations.

This study was conducted with healthy adult Chinese volunteers between January 2017 and June 2017, who were consecutively included from (I) healthcare medical, paramedical and administrative staff of the local hospital, (II) medical students at the same hospital, (III) healthy relatives visiting or accompanying patients and (IV) volunteers enrolled through online announcement of the study.

Inclusion criteria were age from 18 to 90 years, and free consensus to participate in the study. Exclusion criteria were the following: (I) history of rheumatoid arthritis, diabetes mellitus, hypothyroidism, hemophilia, trauma, surgery, symptomatic osteoarthritis, or septic arthritis in any studied joint; (II) any kind of joint pain experienced during any time in the previous month; (III) pregnant or breast-feeding women. Patient's age, sex, height and weight data were collected as demographic characteristics and body mass index (BMI) was subsequently calculated later.

US examinations were performed using Philips IU22 with a 9–12 MHz linear array transducer. Musculoskeletal (MSK) presetting was selected with the standard default mode. The transducer, coupled with several millimeters of ultrasound gel, was smoothly placed perpendicular to the skin to avoid anisotropic artifacts. All examinations were performed by 2 experienced radiologists (QL and TYJ) with more than 8 years of experience in musculoskeletal ultrasonography, and US examination was done by QL or TYJ at random in our study. Schmidt *et al.* have shown excellent inter- and intra-observer agreement (both lager than 0.8) when using similar ultrasound measurement methods (10). According to the OMERACT definition (11), the presence of fluid was defined as an anechoic displaceable and compressible intracapsular area in B mode, and which does not exhibit Doppler signal (*Figure 1*). US examination was performed in peripheral joints, bursae and tendon sheaths based on standard scans (12), and displayed in *Table 1*. Scanning planes showed the maximum amount of joint fluid selected and the three consecutive US measurements were performed for every location to obtain the average value.

SPSS software was used for statistical analysis (SPSS, version 19.0, Chicago III). Descriptive statistics were expressed as means ± standard deviations. Categorical data were described using counts, percentages and 95% confidence intervals. Chi-squared test was used for comparison in detection rate. Independent-sample's t test was used for comparison in fluid thickness. We correlated detection rate and fluid thickness with demographic characters using Spearman correlation analysis. Correlation index (r) was interpreted as 0.8–1.0 strong correlation, 0.5–0.8 moderate correlation, 0.3–0.5 low correlation, and <0.3 weak correlation. Two-sided statistical significance was defined as $P<0.05$. Increase of fluid is considered to be pathological, so we only calculated the upper limit of 95% reference range using the equation: the upper limit = mean + 1.64 SD.

Results

A total of 152 healthy asymptomatic Chinese volunteers were included. The mean age was 48.0±14.1 years with a range of 20–75 years. The mean BMI was 22.58±3.15 kg/m^2 with a range of 15.82-31.51 kg/m^2. Seventy-one participants were male and 81 were female. None of the recruited volunteers were excluded for further analysis. There was detectable ultrasonic fluid in all the 24 kinds of joints, 3 bursae and 1 tendon sheath studied.

Fluid was found in suprapatellar knees in 252/304 (82.9%), which made it the highest one among all the studied structures. Weak positive correlations ($r<0.3$) between detection rate and both age and BMI were found in 21.4% and 7.1% of all the 28 structures studied respectively (*Table S1*). There was no situational (right or left) difference found in detection rate. Gender difference was found in the 2nd, 3rd and 4th PIPs, with the detection rates in these

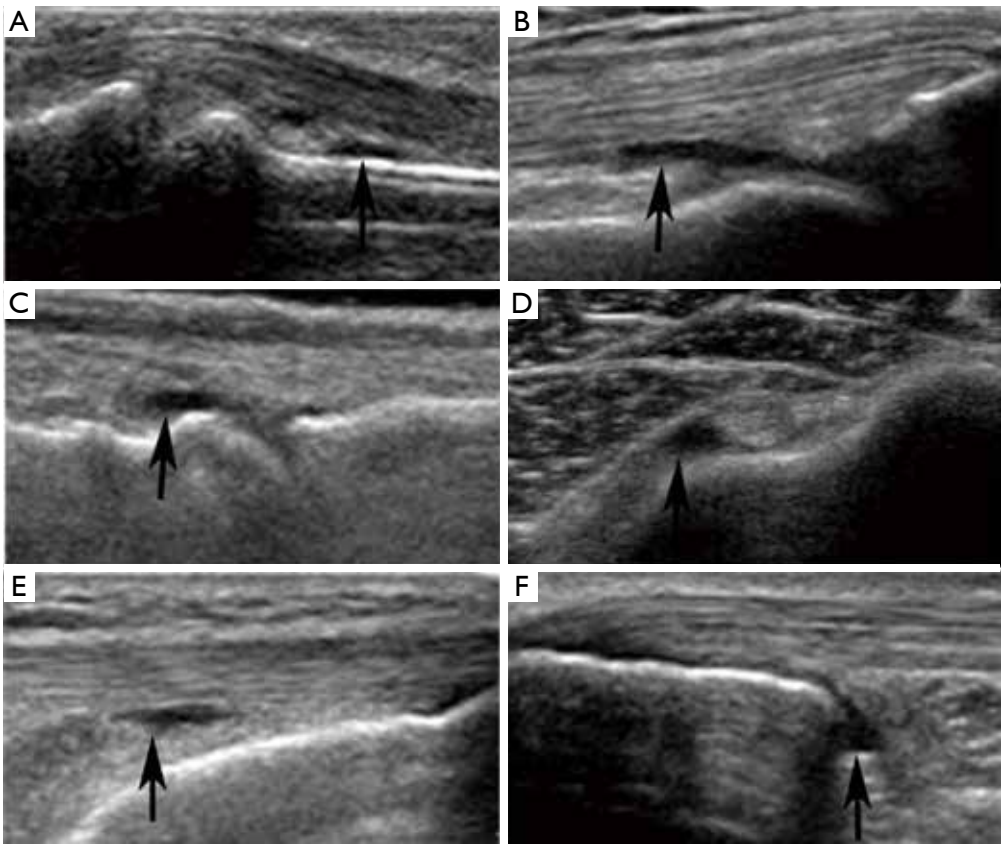

Figure 1 Ultrasound appearance of fluid in a 25-year-old healthy female (arrow). (A) Fluid in PIP 3; (B) fluid in suprapatellar knee; (C) fluid in MTP 1; (D) fluid in tendon sheath of long biceps tendon; (E) fluid in deep infrapatellar bursa; (F) fluid in retrocalcaneal bursa.

PIPs being higher in female subjects (*Table S2*).

The thickest fluid was also found in the suprapatellar knee, and its average fluid thickness was 3.7±1.7 mm. Moderate positive correlation was found between fluid thickness and age in MCP 5 ($r=0.510$, $P<0.05$). Low positive correlations were found between fluid thickness and age in the retrocalcaneal bursae, and between fluid thickness and BMI in the long biceps tendon ($r=0.398$ and 0.228, respectively, both $P<0.05$). The positive correlation between fluid thickness and age was weak in long the biceps tendon ($r=0.181$, $P<0.05$) (*Table S3*). There was no significant difference found between the right and left side in fluid thickness ($P>0.05$) (*Table S4*). As for gender, fluid thickness was higher in women in wrists, MCP5, PIP 4, retrocalcaneal bursae and long biceps tendon ($P<0.05$). Conversely, the fluid thickness of PIP 2 and deep infrapatellar bursae was higher in male subjects ($P<0.05$).

Reference values differed among different joints (*Table 2*). Overall, the upper limits of the 95% reference range for lower limb joints were larger than upper limb joints. For example, the upper limits in the shoulder (gleno-humeral joint), elbow and wrist are ≤3.9, ≤3.5 and ≤3.9 mm, respectively; whereas the suprapatellar knee and ankle are ≤6.6 and ≤5.4 mm, respectively. As for the hands, the upper limits were over 1mm in PIPs and DIPs with larger fluid thickness found in MCPs (approximately 2 mm). Changeable upper limits were found in the feet, and were ≤0.8 mm for MCP5 to ≤4.1 mm for MTP1.

Discussion

High-frequency ultrasound has proven its diagnostic power in musculoskeletal diseases; however, identifying differences between normal and pathologic conditions is still difficult. A previous study (7) which included 46 healthy subjects indicated that fluid was present in 20.9% of PIPs, but less frequent in DIPs (3% DIPs). Schmidt *et al.* reported that fluid in bursae and joints were common findings in healthy

Table 1 US scanning plane and measurement location of fluid in joints, bursa and tendon sheath

Structure	Positioning	Scanning plane	Measurement location
Shoulder (gleno-humeral joint)	Sitting position; 90° flexion of the elbow joint with hand positioned in supination on top of the volunteer's thigh	Anterior and posterior space	Maximum bone-capsule distance
Elbow (radial, coronoid, annular and posterior recess)	Sitting position; Full extension of the elbow joint (ventral scans); flexion of the elbow joint in a 90° angle (dorsal scans)	Longitudinal and transverse	
Wrist (radiocarpal, innercarpal and ulnocarpal joints), MCP 1–5, PIP 1–5, DIP 2–5, MTP 1–5	Sitting position; positioning of the hand on an examining bed	Palmar and dorsal, longitudinal	
Knee (Suprapatellar recess), Ankle (tibio-talar joint)	Supine position with knee joint in neutral position and 30° flexion (Knee); Prone position with hip and knee joints in neutral position (Ankle)	Anterior, longitudinal and transverse	
Deep infrapatellar bursa, retro-calcaneal bursa	Supine position with knee joint in neutral position and 30° flexion (deep infrapatellar bursa); Prone position with hip and knee joints in neutral position (retro-calcaneal bursa)	Longitudinal	Maximum capsule-capsule distance
Subacromial-subdeltoid bursa	See shoulder joint	Longitudinal and transverse	
Long biceps tendon	See shoulder joint	Transverse	Maximum tendon-peritendineum distance at the bicipital groove

MCP, metacarpophalangeal joint; PIP, proximal interphalangeal joint; DIP, distal interphalangeal joint; MTP, metatarsophalangeal joint.

people (10). Our results also suggest that all asymptomatic joints, bursae and tendon sheaths examined in our study have ultrasound-detectable accumulation of synovial fluid, of which the detection rate and fluid thickness vary in different structures. The mean thickness of fluid found in asymptomatic joints is listed in the following descending order: suprapatellar knee (3.7 mm), ankle (3.3 mm), shoulder (2.2 mm), elbow (2.2 mm), wrist (2.1 mm), MTPs (0.7–2.4 mm), MCPs (1.2–1.9 mm), PIPs (0.8–1.2 mm), DIPs (0.8 mm).

Similar to previous studies (7,10,13) which reported no significant difference between the dominant and non-dominant side, we similarly found no difference between the left and right side in both detection rate and fluid rate. These results may indicate that symmetrical parts of healthy subjects have the same anatomical structure, and that there would not be significant difference between the left and right side of a structure under normal conditions. Therefore, through examining and comparing joints on both sides, we can recognize unilateral lesion and assess its severity.

We observed that females had a higher detection rate and fluid thickness than males in most examined structures, especially in upper-limb joints, although many of them did not show statistical difference. According to studies about gender impact on ultrasound measurements, Ellegaard *et al.* suggested that women obtained higher pathological scores than men in healthy small hand joints (14). Poncelet *et al.* determined different deep joint space distance of the acromioclavicular joint between men and women (13). These studies indicate physiological and anatomical differences between men and women, which might be caused by different kinds of labor or exercise. When considering gender influence, it is better to choose the same sex as the normal reference in US examinations of certain structures, especially in the retrocalcaneal bursa, which had a difference between means larger than 1 mm.

Among the studied demographic parameters, the greatest number of examined structures was found to be affected by age, and all of the correlations were positive. We attribute this to the lasting and irreversible degeneration of joints caused by aging which can induce bone changes including spurs and irregularities in the elderly (15). Higher quantitative joint recess measured sonographically

Table 2 Fluid thickness and the upper limits of 95% reference range in healthy asymptomatic population

Location	Mean (mm)	SD (mm)	95% reference range (upper limit, mm)
Shoulder	2.2	1.0	3.9
Elbow	2.2	0.8	3.5
Wrist	2.1	1.1	3.9
MCP1	1.4	1.0	2.9
MCP2	1.9	0.7	3.0
MCP3	1.5	0.6	2.5
MCP4	1.2	0.4	1.9
MCP5	1.2	0.4	1.8
PIP1	0.9	0.3	1.4
PIP2	1.0	0.4	1.7
PIP3	1.2	0.4	1.8
PIP4	1.0	0.4	1.7
PIP5	0.8	0.4	1.4
DIP2	0.8	0.3	1.4
DIP3	0.8	0.2	1.2
DIP4	0.8	0.3	1.3
DIP5	0.8	0.3	1.2
Suprapatellar knee	3.7	1.7	6.6
Ankle	3.3	1.3	5.4
MTP1	2.4	1.1	4.1
MTP2	1.7	0.7	2.9
MTP3	1.4	0.7	2.5
MTP4	1.9	1.2	3.8
MTP5	0.7	0.1	0.8
Subacromial/ subdeltoid bursa	1.5	1.0	3.1
Deep infrapatellar bursa	1.3	0.6	2.2
Retrocalcaneal bursa	2.1	1.3	4.3
Long biceps tendon	2.1	0.8	3.4

has also been reported in older groups (9). Additionally, we found positive correlations with age, especially in small joints like PIP, DIP and MTP, which are similar to results reported by Machado *et al.* whose study detailed a higher percentage of synovial effusion in the hand and foot joints of healthy individuals (9). In our study, we did not exclude the older people with asymptomatic osteoarthritis, because asymptomatic osteoarthritis is of less clinical importance and there is usually no need for intervention. Therefore, when attempting to detect joint fluid in aged but asymptomatic people, we should consider age effects especially in the hand and foot joints.

Positive correlations with BMI were found in the long biceps tendon and MTP1. The long biceps tendon is closely related to motion, and MTP1 is an important weight-bearing joint. Therefore, height and weight might have a greater impact on these two structures. Excessive increases in weight-bearing forces caused by obesity may be detrimental to the lower limbs and feet (16), lead to musculoskeletal pain in the legs, and contribute to overall difficulty of daily movements (17). Obesity can also lead to musculoskeletal disorders in children by promoting biomechanical changes in the lumbar spine and lower extremities (18). Conversely, in patients with rheumatoid arthritis, a higher BMI is associated with a less severe disease outcome (19), and disease activity might also be overestimated in obese patients (20). The above results indicate a close relationship between BMI and joint disease. In our study, the mean BMI was 22.58±3.15 kg/m^2 which was almost within the normal range. Thus, whether an overweight condition affects joint fluid still remains unclear and open for further investigation.

We have found some difference in reference values compared with Schmidt's study (10). The most important influencing factor is that we use mean + 1.64 SD to define the upper limit of the 95% reference range, while they use mean ± 2 SD to calculate the standard reference values. As we supposed that only excessive accumulation of fluid in joints is pathological, it is suitable for us to calculate the upper limit. Another reason for this phenomenon might be different the study populations included. As we have calculated the reference values for healthy asymptomatic people, we might be able to help radiologists and clinicians to better distinguish between normal and abnormal conditions, which is of great importance in clinical practice because excessive fluid accumulation may lead to further examinations or treatments. Our study may also provide

normal controls for future comparative studied in patients with rheumatoid arthritis or other diseases. There are also some limitations in our study. First, we did not study all the ultrasound-detectable peripheral joints and their sonographic findings, such as bone erosion, bursa effusion or tendinopathy. Second, by design, this study lacked Doppler analysis. The strengths of our study include a relatively large number of patients.

Conclusions

Fluid in the peripheral joints, bursae and tendon sheaths of healthy asymptomatic populations can be frequently found by US. The detection rate and fluid thickness vary in different structures. Some of the fluid thickness and detection rates are associated with gender, age or BMI, but no difference has been found between the left and right side joints. While making diagnoses of joint diseases, it is important to choose suitable control groups regarding the relevant factors. Additionally, reference values provided in this study might be helpful to recognize effusion in the healthy asymptomatic Chinese population. Further multi-center studies are still necessary to determine more generally applicable standard reference values.

Acknowledgements

Funding: This study was supported by the National Natural Science Foundation of China (81671696).

Footnote

Conflicts of Interest: The authors have no conflicts of interests to declare.

Ethical Statement: The study was approved by the West China Hospital of Sichuan University Ethics Committee. Informed consent was obtained from all volunteers.

References

1. Dougados M, Jousse-Joulin S, Mistretta F, d'Agostino MA, Backhaus M, Bentin J, Chalès G, Chary-Valckenaere I, Conaghan P, Etchepare F, Gaudin P, Grassi W, van der Heijde D, Sellam J, Naredo E, Szkudlarek M, Wakefield R, Saraux A. Evaluation of several ultrasonography scoring systems for synovitis and comparison to clinical examination: results from a prospective multicentre study of rheumatoid arthritis. Ann Rheum Dis 2010;69:828-33.
2. Ziswiler HR, Aeberli D, Villiger PM, Möller B. High-resolution ultrasound confirms reduced synovial hyperplasia following rituximab treatment in rheumatoid arthritis. Rheumatology (Oxford) 2009;48:939-43.
3. Weidekamm C, Köller M, Weber M, Kainberger F. Diagnostic value of high-resolution B-mode and doppler sonography for imaging of hand and finger joints in rheumatoid arthritis. Arthritis Rheum 2003;48:325-33.
4. Iagnocco A, Perella C, Naredo E, Meenagh G, Ceccarelli F, Tripodo E, Basili S, Valesini G. Etanercept in the treatment of rheumatoid arthritis: clinical follow-up over one year by ultrasonography. Clin Rheumatol 2008;27:491-6.
5. Ng AW, Griffith JF, Fung CS, Lee RK, Tong CS, Wong CW, Tse WL, Ho PC. MR imaging of the traumatic triangular fibrocartilaginous complex tear. Quant Imaging Med Surg 2017;7:443-60.
6. Machado FS, Furtado RN, Takahashi RD, de Buosi AL, Natour J. Sonographic cutoff values for detection of abnormalities in small, medium and large joints: a comparative study between patients with rheumatoid arthritis and healthy volunteers. Ultrasound Med Biol 2015;41:989-98.
7. Rosenberg C, Arrestier S, Etchepare F, Fautrel B, Rozenberg S, Bourgeois P. High frequency of ultrasonographic effusion in interphalangeal joints of healthy subjects: a descriptive study. Joint Bone Spine 2009;76:265-7.
8. Luukkainen R, Ekman P, Luukkainen P, Koski JM. Ultrasonographic findings in metatarsophalangeal and talocrural joints in healthy persons. Clin Rheumatol 2009;28:311-3.
9. Machado FS, Natour J, Takahashi RD, de Buosi AL, Furtado RN. Sonographic assessment of healthy peripheral joints: evaluation according to demographic parameters. J Ultrasound Med 2014;33:2087-98.
10. Schmidt WA, Schmidt H, Schicke B, Gromnica-Ihle E. Standard reference values for musculoskeletal ultrasonography. Ann Rheum Dis 2004;63:988-94.
11. Wakefield RJ, Balint PV, Szkudlarek M, Filippucci E, Backhaus M, D'Agostino MA, Sanchez EN, Iagnocco A, Schmidt WA, Bruyn GA, Bruyn G, Kane D, O'Connor PJ, Manger B, Joshua F, Koski J, Grassi W, Lassere MN, Swen N, Kainberger F, Klauser A, Ostergaard M, Brown AK, Machold KP, Conaghan PG. Musculoskeletal ultrasound including definitions for ultrasonographic pathology. J Rheumatol 2005;32:2485-7.

12. Backhaus M, Burmester GR, Gerber T, Grassi W, Machold KP, Swen WA, Wakefield RJ, Manger B. Guidelines for musculoskeletal ultrasound in rheumatology. Ann Rheum Dis 2001;60:641-9.
13. Poncelet E, Demondion X, Lapègue F, Drizenko A, Cotten A, Francke JP. Anatomic and biometric study of the acromioclavicular joint by ultrasound. Surg Radiol Anat 2003;25:439-45.
14. Ellegaard K, Torp-Pedersen S, Holm CC, Danneskiold-Samsøe B, Bliddal H. Ultrasound in finger joints: findings in normal subjects and pitfalls in the diagnosis of synovial disease. Ultraschall Med 2007;28:401-8.
15. Ustuner E, Toprak U, Baskan B, Oztuna D. Sonographic examination of the common extensor tendon of the forearm at three different locations in the normal asymptomatic population. Surg Radiol Anat 2013;35:547-52.
16. Hills AP, Hennig EM, McDonald M, Bar-Or O. Plantar pressure differences between obese and non-obese adults: a biomechanical analysis. Int J Obes Relat Metab Disord 2001;25:1674-9.
17. Tsuritani I, Honda R, Noborisaka Y, Ishida M, Ishizaki M, Yamada Y. Impact of obesity on musculoskeletal pain and difficulty of daily movements in Japanese middle-aged women. Maturitas 2002;42:23-30.
18. de Sá Pinto AL, de Barros Holanda PM, Radu AS, Villares SM, Lima FR. Musculoskeletal findings in obese children. J Paediatr Child Health 2006;42:341-4.
19. Caplan L, Davis LA, Bright CM, Kerr GS, Lazaro DM, Khan NA, Richards JS, Johnson DS, Cannon GW, Reimold AM, Mikuls TR. Body mass index and the rheumatoid arthritis swollen joint count: an observational study. Arthritis Care Res (Hoboken) 2013;65:101-6.
20. Bauer EM, Ben-Artzi A, Duffy EL, Elashoff DA, Vangala SS, Fitzgerald J, Ranganath VK. Joint-specific assessment of swelling and power Doppler in obese rheumatoid arthritis patients. BMC Musculoskelet Disord 2017;18:99.

Cite this article as: Wang L, Xiang X, Tang Y, Yang Y, Qiu L. Sonographic appearance of fluid in peripheral joints and bursae of healthy asymptomatic Chinese population. Quant Imaging Med Surg 2018;8(8):781-787. doi: 10.21037/qims.2018.09.10

Supplementary

Table S1 Detection rate in healthy asymptomatic population and correlations with age and BMI

Location	Detection number	Detection rate (%) (95% CI)	r	
			Age	BMI
Shoulder	6	2.0 (0.4–3.5)	0.014	–0.044
Elbow	117	38.5 (33.0–44.0)	0.100	–0.060
Wrist	125	41.1 (35.6–46.7)	0.080	–0.106
MCP1	4	1.3 (0–2.6)	0.036	0.014
MCP2	18	5.9 (3.3–8.6)	0.051	–0.345
MCP3	20	6.6 (3.8–9.4)	–0.019	0.029
MCP4	30	9.9 (6.5–13.2)	0.024	0.045
MCP5	25	8.2 (5.1–11.3)	–0.088	0.037
PIP1	9	3.0 (1.0–4.9)	0.099	–0.079
PIP2	53	17.4 (13.1–21.7)	0.004	0.010
PIP3	94	30.9 (25.7–36.1)	0.140*	–0.013
PIP4	61	20.1 (15.5–24.6)	0.152**	–0.024
PIP5	21	6.9 (4.0–9.8)	0.020	0.055
DIP2	7	2.3 (0.6–4.0)	–0.006	–0.012
DIP3	22	7.2 (4.3–10.2)	0.118*	–0.043
DIP4	11	3.6 (1.5–5.7)	0.069	–0.030
DIP5	4	1.3 (0–2.6)	0.042	–0.055
Suprapatellar knee	252	82.9 (78.6–87.2)	0.272*	0.049
Ankle	140	46.1 (40.4–51.7)	0.036	–0.004
MTP1	99	32.6 (27.3–37.9)	0.118*	0.123*
MTP2	16	5.3 (2.7–7.8)	0.106	0.031
MTP3	11	3.6 (1.5–5.7)	–0.035	–0.021
MTP4	3	0.7 (0–1.6)	0.019	0.083
MTP5	3	0.7 (0–1.6)	–0.025	0.061
Subacromial/subdeltoid bursa	35	11.5 (7.9–15.1)	0.061	–0.040
Deep infrapatellar bursa	75	24.7 (19.8–29.5)	–0.041	0.024
Retrocalcaneal bursa	42	13.8 (9.9–17.7)	–0.016	–0.030
Long biceps tendon	125	41.4 (35.6–46.7)	0.165*	0.251*

*P<0.05; **P<0.01. MCP, metacarpophalangeal joint; PIP, proximal interphalangeal joint; DIP, distal interphalangeal joint; MTP, metatarsophalangeal joint.

Table S2 Comparisons of detection rate between right and left sides, and between females and males

Location	Detection rate (%)			Detection rate (%)		
	Right	Left	P value	Female	Male	P value
Shoulder	2.0	2.0	1.000	3.1	0.7	0.220
Elbow	37.5	39.5	0.814	37.0	40.1	0.637
Wrist	40.8	41.4	1.000	43.2	38.7	0.484
MCP1	2.6	0	0.123	0.6	2.1	0.343
MCP2	5.3	6.6	0.809	6.8	4.9	0.628
MCP3	5.9	7.2	0.818	7.4	5.6	0.645
MCP4	11.2	8.6	0.565	8.6	11.3	0.449
MCP5	6.6	9.9	0.404	10.5	5.6	0.146
PIP1	3.3	2.6	1.000	2.5	3.5	0.738
PIP2	20.4	14.5	0.226	23.5	10.6	0.004*
PIP3	32.9	28.9	0.535	38.3	22.5	0.004*
PIP4	19.1	21.1	0.775	25.3	14.1	0.015*
PIP5	6.6	7.2	1.000	8.0	5.6	0.499
DIP2	2.6	2.0	1.000	3.7	0.7	0.126
DIP3	6.6	7.9	0.825	8.0	6.3	0.660
DIP4	3.9	3.3	1.000	4.3	2.8	0.551
DIP5	1.3	1.3	1.000	1.9	0.7	0.626
Suprapatellar knee	84.2	81.6	0.648	83.3	82.4	0.879
Ankle	48.7	43.4	0.421	43.2	49.3	0.301
MTP1	32.9	32.2	1.000	28.4	37.3	0.111
MTP2	4.6	5.9	0.798	4.9	5.6	0.803
MTP3	3.9	3.3	1.000	3.1	4.2	0.760
MTP4	1.3	0.0	0.498	0.6	0.7	1.000
MTP5	0.7	0.7	1.000	0.6	0.7	1.000
Subacromial/subdeltoid bursa	13.8	9.2	0.281	9.3	14.1	0.210
Deep infrapatellar bursa	23.0	26.3	0.595	21.6	28.2	0.230
Retrocalcaneal bursa	15.1	12.5	0.618	14.2	13.4	0.869
Long biceps tendon	40.8	41.1	1.000	44.4	37.3	0.243

MCP, metacarpophalangeal joint; PIP, proximal interphalangeal joint; DIP, distal interphalangeal joint; MTP, metatarsophalangeal joint.

Table S3 Fluid thickness in healthy asymptomatic population and correlations with age and BMI

Location	Mean (mm)	SD (mm)	r	
			Age	BMI
Shoulder	2.2	1.0	–0.412	–0.358
Elbow	2.2	0.8	0.163	0.069
Wrist	2.1	1.1	–0.058	–0.170
MCP1	1.4	1.0	–0.500	–0.105
MCP2	1.9	0.7	0.034	–0.206
MCP3	1.5	0.6	0.014	–0.352
MCP4	1.2	0.4	0.196	–0.206
MCP5	1.2	0.4	0.510**	–0.293
PIP1	0.9	0.3	0.008	–0.308
PIP2	1.0	0.4	0.137	0.056
PIP3	1.2	0.4	0.167	0.087
PIP4	1.0	0.4	0.187	0.035
PIP5	0.8	0.4	0.227	0.029
DIP2	0.8	0.3	–0.199	0.218
DIP3	0.8	0.2	–0.023	0.153
DIP4	0.8	0.3	0.194	0.460
DIP5	0.8	0.3	0.949	0.316
Suprapatellar knee	3.7	1.7	–0.025	0.083
Ankle	3.3	1.3	0.007	–0.030
MTP1	2.4	1.1	0.011	0.024
MTP2	1.7	0.7	0.173	0.355
MTP3	1.4	0.7	–0.128	–0.192
MTP4	1.9	1.2	–1.000	–1.000
MTP5	0.7	0.1	–1.000	–1.000
Subacromial/subdeltoid bursa	1.5	1.0	–0.001	–0.091
Deep infrapatellar bursa	1.3	0.6	0.207	0.176
Retrocalcaneal bursa	2.1	1.3	0.398*	–0.045
Long biceps tendon	2.1	0.8	0.181*	0.228*

*P<0.05; **P<0.01. MCP, metacarpophalangeal joint; PIP, proximal interphalangeal joint; DIP, distal interphalangeal joint; MTP, metatarsophalangeal joint.

Table S4 Comparisons of fluid thickness between right and left sides, and between females and males

Location	Fluid thickness (mm)			Fluid thickness (mm)		
	Right	Left	P value	Female	Male	P value
Shoulder	2.4±1.5	1.9±0.4	0.608	2.2±1.1	2.3[a]	0.916
Elbow	2.2±0.8	2.3±0.7	0.828	2.34±0.8	2.1±0.7	0.106
Wrist	2.2±1.1	2.0±1.1	0.501	2.3±1.3	1.9±0.7	0.025*
MCP1	1.4±1.0	—	—	0.8[a]	1.5±1.1	0.622
MCP2	2.0±0.7	1.8±0.7	0.673	2.1±0.8	1.5±0.3	0.073
MCP3	1.6±0.9	1.3±0.4	0.293	1.5±0.8	1.4±0.3	0.708
MCP4	1.3±0.4	1.2±0.4	0.450	1.3±0.4	1.2±0.3	0.279
MCP5	1.1±0.4	1.2±0.4	0.276	1.3±0.4	1.0±0.2	0.009*
PIP1	0.8±0.2	1.1±0.3	0.193	1.0±0.4	0.9±0.2	0.538
PIP2	1.0±0.4	1.1±0.4	0.606	1.0±0.3	1.3±0.5	0.049*
PIP3	1.2±0.3	1.20±0.4	0.975	1.2±0.3	1.1±0.4	0.376
PIP4	1.1±0.4	0.9±0.4	0.228	1.1±0.5	0.8±0.2	0.005*
PIP5	0.8±0.5	0.8±0.2	0.669	0.8±0.4	0.8±0.3	0.644
DIP2	0.9±0.4	0.7±0.3	0.484	0.9±0.3	0.4[a]	0.204
DIP3	0.9±0.3	0.8±0.2	0.607	0.8±0.2	1.0±0.3	0.054
DIP4	0.9±0.3	0.7±0.2	0.185	0.9±0.3	0.8±0.1	0.579
DIP5	0.9±0.3	0.7±0.2	0.423	0.8±0.3	0.7[a]	0.800
Suprapatellar knee	3.8±1.8	3.7±1.6	0.731	3.7±1.8	3.7±1.7	0.924
Ankle	3.4±1.4	3.1±1.2	0.112	3.4±1.3	3.2±1.4	0.524
MTP1	2.5±1.2	2.2±1.0	0.199	2.2±1.2	2.5±1.0	0.121
MTP2	1.9±0.7	1.5±0.7	0.304	1.6±0.7	1.8±0.8	0.612
MTP3	1.7±0.7	1.1±0.4	0.130	1.2±0.7	1.6±0.6	0.310
MTP4	1.9±1.2	—	—	2.7[a]	1.0[a]	—
MTP5	0.6[a]	0.7[a]	—	0.6[a]	0.7[a]	—
Subacromial/subdeltoid bursa	1.7±1.1	1.4±0.9	0.371	1.5±1.0	1.6±1.0	0.942
Deep infrapatellar bursa	1.4±0.6	1.3±0.5	0.389	1.1±0.4	1.5±0.6	<0.001*
Retrocalcaneal bursa	2.1±1.4	2.2±1.3	0.832	2.6±1.5	1.5±0.7	0.004*
Long biceps tendon	2.1±0.8	2.0±0.8	0.759	2.2±0.9	1.8±0.6	0.002*

*P<0.05. [a], only Mean has been displayed; —, cannot be calculated due to small sample size. MCP, metacarpophalangeal joint; PIP, proximal interphalangeal joint; DIP, distal interphalangeal joint; MTP, metatarsophalangeal joint.

Original Article

Semi-quantitative analysis of pre-treatment morphological and intratumoral characteristics using ^{18}F-fluorodeoxyglucose positron-emission tomography as predictors of treatment outcome in nasal and paranasal squamous cell carcinoma

Noriyuki Fujima[1], Kenji Hirata[2], Tohru Shiga[2], Koichi Yasuda[3,4], Rikiya Onimaru[3], Kazuhiko Tsuchiya[5], Satoshi Kano[6], Takatsugu Mizumachi[6], Akihiro Homma[6], Kohsuke Kudo[1], Hiroki Shirato[3,4]

[1]Department of Diagnostic and Interventional Radiology, Hokkaido University Hospital, Sapporo, Japan; [2]Department of Nuclear Medicine, [3]Department of Radiation Medicine, Hokkaido University Graduate School of Medicine, Sapporo, Japan; [4]The Global Station for Quantum Medical Science and Engineering, Global Institution for Collaborative Research and Education, Sapporo, Japan; [5]Department of Radiation Oncology, Otaru General Hospital, Otaru, Japan; [6]Department of Otolaryngology-Head and Neck Surgery, Hokkaido University Graduate School of Medicine, Sapporo, Japan

Correspondence to: Noriyuki Fujima, MD, PhD. Department of Diagnostic and Interventional Radiology, Hokkaido University Hospital, N15, W7, Kita-Ku, Sapporo 060-8638, Japan. Email: Noriyuki.Fujima@mb9.seikyou.ne.jp.

Background: To investigate the utility of quantitative morphological and intratumoral characteristics obtained by ^{18}F-fluorodeoxyglucose positron-emission tomography/computed tomography (FDG-PET/CT) for the prediction of treatment outcome in patients with nasal or paranasal cavity squamous cell carcinoma (SCC).

Methods: Twenty-four patients with nasal or paranasal cavity SCC who received curative non-surgical therapy (a combination of super-selective arterial cisplatin infusion and radiotherapy) were retrospectively analyzed. From pre-treatment FDG-PET data, a total of 13 parameters of quantitative morphological characteristics (tumor volume, surface area and sphericity), intratumoral characteristics (the maximum and mean standard uptake value, three intratumoral histogram and four textural parameters) and total lesion glycolysis (TLG) were respectively calculated. Information regarding the treatment outcome was determined from the histological diagnosis or clinical follow-up. Each of the 13 quantitative parameters as well as T- and N-stage was assessed for its relation to treatment outcome of local control or failure.

Results: In univariate analysis, significant differences in surface area and sphericity between the local control and failure groups were observed. The receiver operating characteristic (ROC) curve analysis showed that sphericity had the highest accuracy of 0.88. In the multivariate analysis, sphericity was revealed as an independent predictor of the local control or failure.

Conclusions: The quantitative parameters of sphericity are useful to predict the treatment outcome in patients with nasal or paranasal SCC.

Keywords: Head and neck neoplasms; carcinoma, squamous cell; positron-emission tomography

Submitted Jul 03, 2018. Accepted for publication Sep 12, 2018.
doi: 10.21037/qims.2018.09.09
View this article at: http://dx.doi.org/10.21037/qims.2018.09.09

Introduction

Non-surgical treatments such as chemoradiation therapy have been important treatment methods for patients with head and neck squamous cell carcinoma (HNSCC) (1), particularly since they result in less functional impairment than surgical treatment (2). In particular, the combination therapy of super-selective arterial infusions of cisplatin and radiotherapy has become popular because it can achieve a high local control rate even in advanced stage patients with nasal- or paranasal-cavity SCC (3,4). For such a curative nonsurgical treatment, it can be helpful to predict the treatment outcome in order to optimize the subsequent patient management, including the determination of treatment re-planning and the follow-up strategy.

For the evaluation of primary lesions, ^{18}F-fluorodeoxyglucose positron-emission tomography/computed tomography (FDG-PET/CT), which depicts the tumor metabolic rate of glucose, has been a major diagnostic modality. The tumor glucose metabolic rate is one of the important factors reflecting tumor aggressiveness (5,6). Several studies have also investigated FDG-PET/CT parameters, particularly the maximum standardized uptake value (SUVmax), metabolic tumor volume (MTV) and total lesion glycolysis (TLG), for their potential roles in predicting treatment outcomes in HNSCC patients (7-9). Another proposed approach to the evaluation of FDG uptake in HNSCC is determination of the textural features of FDG distribution in the tumor; this method can reveal tumor heterogeneity in greater detail (10-12). In addition, tumor morphological information can also be a useful parameter. FDG-PET/CT data provide rough anatomical information about the tumor revealed by the lesion's elevated FDG uptake. Moreover, the tumor margin can be easily set using the threshold of FDG uptake from FDG-PET/CT imaging, allowing objective quantification of the whole tumor area (13). From this morphological data, several parameters related to the tumor morphological shape can be calculated. FDG-PET/CT analysis can provide many parameters related to morphology or intratumoral characteristics as mentioned above and are also considered to provide useful information for the prediction of treatment outcome as one of imaging biomarker. Some of these parameters may predict the treatment outcome with high diagnostic accuracy.

The aim of this study was to investigate the utility of various semi-quantitative FDG uptake parameters as prognostic factors for patients with nasal- or paranasal-cavity SCC receiving curative super-selective arterial infusion with concomitant radiotherapy.

Methods

Study subjects

Our institutional review board approved this retrospective study protocol, and written informed consent was waived. Twenty-four patients with nasal or paranasal cavity SCC who were treated at our hospital from April 2009 to August 2012 were evaluated. All patients fulfilled the following inclusion criteria: (I) histopathological diagnosis of nasal or paranasal SCC; (II) completion of curative radiotherapy with 70-Gy radiation dose; and (III) availability of pre-treatment FDG-PET/CT data with the specific scan units. All patients were treated using the following protocol: arterial cisplatin infusion (100–120 mg/m^2 per week for 4 weeks) by microcatheter in the feeding arteries of the primary tumor, with concurrent radiation therapy (total 70 Gy/35 fractions). All patients received FDG/PET-CT scans before the full course of treatment.

Clinical assessment

For determination of the final clinical assessment (local control or local failure at the primary lesion), the medical records of patients over the follow-up period were utilized. Local failure was determined by (I) presence of SCC diagnosed by histopathological analysis of surgically resected or biopsy samples, (II) new soft tissue mass development around the post-treatment granulation tissue, or (III) definite enlargement of granulation tissue area during the follow-up. Local control was determined by histopathological diagnosis of the complete absence of SCC in resected tissue, the absence of new lesion development or the enlargement of soft-tissue mass in the post-treatment granulation tissue, during a follow-up of ≥2 years.

Imaging protocol

Image acquisition was performed using a PET/CT scanner (Biograph 64, Asahi-Siemens Medical Technologies, Tokyo). The patients were instructed to fast for ≥6 h before the FDG (4.5 MBq/kg) injection. After the injection, the patients were asked to sit quietly for 60 min. The 425–650 keV of energy window, 58.5 and 21.6 cm of the transaxial and axial fields of view (FOVs) were respectively used for scanning. The 3D-mode emission scan was acquired over 3-min for each bed position. The attenuation correction was performed with X-CT images that were obtained without contrast agent. An iterative technique integrated

with a point spread function (i.e., TrueX) was used for the image reconstruction (14). We conducted the full 3D PET reconstruction with a system matrix derived from point-source measurements. The details of the reconstructed image resolution were as follows: spatial resolution, 8.4 mm full width at half maximum (FWHM); matrix size, 168×168; voxel size, 4.1 mm × 4.1 mm × 2.0 mm. The SUV was calculated as the tissue radioactivity concentration (kBq/mL) divided by the injected dose per body weight (kBq/g) according to the commonly used definition (15).

Image analysis

For the semi-quantitative evaluation of the FDG uptake in the primary tumor, we examined both morphological and intratumoral-characteristic data. Image analyses were performed by a board certified radiologist (Noriyuki Fujima) with 11 years of experience in head and neck radiology. In each tumor, we measured the SUV value with the delineation of the tumor region of interest (ROI). As the tumor ROI, we used the automated ROI determined using the isocontour threshold method. We used an SUV value of 2.5 to define the lesion contouring margins as described in a previous report (16). In addition, another ROI delineation threshold that was adopted in a previous study (=42% of the maximum SUV in the tumor) (17) was also used to validate the measured quantitative parameter values (see the description of the statistical analysis below). When the tumor extended to two or more slices, all slices showing tumor FDG uptake were analyzed. In all patients, both routine CT and magnetic resonance imaging (MRI) data were also used as supplemental information to determine the presence and location of each tumor on FDG-PET/CT images.

For the morphological characteristics analysis, we calculated the tumor volume and tumor surface area from the morphological shape of all selected tumor voxels with an SUV value above 2.5. Sphericity was calculated by a partial modification of the previously reported equations as follows (18,19):

$$Sphericity = \frac{TV}{(1/6)*\sqrt{\frac{TSA^3}{\pi}}}$$

where TV is the tumor volume and TSA is the tumor surface area. The sphericity was defined as the actually measured tumor volume (TV) divided by the calculated volume of the sphere whose surface area was TSA.

For the analysis of intratumoral characteristics, the SUVmean, SUVmax, histogram and textural parameters within the ROI were calculated. SUVmean and SUVmax were respectively calculated as the mean and maximum values in all pixels in all slices in which the tumor was included. The histogram features included the coefficient of variance (CV), kurtosis and skewness. Textural features included the contrast, correlation, energy and homogeneity, calculated based on the gray-level co-occurrence matrix (GLCM) features. The GLCM features comprise detailed information regarding the spatial distribution of signal intensity in the tumor ROI, compared to the histogram parameters. The GLCM is composed of a square plane with rows and columns from zero to the maximum value of the gray scale in the tumor ROI. The GLCM element in row i and column j represents the number of times a given gray tone of value i is horizontally adjacent to gray tone j in the original quantized image. For the sake of simplicity the GLCMs were calculated using only directly adjacent pixels. Details of the GLCM features and the calculation equations have been described previously (20). Histogram or texture parameters were calculated from all pixels in all tumor-containing slices; all pixel data were integrated into a single histogram profile or single GLCM feature map to evaluate the whole volume intratumoral characteristics. In addition, TLG was also calculated by multiplying the tumor volume and mean SUV value. Finally, all parameters of morphological features, SUVmax, SUVmean, histogram parameters, textural parameters, and TLG were calculated for each tumor. The calculation process was performed using a self-developed program written in MATLAB ver. 2012a (MathWorks, Natick, MA).

Statistical analysis

In the univariate analysis, we used the Mann-Whitney U-test to compare the values of a total of 13 parameters (SUVmean, SUVmax, CV, TLG, kurtosis, skewness, contrast, correlation, energy, homogeneity, tumor volume, surface area and sphericity) between the local control and failure groups in their primary site. If a significant difference was obtained for any parameter, such parameter was analyzed by receiver operating characteristic (ROC) curves for the calculation of the area under the curve (AUC). The sensitivity, specificity, positive predictive value, negative predictive value and diagnostic accuracy by the cut-off value obtained with the Youden index were respectively determined. If a significant difference was observed for more

Table 1 Patient characteristics

Characteristics	Number of patients
Age (years)	
Range	43–72
Median	61
Average	60.1
Gender	
Male	21
Female	3
T-stage	
T1	0
T2	1
T3	8
T4a	14
T4b	1
N-stage	
N0	21
N1	2
N2	1
N3	0
Clinical TNM-stage	
I	0
II	1
III	8
IV	15

than two parameters in univariate analysis, these parameters were further analyzed by multivariate logistic regression models to determine whether they had independent predictive value. Additionally, if at least one parameter was determined to be an independent predictor, this parameter was further analyzed for its correlation to T-stage, N-stage and other quantitative FDG-PET/CT parameters assessed in the current study, by using Spearman's rank correlation coefficient.

For the validation of parameter value and its diagnostic power, each independent predictor revealed by multivariate logistic regression analysis was re-calculated using a different ROI delineation method with a threshold that was 42% of maximum SUV as described above. The Intraclass Correlation Coefficient (ICC) of parameter values obtained by ROIs between the SUV threshold of 2.5 and 42% of maximum SUV was calculated. The Mann-Whitney U-test and ROC curve analysis were also respectively performed to assess the local control and failure groups in a manner similar to that described above, by using the parameter values obtained by ROIs with an SUV threshold of 42% in maximum SUV.

Statistical significance was set at P values <0.05. We used SPSS software (IBM, Armonk, NY) for the statistical analyses.

Results

The patient characteristics are summarized in *Table 1*. Among the 24 patients, 7 were revealed to have local failure. The local failure of 5 patients was confirmed by histopathological findings. The remaining 2 cases of local failure and 17 cases of local control were confirmed by clinical diagnosis with reference to our hospital medical records over the follow-up period (mean 70 months; range 49–82 months).

All parameters were successfully obtained for each primary site. For two of the parameters, surface area and sphericity, significant differences between the local control and failure groups were respectively revealed in univariate analysis. Details of all obtained parameters and univariate analyses are presented in *Table 2*. These two parameters of the surface area and sphericity were further assessed by ROC curve analysis. Diagnostic values (the AUC, sensitivity, specificity, positive predictive value, negative predictive value, accuracy and cut-off value) for the prediction of the treatment outcome were determined. The details of the ROC curve analysis are presented in *Table 3*. The parameter with the highest AUCs was the sphericity.

In the multivariate analyses, the sphericity was revealed to be an independent predictor (P=0.03) with an odds ratio of 2.58 (the 95% confidence intervals ranged from 1.37 to 6.74) (*Table 3*). Representative cases of local control and failure are presented in *Figure 1*. The Spearman's rank correlation coefficients between the sphericity and patient characteristics (T-stage and N-stage) or other 12 quantitative parameters are summarized in *Table 4*.

In the validation analysis using a different tumor ROI technique, the sphericity was found to be significantly different between patients with local control and failure by the Mann-Whitney U-test (P=0.005). The results of ROC curve analysis were as follows: AUC =0.87, sensitivity =0.82, specificity =1.0, positive predictive value =1.0, negative

Table 2 Patient characteristics and parameters of the patients with local control and failure

Variables	Presence of local control		P value
	Local control	Local failure	
Patients' characteristics (no. of patients)			
T-stage			0.08
T1	0	0	
T2	1	0	
T3	7	1	
T4	9	6	
N-stage			0.86
N0	15	6	
N1	1	1	
N2	1	0	
N3	0	0	
Image parameters (parameter value)			
SUVmean	7.6±2.2	7.5±1.3	0.99
SUVmax	19.3±6.1	18.3±3.6	0.63
CV	0.43±0.11	0.38±0.11	0.34
TLG	274.5±184.3	326.1±112.9	0.39
Skewness	0.85±0.75	0.84±0.52	0.96
Kurtosis	3.7±3.57	3.83±2.75	0.92
Contrast	6.64±2.78	6.85±2.69	0.86
Correlation	0.63±0.11	0.63±0.06	0.8
Energy	0.023±0.011	0.027±0.018	0.68
Homogeneity	0.45±0.06	0.46±0.05	0.72
Tumor volume	33.2±16.7	42.5±9.4	0.09
Tumor surface area	97.8±29.8	143.3±36.5	0.01*
Sphericity	0.35±0.06	0.27±0.05	0.002*

Data are the mean ± standard deviation. *, statistically significant difference. SUV, standardized uptake value; CV, coefficient of variance; TLG, total lesion glycolysis.

predictive value =0.7, accuracy =0.88 and optimal cut-off value =0.35. Only cut-off value was slightly different from the result obtained by the tumor ROI with SUV threshold 2.5. The ICC of the sphericity values obtained by ROIs between the SUV threshold of 2.5 and 42% of maximum SUV was 0.93.

Discussion

In the current study, the semi-quantitative morphological parameter of sphericity was revealed to be a clinically useful predictor of treatment outcome in patients with nasal- or paranasal-cavity SCC. The difficulty of using pretreatment parameters to predict treatment outcome in advanced-stage SCC patients receiving curative chemoradiation with arterial cisplatin infusion has been demonstrated, although a few reports have described the utility of tumor blood flow or tumor micro-water diffusion as an evaluation tool during treatment using MRI (21,22). The results of the current study will provide supporting information for the prediction of treatment outcome; this information can be used for the adjustment of treatment regimens such as the addition of induction chemotherapy before curative therapy consisting of chemotherapy and concomitant full-dose radiotherapy, or the determination of a follow-up strategy after the treatment. In this way, the information gained from quantitative morphological parameters could lead to more appropriate personalized medicine in patients with nasal- or paranasal-cavity SCC.

The quantitative morphological characteristic of tumor sphericity is considered to reflect the tumor's complicated shape. In the case of an invasive tumor with a complicated shape, the feeding arteries tend to be multi-feeders compared to the simple expanding oval- or round-shape SCC, and this may make the arterial infusion therapy more complicated and difficult. FDG-PET/CT can easily visualize the rough shape of such anatomically complicated tumor by setting a specific SUV threshold. In contrast to

Table 3 ROC and multivariate analysis results

Parameter	The results of ROC curve analysis							The results of multivariate analysis	
	AUC	Sensitivity	Specificity	PPV	NPV	Accuracy	Cut-off value	P value	Odds ratio
Surface area	0.83	0.82	0.71	0.88	0.63	0.79	130	0.31	1.21 (0.87, 1.55)
Sphericity	0.87	0.82	1.0	1.0	0.7	0.88	0.31	0.03	2.58 (1.37, 6.74)

AUC, area under curve; PPV, positive predictive value; NPV, negative predictive value.

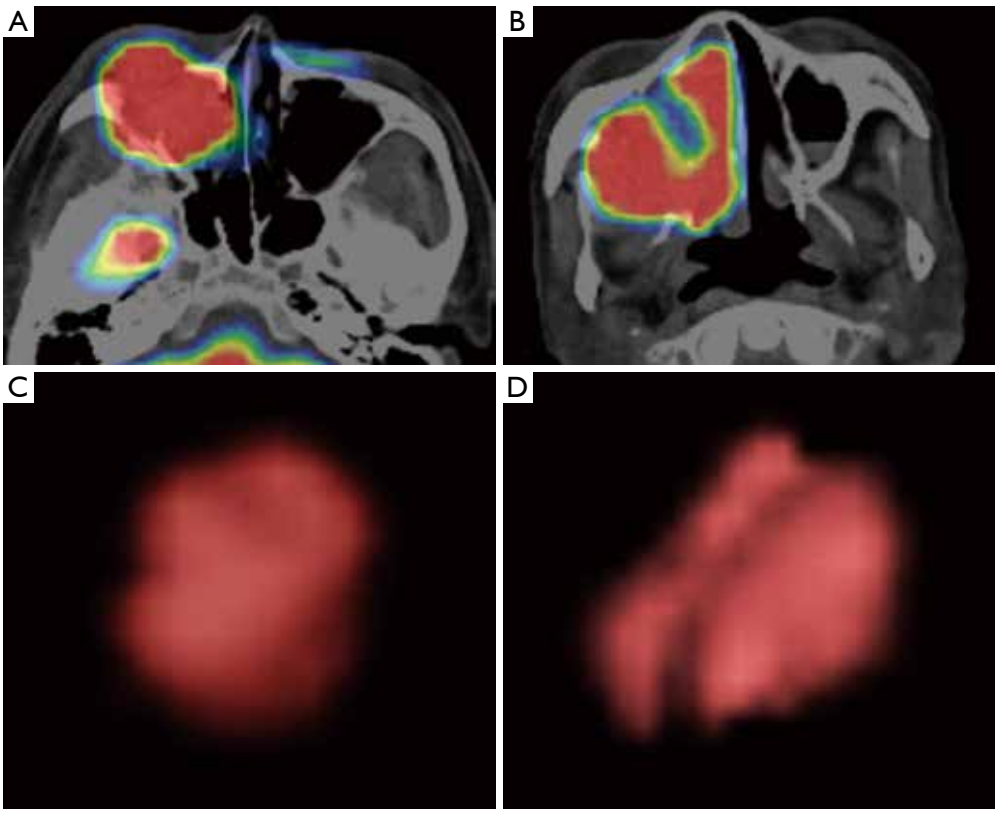

Figure 1 Representative cases of local control and failure. Pretreatment FDG-PET/CT fusion images from cases with local control (A) and failure (B) are shown. The volume rendering of FDG uptake in a lesion (SUV of upper 2.5, front view) from a patient with local control (C) had a less complicated shape compared to that of patient with treatment failure (D). The sphericities of the local control and failure cases were 0.43 and 0.29, respectively.

the parameter of sphericity, tumor volume was higher in the poor-treatment-outcome group, but not significantly so (P value =0.09). From the results of the current study, although tumor volume is generally believed to be a prognostic factor in numerous cancers, including head and neck SCC (23), quantitative information about tumor shape may be more sensitive for the prediction of treatment outcome. In addition, several previous reports have described that the tumor morphological parameter known as "asphericity" was useful as a prognostic factor in patients with HNSCC (24,25). Although their study population was somewhat heterogeneous (including primary sites of naso-, oro-, hypo-pharynx, lip and oral cavity) and did not include patients with nasal and paranasal cavity SCC, the parameter of quantitative tumor shape may be used for most HNSCC patients regardless of the primary site, by integrating the results of the current study and the previous reports described above.

Tumor heterogeneity was not found to be a prognostic factor in the current study. In several previous reports, the parameter of intratumoral heterogeneity was indicated to be a prognostic factor in advanced T-stage oropharyngeal SCC patients (10); higher intratumoral heterogeneity predicted a worse prognosis. The explanation of this discrepancy between studies is not straightforward. We speculated that the difference in treatment regimens—i.e., arterial infusion of cisplatin with concomitant radiotherapy versus systemic chemoradiation may have played a role, but we emphasize that this is only our supposition. In addition, the biological characteristics of oropharyngeal and maxillary cancer are slightly different (26) and may have led to the different results related to the intratumoral heterogeneity as a predictor of treatment outcome.

The current study has several limitations. First, the number of patients was very small. However, the patient population with nasal or paranasal SCC is generally rather

Table 4 Spearman's rank correlation coefficient to the sphericity

Variables	Correlation coefficient
T-stage	−0.32
N-stage	−0.19
SUVmean	−0.07
SUVmax	−0.2
CV	0.23
TLG	−0.17
Skewness	0.15
Kurtosis	0.07
Contrast	−0.11
Correlation	0.21
Energy	−0.24
Homogeneity	−0.28
Tumor volume	−0.21
Tumor surface area	−0.53
Sphericity	1

small. Second, analyses of correlations to other biological factors such as human papillomavirus (HPV) status or tumor histological grade were not performed. To address these limitations, further additional follow-up studies will be needed.

In conclusion, quantitative morphological evaluation of nasal or paranasal SCC by sphericity was indicated to be useful for the prediction of treatment outcome. This parameter could contribute to the appropriate tailoring of treatment strategy for patients with nasal or paranasal SCC.

Acknowledgements

None.

Footnote

Conflicts of Interest: The authors have no conflicts of interest to declare.

Ethical Statement: Our institutional review board approved this retrospective study protocol, and written informed consent was waived.

References

1. Wong SJ, Harari PM, Garden AS, Schwartz M, Bellm L, Chen A, Curran WJ, Murphy BA, Ang KK. Longitudinal Oncology Registry of Head and Neck Carcinoma (LORHAN): analysis of chemoradiation treatment approaches in the United States. Cancer 2011;117:1679-86.
2. Kimata Y, Uchiyama K, Ebihara S, Saikawa M, Hayashi R, Haneda T, Ohyma W, Kishimoto S, Asai M, Nakatsuka T, Harii K. Postoperative complications and functional results after total glossectomy with microvascular reconstruction. Plast Reconstr Surg 2000;106:1028-35.
3. Homma A, Oridate N, Suzuki F, Taki S, Asano T, Yoshida D, Onimaru R, Nishioka T, Shirato H, Fukuda S. Superselective high-dose cisplatin infusion with concomitant radiotherapy in patients with advanced cancer of the nasal cavity and paranasal sinuses: a single institution experience. Cancer 2009;115:4705-14.
4. Homma A, Sakashita T, Yoshida D, Onimaru R, Tsuchiya K, Suzuki F, Yasuda K, Hatakeyama H, Furusawa J, Mizumachi T, Kano S, Inamura N, Taki S, Shirato H, Fukuda S. Superselective intra-arterial cisplatin infusion and concomitant radiotherapy for maxillary sinus cancer. Br J Cancer 2013;109:2980-6.
5. Rohren EM, Turkington TG, Coleman RE. Clinical applications of PET in oncology. Radiology 2004;231:305-32.
6. Kitagawa Y, Sano K, Nishizawa S, Nakamura M, Ogasawara T, Sadato N, Yonekura Y. FDG-PET for prediction of tumour aggressiveness and response to intra-arterial chemotherapy and radiotherapy in head and neck cancer. Eur J Nucl Med Mol Imaging 2003;30:63-71.
7. Higgins KA, Hoang JK, Roach MC, Chino J, Yoo DS, Turkington TG, Brizel DM. Analysis of pretreatment FDG-PET SUV parameters in head-and-neck cancer: tumor SUVmean has superior prognostic value. Int J Radiat Oncol Biol Phys 2012;82:548-53.
8. Taghipour M, Sheikhbahaei S, Marashdeh W, Solnes L, Kiess A, Subramaniam RM. Use of 18F-Fludeoxyglucose-Positron Emission Tomography/Computed Tomography for Patient Management and Outcome in Oropharyngeal Squamous Cell Carcinoma: A Review. JAMA Otolaryngol Head Neck Surg 2016;142:79-85.
9. Moon SH, Choi JY, Lee HJ, Son YI, Baek CH, Ahn YC, Park K, Lee KH, Kim BT. Prognostic value of 18F-FDG PET/CT in patients with squamous cell carcinoma of the tonsil: comparisons of volume-based metabolic parameters. Head Neck 2013;35:15-22.

10. Cheng NM, Fang YH, Lee LY, Chang JT, Tsan DL, Ng SH, Wang HM, Liao CT, Yang LY, Hsu CH, Yen TC. Zone-size nonuniformity of 18F-FDG PET regional textural features predicts survival in patients with oropharyngeal cancer. Eur J Nucl Med Mol Imaging 2015;42:419-28.
11. Wang HM, Cheng NM, Lee LY, Fang YH, Chang JT, Tsan DL, Ng SH, Liao CT, Yang LY, Yen TC. Heterogeneity of (18)F-FDG PET combined with expression of EGFR may improve the prognostic stratification of advanced oropharyngeal carcinoma. Int J Cancer 2016;138:731-8.
12. Chan SC, Cheng NM, Hsieh CH, Ng SH, Lin CY, Yen TC, Hsu CL, Wan HM, Liao CT, Chang KP, Wang JJ. Multiparametric imaging using 18F-FDG PET/CT heterogeneity parameters and functional MRI techniques: prognostic significance in patients with primary advanced oropharyngeal or hypopharyngeal squamous cell carcinoma treated with chemoradiotherapy. Oncotarget 2017;8:62606-21.
13. Fujima N, Sakashita T, Homma A, Hirata K, Shiga T, Kudo K, Shirato H. Glucose Metabolism and Its Complicated Relationship with Tumor Growth and Perfusion in Head and Neck Squamous Cell Carcinoma. PLoS One 2016;11:e0166236.
14. Panin VY, Kehren F, Michel C, Casey M. Fully 3-D PET reconstruction with system matrix derived from point source measurements. IEEE Trans Med Imaging 2006;25:907-21.
15. Sato J, Kitagawa Y, Yamazaki Y, Hata H, Asaka T, Miyakoshi M, Okamoto S, Shiga T, Shindoh M, Kuge Y, Tamaki N. Advantage of FMISO-PET over FDG-PET for predicting histological response to preoperative chemotherapy in patients with oral squamous cell carcinoma. Eur J Nucl Med Mol Imaging 2014;41:2031-41.
16. Chang KP, Tsang NM, Liao CT, Hsu CL, Chung MJ, Lo CW, Chan SC, Ng SH, Wang HM, Yen TC. Prognostic significance of 18F-FDG PET parameters and plasma Epstein-Barr virus DNA load in patients with nasopharyngeal carcinoma. J Nucl Med 2012;53:21-8.
17. Lim R, Eaton A, Lee NY, Setton J, Ohri N, Rao S, Wong R, Fury M, Schöder H. 18F-FDG PET/CT metabolic tumor volume and total lesion glycolysis predict outcome in oropharyngeal squamous cell carcinoma. J Nucl Med 2012;53:1506-13.
18. Dhara AK, Mukhopadhyay S, Saha P, Garg M, Khandelwal N. Differential geometry-based techniques for characterization of boundary roughness of pulmonary nodules in CT images. Int J Comput Assist Radiol Surg 2016;11:337-49.
19. Nagano N, Matsuo T, Itoh T, Tomonari K, Shiraishi J. Development of a computer-aided diagnosis system for the distinction between benign and malignant gastric lesions. Nihon Hoshasen Gijutsu Gakkai zasshi 2012;68:1474-85.
20. Dang M, Lysack JT, Wu T, Matthews TW, Chandarana SP, Brockton NT, Bose P, Bansal G, Cheng H, Mitchell JR, Dort JC. MRI texture analysis predicts p53 status in head and neck squamous cell carcinoma. AJNR Am J Neuroradiol 2015;36:166-70.
21. Fujima N, Yoshida D, Sakashita T, Homma A, Tsukahara A, Tha KK, Kudo K, Shirato H. Usefulness of Pseudocontinuous Arterial Spin-Labeling for the Assessment of Patients with Head and Neck Squamous Cell Carcinoma by Measuring Tumor Blood Flow in the Pretreatment and Early Treatment Period. AJNR Am J Neuroradiol 2016;37:342-8.
22. Fujima N, Yoshida D, Sakashita T, Homma A, Tsukahara A, Shimizu Y, Tha KK, Kudo K, Shirato H. Prediction of the treatment outcome using intravoxel incoherent motion and diffusional kurtosis imaging in nasal or sinonasal squamous cell carcinoma patients. Eur Radiol 2017;27:956-65.
23. Strongin A, Yovino S, Taylor R, Wolf J, Cullen K, Zimrin A, Strome S, Regine W, Suntharalingam M. Primary tumor volume is an important predictor of clinical outcomes among patients with locally advanced squamous cell cancer of the head and neck treated with definitive chemoradiotherapy. Int J Radiat Oncol Biol Phys 2012;82:1823-30.
24. Apostolova I, Steffen IG, Wedel F, Lougovski A, Marnitz S, Derlin T, Amthauer H, Buchert R, Hofheinz F, Brenner W. Asphericity of pretherapeutic tumour FDG uptake provides independent prognostic value in head-and-neck cancer. Eur Radiol 2014;24:2077-87.
25. Hofheinz F, Lougovski A, Zöphel K, Hentschel M, Steffen IG, Apostolova I, Wedel F, Buchert R, Baumann M, Brenner W, Kotzerke J, van den Hoff J. Increased evidence for the prognostic value of primary tumor asphericity in pretherapeutic FDG PET for risk stratification in patients with head and neck cancer. Eur J Nucl Med Mol Imaging 2015;42:429-37.
26. Dok R, Nuyts S. HPV Positive Head and Neck Cancers: Molecular Pathogenesis and Evolving Treatment Strategies. Cancers (Basel) 2016;8(4).

Cite this article as: Fujima N, Hirata K, Shiga T, Yasuda K, Onimaru R, Tsuchiya K, Kano S, Mizumachi T, Homma A, Kudo K, Shirato H. Semi-quantitative analysis of pre-treatment morphological and intratumoral characteristics using ^{18}F-fluorodeoxyglucose positron-emission tomography as predictors of treatment outcome in nasal and paranasal squamous cell carcinoma. Quant Imaging Med Surg 2018;8(8):788-795. doi: 10.21037/qims.2018.09.09

Original Article

Percutaneous ultrasound-guided balloon-assisted embolization of iatrogenic femoral artery pseudoaneurysms with Glubran®2 cyanoacrylate glue: safety, efficacy and outcomes

Loïc Griviau[1], Olivier Chevallier[1], Clément Marcelin[2], Motoki Nakai[3], Lorenzo Pescatori[1], Christophe Galland[1], Marco Midulla[1], Nicolas Falvo[1], Romaric Loffroy[1]

[1]Department of Vascular and Interventional Radiology, Image-Guided Therapy Center, François-Mitterrand University Hospital, Dijon, France; [2]Department of Diagnostic and Therapeutic Imaging, Pellegrin University Hospital, Bordeaux, France; [3]Department of Radiology, Wakayama Medical University, Wakayamashi, Japan

Correspondence to: Prof. Romaric Loffroy, MD, PhD. Department of Vascular and Interventional Radiology, Image-Guided Therapy Center, François-Mitterrand University Hospital, 14 Rue Paul Gaffarel, BP 77908, 21079 Dijon Cedex, France. Email: romaric.loffroy@chu-dijon.fr.

Background: Femoral pseudoaneurysm (PA) is a frequent complication of arterial access for endovascular procedures. Surgery has traditionally been considered as the gold standard of therapy. We aimed to report our experience of percutaneous ultrasound (US)-guided balloon-assisted embolization with cyanoacrylate glue for the treatment of iatrogenic femoral PAs.

Methods: Retrospective two-center study of patients with femoral iatrogenic PAs treated by N-butyl cyanoacrylate-methacryloxy sulfolane (NBCA-MS) Glubran®2 glue embolization between July 2013 and November 2017. All patients underwent contralateral arterial access with balloon placement of an appropriate size in front of the PA neck before glue/lipiodol embolization in a 1:1 ratio by percutaneous US-guided puncture of the aneurysmal sac under fluoroscopy control.

Results: Twenty-three patients (12 females, 11 males; median age, 79 years; range, 18–93 years) were included. Median PA size was 34 mm (range, 17–60 mm). The median time to treatment was 5 days (range, 1–30 days). Twenty patients (86.9%) were successfully treated by glue injection alone. The three remaining patients (13.1%) with persistent PA or associated arterial-venous fistula were immediately treated during the same procedure by additional stent-graft. Then, overall immediate and 1-month clinical success rates were 100%. No surgical conversion was necessary. No recurrence was reported during the median follow-up of 11 months (range, 2–73 months). Two (8.7%) puncture-related complications occurred at the contralateral arterial access site, which spontaneously resolved. No non-target glue embolization occurred.

Conclusions: US-guided balloon-assisted glue embolization is safe and effective to treat iatrogenic femoral PAs in most cases, offering complete exclusion of the PA and avoiding the morbidity of open surgery.

Keywords: Pseudoaneurysm (PA); femoral artery; embolization; cyanoacrylate glue; access site complication

Submitted Sep 03, 2018. Accepted for publication Sep 12, 2018.
doi: 10.21037/qims.2018.09.12
View this article at: http://dx.doi.org/10.21037/qims.2018.09.12

Introduction

Iatrogenic pseudoaneurysm (PA) is a classical complication of arterial percutaneous diagnostic angiography or interventional procedures which occurs in 0.2–2.6% of cases (1,2).

Several therapeutic options have been described for the treatment of PAs, including surgery, ultrasound (US)-guided compression, coil embolization, stent-graft placement, or percutaneous thrombin injection. US-guided compression is effective in a large proportion of patient but is associated

with pain and discomfort (3-6). Thrombin injection is more effective but at risk of distal spillage in limb arteries and anaphylaxis. Furthermore, thrombin is quite expensive (5-7) and not available everywhere. Surgical interventions are more invasive but still have a role to play in case of failure of others techniques or in patients presenting with mass effect (8).

N-butyl cyanoacrylate methacryloxy sulfolane (NBCA-MS) is a well-known glue comprising a proprietary comonomer as approved by the European Community for internal human use (9,10). This synthetically derived glue shows rapid polymerization (1–5 s), but complete sealing occurs in approximately 5 min. Additionally, NBCA-MS presents high echogenicity and for this reason it is easily detectable by US when injected in vessels or tissues. Lastly, the efficacy of glue is not affected by anticoagulant or antiplatelet therapy. Aytekin *et al.* (11) first described the use of glue injection as first-line therapy of iatrogenic PAs and Del Corso *et al.* (12) reported a high success rate of microinjections of cyanoacrylate glue after US-guided PAs compression. However, the main risk of glue injection by direct puncture of a pulsating femoral mass is distal spillage of glue in the native artery through the pseudoaneurysmal neck (13). To minimize such complications, US-guided compression of the PA's neck before NBCA-MS injection into the sac may be performed but remains difficult, and is often times ineffective and painful because of the presence of hematoma. Percutaneous US-guided glue injection into the sac with a balloon-assisted technique might be a good option in order to avoid distal spillage of glue in limb arteries.

In this study, we evaluated the safety, efficacy and utility of direct percutaneous injection of NBCA-MS with balloon occlusion for embolization of iatrogenic femoral PAs.

Methods

Study population

Retrospective study of 23 iatrogenic PAs treated with percutaneous US-guided balloon-assisted NBCA-MS glue embolization in 23 consecutive patients between July 2013 and November 2017 in two tertiary centers. Inclusion criteria were the presence of post-arterial catheterization iatrogenic PA at the femoral puncture site, whatever the size of the sac, after failed or contraindicated US-guided compression, or not.

Due to the retrospective nature of this study, our Ethics Committee waived the requirement for informed patient consent.

Imaging evaluation

In all 23 patients, the diagnosis of PA was confirmed by color Doppler US. For each lesion, the size of the aneurysmal sac was measured and the relationship to the artery from which it originated was noted. Pre-procedural US evaluation also included assessment of the neck length, PA chamber diameter, presence of arteriovenous fistula, and diameter of the native artery.

Embolization procedure

All patients underwent diagnostic angiography under local anesthesia by contralateral femoral approach through a long 45 cm × 6.0-French sheath (Terumo, Tokyo, Japan) by crossover technique. Selective cannulation of the feeding artery was then performed. A 0.035" Mustang™ balloon dilatation catheter of appropriate size (5 to 7 mm in diameter, 4 cm in length) (Boston Scientific, San Jose, CA) was inflated in front of the PA neck to prevent distal embolization due to escape of the material from the aneurysmal cavity. No heparin was given during the procedure. After local anesthesia just superficial to the PA, US-guided puncture of the PA sac was performed with a 17-G metallic needle previously flushed with 5% dextrose solution, and already connected to a 5 mL luer-lock syringe loaded with a 1:1 ratio mixture of NBCA-MS (Glubran®2, General Enterprise Marketing, Viareggio, Italy) and Lipiodol® Ultra-Fluide (Guerbet, Aulnay-sous-Bois, France). Then, injection of the mixture into the aneurysmal cavity was slowly performed under fluoroscopy guidance to visualize the glue distribution until complete filling of the sac (*Figure 1*). The glue was allowed to polymerize for a few seconds after injection, and then the needle was withdrawn. Overall, 1.5 to 5 mL of the mixture was injected for each patient. Balloon catheter was remained inflated for 3 minutes after injection to allow complete and definitive polymerization of NBCA-MS. Effectiveness of the procedure was assessed by arteriogram. If the PA sac was not totally filled by glue with persistent perfusion, further injections were administered, repeating each step above until complete occlusion was achieved. Since the needle became blocked with glue each time, a new one was used for each injection. In case of impossibility to totally exclude the lesion despite several injections for anatomical reasons, a Viabahn® stent-graft (W.L. Gore & Associates, Newark, DE) was then deployed in front of the PA neck during the same procedure. A FemoSeal™ (Terumo) or AngioSeal™

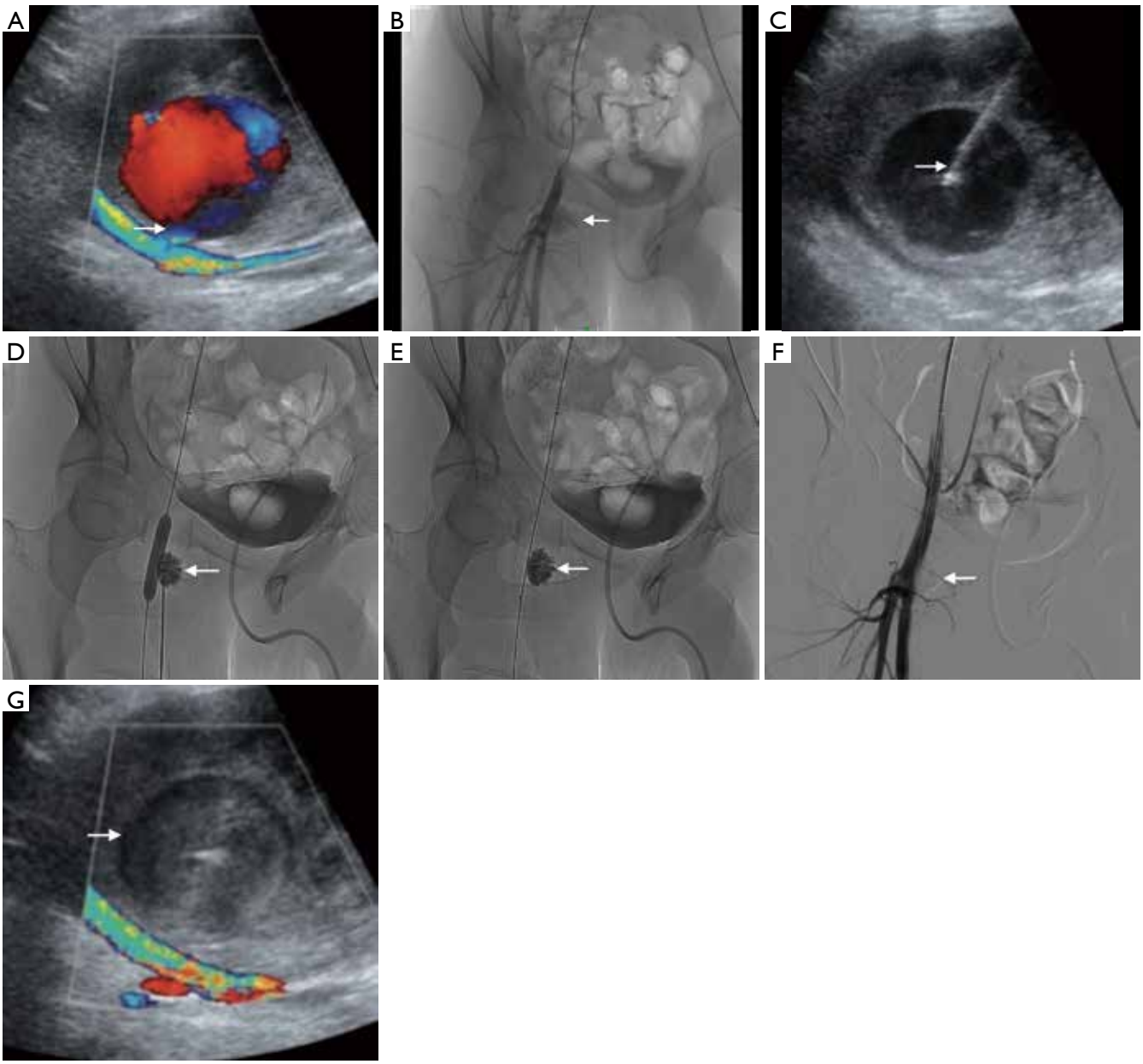

Figure 1 Example of a 62-year-old man who developed a pulsatile mass with pain and groin hematoma 2 days after coronary angioplasty. (A) Color-Doppler US at the groin puncture site showed a 23 mm × 13 mm PA arising from the right proximal superficial femoral artery. The PA had 1 lobe and its neck is well seen (arrow); (B) arteriography by crossover from the left side confirmed the PA from the superficial femoral artery (arrow); (C) the PA sac was then punctured under US guidance with a 17-G metallic needle with hyperechoic tip (arrow); (D) after inflating a Mustang™ balloon of 7 mm in diameter in the parent artery in front of the PA neck to avoid reflux, a mixture of NBCA-MS (Glubran®2) and Lipiodol Ultra-Fluide in a ratio of 1:1 was injected into the PA sac under fluoroscopy control until complete filling of the PA (arrow); (E) image after deflating easily the balloon showed, 3 minutes after the end of glue injection, showed no glue migration (arrow); (F) angiographic control after gluing demonstrated complete embolization of the PA (arrow) and confirmed patency of the parent artery; (G) Color-Doppler images obtained 1 day after the procedure confirmed that the absence of flow in the thrombosed PA sac and complete exclusion of the lesion (arrow). US, ultrasound; PA, pseudoaneurysm; NBCA-MS, N-butyl cyanoacrylate-methacryloxy sulfolane.

(St. Jude Medical) vascular closure device was systematically used at the contralateral femoral puncture site. Color-Doppler US examination was performed at 1 day and again at 1, 3, and 12 months after the procedure.

Data collection

In the framework of this study, we retrospectively collected each patient's demographic data, clinical presentation, underlying etiology and interventional data. Demographic data included age and gender, whereas interventional data included endovascular treatment, the nature of the procedure, the culprit embolized vessel, the angiographic success, the patency of the native artery, the US features at 1 day, the complications and recurrence within 1 month following the procedure.

Immediate success was defined as a complete occlusion of the targeted pseudoaneurysmal sac on final angiography. Primary clinical success was defined as immediate success with glue injection alone. Stent-assisted clinical success was defined as immediate success after glue injection and additional stent-graft placement. All complications were recorded and classified as minor or major complications according to the Society of Interventional Radiology classification system. Procedural time was measured from the induction of local anesthesia until the last glue injection.

Statistical analysis

Descriptive statistics and parameters, such as frequencies and percentages, were used and provided in order to accurately describe our experience regarding the embolization of PAs using Glubran®2. Values are presented as means ± SDs for variables with normal distribution.

Results

Patient characteristics

Twenty-three patients (12 females, 11 males; mean age, 73.0±13.4 years; range, 18–93 years) were treated with US-guided balloon-assisted NBCA-MS glue embolization in the present study. Mean time to treatment was 7.2±7.4 days (range, 1–30 days). Sixteen (69.6%) of the 23 patients had groin hematoma. Eleven patients (47.8%) were under anticoagulant therapy and twelve (52.2%) were under antiplatelet therapy. Common femoral artery, superficial femoral artery, and deep femoral artery were involved in 47.8%, 47.8%, and 4.3%, respectively. The mean PA size was 33.0±10.7 mm (range, 17–60 mm). Nineteen PAs had 1 lobe (82.6%), and four (17.4%) were polylobulate. Neck length ranged from 0 to 6 mm (mean, 2.1±1.7 mm). Characteristics of treated PAs are listed in *Table 1*.

None of the 23 patients presented with neuropathy or soft-tissue necrosis. In 1 case (4.3%), an arterial-venous fistula was associated with PA and treated with additional arterial stent-graft. The mean volume of glue injected per patient was 2.1±1.6 mL, but the amounts ranged from 1.5 to 5 mL. In 15 patients (65.2%), the PAs were successfully occluded with a single injection. The other 8 lesions required additional glue injections (range, 2–4). Needle occlusion occurred in 2 cases (8.7%) and required needle substitution.

Procedural outcomes

Mean time of treatment was 41.8±18.9 min (range, 17–87 min). Twenty (86.9%) of the 23 PAs were successfully treated with glue injection alone. The three remaining patients (13.1%) required additional arterial stent-graft placement because of incomplete occlusion of the sac despite several injections (2 patients) or because of the presence of an arterial-venous fistula associated with PA (1 patient). Stent-graft was placed in the common femoral artery in 2 patients and in the superficial femoral artery in 1 patient, without compromising the deep femoral artery patency. All the PAs were finally occluded 1 day after the procedure and the 1-month clinical success was 100%. None of the patients developed recurrence in 2–73 months (mean, 15.4±15.2 months). In all cases, Doppler US confirmed that the patency of the femoral artery immediately after and 1 day after the procedure. Two patients (9%) complained of temporary mild pain after the intervention, successfully managed with symptomatic analgesic treatment. Outcomes of embolization are reported in *Table 2*.

Complications

All procedures were performed under local anesthesia, with no need for anesthesiology support. No distal spillage of glue or thrombotic material in the native artery or limb arteries was noted during or after the procedure. No bleeding, non-target glue embolization or leakage through the balloon, native artery stenosis or thrombosis, allergic reaction, infection, skin ischemia, or PA rupture were observed.

Table 1 Characteristics of treated pseudoaneurysms in 23 patients

Variable	No. (%)
Age (years)	
Mean ± SD	73.0±13.4
Median [range]	79 [18–93]
Sex	
Female	12 (52.2)
Male	11 (47.8)
Time to treatment (days)	
Mean ± SD	7.2±7.4
Median [range]	5 [1–30]
Symptomatic	
No	7 (30.4)
Yes	16 (69.6)
Anticoagulant therapy	
None	12 (52.2)
Preventive	4 (17.4)
Curative	7 (30.4)
Antiplatelet therapy	
None	11 (47.8)
Single	7 (30.4)
Double	5 (21.7)
Femoral artery involved	
Common femoral artery	11 (47.8)
Superficial femoral artery	11 (47.8)
Deep femoral artery	1 (4.3)
Femoral side involved	
Right side	20 (87.0)
Left side	3 (13.0)
Pseudoaneurysm feature	
Unilobate	19 (82.6)
Polylobate	4 (17.4)
Size of pseudoaneurysm chamber (mm)	
Mean ± SD	33.0±10.7
Median [range]	34 [17–60]
Size of pseudoaneurysm neck (mm)	
Mean ± SD	2.1±1.7
Median [range]	2 [0–6]
Diameter of the parent artery (mm)	
Mean ± SD	7.9±1.4
Median [range]	7 [6–12]

Table 2 Outcomes of embolization in 23 patients

Variable	No. (%)
Immediate success	23 (100.0)
Primary clinical success	20 (86.9)
Stent-assisted clinical success	23 (100.0)
One-day clinical success	23 (100.0)
One-month clinical success	23 (100.0)
Procedural time (min)	
Mean ± SD	41.8±18.9
Median [range]	36.5 [17–87]
Complications	
Minor	1 (4.3)
Major	1 (4.3)
Non-target glue embolization	0 (0)
One-day US patency of the parent artery	23 (100.0)
Hospital discharge (days)	
Mean ± SD	2.3±1.6
Median [range]	2.4 [1–5]
One-month mortality rate	
Related to the procedure	0 (0)
Unrelated to the procedure	1 (4.3)
Follow-up (months)	
Mean ± SD	15.4±15.2
Median [range]	11 [2–73]
Recurrence rate at mean follow-up	0 (0)
Residual inflammation at the puncture site	0 (0)

Balloon dilatation catheter was deflated in all patients without any issue as gluing or damage. No secondary surgical treatment was needed.

Minor complication occurred in 1 patient (4%) who had contralateral iatrogenic PA <5 mm at the femoral puncture site, but spontaneously resolved within 2 days, with no prolonged hospital stay. Major complication was reported in 1 other patient (4%) who presented a 6-cm groin hematoma at the contralateral femoral puncture. The patient needed prolonged hospital stay for surveillance but surgery was not required. One 73-year-old patient with several comorbidities died within 1 month from unrelated cause to the procedure.

Discussion

In the present study, US-guided balloon-assisted NBCA-MS glue injection alone into the aneurysmal sac proved to be safe and effective in the large majority of patients with iatrogenic femoral PAs.

Femoral artery PAs usually develop in the groin after catheterization for endovascular procedures. These lesions are more and more frequent due to the increasing number of angiographic procedures and patients who are on anticoagulant therapy. Natural history of PAs is spontaneous resolution within 2 weeks, at least for the smallest ones. However, waiting for spontaneous thrombosis may lead to longer hospital stay, decubitus complication and increased cost. Moreover, PAs are frequently symptomatic and source of discomfort for patients. For these reasons, the current trend is to treat PAs once diagnosed.

The gold standard treatment for PAs is surgery but it can lead to local complications and prolonged hospitalization. Several nonsurgical approaches have been then described. US-guided compression is an effective treatment for femoral PAs, with success rates of ranging from 70% to 90% in patients without anticoagulation therapy (14,15). Nevertheless, this method has significant limitations. It is painful and time-consuming (14,16-18). It also gives poorer results in patient who are taking anticoagulants. Lastly, this procedure may be impossible or challenging to perform in obese patients, and is usually uncomfortable for both patients and physicians. As an alternative, direct percutaneous embolization of the PA sac with different embolic materials has been reported. Thrombin is the most popular embolic agent used for percutaneous occlusion of femoral PAs because it causes fast and efficient thrombosis in the aneurysmal sac without filling it with foreign material (3,6,19-23). However, some complications may occur with this agent, including allergic reaction and distal thrombosis of the parent artery by leakage through the PA neck (24). Kurzawski *et al.* (7) prospectively studied 353 patients treated by thrombin injection and reported 53 (15%) arterial micro-embolizations and 1 (0.3%) pulmonary embolism in a case of concomitant arterial-venous fistula. Also, thrombin is not available everywhere, as is the situation in France, and is quite expensive.

NBCA glue is a potential alternative to thrombin but is rarely used for treating femoral PAs. Indeed, only two series have reported results of glue embolization for PAs by direct puncture of the sac (11,12). Aytekin *et al.* (11) employed the glue as an alternative to thrombin to induce thrombosis of the PA cavity. In contrast, Del Corso *et al.* (12) induced collapse of the PA chamber and then stuck its superior and inferior walls together with glue. They thus obtained the disappearance of the PA chamber. Regarding authorized glues, NBCA-MS (Glubran®2) is a well-known surgical glue in which NBCA is combined with another monomer, metacryloxysulpholane, to produce a more pliable and stable polymer whose milder exothermic reaction (45 ℃) results in less inflammation and histotoxicity than Histoacryl® or Trufill®, which are respectively not allowed for endovascular purpose and not available in Europe (24). Glubran2® has the advantage of offering fast and permanent embolization, independently of coagulation disorders. It has also the advantage of being cheap in comparison with thrombin. No allergic reaction has been described (25). NBCA-MS is naturally resorbed in soft tissue with time and does not act as foreign material like coils. However, the main risk of direct percutaneous embolization with NBCA glue is distal embolization due to escape of the material from the pseudoaneurysmal sac before it is completely polymerized. To prevent this complication, Aytekin *et al.* (11) and Del Corso *et al.* (12) compressed the neck of the PA with the US probe during injection, and held the probe in place until polymerization was complete. Indeed, it is important to make sure that the flow between the aneurysm and the parent artery is stopped by compression before injection of NBCA glue. However, the compression is often times impossible, painful or not sufficient to cease flow. In that case, NBCA should be used with balloon protection. This is the technique we used in the current study as first treatment of iatrogenic femoral artery PAs. In this technique, an insufflated balloon is placed in the vessel to occlude the neck of the PA and avoid reflux of glue into the native artery.

Finally, unlike the technique described by Del Corso *et al.* (12), we mixed cyanoacrylate glue with Lipiodol to make it radiopaque. Indeed, even if glue presents high echogenicity, it is radiotransparent and cannot be visualized under fluoroscopy guidance without contrast medium. In our modified technique, US was only used for puncture of the PA sac but injection of glue was performed under fluoroscopy. It is then easier to check any leakage thanks to contrast medium. The addition of Lipiodol increases polymerization time. For this reason, we used a 50:50 dilution because this corresponds to 2 to 3 seconds polymerization time (26), which is adequate for occluding an aneurysm.

This balloon-assisted method is well tolerated and may

be easily and promptly performed even in weak patients with painful groin hematoma, potentially reducing hospital stay. The risk of leakage into the limb arteries is then reduced without risk of gluing the balloon wall. Only two patients complained of temporary mild pain after the intervention, but none during the follow-up. Furthermore, this approach may be useful in case of failure of filling of the PA sac with glue, the contralateral arterial access then allowing final treatment of the PA at the same time by stent-graft placement in front of the neck, as it was performed for three patients in the present study. However, the main drawback of our technique is the need for contralateral arterial access that can lead to the same kind of complication, with PA formation, as we reported in 1 patient, which spontaneously resolved.

Our study had some limitations. First, conclusions must be drawn with caution because of the retrospective nature of the current study and the small number of patients included. Second, data on factors predisposing to PAs as sheath diameter, use of vascular closure devices, hypertension, and obesity were not available for most of initial endovascular procedures. The last limitation is the lack of a control arm. Future larger studies are needed to confirm the safety and efficacy of this intervention with glue and to compare it with other standard percutaneous treatments, especially with thrombin injection.

In conclusion, our study demonstrates that balloon-assisted NBCA-MS glue embolization is a safe and effective alternative for US-guided direct percutaneous occlusion of iatrogenic femoral artery PAs. This is the first study describing the injection of glue under fluoroscopy guidance. It offers complete exclusion of the PA in most cases and avoid the need for surgery. This technique is especially suitable to prevent distal embolization thanks to balloon occlusion of the native artery. Furthermore, the low cost of glue in comparison with thrombin may have significant economic impact in the current management of patients with iatrogenic PAs.

Acknowledgements

None.

Footnote

Conflicts of Interest: The authors have no conflicts of interest to declare.

Ethical Statement: This retrospective study was performed in compliance with the requirements of the institutional review board and approved by the institution ethical committee. Informed consent was waived.

References

1. Katzenschlager R, Ugurluoglu A, Ahmadi A, Hülsmann M, Koppensteiner R, Larch E, Maca T, Minar E, Stümpflen A, Ehringer H. Incidence of pseudoaneurysm after diagnostic and therapeutic angiography. Radiology 1995;195:463-6.
2. Kresowik TF, Khoury MD, Miller BV, Winniford MD, Shamma AR, Sharp WJ, Blecha MB, Corson JD. A prospective study of the incidence and natural history of femoral vascular complications after percutaneous transluminal coronary angioplasty. J Vasc Surg 1991;13:328-33; discussion 333-5.
3. Grewe PH, Mügge A, Germing A, Harrer E, Baberg H, Hanefeld C, Deneke T. Occlusion of pseudoaneurysms using human or bovine thrombin using contrast-enhanced ultrasound guidance. Am J Cardiol 2004;93:1540-2.
4. Kang SS, Labropoulos N, Mansour MA, Baker WH. Percutaneous ultrasound guided thrombin injection: a new method for treating postcatheterization femoral pseudoaneurysms. J Vasc Surg 1998;27:1032-8.
5. Pope M, Johnston KW. Anaphylaxis after thrombin injection of a femoral pseudoaneurysm: recommendations for prevention. J Vasc Surg 2000;32:190-1.
6. Taylor BS, Rhee RY, Muluk S, Trachtenberg J, Walters D, Steed DL, Makaroun MS. Thrombin injection versus compression of femoral artery pseudoaneurysms. J Vasc Surg 1999;30:1052-9.
7. Kurzawski J, Sadowski M, Janion-Sadowska A. Complications of percutaneous thrombin injection in patients with postcatheterization femoral pseudoaneurysm. J Clin Ultrasound 2016;44:188-95.
8. Savolainen H, Baumgartner I, Schmidli J, Heller G, Do DD, Willenberg T. Femoral pseudoaneurysms requiring surgical treatment. Trauma Mon 2012;16:194-7.
9. Stoesslein F, Ditscherlein G, Romaniuk PA. Experimental studies on new liquid embolization mixtures (histoacryl-lipiodol, histoacryl-panthopaque). Cardiovasc Intervent Radiol 1982;5:264-7.
10. Abdulmalak G, Chevallier O, Falvo N, Di Marco L, Bertaut A, Moulin B, et al. Safety and efficacy of transcatheter embolization with Glubran®2 cyanoacrylate

glue for acute arterial bleeding: a single-center experience with 104 patients. Abdom Radiol (NY) 2018;43:723-33.
11. Aytekin C, Firat A, Yildirim E, Kirbas I, Boyvat F. Ultrasound-guided glue injection as alternative treatment of femoral pseudoaneurysms. Cardiovasc Intervent Radiol 2004;27:612-5.
12. Del Corso A, Vergaro G. Percutaneous treatment of iatrogenic pseudoaneurysms by cyanoacrylate-based wall-gluing. Cardiovasc Intervent Radiol 2013;36:669-75.
13. Mittal R, Stephen E, Keshava SN, Moses V, Agarwal S. Percutaneous cyanoacrylate glue embolization for peripheral pseudoaneurysms: an alternative treatment. Indian J Surg 2012;74:483-5.
14. Fellmeth BD, Roberts AC, Bookstein JJ, Freischlag JA, Forsythe JR, Buckner NK, Hye RJ. Postangiographic femoral artery injuries: nonsurgical repair with US-guided compression. Radiology 1991;178:671-5.
15. Lange P, Houe T, Helgstrand UJ. The efficacy of ultrasound-guided compression of iatrogenic femoral pseudo-aneurysms. Eur J Vasc Endovasc Surg 2001;21:248-50.
16. Coley BD, Roberts AC, Fellmeth BD, Valji K, Bookstein JJ, Hye RJ. Postangiographic femoral artery pseudoaneurysms: further experience with US-guided compression repair. Radiology 1995;194:307-11.
17. Hajarizadeh H, LaRosa CR, Cardullo P, Rohrer MJ, Cutler BS. Ultrasound-guided compression of iatrogenic femoral pseudoaneurysm failure, recurrence, and long-term results. J Vasc Surg 1995;22:425-30.
18. Cox GS, Young JR, Gray BR, Grubb MW, Hertzer NR. Ultrasound-guided compression repair of postcatheterization pseudoaneurysms: results of treatment in one hundred cases. J Vasc Surg 1994;19:683-6.
19. Sultan S, Nicholls S, Madhavan P, Colgan MP, Moore D, Shanik G. Ultrasound guided human thrombin injection. A new modality in the management of femoral artery pseudo-aneurysms. Eur J Vasc Endovasc Surg 2001;22:542-5.
20. Liau CS, Ho FM, Chen MF, Lee YT. Treatment of iatrogenic femoral artery pseudoaneurysm with percutaneous thrombin injection. J Vasc Surg 1997;26:18-23.
21. Ergun O, Çeltikçi P, Güneş Tatar İ, Yılmaz M, Hekimoğlu B. Percutaneous thrombin injection treatment of a femoral artery pseudoaneurysm with simultaneous arterial balloon occlusion: Case report and review of the literature. Turk Kardiyol Dern Ars 2016;44:684-9.
22. Weinmann EE, Chayen D, Kobzantzev ZV, Zaretsky M, Bass A. Treatment of postcatheterisation false aneurysms: ultrasound-guided compression vs ultrasound-guided thrombin injection. Eur J Vasc Endovasc Surg 2002;23:68-72.
23. Cope C, Zeit R. Coagulation of aneurysms by direct percutaneous thrombin injection. AJR Am J Roentgenol 1986;147:383-7.
24. Loffroy R. N-butyl cyanoacrylate glue: the best hemostatic embolic agent for patients with acute arterial bleeding. Cardiovasc Intervent Radiol 2017;40:1290-1.
25. Loffroy R, Gui B, Cercueil JP, Krausé D. Endovascular therapeutic embolization: an overwiew of occluding agents and their effects on embolised tissues. Curr Vasc Pharmacol 2009;7:250-63.
26. Berthod PE, Chevallier O, Latournerie M, Gehin S, Falvo N, Midulla M, Loffroy R. Atypical use of ALN inferior vena cava filters as protection devices prior to embolization of a large portosystemic shunt with Amplatzer Vascular Plugs and Glubran 2 cyanoacrylate glue. Quant Imaging Med Surg 2018;8:452-6.

Cite this article as: Griviau L, Chevallier O, Marcelin C, Nakai M, Pescatori L, Galland C, Midulla M, Falvo N, Loffroy R. Percutaneous ultrasound-guided balloon-assisted embolization of iatrogenic femoral artery pseudoaneurysms with Glubran®2 cyanoacrylate glue: safety, efficacy and outcomes. Quant Imaging Med Surg 2018;8(8):796-803. doi: 10.21037/qims.2018.09.12

Review Article

CT cinematic rendering for pelvic primary tumor photorealistic visualization

Jun Yang, Kun Li, Huiyuan Deng, Jun Feng, Yong Fei, Yiren Jin, Chengde Liao, Qinqing Li

Department of Radiology, The Third Affiliated Hospital of Kunming Medical University, Yunnan Cancer Hospital, Kunming 650118, China

Correspondence to: Qinqing Li; Chengde Liao. Department of Radiology, The Third Affiliated Hospital of Kunming Medical University, Yunnan Cancer Hospital, No. 519 Kunzhou Road, Xishan District, Kunming 650118, China. Email: qinqing_81@163.com; 846681160@qq.com.

Abstract: Pelvic tumors can be both complicated and challenging, and computed tomography (CT) has played an important role in the diagnosis and treatment planning of these conditions. Cinematic rendering (CR) is a new method of 3D imaging using CT volumetric data. Unlike traditional 3D methods, CR uses the global illumination model to produce high-definition surface details and shadow effects to generate photorealistic images. In this pictorial review, a series of primary pelvic tumor cases are presented to demonstrate the potential value of CR relative to conventional volume rendering (VR). This technique holds great potential in disease diagnosis, preoperative planning, medical education and patient communication.

Keywords: Cinematic rendering (CR); pelvic tumor; imaging; computed tomography (CT)

Submitted Jul 25, 2018. Accepted for publication Sep 21, 2018.
doi: 10.21037/qims.2018.09.21
View this article at: http://dx.doi.org/10.21037/qims.2018.09.21

Introduction

At present, computed tomography (CT) is widely used in clinical practice with improvements in its resolution and image quality being made over recent decades. In addition to these advancements, the increase in computing power has made the more demanding visualization algorithms possible. For instance, volumetric data obtained from routine scans can now be reconstructed in 3D visualization. Currently, two types of 3D rendering techniques are commonly used to visualize volumetric 3D data: surface shaded display (SSD) and volume rendering (VR). These techniques provide a global overview of volumetric data, along with detailed anatomical and pathological information which is usually more difficult to discern in conventional 2D images (1). SSD is considered to be the predecessor of the VR technique (VRT) and uses simple attenuation threshold segmentation to identify and display the surface of the object. Meanwhile, VRT forms images based on volumetric data and assigns different colors and transparency to different attenuations (2). Another new imaging method, cinematic rendering (CR), which is not yet in clinical use, is capable of 3D visualization of volumetric data. One improvement of CR compared with traditional VR is the use of a photo-editing spherical panorama to illuminate the scanned object (3). CR uses a global lighting model and direct and indirect lighting to create an image for rendering quality (4). This novel technology provides detailed photorealistic visualization of high-density objects, including contrast-enhanced blood vessels, vascularized structures, tissues, organs, and bones (1). Although some pioneering studies have demonstrated that CR exhibits great prospects in clinical application (1,5-7), these studies were mainly performed to assess the cardiovascular system, abdominal organs, and traumatic fractures, and have not been performed for bone tumors, especially pelvic ones.

In this pictorial review, we discuss the role of CR in primary pelvic tumors and provide examples compared with VRT, demonstrating that CR is helpful in the diagnosis and evaluation of pelvic bone tumors. For our data, volumetric CT data were obtained from standard protocol on Siemens CT scanners (SOMATOM Definition AS or SOMATOM Force) and thin-slice images (1 mm) were reconstructed from 0.6 mm isotropic voxels. This volumetric raw data was

then used to create VR and CR images. VR reconstructions were created at a multimodality workstation (syngo.via, version VB10B, Siemens, Erlangen, Germany), and CR images were created with prototype software (syngo.via Frontier, version 1.2.0) in this workstation.

Normal pelvic anatomy

The pelvis consists of the left and right hips, sacrum and coccyx. CR produces cinematic images that can more clearly present the complex anatomy of the pelvis. *Figure 1* illustrates the normal pelvic anatomy as observed on CR and VR images. The hip bone is composed of the ilium, ischial and pubis bone. The acetabulum, a fusion of these three bones on each lateral side, is the site where the femoral head is located. The ilium is the largest of the three bones and is located in the upper part of the hip bone. The ischium is located in the lower back of the hip and can be divided into two parts, the body and the ramus. The ischial tuberosity is formed at the back of the body and the ramus, which is the sitting point for the weight of the sitting position. The ischial tuberosity is the lowest part of the ischium and can be observed on the body surface. CR presents 3D photorealistic anatomy of the pelvis from different angles and provides different view settings. In addition to observing the pelvic bone, CR can also clearly and intuitively observe pelvic vessels. It is easy to observe the variability of the blood vessels, the artery providing blood supply to the tumor, and the adjacent relationship between the tumor and blood vessels. The abdominal aorta to the lower edge of the fourth lumbar vertebral body is divided into the left and right common iliac artery; the common iliac artery is divided into the iliac crest and the external artery at the sacroiliac joint height. The two branches of the external iliac artery that can also be identified on the CR are the inferior epigastric artery and the deep iliac artery. Furthermore, CR can provide more anatomical information for the assessment of congenital pelvic anomalies.

Primary malignant pelvic tumors

Primary malignant pelvic tumors are not uncommon and include two main types: sarcomas, such as chondrosarcoma, osteosarcoma and Ewing's sarcoma; and hematological malignancies, such as lymphoma, multiple myeloma and plasmacytoma.

Chondrosarcoma

Chondrosarcoma is the most common primary malignant tumor of the pelvic bone, accounting for approximately 32% of cases, and is characterized by malignant proliferation of the cartilage-like matrix (8). Chondrosarcomas are most commonly located in the ilium and acetabulum. Chondrosarcoma is resistant to chemotherapy and radiation therapy, and extensive local excision is the only treatment. Imaging studies of the extent of the lesion are particularly important. The imaging performance of chondrosarcoma depends on the grade of the lesion. Low-grade lesions are typically small and often intraosseous with mild expansion of the cortical bone, and have clear boundaries, clear cartilage mineralization, and no soft tissue mass. High-grade chondrosarcoma often presents with expansive bone destruction, contains a large number of tumor stroma, and is surrounded by various calcifications and soft tissue masses. CR provides the tumor location from different angles, which helps surgeons to conceive the operation mode prospectively. Moreover, CR can vividly display various forms of calcification, such as amorphous and irregular calcification, and can completely reveal the panorama of calcifications (*Figure 2*).

Osteosarcoma

Osteosarcoma shows a bimodal age distribution. The first peak occurs in adolescents, and the second peak occurs in the elderly (9). Pelvic osteosarcoma is rare, accounting for only 7.2% of patients with osteosarcoma (10). Osteosarcoma, which occurs in the pelvis, is typically located at the back of the iliac wing and expands into the sacrum and lower lumbar spine (11). Osteosarcoma often presents with bone destruction, tumor bone formation and periosteal reactions. Tumor bone typically is fluffy and amorphous and exhibits cloud-like mineralization characteristics of osteoid matrix production. Codman triangles appear when the soft tissue components of the tumor cause the periosteum to bulge and be destroyed. Pelvic osteosarcoma is often accompanied by a soft tissue mass. Pelvic osteosarcoma is more often extended across the sacroiliac joint and hip joints compared with the extremities (12). CR can display the extensive tumor neovascularity and relationship with feeding vessels with different setting windows, which are important in presurgical planning (*Figure 3A,B,C*). CR images provide an even greater

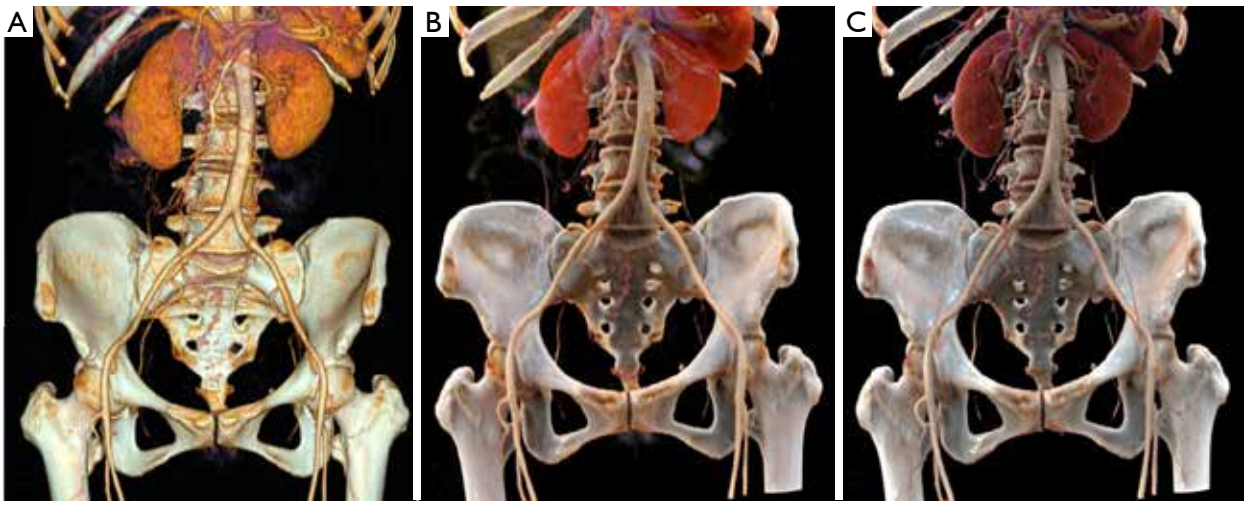

Figure 1 Normal pelvic anatomy. (A) VR; (B,C) CR with different window levels and width settings. VR, volume rendering; CR, cinematic rendering.

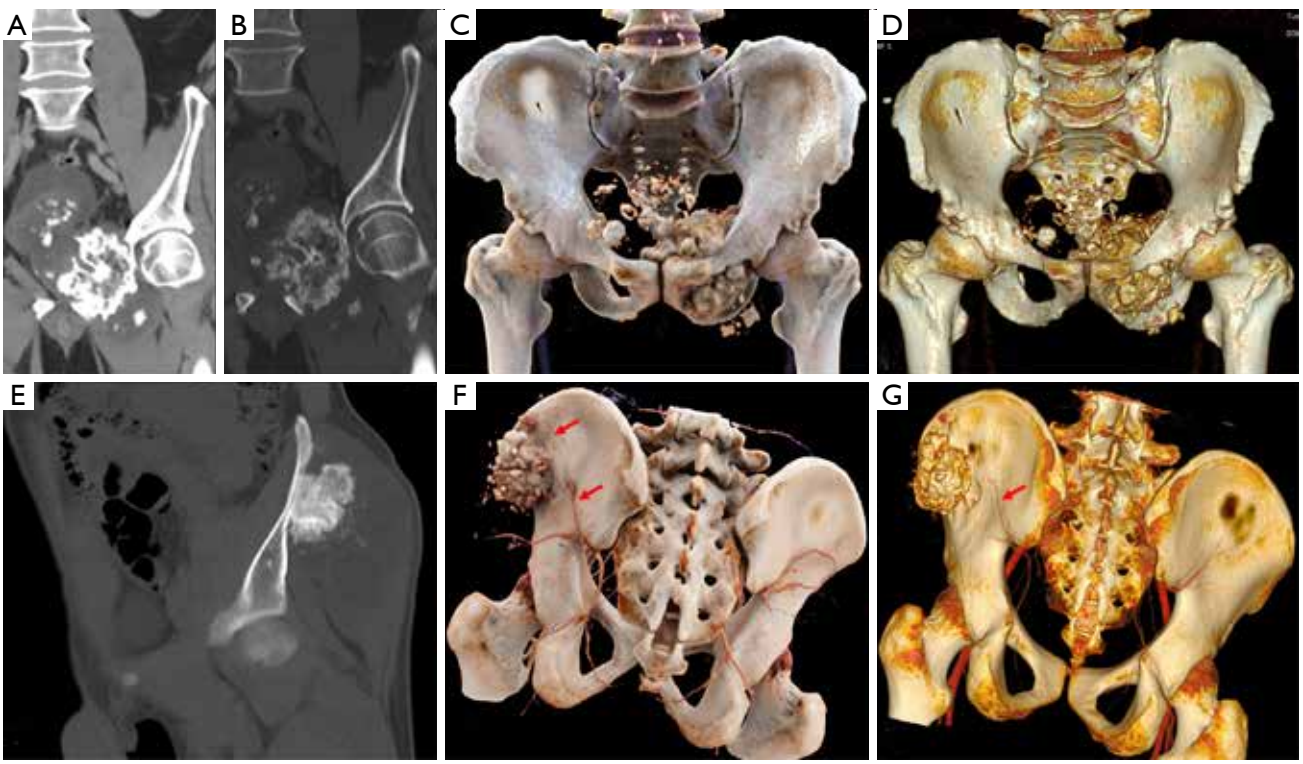

Figure 2 (A-D) Left superior branch of a pubis chondrosarcoma grade 2. A 59-year-old male presented with left lower extremity pain for 1 year that was aggravated for 1 month. The CT image shows a large destructive mixed mass arising from the left superior branch of the pubis, and a huge irregular soft tissue mass surrounds the mass (A,B). CR (C) demonstrated scattered patches, spots and circular calcification in the tumor more realistically than VR (D). (E-G) Left iliac wing chondrosarcoma grade 3. A 19-year-old male presented a left iliac progressive mass with pain for 3 months that was aggravated at night. The left iliac wing exhibited bone destruction, and multiple ring-shaped cartilaginous calcifications were found in the mass (E). CR (F) and VR (G) can evaluate lesions and their vessels from different angles, and CR shows these more clearly (red arrows). CT, computed tomography; CR, cinematic rendering; VR, volume rendering.

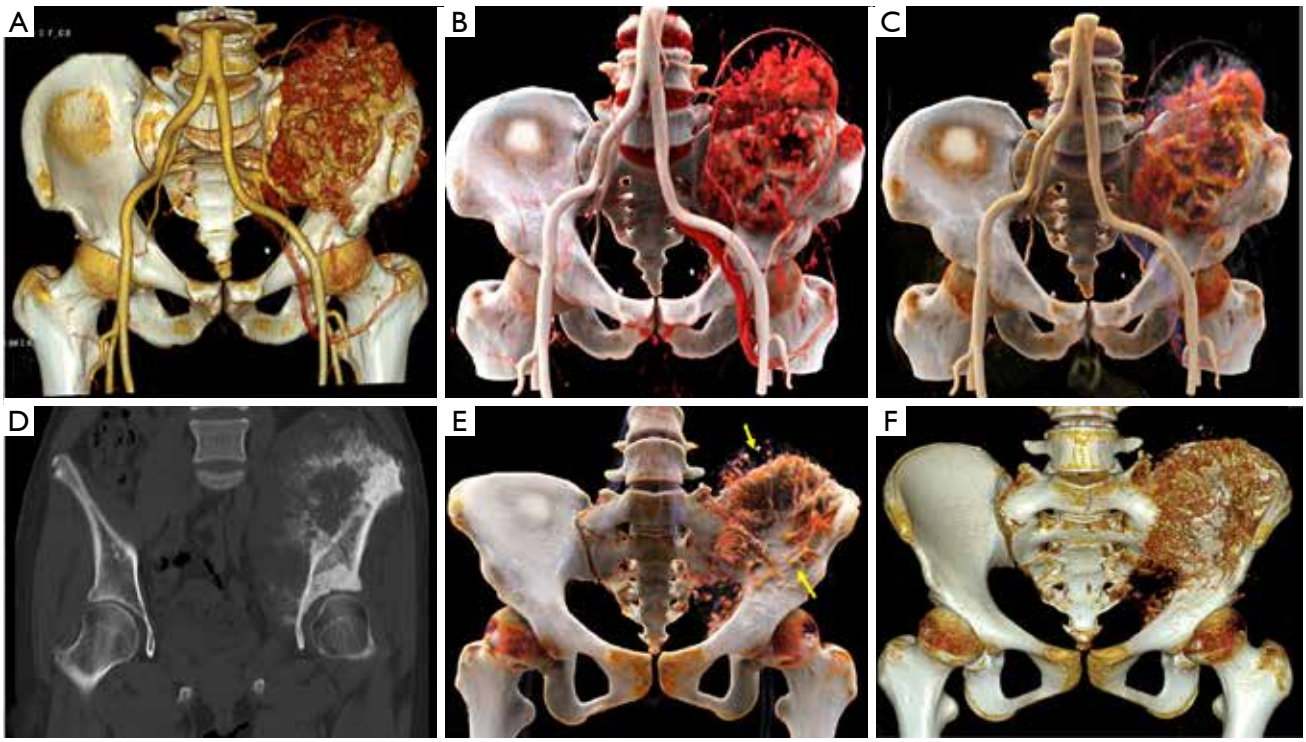

Figure 3 (A-C) A 49-year-old male presented with left ilium lumber pain for 2 months. The left iliac bone was extensively damaged by a huge soft tissue mass that extended to the left iliopsoas and glutaeus. A large number of tumor bones were observed in the mass, and a needle-like periosteal reaction was observed on the surface of the iliac bone. The left iliac bone was involved, but the bony structure of the sacral joint surface was normal. Most of the soft tissue masses exhibited significant inhomogeneous enhancement. Vessel contour is smoother on CR (B,C) compared to VR (A). (D-F) A 14-year-old female presented with left hip pain for 1 month that was aggravated with swelling for two weeks. The entire left iliac and acetabular destruction exhibited the ivory-like change (yellow arrows) (D). The density was inhomogeneous, and the lesion involved the sacroiliac and hip joint. The mass boundary was ill defined, and intratumoral radial high-density tumor bone was observed in CR (E) and VR (F). The pathological result was chondrocyte osteosarcoma. CR, cinematic rendering; VR, volume rendering.

level of detail, and CR presents a more realistic and vivid appearance of the tumor bone (*Figure 3D,E,F*).

Ewing's sarcoma

Ewing's sarcoma is a malignant, small, round, blue-cell tumor of the bone and soft tissue. Ewing's sarcoma is the second most common bone malignancy in children and adolescents, often occurring in the pelvis. Imaging findings include moth-eaten appearance, permeative bone destruction, onion skin features or thorn-like periosteal reaction with soft tissue masses (13). Due to the irregular pelvic morphology, Ewing's sarcoma that occurs in the pelvis rarely exhibits typical onion skin-like changes. The soft tissue mass around the tumor is typically larger than the bone destruction area, and the tumor margin is often ill defined and infiltrative. CR is beneficial for observing sacroiliac joint involvement and formulating the virtual pelvic reconstruction plan (*Figures 4,5*).

Multiple myeloma (MM) and plasmacytoma

MM is a malignant plasma cell disease that originates in plasma cells in the bone marrow and primarily involves the midshaft bone, especially in the spine, pelvis and skull. Bone destruction occurs as a result of the proliferation of plasma cells distributed in the bone marrow. The flat bones (vertebral bodies, skulls, pelvis) are particularly vulnerable as these bones contain a large amount of red bone marrow. Plasmacytoma is a solitary lesion that is similar to myeloma

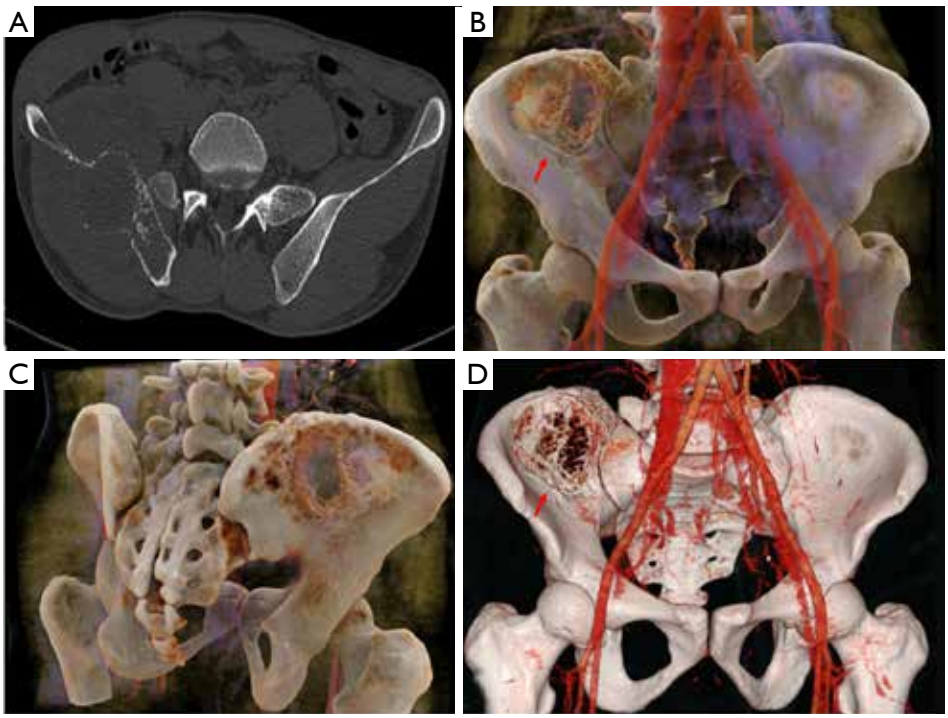

Figure 4 A 33-year-old male presented with right hip pain for more than one year (obvious at night) that was aggravated with numbness of the lower extremities and activity disorder for 3 weeks. 2D CT image (A), CR (B and C) and VR (D) show that the right iliac bone exhibits widespread osteolytic destruction, and the edge is well defined (red arrows). Contiguous spread of this mass is not across the sacroiliac joint into the right sacrum. CT, computed tomography; CR, cinematic rendering; VR, volume rendering.

with large numbers of plasma cells. Plasmacytoma is generally considered an early manifestation of multiple myeloma, so the prognosis is better. Imaging findings include diffuse osteoporosis, osteolytic bone destruction, and no hardening of the edges. The lesions are separated from each other and are similar in size. On an X-ray of the skull, plasmacytoma appears as "punched-out" lesions. Compression fracture of the vertebral body and soft tissue mass is typically observed on CT. CR and VR can be used to observe the lesions in a comprehensive manner, and CR offers superior details and pathological fractures (*Figures 6,7*).

Lymphoma

Primary non-Hodgkin lymphoma (PHL) very rarely occurs in bone. PHL arises in the diaphysis of long bones or in flat bones of the axial skeleton. PHL also includes small round cell tumors that rarely occur in the pelvic region and tends to occur in older ages (8). Imaging findings include osteolytic bone destruction, subtle cortical destruction, and periosteal reactions, and show normal tissue surrounded by tumor: all similar imaging findings to Ewing's sarcoma. However, the soft tissue masses are smaller than Ewing's sarcoma, and sclerosis may be more prominent (14). Lymphoma that occurs in the vertebral body can involve intervertebral discs and continuous vertebral bodies. The relationship between tumor and pelvic blood vessels can be clearly displayed on CR at different levels, and vascular and bone destruction can be observed simultaneously (*Figure 8*).

Chordoma

Chordoma is a slow-growing, low-grade malignant tumor that originates from the hereditary spinal cord remnant at the end of the spine (15). Most of the chordomas that occur in the pelvis are found in the sacrum, especially the fourth and fifth sacral vertebra. Imaging findings include lytic destruction in the inferior portion of the sacrum and coccyx and a clear boundary of the mass without an osteosclerotic

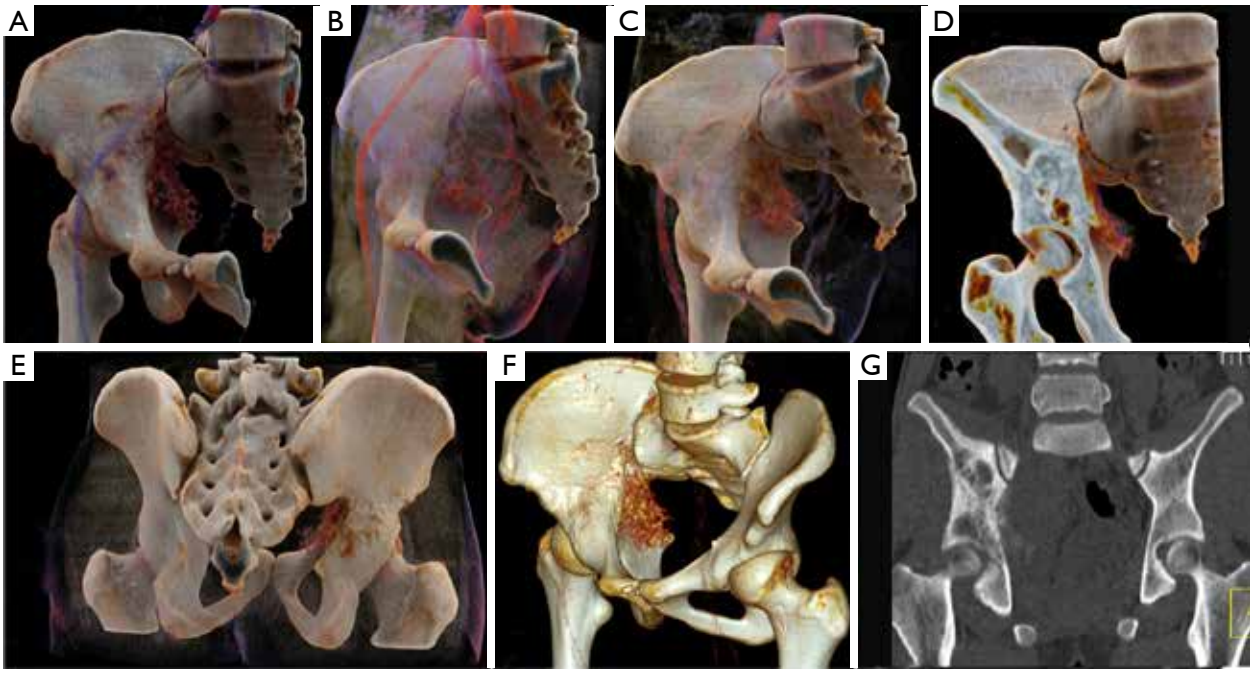

Figure 5 A 17-year-old male presented with a right hip mass that had gradually increased for 1 year. CR (A-E), VR (F) and 2D CT image (G) show the right iliac bone destruction. The tumor had an abundant blood supply, and the sacroiliac joint was not involved. CT, computed tomography; CR, cinematic rendering; VR, volume rendering.

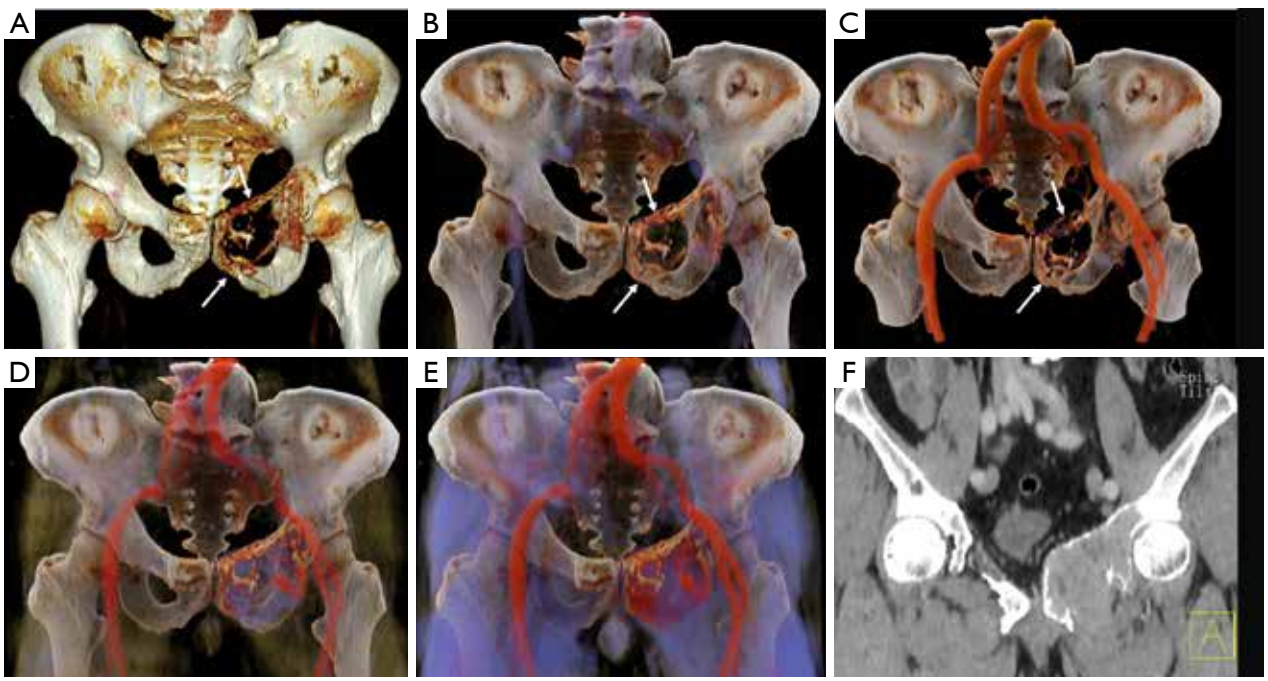

Figure 6 A 61-year-old male with left hip pain for 6 months. VR (A), CR (B-E) and a 2D CT image (F) demonstrate osteolytic destruction of the left acetabulum and pubic bone and the formation of soft tissue masses. CR dynamically shows tumor enhancement of the tumor through different window adjustment techniques. CR shows details of bone destruction more clearly than VR (white arrows). CT, computed tomography; CR, cinematic rendering; VR, volume rendering.

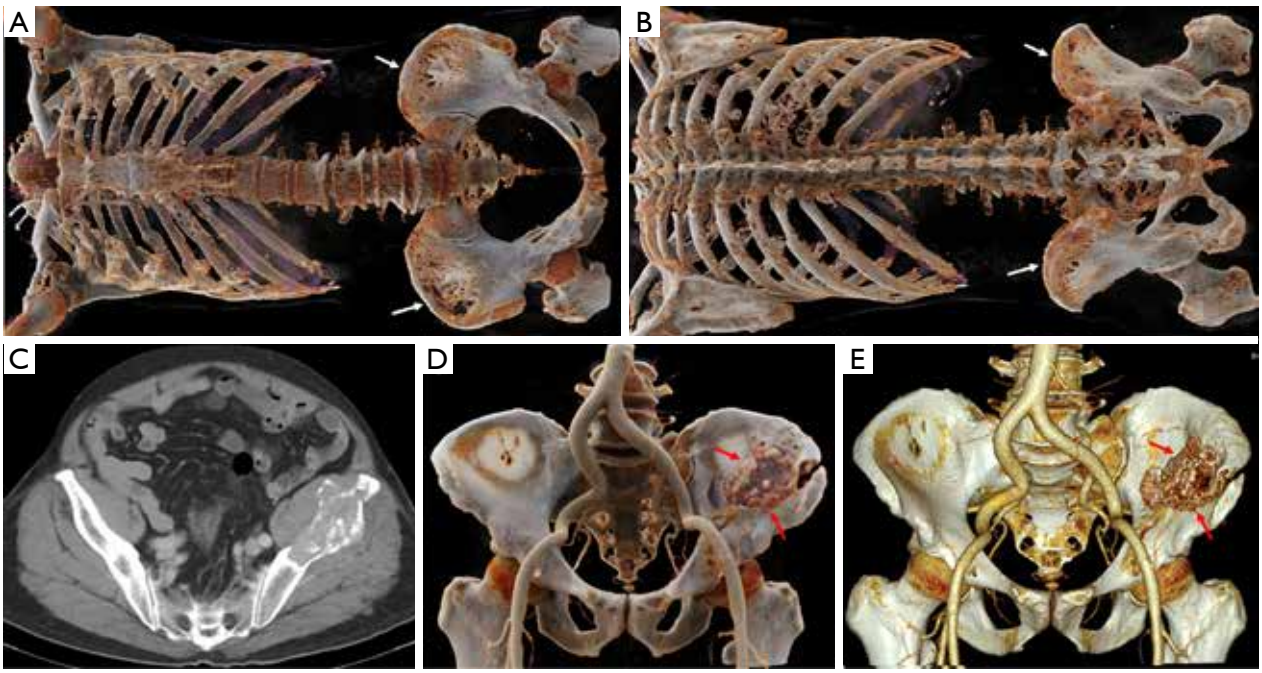

Figure 7 (A,B) CR. A 65-year-old female presented with pain in the back of the waist for 2 months that became gradually aggravated. Diffuse, "punched-out" osteolytic lesions are noted throughout the thoracic and lumbar vertebra, ribs and pelvis (white arrows indicate iliac wing destruction). (C-E) A 67-year-old male presented with left hip pain for more than 4 years that was aggravated for 1 month. The left ilium body and wing exhibit slightly expansive, osteolytic and extensive bone destruction with a large soft-tissue mass (C). Numerous stripe calcifications can be observed in CR (D) and VR (E) (red arrows), and pathological fractures of the ilium are visible around the mass. CR, cinematic rendering; VR, volume rendering.

rim, with tumor calcification observed in 50% to 60% of cases (16). CR and VR can both be used to observe lesions from different angles and remove areas of occlusions, but CR offers more detailed and photorealistic images (*Figure 9*).

Benign pelvic tumors

Osteochondroma

Osteochondroma is a common benign bone tumor that often occurs in long tubular bones, especially in the femur, humerus and tibia. The knee, ilium, hand and foot are also common locations. Osteochondroma is usually asymptomatic, and symptoms appear when the tumor grows and compresses the blood vessels and nervous system. The osteochondromas of the pubic and ischia may compress the urogenital structures. Radiographically, osteochondroma appears as a lesion composed of cortical and medullary bone protruding from, and continuous with, the underlying bone (17). The bony continuous area between the mother bone and osteochondroma can be wide or narrow (*Figures 10,11*). CR can realistically display the relationship between the tumor and the parent bone from different views. Osteochondroma grows slowly, but if it grows too fast or suddenly increases, it may become chondrosarcoma (*Figure 12*).

Giant cell tumor (GCT)

GCTs mainly occur in young patients between 20 and 30 years of age and exhibit a female predominance (16). GCT rarely occurs in the pelvis but when it does it is mainly found in the sacrum. GCT often exhibits osteolytic destruction, cortical expansion with a cortical shell and bony separation. GCTs have a well-defined border, no hardening of the rim, and eccentric growth that can extend to adjacent articular surfaces, often occurring at the end of the bone with closed physes (18). Due to secondary aneurysmal bone cysts (ABCs), GCTs can also contain liquid-liquid levels which typically indicate hemorrhage with sedimentation (15).

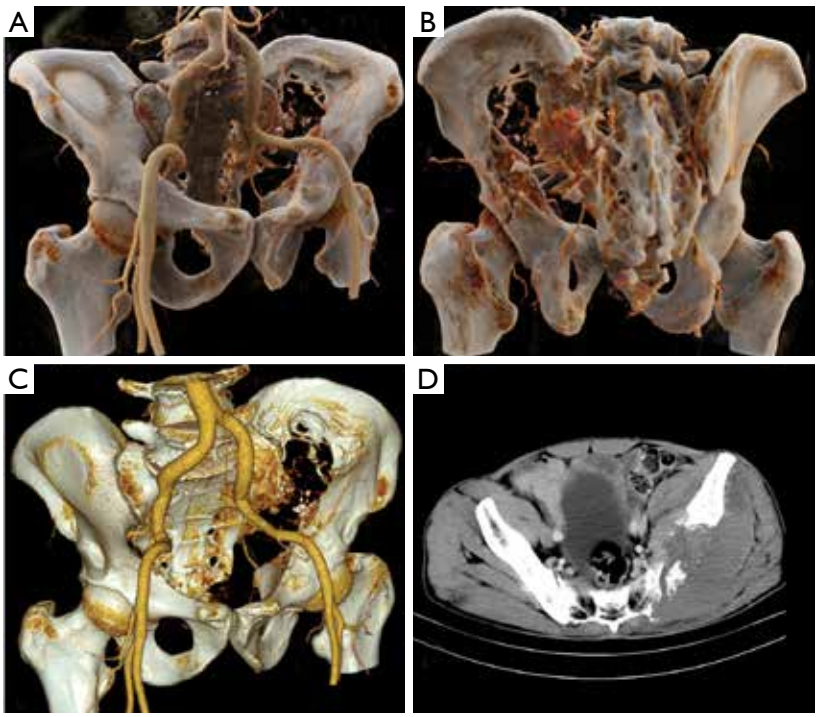

Figure 8 A 48-year-old male presented with left hip and lower limb pain for 8 months that was aggravated with swelling for 6 months. The left iliac bone, acetabulum and sacral bone show extensive moth-eaten osteolysis and no reactive sclerosis, with an irregular soft tissue mass (A-C). CR (A and B) demonstrated more details than VR (C). The lesion was characterized by inhomogeneous enhancement (D). CR, cinematic rendering; VR, volume rendering.

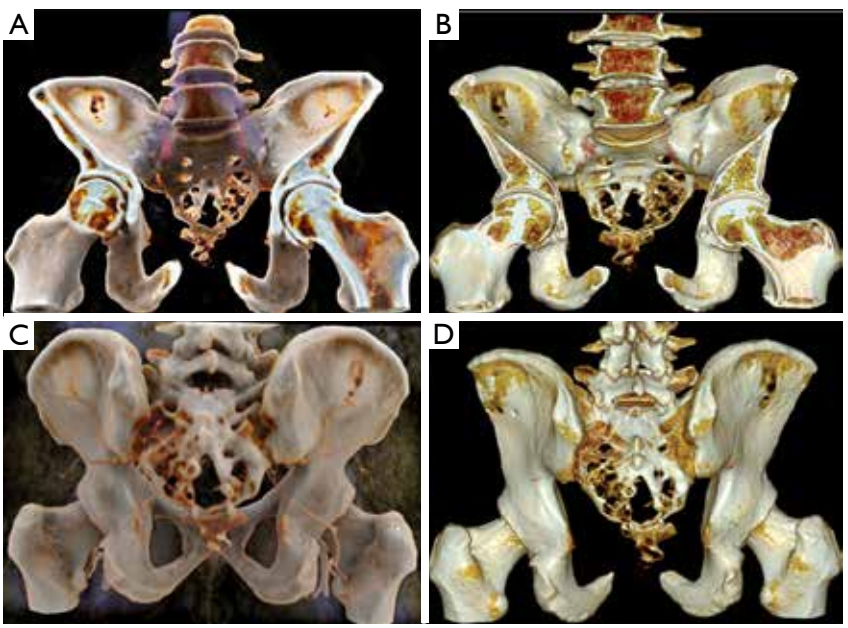

Figure 9 Front view (A and B) and back view (C and D). A 55-year-old male presented with lumbosacral pain for more than 6 months that was aggravated for 1 week. CR (A and C) and VR (B and D) presented 2–4 sacral bony destruction sites with a residual bone crest and calcification inside. CR, cinematic rendering; VR, volume rendering.

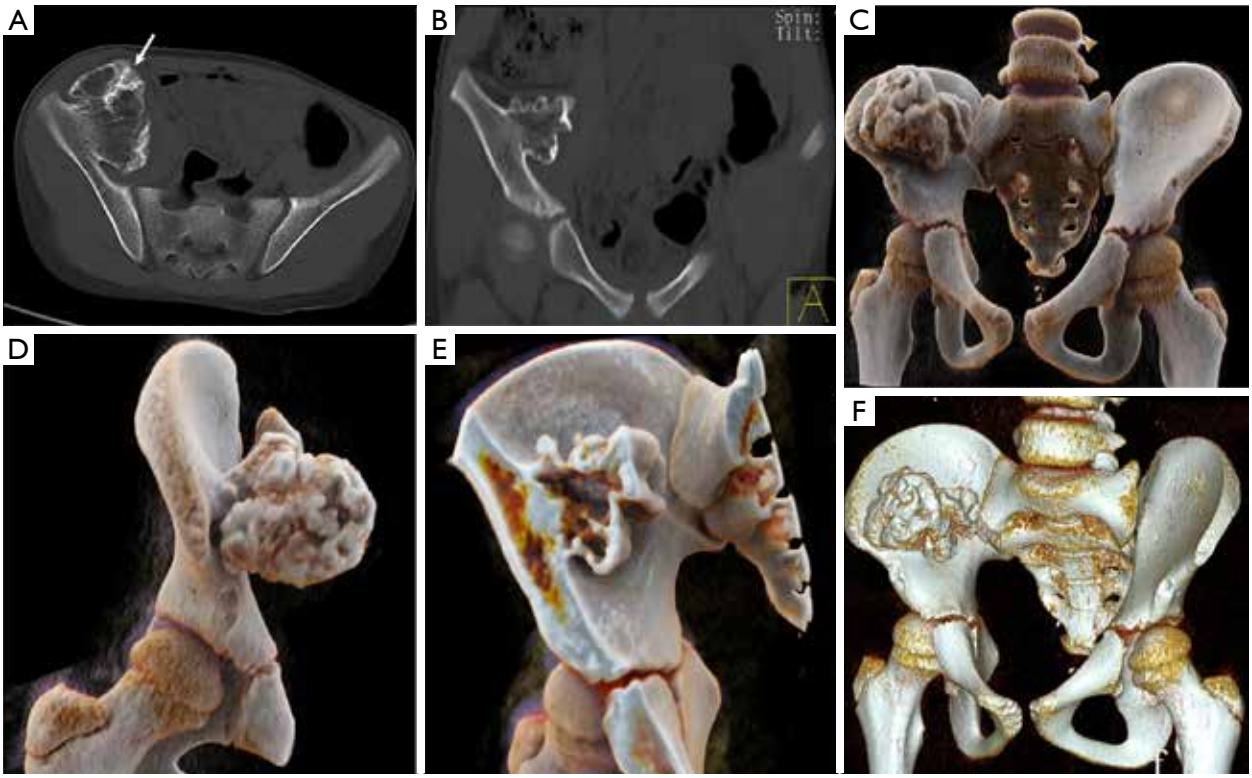

Figure 10 (A-F) Benign solitary osteochondroma of the ilium in an 8-year-old child. Axial CT scan (A) and coronal position reconstruction (B), CR (C-E) and VR (F) images show the marrow and cortical continuity of an osteochondroma and the underlying illium. The lump is cauliflower-like, and the edge is partially hardened (arrow). CT, computed tomography; CR, cinematic rendering; VR, volume rendering.

Imaging findings of GCTs in the pelvis are less likely to demonstrate the classical appearance of those in the long bones. CR can adjust the display parameters to provide information on different tissue types and better visualize soft tissue and bone. CR reconstruction can be performed using different transparencies of the soft tissue and can display tumor detail and enhancement (*Figure 13*). As with MPR and VRT, CR can tailor the lesion using the clip plane in any direction to better display the internal structure and overall panorama of the lesion.

Chondroblastoma (CB)

CB is a rare benign tumor that accounts for less than 1% of all primary bone tumors (19). CB typically occurs in the proximal humeral epiphysis or femoral and tibial condyles, and is rarely located in the pelvis. CB often occurs in young people, generally in adolescents, with a male to female ratio of 2:1 (20,21). *Figure 14* provides two rare cases of pelvic CB. Imaging findings demonstrate a well-defined eccentric oval or round lytic lesion with some expansion and a thin sclerotic rim. Punctate and flocculent calcification is often noted in the center of mass, and the mass occasionally contains fluid levels. Imaging features may be similar with chondrosarcoma, but the age of onset is younger.

Fibrous dysplasia (FD)

FD is a tumor-like lesion that occurs in the bone. It refers to normal marrow and cancellous bone in any part of the body, replaced by abnormal fibrous tissue and immature trabecular bone, leading to osteolytic lesion, fracture, and deformity. The disease manifests as monostotic bone or polyostotic bones. Pelvic bones are frequently involved in the polyostotic form (22). Radiologically, FD presents as a mild to moderate expansion of marrow with a ground glass appearance, mild sclerotic rim, no periosteal reaction and a soft mass (*Figure 15A,B,C*). Utilizing varying window widths

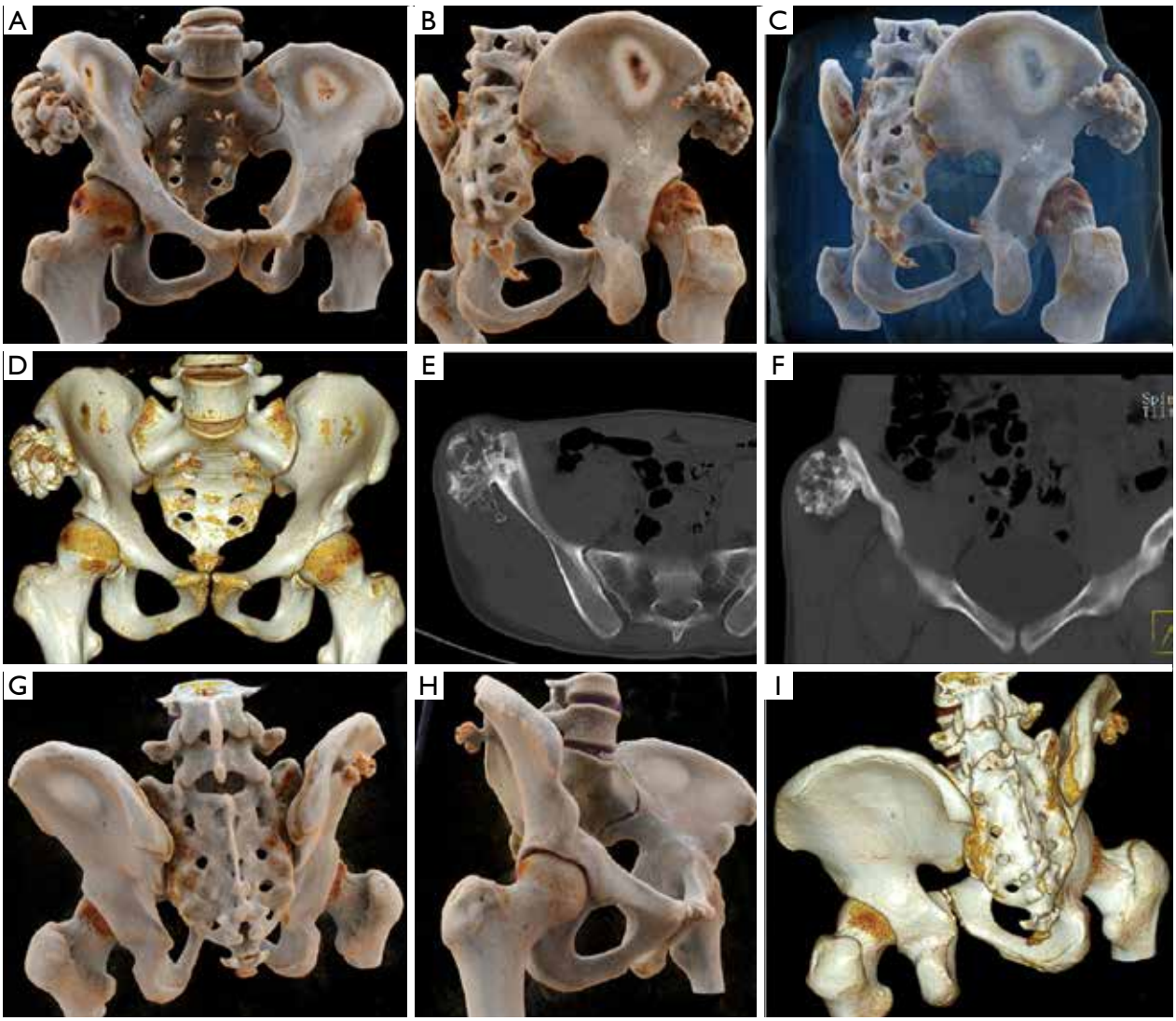

Figure 11 (A-F) A 21-year-old man with osteochondroma of the right ilium for 3 years. CR (A-C), VR (D), axial CT scan (E) and coronal position reconstruction (F) images demonstrate a pedunculated osteochondroma with wide and cortical continuity to the underlying ilium. (G-I) A 15-year-old man with osteochondroma in the posterior of the ilium. CR (G and H) and VR (I) reveal a pedunculated osteochondroma with marrow and cortical continuity to the underlying mother bone. CR, cinematic rendering; VR, volume rendering.

and cut planes of CR, it is possible to display the internal structure of the bone destruction zone (*Figure 15D,E,F,G*). CR provides a better overall appreciation of the degree of lesion and joint deformity.

ABC

ABC is a benign tumor-like lesion that most often occurs in long bones, followed by the pelvis and the spine (23). Primary ABC often occurs under the age of 20, with patients usually presenting with localized pain and swelling. The radiologic features of the lesions show well-defined osteolytic areas with fluid-fluid levels inside the tumor. Bone destruction is marked by expansion with a thinned cortex, and without calcified matrix. At the later stage of development, the outline of the cortex is clear, forming the appearance of the soap bubbles (*Figure 16*).

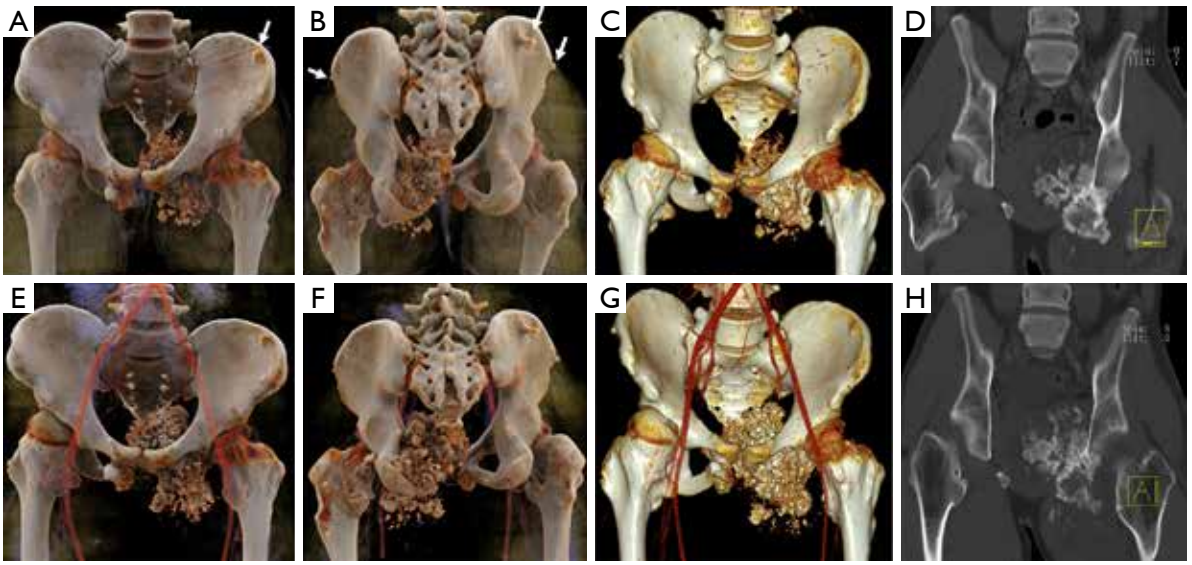

Figure 12 (A-H) A 19-year-old man with multiple osteochondroma for ten years. CR (A and B), VR (C), and CT coronal position reconstruction (D) images demonstrate left sciatic bone destruction and an exogenous lobular mass, with many round and high-density calcifications in the tumor. After 4 months, the tumor was significantly enlarged (E-H), and the pathology confirmed that the tumor became chondrosarcoma. In addition, multiple osteochondromas were observed from different views (arrows). CR (E and F), VR (G), and CT coronal position reconstruction (H). CT, computed tomography; CR, cinematic rendering; VR, volume rendering.

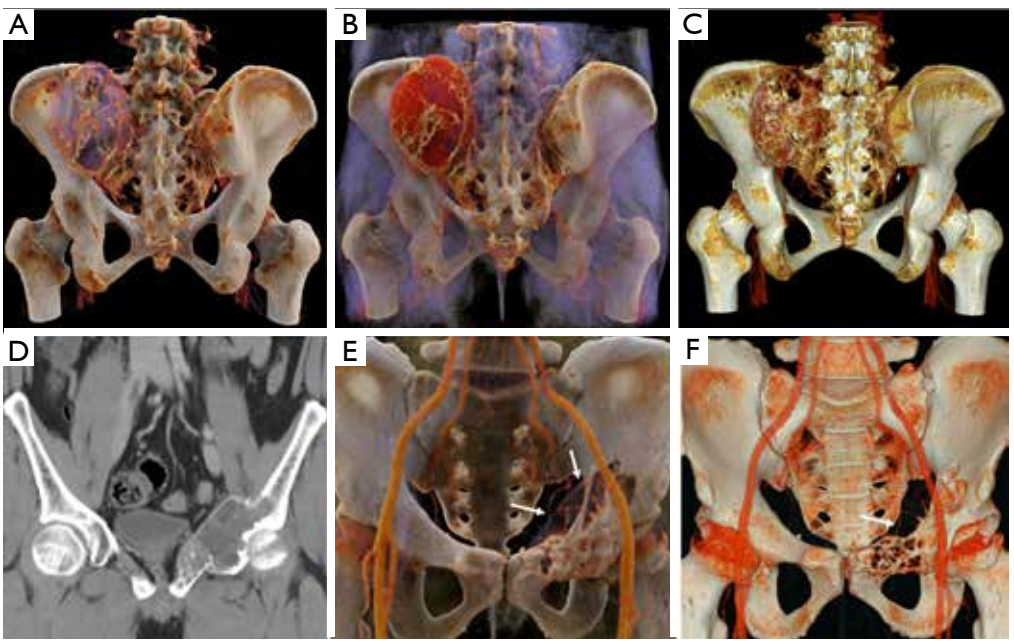

Figure 13 (A-C) A 59-year-old female presented with pain in the left lump and sacrum for one year. CT reveals an expanding destructive lesion in the left iliac and sacrum with a soft tissue mass, and the lesion is located across the sacroiliac joint. CR (A and B) can be performed using different transparencies of the tumor. Numerous intratumoral bony separations are noted in CR and VR (C). The density of the lesion is homogeneous, and the lesion exhibits obvious inhomogeneous enhancement. The CT value is approximately 121 HU. (D-F) A 37-year-old male presented with left hip pain for 1 year that was aggregated for 6 months. The left pubic bone exhibits expansive bone destruction, and liquid-liquid levels are present in the tumor (D). CR (E) and VR (F) can clearly demonstrate bone cortex thinning and multiple bony separations (white arrows). CT, computed tomography; CR, cinematic rendering; VR, volume rendering.

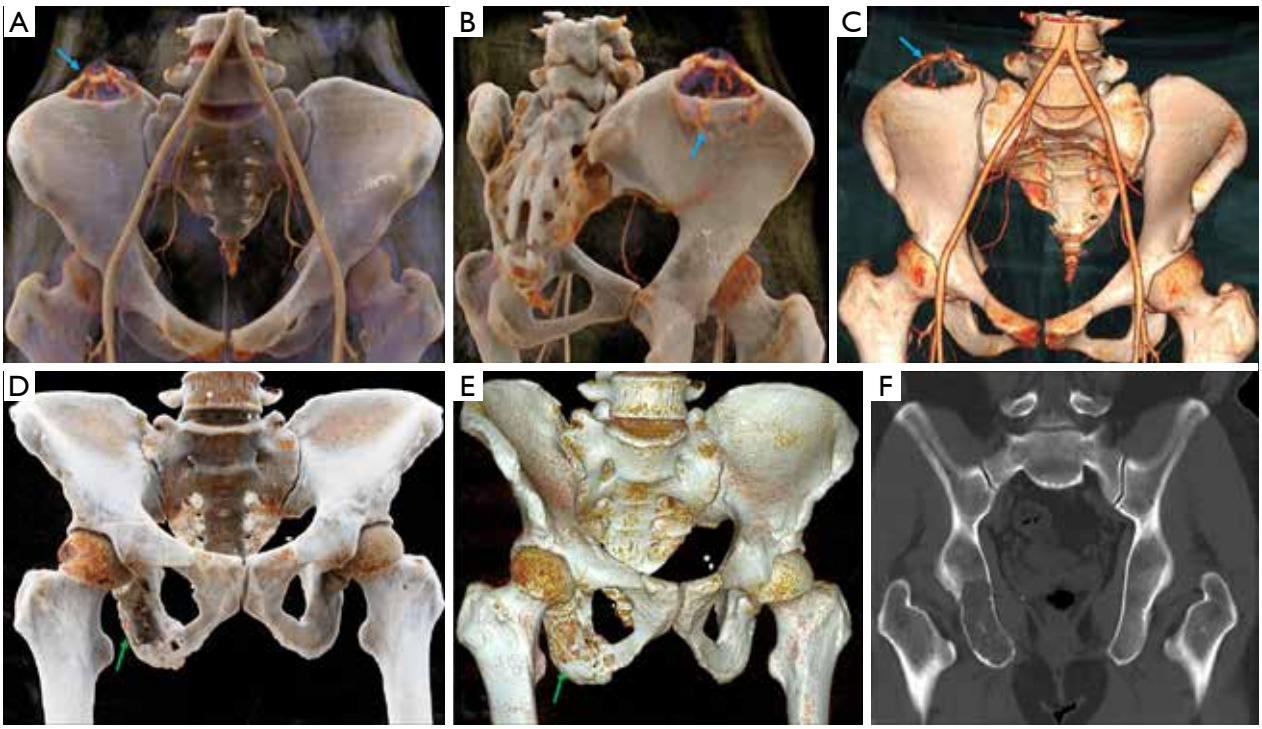

Figure 14 (A-C) A 14-year-old female presented with right iliac pain lasting 5 months. The right iliac wing was moderately expansive, and lytic destruction can be seen in CR (A and B) and VR (C). CR shows that the residual bone crest of bone destruction is superior to that of VR (blue arrows). (D-F) A 46-year-old male presented with right hip and near thigh root pain lasting more than one year. The right ischial bone and acetabulum exhibit moderately expansive destruction in CR (D) and VR (E). The cortex is thinner and discontinuous. The boundary is well defined, and no sclerotic rim is observed (F). CR showed that the internal structure of the bone destruction area was better than that of VR (green arrows). CR, cinematic rendering; VR, volume rendering.

Discussion

In this manuscript, we present a series of primary pelvic tumors highlighting the important differences between potential CR and traditional VR. The most significant difference between CR and VR is that CR uses the global illumination model, which is more complex and can generate more high-quality photorealistic images than the traditional ray-casting model. Although the traditional 2D and 3D play important roles in preoperative plans for pelvic tumors, CR visualization can provide additional value by enhancing the details and photorealism. By adjusting the image window, CR can provide dynamic, continuous observation of the lesion, from its surface to its interior, and photo-realistically and comprehensively display the lesion panorama. Due to the use of complex light-efficient dynamic light patterns (i.e., soft shadows) visual depth perception is improved; in other words, this technique can generate an approximate realistic reconstruction of adjacent and distant spatial structures in different depth planes of an image (3). This unique technological feat cannot be achieved by other traditional radiological methods. By providing high-quality realistic images, CR has helped orthopaedic multidisciplinary teams (MDTs) to develop treatment protocols, thus facilitating patient communication. Indeed, Berger *et al.* (24) found that most radiologists and orthopedic surgeons thought CR images give a more natural and clearer depiction of anatomic structures. Using this technique can improve the exchange of information between clinicians and radiologists. In addition, it is helpful for clinicians to understand the signs of radiology, such as intratumoral bony separations of FD (*Figure 15*) and the soapy-like appearance of ABCs (*Figure 16*).

CR is also helpful for determining the regional location of pelvic tumors, aiding in patient comprehension, facilitating clinical decision making, and promoting the accuracy of 3D-printed models. Three-dimensional high-definition vascular maps of CR can reveal the degree of tumor

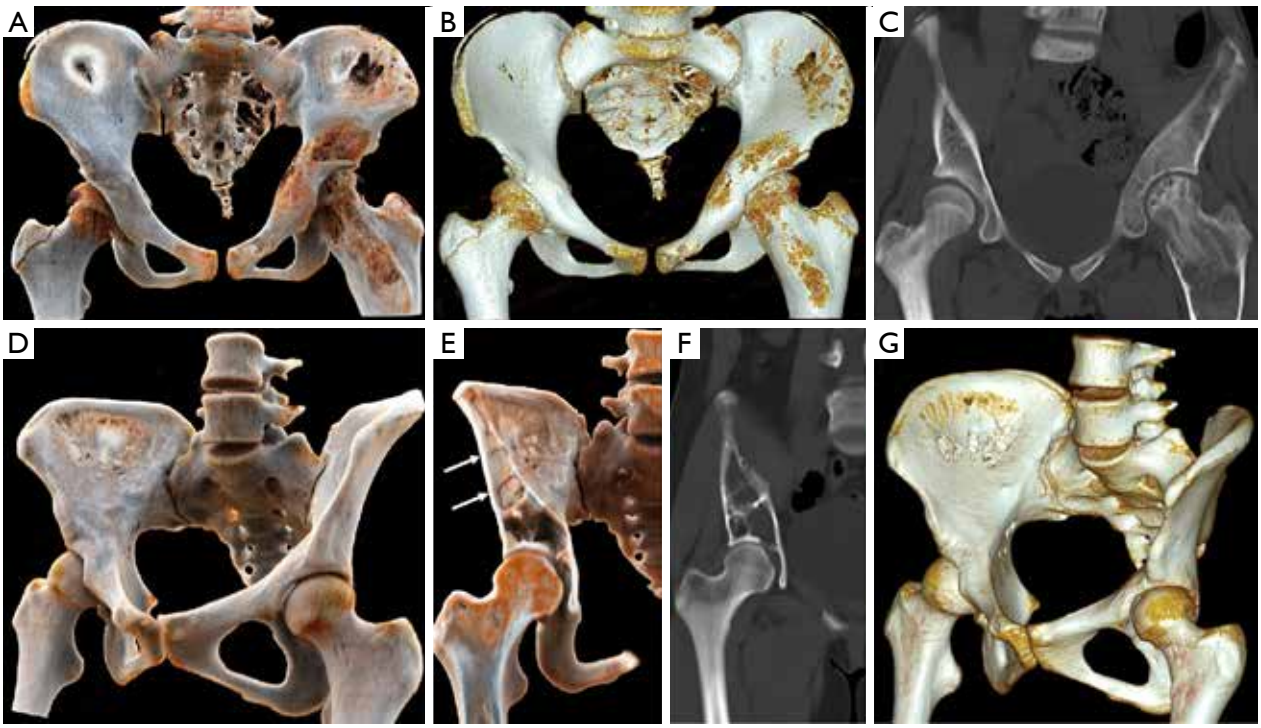

Figure 15 (A-C) Multiple bone fibrous dysplasia (polyostotic). An 11-year-old female presented with lame left lower extremities lasting for 1 year. The left iliac, acetabulum and femur exhibit mixed bone destruction. The lesion is moderately expanded with a mixture of sclerosis, ground-glass, and lytic regions and lacks a sclerotic rim. Deformity of the femoral valgus is clearly visible in CR. (D-G) A 17-year-old female presented with right pelvis fibrous dysplasia (monostotic). The right iliac and acetabulum exhibit well-defined lytic destruction with bony expansion and many bony separations inside. The CR displays the intratumoral bony separations as well (white arrows). A, D, and E are CR images; B and G are VR images; C and F are coronal 2D CT images. CR, cinematic rendering; VR, volume rendering.

invasion, aid in the determination of tumor resectability and determine the revascularization scheme (*Figures 3*,*6*,*8*) (25). Furthermore, the globalized presentation of CR helps surgeons develop personalized preoperative pelvic protocols and pelvic reconstruction protocols. In the process of CR imaging, the radiologist or surgeon needs to interact with the workstation in real time and optimize the appropriate template and window setting, so the pathological features and anatomy can be better displayed according to the situation. In the process of imaging using CR, radiologists and surgeons, by using multi-angle and multi-level observation, can better understand the pathology of the lesions and the spatial relationship with the surrounding tissues, simulating the findings in the surgery and boosting the surgeons' confidence. It may even save time during surgery. In addition, because CR shows details better than traditional 3D imaging, it can accurately display pelvic tumor invasion of blood vessels or joints, which can improve limb salvage rate and prevent excessive damage. At present, diagnosis relies mainly on the traditional method based on plane reconstruction, but the diagnosis of complex diseases may benefit from the flexibility and expressiveness of this new CR technology (26). The textural features of internal heterogeneity and necrosis in large tumors can be optimally displayed through CR (6). Understanding these textural features can aid in disease diagnosis. The various internal morphologies of the tumor bone and calcification noted in the cases in this study were displayed extremely realistically through CR. High-density objects, such as bone, or contrast-enhanced structures, such as blood vessels and hyper-enhanced tumors, e.g., GCT, are ideal for reconstruction through CR and can be represented with high quality in CR. However, in some deep areas where light is easily blocked and in hypo-enhanced lesions, the performance of CR is not outstanding.

In addition to clinical applications, CR can also be used

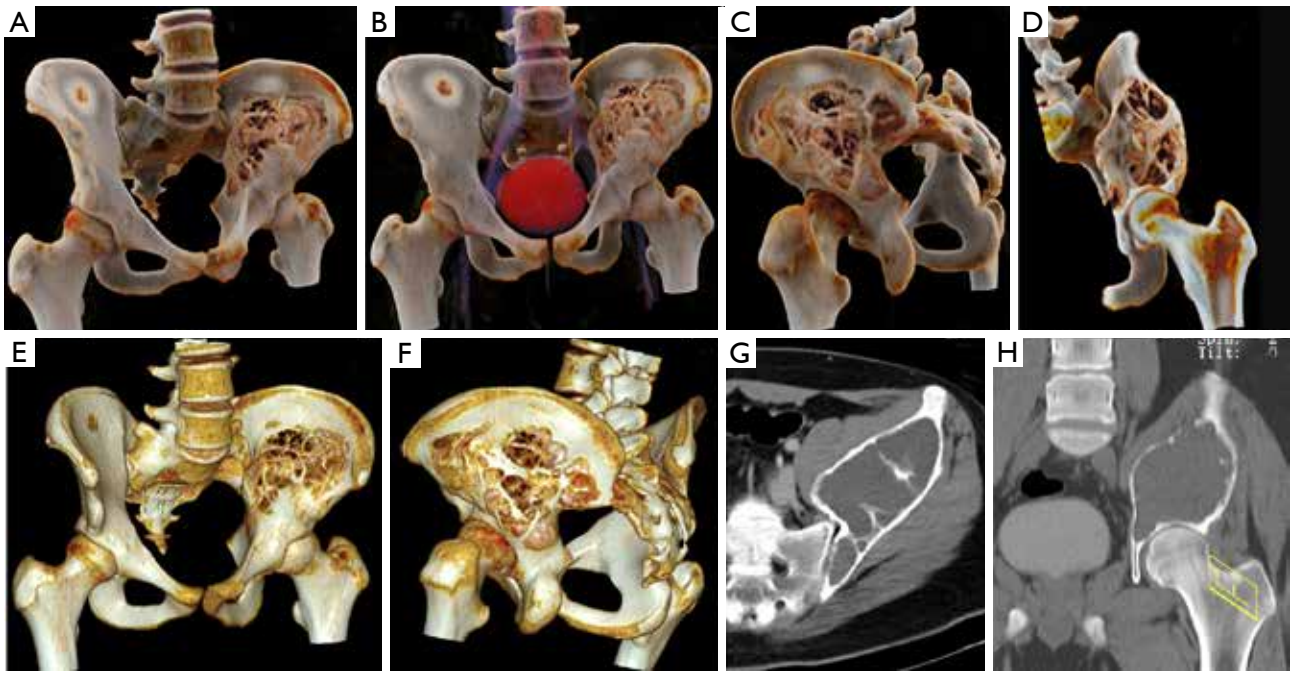

Figure 16 A 14-year-old male with ABC in the ilium. CR (A-D), VR (E and F), and 2D CT (G and H) images demonstrate expanded left iliac bone destruction and a soap bubble-like appearance. The cortex is thin and discontinuous. aneurysmal bone cyst; CT, computed tomography; CR, cinematic rendering; VR, volume rendering.

in medical education. For instance, CR can be applied as a new technique for teaching anatomy. This new teaching method makes it easier for beginners to understand complex anatomical structures while saving cadavers and accelerating the journey from the bench to the bedside. The anatomy of the pelvis revealed by CR in *Figure 1* is a good example of this imaging as an educational aid. In addition, CR has the potential to achieve virtual simulation of layer-by-layer dissection of the anatomy of a human corpse, and the integration of CR into navigation tools and 3D vision labs may partially replace the anatomy curriculum using corpses (3).

Although CR is a new technology, several limitations should be noted. Compared with VR, CR uses more complex algorithms and requires more powerful processors and longer processing times. Second, the shadow effect produced by the global illumination model does make the image photorealistic, but this shadow effect may obscure small lesions and even important pathology. Finally, compared with VRT, CR exhibits no obvious advantage in hypo-enhanced soft tissue tumors and requires further improvements. If CR can integrate the region-growth method, it may achieve better results.

In conclusion, CR is a new and promising imaging technique that exhibits a wide range of uses in the diagnosis of pelvic tumors, tumor division, preoperative planning, and communication with patients. Compared with traditional VR, the main innovation of CR is the ability to present CT volume data more naturally and photo-realistically with a rich and colorful template. When you view these images, you are not only diagnosing a condition but also observing important details.

Acknowledgements

Funding: This study was supported by the National Natural Science Foundation of China (Grant No. 81703155), the Yunnan Applied Basic Research Projects-KMU Joint Special Project [Grant no. 2017FE468(-071)] and the Yunnan Health Training Project of High Level Talents (H-2017005) and the Yunnan Doctoral Student New Scholar Award (2017).

Footnote

Conflicts of Interest: The authors have no conflicts of interest to declare.

References

1. Rowe SP, Johnson PT, Fishman EK. Cinematic rendering of cardiac CT volumetric data: Principles and initial observations. J Cardiovasc Comput Tomogr 2018;12:56-9.
2. Ebert LC, Schweitzer W, Gascho D, Ruder TD, Flach PM, Thali MJ, Ampanozi G. Forensic 3D Visualization of CT Data Using Cinematic Volume Rendering: A Preliminary Study. AJR Am J Roentgenol 2017;208:233-40.
3. Glemser PA, Engel K, Simons D, Steffens J, Schlemmer HP, Orakcioglu B. A New Approach for Photorealistic Visualization of Rendered Computed Tomography Images. World Neurosurg 2018;114:e283-92.
4. Johnson PT, Schneider R, Lugo-Fagundo C, Johnson MB, Fishman EK. MDCT Angiography With 3D Rendering: A Novel Cinematic Rendering Algorithm for Enhanced Anatomic Detail. AJR Am J Roentgenol 2017;209:309-12.
5. Rowe SP, Meyer AR, Gorin MA, Johnson PT, Fishman EK. 3D CT of renal pathology: initial experience with cinematic rendering. Abdom Radiol (NY) 2018. [Epub ahead of print]. doi: 10.1007/s00261-018-1644-7.
6. Rowe SP, Chu LC, Fishman EK. Evaluation of Stomach Neoplasms With 3-Dimensional Computed Tomography: Focus on the Potential Role of Cinematic Rendering. J Comput Assist Tomogr 2018;42:661-6.
7. Rowe SP, Fritz J, Fishman EK. CT evaluation of musculoskeletal trauma: initial experience with cinematic rendering. Emerg Radiol 2018;25:93-101.
8. Rajiah P, Ilaslan H, Sundaram M. Imaging of sarcomas of pelvic bones. Semin Ultrasound CT MR 2011;32:433-41.
9. Ottaviani G, Jaffe N. The epidemiology of osteosarcoma. Cancer Treat Res 2009;152:3-13.
10. Parry MC, Laitinen M, Albergo J, Jeys L, Carter S, Gaston C, Sumathi V, Grimer R. Osteosarcoma of the pelvis. Bone Joint J 2016;98-B:555-63.
11. Donati D, Giacomini S, Gozzi E, Ferrari S, Sangiorgi L, Tienghi A, DeGroot H, Bertoni F, Bacchini P, Bacci G, Mercuri M. Osteosarcoma of the pelvis. Eur J Surg Oncol 2004;30:332-40.
12. Park SK, Lee IS, Cho KH, Lee YH, Yi JH, Choi KU. Osteosarcoma of pelvic bones: imaging features. Clin Imaging 2017;41:59-64.
13. Sun Y, Liu X, Pan S, Deng C, Li X, Guo Q. Analysis of imaging characteristics of primary malignant bone tumors in children. Oncol Lett 2017;14:5801-10.
14. Bloem JL, Reidsma, II. Bone and soft tissue tumors of hip and pelvis. Eur J Radiol 2012;81:3793-801.
15. Ong KO, Ritchie DA. Pictorial essay: tumours and pseudotumours of sacrum. Can Assoc Radiol J 2014;65:113-20.
16. Gerber S, Ollivier L, Leclere J, Vanel D, Missenard G, Brisse H, de Pinieux G, Neuenschwander S. Imaging of sacral tumours. Skeletal Radiol 2008;37:277-89.
17. Murphey MD, Choi JJ, Kransdorf MJ, Flemming DJ, Gannon FH. Imaging of osteochondroma: variants and complications with radiologic-pathologic correlation. Radiographics 2000;20:1407-34.
18. Chakarun CJ, Forrester DM, Gottsegen CJ, Patel DB, White EA, Matcuk GR, Jr. Giant cell tumor of bone: review, mimics, and new developments in treatment. Radiographics 2013;33:197-211.
19. Suneja R, Grimer RJ, Belthur M, Jeys L, Carter SR, Tillman RM, Davies AM. Chondroblastoma of bone: long-term results and functional outcome after intralesional curettage. J Bone Joint Surg Br 2005;87:974-8.
20. Lin PP, Thenappan A, Deavers MT, Lewis VO, Yasko AW. Treatment and prognosis of chondroblastoma. Clin Orthop Relat Res 2005;438:103-9.
21. De Mattos CB, Angsanuntsukh C, Arkader A, Dormans JP. Chondroblastoma and chondromyxoid fibroma. J Am Acad Orthop Surg 2013;21:225-33.
22. Ozsen M, Yalcinkaya U, Bilgen MS, Yazici Z. Fibrous Dysplasia: Clinicopathologic Presentation of 36 Cases. Turk Patoloji Derg 2018;34:234-41.
23. Motamedi K, Seeger LL. Benign bone tumors. Radiol Clin North Am 2011;49:1115-34, v.
24. Berger F, Ebert L, Kubik-Huch R, Eid K, Thali M, Niemann T. Application of Cinematic Rendering in Clinical Routine CT Examination of Ankle Sprains. AJR Am J Roentgenol 2018;211:887-90.
25. Chu LC, Johnson PT, Fishman EK. Cinematic rendering of pancreatic neoplasms: preliminary observations and opportunities. Abdom Radiol (NY) 2018. [Epub ahead of print]. doi: 10.1007/s00261-018-1559-3.
26. Comaniciu D, Engel K, Georgescu B, Mansi T. Shaping the future through innovations: From medical imaging to precision medicine. Med Image Anal 2016;33:19-26.

Cite this article as: Yang J, Li K, Deng H, Feng J, Fei Y, Jin Y, Liao C, Li Q. CT cinematic rendering for pelvic primary tumor photorealistic visualization. Quant Imaging Med Surg 2018;8(8):804-818. doi: 10.21037/qims.2018.09.21

Review Article

Concurrent mapping of brain activation from multiple subjects during social interaction by hyperscanning: a mini-review

Meng-Yun Wang[1], Ping Luan[2], Juan Zhang[3], Yu-Tao Xiang[1], Haijing Niu[4], Zhen Yuan[1]

[1]Faculty of Health Sciences, University of Macau, Taipa, Macau SAR, China; [2]Medical Center, Shenzhen University Health Science Center, Shenzhen 518060, China; [3]Faculty of Education, University of Macau, Taipa, Macau SAR, China; [4]State Key Lab of Cognitive Neuroscience & Learning, Beijing Normal University, Beijing 100875, China

Correspondence to: Prof. Zhen Yuan. Faculty of Health Sciences, University of Macau, Taipa, Macau SAR, China. Email: zhenyuan@umac.mo.

Abstract: Social interaction plays an essential role in acquiring knowledge and developing our own personalities in our daily life. Meanwhile, functional magnetic resonance imaging (fMRI)-, electroencephalograph (EEG)-, and functional near inferred spectroscopy (fNIRS)-hyperscanning, enables us to concurrently map brain activation from two or more participants who are engaged in social interaction simultaneously. In this review, we first highlight the recent technologies advances and the most significant findings towards social interaction by using the hyperscanning method. In addition, we also illustrate several well-designed hyperscanning tasks that have been extensively adopted for the study of social interaction. Basically, hyperscanning contains six categories of experimental paradigms that can track the interactive neural process of interest. Furthermore, it contains two main elucidated neural systems which are involved in social interaction, including the mirror neuron system (MNS) and mentalizing system (MS). Finally, future research directions and clinical implications that are associated with hyperscanning are also highlighted and discussed.

Keywords: Hyperscanning; social neuroscience; functional neuroimaging

Submitted Aug 28, 2018. Accepted for publication Sep 06, 2018.
doi: 10.21037/qims.2018.09.07
View this article at: http://dx.doi.org/10.21037/qims.2018.09.07

Introduction

Our communication or social interactions with one another is essential for us to acquire knowledge and to develop our own personalities. Although the forms of social interactions are very broad including imitations, exchanges, completions and cooperation, as well as making decisions (1), we basically exchange our thoughts and ideas in two different manners. The dominant manner is through our sophisticated languages, which is also a characteristic that distinguishing ourselves from other creatures (1,2). The other way is by using non-verbal signs, such as our gestures and facial expressions, which can provide us with additional auxiliary information for social interactions (1,2).

Interestingly enough, although our social nature has been shaped for hundreds and thousands of years, neuroscience studies only just began to shed light on social interaction in the recent years (1,3,4). More importantly, previous neuroimaging studies have exhibited two basic limitations in elucidating neural correlates of social interactions. The first restriction is from the low ecological validity, since most of the previous experiments were performed in an enclosed room, in which individuals were instructed by computer programs, to complete the test tasks (2). However, this is not the case for social interactions in real life, in which individuals need to talk and act with each other simultaneously in a more natural way. Therefore, further neuroscience or neuroimaging studies should be performed by using a more realistic experimental paradigm which can duplicate a real-life situation. The other limitation is that previous studies can only acquire brain data from a single participant each time (5). However, as two or more individuals are engaged in social

interactions, it is essential to conduct a concurrent recording from multiple subjects with multiple setups rather than to perform it in isolation (1,2,5).

Recently, a new strategy that had combined two functional magnetic resonance imaging (fMRI) machines together for simultaneously measuring two participants' brain activity was adopted, which was coined as "hyperscanning" method (6). Since then, extensive hyperscanning studies have been performed, which improves our understanding of brain-to-brain synchronization during a social interaction (7). To date, hyperscanning has enabled the inspection of social interaction by using various neuroimaging techniques such as electroencephalograph (EEG) (8-30), functional near inferred spectroscopy (fNIRS) (31-48) and fMRI (49-55). Meanwhile, the experimental paradigms involved in hyperscanning studies can be categorized into six types of tasks: (I) imitation tasks; (II) coordination/joint tasks; (III) eye contact/gaze tasks; (IV) economic games/exchanges; (V) cooperation and competition tasks; and (VI) interactions under natural scenario. In particular, it is noted that during the performance of all those tasks, two major neural systems are largely involved (1,2,5). One is the mirror neuron system (MNS), which plays an important role in tasks involving movements, such as imitation and coordination/joint tasks (56). The other is a mentalizing system (MS), which is engaged in tasks pertaining to the inferences of yourself or others' intentions or thoughts (57), such as the economic game (58) and natural social interactions (33,36).

In this review, fMRI, EEG and fNIRS hyperscanning neuroimaging technologies which have engaged in social interaction are first introduced. Then, the representative experimental paradigms that were extensively adopted in hyperscanning, are also summarized in detail. Subsequently, two core neural systems involved in social interactions are carefully demonstrated. One is MNS, which consists of the primary motor, sensory cortex and parietal cortex, and is responsible for the imitation process; the second one is MS comprising the TPJ (temporal-parietal cortex) and PFC (prefrontal cortex), which is in charge of a more complex cognitive process. More importantly, the future of research perspectives and clinical implications of hyperscanning, are stated clearly in the final section.

Hyperscanning neuroimaging techniques

fMRI hyperscanning

As it is hard to place two or more participants into one fMRI tube, two or more fMRI machines should be utilized for an fMRI hyperscanning method to simultaneously record multiple participants' brain signals. In that circumstance, two or more remote fMRI apparatus can be connected by an intranet, while the data sets are stored in a host client (*Figure 1A*) (6). To date, several fMRI hyperscanning studies (49-55) have been conducted to inspect the inter-brain synchrony (*Table 1*). For example, neural correlates of trust between two individuals, had been examined by fMRI hyperscanning. They had discovered that trust is an essential social process, involved in all human interaction (54). Inarguably, fMRI hyperscanning has exhibited its advantages in mapping the coherence of brain regions which were associated with social interaction with high structural accuracy and excellent imaging depth. However, it is not accessible and available for everyone, because of the high cost of multiple fMRI setups. More importantly, the ecological validity is also relatively low, since the lab was under the controlled circumstances for fMRI, and is significantly different from real life.

EEG hyperscanning

Since the electrical activity of human brain was firstly recorded by Hans Berger in 1924, EEG has become a core neuroimaging tool in the study of cognition and diseases (59,60). More importantly, EEG is also one of the most powerful techniques for noninvasively exploring neural oscillations (61), in which the EEG signals are originated from the synchronized synaptic activity in populations of cortical neurons (62). Although EEG has been extensively utilized for mapping single individual's brain dynamics underlying specific cognitive tasks, the potential of EEG in exploring the inter-brain interactions or inter-brain connections has not been fully exploited.

Recently, a number of EEG hyperscanning studies (*Table 2*) were conducted (8-30), aiming to reveal the complex brain interactions between two or multiple participants, as illustrated in *Figure 1B* (26). These studies exhibited that EEG hyperscanning can map the moment-to-moment interactions between two or more individuals simultaneously, which can elucidate how co-variations of the tested individuals' brain activations are correlated with their social interactions. However, despite EEG being suitable to inspect inter-brain synchronization due to its high time resolution, it is still very challenging for EEG to capture the neural activity from deep brain structures.

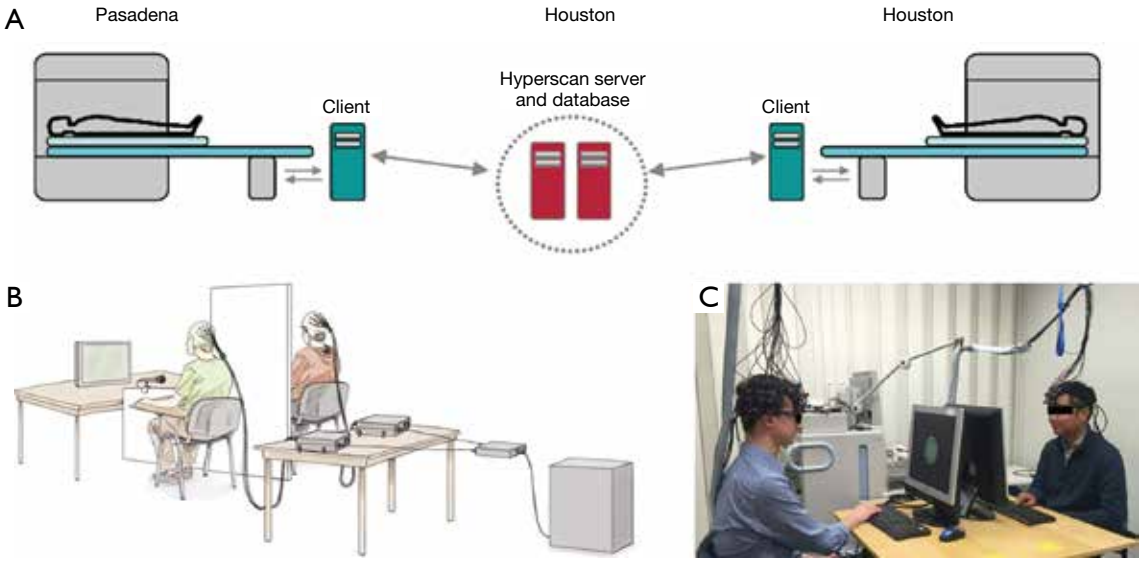

Figure 1 Configurations of hyperscanning studies. (A) fMRI hyperscanning; (B) EEG hyperscanning; and (C) fNIRS hyperscanning. (A) was adapted from reference (52) with permission from John Wiley and Sons. (B) and (C) were adopted from reference (26) and (44), respectively, under a Creative Commons Attribution 4.0 International License (http://creativecommons.org/licenses/by/4.0/). fMRI, functional magnetic resonance imaging; EEG, electroencephalograph; fNIRS, functional near inferred spectroscopy.

fNIRS hyperscanning

fNIRS is also a noninvasive and affordable neuroimaging technique, which utilizes the near-infrared light to image brain activation, by measuring the concentration changes of oxyhemoglobin (HbO) and deoxyhemoglobin (HbR) (63-65). In addition, fNIRS has exhibited its unbeatable advantages in inspecting infants or children's brain activation (66) since it is relatively more tolerant with movement artifacts. More importantly, fNIRS hyperscanning (*Table 3*) can ideally be applied to a natural scenario (33,35,36,39), as illustrated in *Figure 1C*. Although fNIRS has a better temporal resolution when compared to fMRI, it has the low spatial resolution and limited capability to detect deep brain structures.

Hyperscanning paradigms adopted in social interaction

Altogether, there were about six categories of experimental paradigms that were routinely used by the hyperscanning method in the investigation of social interaction.

Imitation tasks

The first category is the imitation tasks, during which one participant imitates the others' movements or behaviors. Although we cannot request one participant to teach the others how to perform specific tasks in the laboratory, we can still instruct one participant to simulate the other individual's actions or behaviors (*Figure 2A*). For example, in one EEG hyperscanning study (17), the participant was instructed to imitate the counterpart's meaningless hand movements. The results showed that inter-brain synchronization of right centroparietal regions at alpha-mu band was strongly correlated with the interactional synchrony (*Figure 2B*).

Coordination tasks

The second category is the coordination tasks, in which two or more participants need to try their best to act in a synchronized manner. Interestingly, behavioral synchronization in our daily life is one mechanism through which we coordinate our behaviors during social interaction. For example, when we are walking together, our footsteps might be unconsciously synchronized with one another even though our foot lengths and our intrinsic cycles are totally different (22). In addition, coordination/joint movements can also be synchronized, such as self-paced rhythmic finger movements (15,16). In particular, a number of EEG or fNIRS hyperscanning studies have

Table 1 fMRI hyperscanning

Authors	Neuroimaging methods	Subjects	Paradigms	Main discoveries
Montague *et al.*, 2002, *Neuoimage*	Two 1.5 T fMRI	3 pairs; gender: N/A; relationship: N/A	Game theory (a deceive game)	The very first hyperscanning study, where the term 'hyperscanning' was coined in this study
King-Casas *et al.*, 2005, *Science*	Two 3 T fMRI	48 pairs; gender: N/A; relationship: strangers	Game theory (trust game)	The study extends previous model-based fMRI studies into the social domain and broaden our view of the spectrum of functions implemented by the dorsal striatum
Fliessbach *et al.*, 2007, *Science*	One 3 T fMRI, one 1.5 T fMRI	19 pairs (5 subs were excluded); gender: all male; relationship: N/A	A simple estimation task that entailed monetary rewards for correct answers	A variation in the comparison subject's payment affects BOLD responses in the ventral striatum
Krueger *et al.*, 2007, *PNAS*	Two 3 T fMRI	22 pairs; gender: 11 F-F; 11 M-M; relationship: strangers	Game theory (trust game)	The paracingulate cortex is critically involved in building a trust relationship by inferring another person's intentions to predict subsequent behavior. Conditional trust selectively activated the ventral tegmental area, a region linked to the evaluation of expected and realized reward, whereas unconditional trust selectively activated the septal area, a region linked to social attachment behavior
Stolk *et al.*, 2014, *PNAS*	One 3 T fMRI, one 1.5 T fMRI	27 pairs; gender: all male; relationship: N/A	Cooperation task (jointly create a goal configuration of two geometrical tokens)	Establishing mutual understanding of novel signals synchronizes cerebral dynamics across communicators' right temporal lobes
Spiegelhalder *et al.*, 2014, *BBR*	Two 3 T fMRI	11 pairs; gender: all female; relationship: good friends	Natural scenario (live dialog)	The time course of neural activity in areas associated with speech production was coupled with the time course of neural activity in the interlocutor's auditory cortex
Koike *et al.*, 2016, *Neuroimage*	Two 3 T fMRI	Gender: same gender; relationship: stranger; Exp. 1: 17 pairs (9 M-M;8 F-F); Exp. 2: 15 pairs (8 M-M;7 F-F); Exp. 3: 16 pairs (6 M-M;10 F-F)	Eye contact/gaze tasks (mutual gaze task: eye to eye) (joint attention task: eyes on other stuff together)	The right inferior frontal gyrus had been activated both by initiating and responding to joint attention
Shaw *et al.*, 2018, *Sci Rep*	Two 3 T fMRI	19 pairs; gender: all male; relationship: strangers	Game theory (ultimatum game)	Brain signals implicated in social decision making are modulated by the estimates of expected utility and become correlated more strongly between interacting players who reciprocate one another

Main discoveries were directly extracted or adapted from the article's abstracts, which is also applied to the *Tables 2,3*. The situation of subjects in fMRI hyperscanning is two subjects lying in fMRI tubes separately. *PNAS*, *Proceedings of the National Academy of Sciences of the United States of America*; *BBR*, *Behavioural Brain Research*; N/A, not available means the authors did not explicitly depict their subjects' relationship or the exact numbers of gender pairs even though some studies addressed the overall numbers of genders.

Table 2 EEG hyperscanning

Authors	Neuroimaging methods	Subjects	Paradigms	Analytic method	Main discoveries/contributions
Tognoli *et al.*, 2007, *PNAS*	Two 60-channel EEG	8 pairs; gender: 4 gender-mixed; 3 M-M; 1 F-F; relationship: N/A; situation: face to face	Coordination/joint tasks (self-paced rhythmic finger movements)	Power comparison	A pair of oscillatory components located above right centroparietal cortex distinguished effective from ineffective coordination: increase of phi1 favored independent behavior and increase of phi2 favored coordinated behavior. Phi (9.2–11.5 Hz)
Fallani *et al.*, 2010, *PLos One*	Two 64-channel EEG	26 pairs; gender: N/A; relationship: N/A; situation: N/A	Game theory (prisoner's dilemma game)	Partial directed coherence, graph theory	The hyper-brain networks of two defector couples have significantly less inter-brain links and overall higher modularity than couples playing cooperative or tit-for-tat strategies. The decision to defect can be "read" in advance by evaluating the changes of connectivity pattern in the hyper-brain network
Dumas *et al.*, 2010, *PLos One*	Two 32-channel EEG	9 pairs; gender: 5 F-F; 6M-M (3 pairs were excluded, but not know which pair); relationship: N/A; situation: separated into two room	Imitation tasks (imitate counterparts' hands movements)	Phase locking value (PLV)	States of interactional synchrony correlate with the emergence of an interbrain synchronizing network in the alpha-mu band between the right centroparietal regions
Babiloni *et al.*, 2011, *Cortex*	Four 30-channel EEG	One quartet (four men) of professional saxophonists; situation: side by side	Natural scenario (music performance)	Power comparison	During the resting state, dominant EEG power density values were observed at alpha band (8-12 Hz) in posterior cortex. During the music performance, alpha power density values decreased in amplitude in several cortical regions, whereas power density values enhanced within narrow high-frequency bands
Babiloni *et al.*, 2012, *Neuroimage*	Four 30-channel EEG	Three quartets (12 men) of professional saxophonists; situation: side by side	Natural scenario (music performance)	Power comparison	The higher the empathy quotient test score, the higher the alpha desynchronization in right BA 44/45 during the OBSERVATION referenced to RESTING condition
Naeem *et al.*, 2012, *Neuroimage*	Two 60-channel EEG	6 pairs; gender: 3 mixed; 2 M-M; 1 F-F; relationship: N/A; situation: face to face	Coordination/joint tasks (adopted from Tognoli *et al.*, 2007)	Power comparison; PLV	Clear and systematic modulation of mu band activity in the 10–12 Hz range as a function of coordination context
Yun *et al.*, 2012, *Sci Rep*	Two 128-channel EEG	10 pairs; gender: all male; relationship: N/A; situation: face to face	Coordination/joint tasks (hand movement task)	PLV; source localization	Synchrony of both fingertip movement and neural activity between the two participants increased after cooperative interaction

Table 2 (*continued*)

Table 2 (*continued*)

Authors	Neuroimaging methods	Subjects	Paradigms	Analytic method	Main discoveries/contributions
Konvalinka *et al.*, 2014, *Neuroimage*	Two 32-channel EEG	9 pairs; gender: N/A; relationship: N/A; situation: back to back	Coordination/joint tasks (a synchronized finger-tapping task)	Power comparison Multivariate classification analysis	The interactive condition was characterized by a stronger suppression of alpha and low-beta oscillations over motor and frontal areas in contrast to the non-interactive computer condition. Leaders invest more resources in prospective planning and control
Menoret *et al.*, 2014, *Neuropsychologia*	Two 32-channel EEG	20 pairs; gender: 6 mixed, 7 M-M, 7 F-F; relationship: N/A; situation: face to face	Coordination/joint tasks (complete a goal with human or robot)		Acting in a social context induced analogous modulations of motor and sensorimotor regions in observer and actor
Toppi *et al.*, 2016, *PLos One*	Two 16-channel EEG	6 pairs civil pilots; gender: 5 M-M; 1 M-F; relationship: all from the national Italian airline (Alitalia)	Cooperation task (a simulated flight)	Event related potentials (ERPs), power comparison	During the most cooperative flight phases pilots showed, in fact, dense patterns of interbrain connectivity, mainly linking frontal and parietal brain areas. On the contrary, the amount of interbrain connections went close to zero in the non-cooperative phase
Mu *et al.*, 2016, *SCAN*	Two 32-channel EEG	Exp. 1: 34 pairs; gender: 17 M-M; 17 F-F; relationship: stranger; Exp. 2: 30 pairs; gender: all male; relationship: stranger; situation: separated by two monitors (*Figure 1B*)	Coordination/joint task (a dyad to synchronize with a partner by counting in mind rhythmically)	PLV	First evidence that oxytocin enhances inter-brain synchrony in male adults to facilitate social coordination
Mu *et al.*, 2017, *SCAN*	Two 32-channel EEG	Exp. 2: 45 pairs; gender: same gender; relationship: N/A; situation: separated by two monitors (*Figure 1B*)	Coordination task (same as Mu *et al.*, 2016)	PLV	Interbrain synchrony of gamma band oscillations is enhanced when people are under high threat, and increased gamma interbrain synchrony is associated with lower dyadic interpersonal time lag (i.e., higher coordination)
Jahng *et al.*, 2017, *Neuroimage*	Two 64-channel EEG	10 pairs; gender: all male; relationship: stranger; situation: face to face; face-blocked	Game theory (prisoner's dilemma game)	Power comparison, PLV	The power of the alpha frequency band (8–13 Hz) in the right temporoparietal region immediately after seeing a round outcome significantly differed between face-to-face and face-blocked conditions and predicted whether an individual would adopt a 'cooperation' or 'defection' strategy

Table 2 (*continued*)

Table 2 (*continued*)

Authors	Neuroimaging methods	Subjects	Paradigms	Analytic method	Main discoveries/contributions
Szymanski *et al.*, 2017, *Neuroimage*	Two 64-channel EEG	25 pairs; gender: 12 M-M; 13 F-F; relationship: stranger; situation: side by side	Cooperation game (a visual search task)	PLV	The inter-team differences in behavioral performance gain in the visual search task were reliably associated with inter-team differences in local and inter-brain phase synchronization
Dikker *et al.*, 2017, Current *Biology*	Twelve 14-channel wireless EEG	A group [12] of high school students; gender: 9 F; 3 M; relationship: classmates; situation: sit as a circle	Natural scenario (taking class)	Spectral coherence	They find that students' brainwaves are more in sync with each other when they are more engaged during class. Brain-to-brain synchrony is also reflective of how much students like the teacher and each other
Kinreich *et al.*, 2017, *Sci Rep*	Two 32-channel EEG	24 pairs romantic partners; 25 pairs strangers; situation: face to face with 45 degree	Natural scenario (talk with each other)	Power	Neural synchrony was found for couples, but not for strangers, localized to temporal-parietal structures and expressed in gamma rhythms
Perez *et al.*, 2017, *Sci Rep*	Two 32-channel EEG	15 pairs; gender: 8 M-M;7 F-F; relationship: stranger; situation: side by side with a board	Natural scenario (talk with each other)	PLV	interpersonal synchronization is mediated in part by a lower-level sensory mechanism of speech-to-brain synchronization, but also by the interactive process that takes place in the situation per se
Leong *et al.*, 2017, *PNAS*	Two 2-channel (C3 C4) EEG	Exp. 2: one adult (F) with 29 infants; gender: 29 infants (15 M; 14 F); relationship: N/A; situation: face to face	Natural scenario (infants viewed an adult in a live context, singing with direct or indirect gaze)	General partial directed coherence, G-causality	During live interactions, infants also influenced the adult more during direct than indirect gaze. Further, infants vocalized more frequently during live direct gaze, and individual infants who vocalized longer also elicited stronger synchronization from the adult
Hu *et al.*, 2018, *Biological Psychology*	Two 64-channel EEG	15 pairs; gender: all female; relationship: stranger; situation: face to face	Game theory (prisoner's dilemma game)	PLV	The results showed a higher cooperation rate and larger theta/alpha-band inter-brain synchrony in condition human-human (H-H) than in human-machine. In the condition H-H, there were larger centrofrontal theta band and centroparietal alpha-band inter-brain synchrony in tasks set for high cooperation
Ahn *et al.*, 2018, *Human Brain Mapping*	Two 19-channel EEG with 146-channel MEG	5 pairs; gender: 1 Mixed; 4 M-M; relationship: stranger; situation: separated in two rooms communicating through cameras	Natural scenario (live dialog)	Power spectral density (PSD), weighted PLV	This hyperscanning study using simultaneous EEG/MEG is the first to identify the oscillations and interbrain phase synchronization involved in turn-taking verbal interactions

Table 2 (*continued*)

Table 2 (*continued*)

Authors	Neuroimaging methods	Subjects	Paradigms	Analytic method	Main discoveries/contributions
Kawasaki *et al.*, 2018, *Neuropsychologia*	Two 27-channel EEG	17 pairs; gender: 8 F-F; 7 M-M; 2 mixed; relationship: 6 pairs were strangers and 11 pairs were acquaintances; situation: back to back	Coordination task (match their partners' tapping intervals using visual feedback)	PLV	Alpha-(approximately 12 Hz) and beta-(approximately 20 Hz) amplitude modulation in the left motor areas
Ciaramidaro *et al.*, 2018, *Sci Rep*	One 128-channel EEG was separated into two 64-channel EEG	21 pairs; gender: all male; relationship: N/A; situation: N/A	Third party punishment game	G-causality (partial directed coherence), graph theory	To their knowledge, this report is the first multiple-brain connectivity study to investigate empathic compassion and altruistic punishment
Goldstein *et al.*, 2018, *PNAS*	One 64-channel EEG was separated into two 32-channel EEG	22 couples (4 were married); situation: side by side with face to face	Natural scenario (perceiving pain under touch/no-touch condition)	Circular correlation coefficients	Hand-holding during pain administration increases brain-to-brain coupling in a network that mainly involves the central regions of the pain target and the right hemisphere of the pain observer. Moreover, brain-to-brain coupling in this network was found to correlate with analgesia magnitude and observer's empathic accuracy

Main discoveries/contributions were directly extracted or adapted from the articles' abstracts. *PNAS*, *Proceedings of the National Academy of Sciences of the United States of America*; *SCAN*, *Social Cognitive and Affective Neuroscience*; N/A, not available means the authors did not explicitly depict their subjects' relationship or the exact number of gender pairs even though some studies addressed the overall numbers of genders.

been performed to examine the neural synchronizations in coordination/joint movements (9,15,16,20,22,24,29). One example was illustrated in the previous reports (20,24), in which dyads were instructed to synchronize with each other by counting in their mind rhythmically. This study also examined how the social context such as threats, or oxytocin, affected the coordinated movements (20,24), which showed that oxytocin can enhance inter-brain synchronization to facilitate social coordination (20).

Eye contact/gaze tasks

The third category was the eye contact or gaze tasks, in which dyads are instructed to look in each other's eyes, or look towards the third object. Interestingly, the mutual gaze or eye-to-eye contact has the functions that offer pivotal social cues in social interaction and communication. In particular, a universally recognized social link or a pipeline can be established during a non-verbal communication through eye contact or a mutual gaze (35). Importantly, we can infer the others' intentions as well using eye-to-eye contact (50). Further, eye-to-eye contact, through which reciprocal information between individuals are dynamically exchanged, provides a great opportunity to model the neural mechanisms of human interpersonal communication by hyperscanning neuroimaging techniques (35,50). For example, an interesting study was performed, in which the dyads were instructed to look at each other's eyes or eyes in portraits (35). And they discovered that the inter-brain coherence of the left superior temporal, middle temporal and supramarginal gyri as well as the pre- and supplementary motor cortices were significantly increased in the eye-to-eye contact case when compared to the data from the eye-to-picture gaze case (35).

Table 3 fNIRS hyperscanning

Authors	Neuroimaging methods	Subjects	Paradigms	Analytic method	Main discoveries/contributions
Cui *et al.*, 2012, *Neuroimage*	22-channel for each subject within one fNIRS system (frontal lobe)	11 pairs; gender: 8 mixed; 2 F-F; 1 M-M; relationship: 3 pairs were strangers and 8 pairs were acquaintances; situation: side by side	Cooperation and competition task	WTC	This work represents the first use of a single NIRS instrument for simultaneous measurements of brain activity in two people
Holper *et al.*, 2012, *Neuroimage*	Two 4-channel wireless fNIRS sensors (premotor cortices)	8 pairs; gender: N/A (7 F; 9 M); relationship: N/A; situation: face to face	Coordination/ joint tasks (a paced finger-tapping task)	WTC; GC	The signal of the model G-caused that of the imitator to a greater extent as compared to vice versa
Jiang *et al.*, 2012, *JN*	20-channel for each subject within one fNIRS system (left frontal, temporal, and parietal cortices)	10 pairs; gender: 4 M-M; 6 F-F; relationship: acquaintance; situation: face to face; back to back	Natural scenario (live dialog)	WTC; Fisher linear discrimination analysis	Face-to-face communication, particularly dialog, has special neural features that other types of communication do not have and that the neural synchronization between partners may underlie successful face-to-face communication
Cheng *et al.*, 2015, *Human Brain Mapping*	22-channel for each subject within one fNIRS system (frontal lobe)	45 pairs; gender: 16 mixed; 14 M-M; 15 F-F; relationship: stranger; situation: side by side	Cooperation and competition task (task from Cui *et al.*, 2012)	WTC	Partners with opposite gender showed significant task-related cross-brain coherence in frontal region whereas the cooperation in same gender dyads was not associated with such synchronization
Jiang *et al.*, 2015, *PNAS*	10-channel for each subject within one fNIRS system (left IFC and TPJ)	12 three-person groups; gender: 6 female groups; 6 male groups; relationship: stranger; situation of pairs: face to face	Natural scenario (group discussion)	WTC; GC; Fisher linear discrimination analysis	These results suggest that leaders emerge because they are able to say the right things at the right time
Liu *et al.*, 2015, *Brain & Cognition*	19-channel for each subject within one fNIRS system (the bilateral frontoparietal)	10 pairs; gender: 7 M-M; 3 F-F; relationship: N/A; situation: side by side with no board	Cooperation and competition task (a turn-taking game)	Pearson correlation (time domain)	The competitor may actively trace the builder's disk manipulation, leading to deeper mind-set synchronization in the competition condition, while the cooperator may passively follow the builder's move, leading to shallower mind-set synchronization in the cooperation condition
Osaka *et al.*, 2015, *Frontiers in Psychology*	34-channel for each subject within one fNIRS system (bilateral hemisphere)	29 pairs; gender: 17 M-M; 12 F-F; relationship: stranger; situation: face to face; separated by a board	Natural scenario (sing)	WTC	A significant increase in the neural synchronization of the left inferior frontal cortex compared with singing or humming alone

Table 3 (*continued*)

Table 3 (*continued*)

Authors	Neuroimaging methods	Subjects	Paradigms	Analytic method	Main discoveries/contributions
Tang *et al.*, 2016, *SCAN*	19-channel for each subject within one fNIRS system (right dlPFC and TPJ)	97 pairs; gender: 52 F-F; 45 M-M; relationship: stranger; situation: face to face; separated by a board	Game theory (ultimatum game)	WTC	FNIRS results indicated increased interpersonal brain synchronizations during face-to-face interactions in rTPJ (but not in rDLPFC) with greater shared intentionality between partners
Nozawa *et al.*, 2016, *Neuroimage*	Four 2-channel wireless fNIRS devices (frontopolar)	12 groups of four subjects; gender: 5 male groups; 4 female groups; 3 mixed group; relationship: 2 groups were strangers and 10 groups were acquaintances; situation: face to each other	Cooperation task (a modified Japanese cooperative word-chain game)	WTC	This study provides a prospective technical basis for future hyperscanning studies during daily communicative activities
Pan *et al.*, 2016, *Human Brain Mapping*	22-channel for each subject within one fNIRS system (right frontoparietal region)	All male-female pairs; 17 lover pairs; 16 friend pairs; 16 stranger pairs; situation: pairs were separated by a board	Cooperation and competition task (task from Cui *et al.*, 2012)	WTC; GC	Lover dyads demonstrated increased IBS in right superior frontal cortex. Lover dyads revealed stronger directional synchronization from females to males than from males to females
Liu *et al.*, 2016, *Frontiers in Human Neuroscience*	19-channel for each subject within one fNIRS system (rPFC; rSTS)	9 pairs; gender: 5 mixed; 2 M-M; 2 F-F; relationship: stranger; situation: face to face	Natural scenario (playing the Jenga™)	WTC	BA9 may be particularly engaged when theory-of-mind (ToM) is required for cooperative social interaction
Baker *et al.*, 2016, *Sci Rep*	19-channel for each subject within one fNIRS system (rPFC; r-temporal cortex)	111 pairs; gender: 34 mixed; 39 M-M; 38 F-F; relationship: stranger; situation: side by side	Cooperation task (task from Cui *et al.*, 2012)	WTC	Female/female dyad's exhibited significant inter-brain coherence within the right temporal cortex, while significant coherence in male/male dyads occurred in the right inferior prefrontal cortex
Hirsch *et al.*, 2017, *Neuroimage*	42-channel for each subject within one fNIRS system with eye-tracking (bilateral hemisphere)	19 pairs; gender: 10 mixed; 6 F-F; 3M-M; relationship: participants were either strangers prior to the experiment or casually acquainted as classmates; situation: face to face	Eye contact/ gaze tasks (eye to eye contact)	WTC; PPI	A left frontal, temporal, and parietal long-range network mediates neural responses during eye-to-eye contact between dyads
Zhang *et al.*, 2017, *Sci Rep*	19-channel for each subject within one fNIRS system (frontal and left temporal cortices)	30 pairs; gender: 13 M-M; 17 F-F; relationship: stranger; situation: face to face	Natural scenario (a card game)	WTC; GC	This study was the first to investigate such inter-brain correlates of deception in real face-to-face interactions

Table 3 (*continued*)

Table 3 (*continued*)

Authors	Neuroimaging methods	Subjects	Paradigms	Analytic method	Main discoveries/contributions
Liu *et al.*, 2017, *Sci Rep*	48-channel for each subject within one fNIRS system (bilateral hemisphere)	22 pairs; gender: all male; relationship: level of friendship was assessed by using a self-report questionnaire; situation: side by side	Cooperation and competition task (a turn-taking game, same as Liu *et al.*, 2015)	linear regression analysis (time domain)	The right pSTS may be commonly involved in both cooperation and competition tasks while the right IPL may be more important for competition task
Xue *et al.*, 2018, *Neuroimage*	46-channel for each subject within one fNIRS system (prefrontal cortex and rTPJ)	30 pairs; gender: N/A; relationship: stranger; situation of pairs: face to face	Natural scenario (solve a realistic presented problem)	WTC	When two less-creative individuals worked on a creativity problem together, they tended to cooperate with each other (indicated by both behaviour index and increased IBS at rDLPFC and rTPJ), which benefited their creative performance
Reindl *et al.*, 2018, *Neuroimage*	22-channel for each subject within one fNIRS system (prefrontal cortex)	30 pairs; gender: 13 mother-daughter pairs; 17 mother-son pairs; 1 father-daughter pair; 2 father-son pairs; relationship: parents with their own kids; situation: side by side; situation of pairs: side by side with no board	Cooperation and competition task (adopted from Cui *et al.*, 2012)	WTC	Brain-to-brain synchrony may represent an underlying neural mechanism of the emotional connection between parent and child, which is linked to the child's development of adaptive emotion regulation
Dai *et al.*, 2018, *Nature Communications*	11-channel for each subject within one fNIRS system (left frontal, temporal, and parietal cortices)	21 groups of three subjects; gender: 11 male groups; 10 female groups; relationship: stranger; situation: face to face; back to back	Natural scenario (group discussion)	WTC	Selectively enhanced interpersonal neural synchronization (INS) between the listener and the attended speaker at left temporal–parietal junction, compared with that between the listener and the unattended speaker across different multi-speaker situations

Main discoveries/contributions were directly extracted or adapted from the articles' abstracts. *PNAS*, *Proceedings of the National Academy of Sciences of the United States of America*; *SCAN*, *Social Cognitive and Affective Neuroscience*; N/A, not available, meaning the authors did not explicitly depict their subjects' relationship or the exact numbers of gender pairs even though some studies addressed the overall numbers of genders; WTC, wavelet transform coherence; GC, granger causality; PPI, psychophysiological interaction.

Economic games involving game theory/exchange tasks

The fourth category is playing economic games/exchange tasks, in which one participant provided an economic offer while the counterpart need to make a decision on whether they wanted to take it or not. Game theory can offer a rich collection of both behavioral tasks and well-specified models aiming to articulate social interactions where decision-makers have to interact with one another (58). By contrast, exchange is the most basic type of social interaction, which involves a social process whereby social behavior is exchanged for some type of reward for equal or greater value. One instantiation of game theory/exchange is the trust game, in which one participant need decide how much money should be returned to your opponent (52), as illustrated in *Figure 3A*. One hyperscanning study illustrated that the paracingulate cortex is critically involved in building a trustworthy relationship (54). In addition, the prisoner's dilemma game was also utilized as a task for the design of hyperscanning. This required the two participants

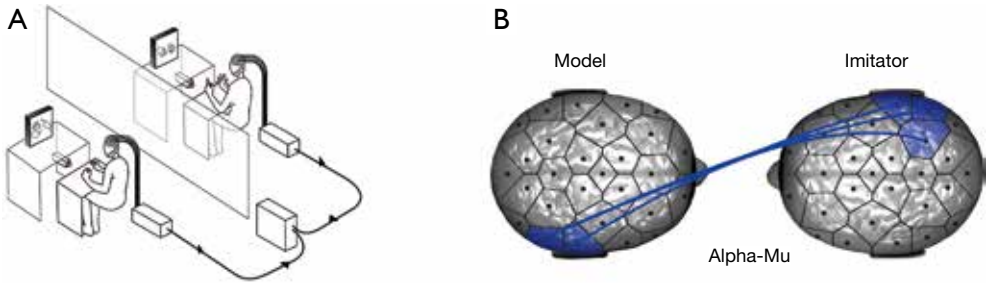

Figure 2 An example study of imitation tasks. (A) Schematic of the imitation task. One participant imitated the second one's movements through cameras. (B) EEG hyperscanning results based on the imitation task. Inter-brain synchronization of the right centroparietal regions at alpha-mu band was associated with the interactional synchrony. (A) and (B) were adopted from reference (17) under the terms of the Creative Commons Attribution License. EEG, electroencephalograph.

to make their own decisions simultaneously (*Figure 3B*). The prisoner's dilemma game usually consists of three experimental conditions: win-win, lose-lose, and a tit for tat case (14,21,27). Interestingly, previous reports have demonstrated that the decision to defect can be decoded in advance by monitoring the changes of connectivity patterns, as shown in *Figure 3C* (21). Further, the ultimatum game is also applied to the paradigm design for hyperscanning (*Figure 3D*), in which one participant need decide to take your opponent's offer or not (34,55).

Cooperation and competition tasks

The fifth category is cooperation and competition tasks, in which participants need to achieve a goal cooperatively or competitively. Cooperation and competition tasks are ubiquitous, in which goals should be obtained efficiently. One representative paradigm used in the hyperscanning studies was to explore the brain synchronization's underlying cooperation or competition, as plotted in *Figure 4A*, which consisted of three conditions: the cooperate, competitive, and control conditions (31). Interestingly, this paradigm was first initiated in 2012, and later was utilized to examine the brain coherence differences between groups of the same sex and of mixed sexes (*Figure 4B*) (40,44), groups with lovers and strangers (*Figure 4C*) (42), or groups with parents verse the child and the stranger verse the child (38). In addition, other paradigm designs were also formulated to inspect the inter-brain synchronization engaged in cooperation and competition (13,32,41,46).

Natural scenario

The paradigms mentioned above do offer great opportunities in inspecting the inter-brain dynamics during social interaction. However, only social interaction through a natural scenario can reflect the real situations in our daily life, which is also the dominated way of communication and thought exchange. An interesting test has been performed, in which two participants were instructed to have conversations with each other while their neural data was concurrently recorded (25,26,28,33,36,39,51). Intriguingly, their findings showed that inter-brain synchronization was higher for a face-to-face talk case, as compared to that of the back-to-back talk case (39). In addition, neural synchronization under other circumstances was also explored, such as music playing (18,19), singing together (43), playing games (47,48) or taking a class (10). For example, one study showed that during class time, students' brainwaves are more in sync with each other while they are highly engaged in the teaching (10).

Neural systems involved in hyperscanning during social interaction

Two main neural systems are involved in inter-brain connections (1,2,5). One is the MNS, which includes the primary motor cortex and posterior parietal cortex. The second one is the MS, which consists of the temporal-parietal junction (TPJ), precuneus and prefrontal cortex (PFC).

MNS

When we imitate or even just see the others' actions or movements, neurons in the MNS are fired. This phenomenon was discovered in both monkey and human brains (56). In human brains, the MNS (*Figure 5*) consists of the inferior frontal gyrus (IFG) and inferior parietal lobule

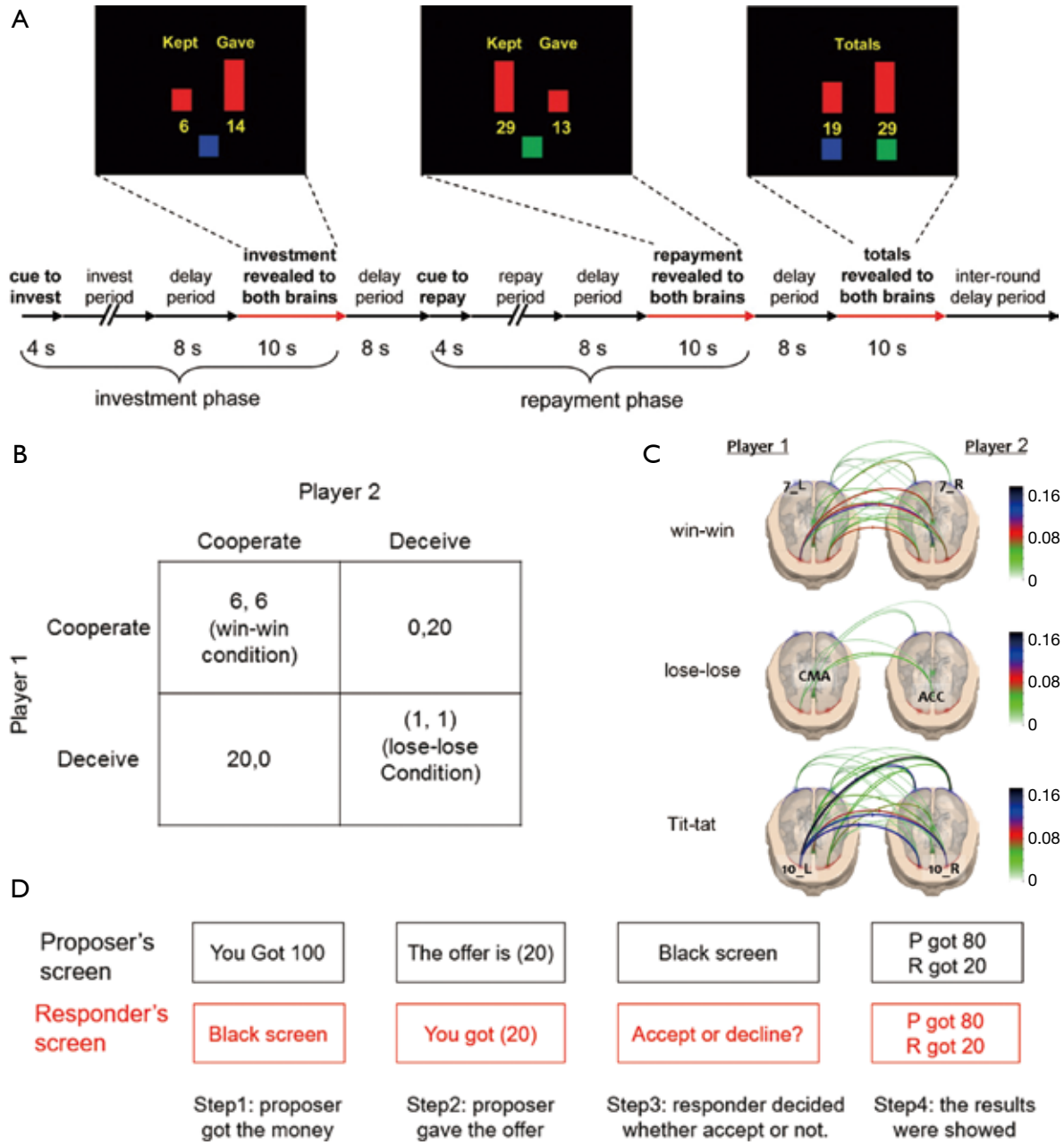

Figure 3 Procedures of three economic tasks involving game theory. (A) Schematic of the trust game. Two participants are denoted as "investor" or "trustee". The investor is assigned with amount of money ($20) and then decided how much to give to the trustee as an investment. After the decision made by the investor with amount of money ($14), the investment income would be tripled ($42). At this time, the trustee needs decide how much to be returned to the investor ($13). The results would be that the investor and trustee get $19 and $29, respectively (52). (B) Schematic of prisoner's dilemma game. Win-win condition denotes that the two participants trust each other and they both win the rewards. Lose-lose condition represents that the two individuals deceive each other, and they both lose the money. Tit for tat condition denotes that if your partner deceives you, you might do the same in the next round as a counterattack. (C) The brain synchronization at alpha band under different conditions (21). (D) Schematic of the ultimatum game. Two participants were randomly assigned to a 'proposer' who gave the offer or 'responder' who decided whether to accept the offer or not. (A) was adapted from (52) with permission from The American Association for the Advancement of Science. (C) was adapted from (21) under the terms of the Creative Commons Attribution License.

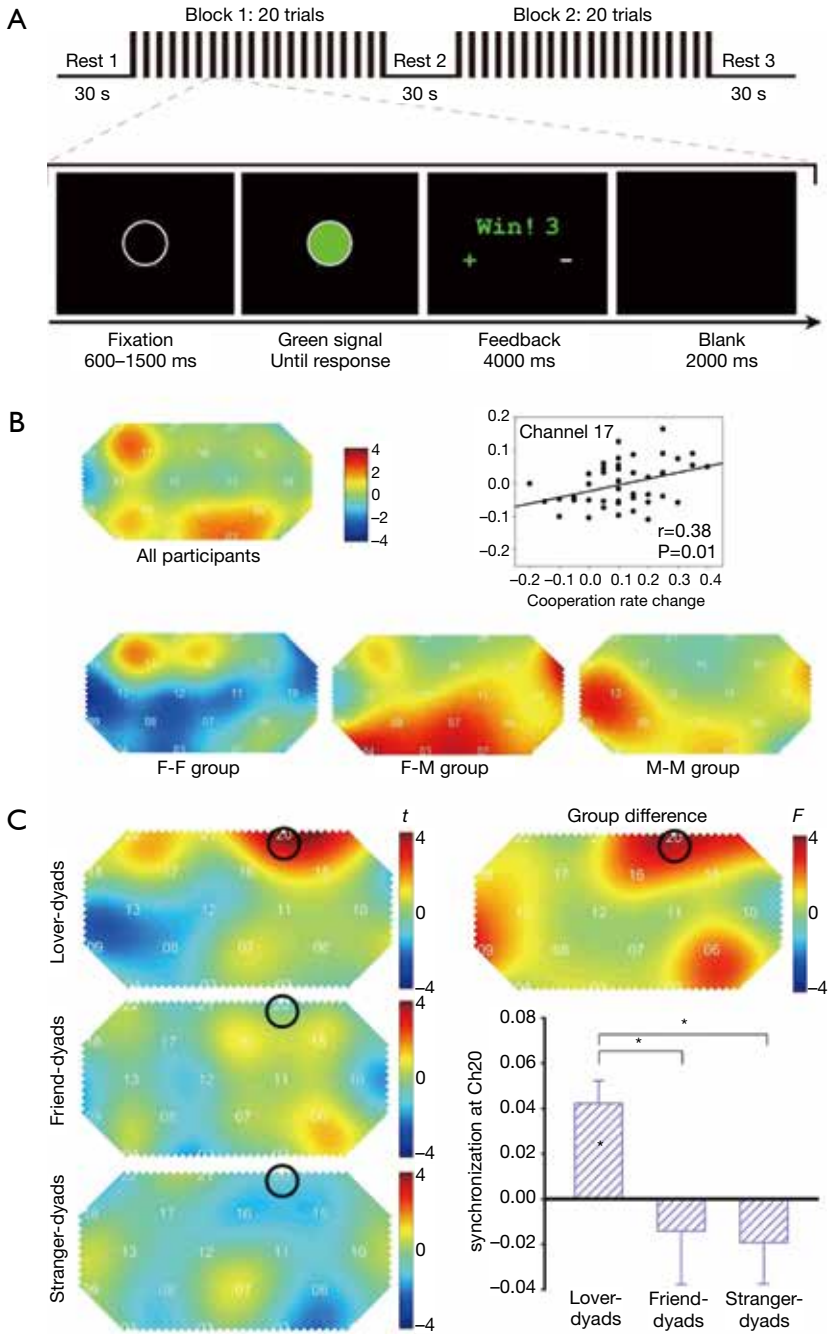

Figure 4 An instantiation of cooperation and competition tasks. (A) Schematic of the cooperation and competition tasks. In cooperate condition, both participants needed press a button as soon as possible after seeing blue circles. If their respond time difference was smaller than the threshold, both of them got the rewards. However, if the difference was larger than the threshold, they should get nothing. In competition condition, after seeing the blue circle, the one who responded faster won the game. In control condition, one participant reacted to blue circles and the other one just watched it (42). (B) Inter-brain coherence underlying the cooperation condition for different gender groups. F-F represented female-female, M-M denoted male-male, and F-M denoted female-male. (C) Inter-brain synchronization underlying cooperation condition associated with different relationships. (A-C) were adapted from (40,42) with permission from John Wiley and Sons.

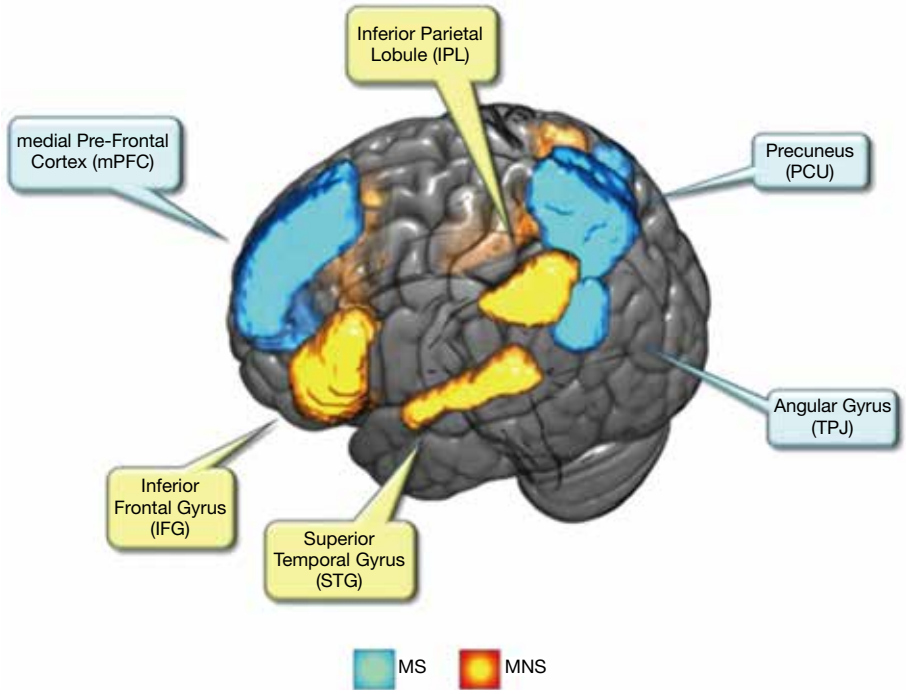

Figure 5 Two main brain systems involved in social interaction. This picture was adapted from reference (67) under a Creative Commons Attribution 4.0 International License (http://creativecommons.org/licenses/by/4.0/).

(IPL), which is related to language, motor and sensory detection. In addition, the superior temporal gyrus (STG) also plays an essential role in imitations, which can provide additional visual information inputs (56), in which the encoded information of imitated actions is first transformed into a more sophisticated visual representation through STG and then is delivered to the IPL. Once the IPL is activated, potential movements are able to be executed. In addition, the IFG is also activated to manipulate the potential action, which can provide additional supplemental information, such as the goal of the action.

The present hyperscanning studies associated with imitation show empirical evidence that MNS is involved in dual participant imitation (8,17). For example, one study demonstrated that when two participants were synchronized in behaviors, their brains were also tuned to the same frequency. Consequently, an inter-brain sychornizing network in the alpha-mu band between the right centroparietal regions was produced (*Figure 2B*).

MS

Besides imitating others' actions, we might as well try to understand others' intentions or emotions by their gestures, behaviors and facial expressions, which is termed as mentalizing (57,68). The TPJ and PFC particularly, and the dorsomedial PFC (DMPFC) are the two main brain regions associated with the mentalizing process (68).

The TPJ is the boundary brain region between the temporal and parietal cortex, which is labelled in a red circled area in *Figure 5* (67). As depicted in a previous study (69), the mentalizing process contains two steps. In the first step, the static social images are coded as a neural representation from the extrastriate body area. For step two, the encoded representations are constructed to generate moving social entities, and are then incorporated into a context for interpreting the intention. Interestingly, several fNIRS hyperscanning studies have highlighted the TPJ as their region of interest (33,34,39). For example, in an adapted version of the ultimatum game, the interpersonal brain coherence for the right TPJ was higher for underlying the face-to-face condition, than that of the face blocked condition. This indicated the functions of right TPJ, is collaborative in social interactions (34).

The PFC, likes a commander, is also involved in the mentalizing processes. It is responsible for the planning, regulation, integrating of information, and other high cognitive functions. Accumulated neuroimaging evidences

have shown that the PFC was related to interpersonal brain synchronization (31-34,39,41). For example, the inter-brain coherence in left inferior frontal cortex was significantly higher in face-to-face dialogues, than those from back-to-back dialogues, face-to-face monologue, or back-to-back monologues (39).

In summary, both MNS and MS play vital roles in social interactions, although the relationship between them is still unclear. A few studies demonstrated that they are collaborated (70), whereas additional reports also stated that MNS is inferior to MS (57).

Future perspectives and clinical implications of hyperscanning

Multimodality hyperscanning

Further investigation should be performed by using EEG-fNIRS, fNIRS-fMRI or EEG-fMRI hyperscanning techniques, since the multimodality neuroimaging methods can take advantage of the high temporal resolution of the EEG/fNIRS and the high spatial resolutions of an fMRI. To date, hyperscanning studies that utilize two or three neuroimaging modalities (e.g., EEG & fNIRS fusion) have not been extensively examined. Interestingly, multimodality can provide us new perspectives that a single modality cannot offer, because each neuroimaging method possesses its own advantages. For example, our group recently discovered that a combed EEG and fNIRS can enhance the sensitivity of lie detections (71). Although this is not a hyperscanning study, it enlightens us to more intriguing results or findings about the inter-brain dynamics which can be identified by applying a multimodality hyperscanning method for testing social interaction. In particular, more linked neural information can be revealed, based on the fused measures from neurovascular and neuroelectrical signals, which enable us to gain a more full understanding of the inter-brain effects during social interactions in our daily life.

Applications of hyperscanning in education and interrelationships

For most of the hyperscanning studies, neural data were recorded with two participants simultaneously, although several studies were also conducted by acquiring the brain signals from three or multiple participants (10,33,36). However, inspecting multiple individuals' brain dynamics is crucial in some circumstances such as for the teaching and education settings. For example, one study demonstrated that students' brain-to-brain group synchrony can track not only classroom engagement but also classroom social dynamics (10). But they did not explore the neural dynamics between teachers and students. In addition, the teaching style that can stimulate students' inter-brain synchronization by inspecting the neural dynamics between teachers and students should be further investigated.

Interestingly, hyperscanning can also be applied to examining the interactions between an adult and a child (11,38) and interpersonal relationships, such as lovers (12,25,42). For example, lovers who held their hands together exhibited their capability in alleviating their pain perception (12).

Clinical implications

The hyperscanning method has exhibited a potential for the study of inter-brain synchronization of normal individuals during social interaction. In contrast, hyperscanning of abnormal individuals might manifest an aberrant, or null interpersonal dynamics for disorder detection, particularly those in social deficiencies such as autism and schizophrenia. For example, a previous hyperscanning study showed that autism patients have the ability in recognizing their counterparty's intentions, but they cannot convey this information (72). To date, inspecting the interpersonal neural synchronizations among aberrant populations is still lacking. As a result, it is urgent for us to elucidate the neural mechanisms underlying those social deficits disorders by hyperscanning (1), which can pave a new avenue for improving the detection and treatment of neurological or psychiatric disorders.

Acknowledgements

Funding: This work was supported by the University of Macau (MYRG2016-00110-FHS and MYRG2018-00081-FHS), and the Macao Science and Technology Development Fund (FDCT 025/2015/A1 and FDCT 0011/2018/A1).

Footnote

Conflicts of Interest: The authors have no conflicts of interest

to declare.

References

1. Hari R, Kujala MV. Brain basis of human social interaction: from concepts to brain imaging. Physiol Rev 2009;89:453-79.
2. Hasson U, Ghazanfar AA, Galantucci B, Garrod S, Keysers C. Brain-to-brain coupling: a mechanism for creating and sharing a social world. Trends Cogn Sci 2012;16:114-21.
3. Van Overwalle F. A dissociation between social mentalizing and general reasoning. Neuroimage 2011;54:1589-99.
4. Van Overwalle F. Social cognition and the brain: a meta-analysis. Hum Brain Mapp 2009;30:829-58.
5. Schilbach L, Timmermans B, Reddy V, Costall A, Bente G, Schlicht T, Vogeley K. Toward a second-person neuroscience. Behav Brain Sci 2013;36:393-414.
6. Montague PR, Berns GS, Cohen JD, McClure SM, Pagnoni G, Dhamala M, Wiest MC, Karpov I, King RD, Apple N. Hyperscanning: simultaneous fMRI during linked social interactions. Neuroimage 2002;16:1159-64.
7. Babiloni F, Astolfi L. Social neuroscience and hyperscanning techniques: past, present and future. Neurosci Biobehav Rev 2014;44:76-93.
8. Ménoret M, Varnet L, Fargier R, Cheylus A, Curie A, Des Portes V, Nazir TA, Paulignan Y. Neural correlates of non-verbal social interactions: a dual-EEG study. Neuropsychologia 2014;55:85-97.
9. Konvalinka I, Bauer M, Stahlhut C, Hansen LK, Roepstorff A, Frith CD. Frontal alpha oscillations distinguish leaders from followers: multivariate decoding of mutually interacting brains. Neuroimage 2014;94:79-88.
10. Dikker S, Wan L, Davidesco I, Kaggen L, Oostrik M, McClintock J, Rowland J, Michalareas G, Van Bavel JJ, Ding M. Brain-to-brain synchrony tracks real-world dynamic group interactions in the classroom. Curr Biol 2017;27:1375-80.
11. Leong V, Byrne E, Clackson K, Georgieva S, Lam S, Wass S. Speaker gaze increases information coupling between infant and adult brains. Proc Natl Acad Sci U S A 2017;114:13290-5.
12. Goldstein P, Weissman-Fogel I, Dumas G, Shamay-Tsoory SG. Brain-to-brain coupling during handholding is associated with pain reduction. Proc Natl Acad Sci U S A 2018;115:E2528-37.
13. Szymanski C, Pesquita A, Brennan AA, Perdikis D, Enns JT, Brick TR, Müller V, Lindenberger U. Teams on the same wavelength perform better: Inter-brain phase synchronization constitutes a neural substrate for social facilitation. Neuroimage 2017;152:425-36.
14. Jahng J, Kralik JD, Hwang DU, Jeong J. Neural dynamics of two players when using nonverbal cues to gauge intentions to cooperate during the Prisoner's Dilemma Game. Neuroimage 2017;157:263-74.
15. Naeem M, Prasad G, Watson DR, Kelso JS. Electrophysiological signatures of intentional social coordination in the 10–12Hz range. Neuroimage 2012;59:1795-803.
16. Tognoli E, Lagarde J, DeGuzman GC, Kelso JS. The phi complex as a neuromarker of human social coordination. Proc Natl Acad Sci U S A 2007;104:8190-5.
17. Dumas G, Nadel J, Soussignan R, Martinerie J, Garnero L. Inter-brain synchronization during social interaction. PLoS One 2010;5:e12166.
18. Babiloni C, Buffo P, Vecchio F, Marzano N, Del Percio C, Spada D, Rossi S, Bruni I, Rossini PM, Perani D. Brains "in concert": frontal oscillatory alpha rhythms and empathy in professional musicians. Neuroimage 2012;60:105-16.
19. Babiloni C, Vecchio F, Infarinato F, Buffo P, Marzano N, Spada D, Rossi S, Bruni I, Rossini PM, Perani D. Simultaneous recording of electroencephalographic data in musicians playing in ensemble. Cortex 2011;47:1082-90.
20. Mu Y, Guo C, Han S. Oxytocin enhances inter-brain synchrony during social coordination in male adults. Soc Cogn Affect Neurosci 2016;11:1882-93.
21. De Vico Fallani F, Nicosia V, Sinatra R, Astolfi L, Cincotti F, Mattia D, Wilke C, Doud A, Latora V, He B. Defecting or not defecting: how to "read" human behavior during cooperative games by EEG measurements. PLoS One 2010;5:e14187.
22. Yun K, Watanabe K, Shimojo S. Interpersonal body and neural synchronization as a marker of implicit social interaction. Sci Rep 2012;2:959.
23. Toppi J, Borghini G, Petti M, He EJ, De Giusti V, He B, Astolfi L, Babiloni F. Investigating cooperative behavior in ecological settings: an EEG hyperscanning study. PLoS One 2016;11:e0154236.
24. Mu Y, Han S, Gelfand MJ. The role of gamma interbrain synchrony in social coordination when humans face territorial threats. Soc Cogn Affect Neurosci 2017;12:1614-23.
25. Kinreich S, Djalovski A, Kraus L, Louzoun Y, Feldman R. Brain-to-brain synchrony during naturalistic social interactions. Sci Rep 2017;7:17060.
26. Pérez A, Carreiras M, Duñabeitia JA. Brain-to-brain entrainment: EEG interbrain synchronization while

speaking and listening. Sci Rep 2017;7:4190.
27. Hu Y, Pan Y, Shi X, Cai Q, Li X, Cheng X. Inter-brain synchrony and cooperation context in interactive decision making. Biol Psychol 2018;133:54-62.
28. Ahn S, Cho H, Kwon M, Kim K, Kwon H, Kim BS, Chang WS, Chang JW, Jun SC. Interbrain phase synchronization during turn-taking verbal interaction—a hyperscanning study using simultaneous EEG/MEG. Hum Brain Mapp 2018;39:171-88.
29. Kawasaki M, Kitajo K, Yamaguchi Y. Sensory-motor synchronization in the brain corresponds to behavioral synchronization between individuals. Neuropsychologia 2018;119:59-67.
30. Ciaramidaro A, Toppi J, Casper C, Freitag C, Siniatchkin M, Astolfi L. Multiple-Brain Connectivity During Third Party Punishment: an EEG Hyperscanning Study. Sci Rep 2018;8:6822.
31. Cui X, Bryant DM, Reiss AL. NIRS-based hyperscanning reveals increased interpersonal coherence in superior frontal cortex during cooperation. Neuroimage 2012;59:2430-7.
32. Nozawa T, Sasaki Y, Sakaki K, Yokoyama R, Kawashima R. Interpersonal frontopolar neural synchronization in group communication: An exploration toward fNIRS hyperscanning of natural interactions. Neuroimage 2016;133:484-97.
33. Jiang J, Chen C, Dai B, Shi G, Ding G, Liu L, Lu C. Leader emergence through interpersonal neural synchronization. Proc Natl Acad Sci U S A 2015;112:4274-9.
34. Tang H, Mai X, Wang S, Zhu C, Krueger F, Liu C. Interpersonal brain synchronization in the right temporo-parietal junction during face-to-face economic exchange. Soc Cogn Affect Neurosci 2016;11:23-32.
35. Hirsch J, Zhang X, Noah JA, Ono Y. Frontal temporal and parietal systems synchronize within and across brains during live eye-to-eye contact. Neuroimage 2017;157:314-30.
36. Dai B, Chen C, Long Y, Zheng L, Zhao H, Bai X, Liu W, Zhang Y, Liu L, Guo T. Neural mechanisms for selectively tuning in to the target speaker in a naturalistic noisy situation. Nat Commun 2018;9:2405.
37. Holper L, Scholkmann F, Wolf M. Between-brain connectivity during imitation measured by fNIRS. Neuroimage 2012;63:212-22.
38. Reindl V, Gerloff C, Scharke W, Konrad K. Brain-to-brain synchrony in parent-child dyads and the relationship with emotion regulation revealed by fNIRS-based hyperscanning. Neuroimage 2018;178:493-502.
39. Jiang J, Dai B, Peng D, Zhu C, Liu L, Lu C. Neural synchronization during face-to-face communication. J Neurosci 2012;32:16064-9.
40. Cheng X, Li X, Hu Y. Synchronous brain activity during cooperative exchange depends on gender of partner: A fNIRS-based hyperscanning study. Hum Brain Mapp 2015;36:2039-48.
41. Liu T, Saito H, Oi M. Role of the right inferior frontal gyrus in turn-based cooperation and competition: a near-infrared spectroscopy study. Brain Cogn 2015;99:17-23.
42. Pan Y, Cheng X, Zhang Z, Li X, Hu Y. Cooperation in lovers: An f NIRS-based hyperscanning study. Hum Brain Mapp 2017;38:831-41.
43. Osaka N, Minamoto T, Yaoi K, Azuma M, Shimada YM, Osaka M. How two brains make one synchronized mind in the inferior frontal cortex: fNIRS-based hyperscanning during cooperative singing. Front Psychol 2015;6:1811.
44. Baker JM, Liu N, Cui X, Vrticka P, Saggar M, Hosseini SH, Reiss AL. Sex differences in neural and behavioral signatures of cooperation revealed by fNIRS hyperscanning. Sci Rep 2016;6:26492.
45. Xue H, Lu K, Hao N. Cooperation makes two less-creative individuals turn into a highly-creative pair. Neuroimage 2018;172:527-37.
46. Liu T, Saito G, Lin C, Saito H. Inter-brain network underlying turn-based cooperation and competition: A hyperscanning study using near-infrared spectroscopy. Sci Rep 2017;7:8684.
47. Zhang M, Liu T, Pelowski M, Yu D. Gender difference in spontaneous deception: A hyperscanning study using functional near-infrared spectroscopy. Sci Rep 2017;7:7508.
48. Liu N, Mok C, Witt EE, Pradhan AH, Chen JE, Reiss AL. NIRS-based hyperscanning reveals inter-brain neural synchronization during cooperative Jenga game with face-to-face communication. Front Hum Neurosci 2016;10:82.
49. Stolk A, Noordzij ML, Verhagen L, Volman I, Schoffelen J-M, Oostenveld R, Hagoort P, Toni I. Cerebral coherence between communicators marks the emergence of meaning. Proc Natl Acad Sci U S A 2014;111:18183-8.
50. Koike T, Tanabe HC, Okazaki S, Nakagawa E, Sasaki AT, Shimada K, Sugawara SK, Takahashi HK, Yoshihara K, Bosch-Bayard J. Neural substrates of shared attention as social memory: A hyperscanning functional magnetic resonance imaging study. Neuroimage 2016;125:401-12.
51. Spiegelhalder K, Ohlendorf S, Regen W, Feige B, van Elst LT, Weiller C, Hennig J, Berger M, Tüscher O. Interindividual synchronization of brain activity during live verbal communication. Behav Brain Res 2014;258:75-9.

52. King-Casas B, Tomlin D, Anen C, Camerer CF, Quartz SR, Montague PR. Getting to know you: reputation and trust in a two-person economic exchange. Science 2005;308:78-83.
53. Fliessbach K, Weber B, Trautner P, Dohmen T, Sunde U, Elger CE, Falk A. Social comparison affects reward-related brain activity in the human ventral striatum. Science 2007;318:1305-8.
54. Krueger F, McCabe K, Moll J, Kriegeskorte N, Zahn R, Strenziok M, Heinecke A, Grafman J. Neural correlates of trust. Proc Natl Acad Sci U S A 2007;104:20084-9.
55. Shaw DJ, Czekóová K, Staněk R, Mareček R, Urbánek T, Špalek J, Kopečková L, Řezáč J, Brázdil M. A dual-fMRI investigation of the iterated Ultimatum Game reveals that reciprocal behaviour is associated with neural alignment. Sci Rep 2018;8:10896.
56. Iacoboni M, Dapretto M. The mirror neuron system and the consequences of its dysfunction. Nat Rev Neurosci 2006;7:942-51.
57. Frith CD, Frith U. The neural basis of mentalizing. Neuron 2006;50:531-4.
58. Sanfey AG. Social decision-making: insights from game theory and neuroscience. Science 2007;318:598-602.
59. Rösler F. From single-channel recordings to brain-mapping devices: the impact of electroencephalography on experimental psychology. Hist Psychol 2005;8:95.
60. Zhang ZM, Wang MY, Guo X, Miao X, Zhang T, Gao D, Yuan Z. Attentional avoidance of threats in obsessive compulsive disorder: An event related potential study. Behav Res Ther 2017;97:96-104.
61. Cohen MX. Where does EEG come from and what does it mean? Trends Neurosci 2017;40:208-18.
62. Jackson AF, Bolger DJ. The neurophysiological bases of EEG and EEG measurement: A review for the rest of us. Psychophysiology 2014;51:1061-71.
63. Wang M-Y, Lu F-M, Hu Z, Zhang J, Yuan Z. Optical mapping of prefrontal brain connectivity and activation during emotion anticipation. Behav Brain Res 2018;350:122-8.
64. He Y, Wang MY, Li D, Yuan Z. Optical mapping of brain activation during the English to Chinese and Chinese to English sight translation. Biomed Opt Express 2017;8:5399-411.
65. Wang MY, Zhang J, Lu FM, Xiang YT, Yuan Z. Neuroticism and conscientiousness respectively positively and negatively correlated with the network characteristic path length in dorsal lateral prefrontal cortex: A resting-state fNIRS study. Brain Behav 2018:e01074.
66. Lloyd-Fox S, Blasi A, Elwell C. Illuminating the developing brain: the past, present and future of functional near infrared spectroscopy. Neurosci Biobehav Rev 2010;34:269-84.
67. Begliomini C, Cavallo A, Manera V, Becchio C, Stramare R, Miotto D, Castiello U. Potential for social involvement modulates activity within the mirror and the mentalizing systems. Sci Rep 2017;7:14967.
68. Saxe R. Uniquely human social cognition. Curr Opin Neurobiol 2006;16:235-9.
69. Carter RM, Huettel SA. A nexus model of the temporal–parietal junction. Trends Cogn Sci 2013;17:328-36.
70. Van Overwalle F, Baetens K. Understanding others' actions and goals by mirror and mentalizing systems: a meta-analysis. Neuroimage 2009;48:564-84.
71. Lin X, Sai L, Yuan Z. Detecting Concealed Information with Fused Electroencephalography and Functional Near-infrared Spectroscopy. Neuroscience 2018;386:284-94.
72. Chiu PH, Kayali MA, Kishida KT, Tomlin D, Klinger LG, Klinger MR, Montague PR. Self responses along cingulate cortex reveal quantitative neural phenotype for high-functioning autism. Neuron 2008;57:463-73.

Cite this article as: Wang MY, Luan P, Zhang J, Xiang YT, Niu H, Yuan Z. Concurrent mapping of brain activation from multiple subjects during social interaction by hyperscanning: a mini-review. Quant Imaging Med Surg 2018;8(8):819-837. doi: 10.21037/qims.2018.09.07

Review Article

Functional probes for cardiovascular molecular imaging

Yun Zeng[1], Jing Zhu[2], Junqing Wang[2,3], Paramanantham Parasuraman[4], Siddhardha Busi[4], Surya M. Nauli[5], Yì Xiáng J. Wáng[3], Rajasekharreddy Pala[2,5], Gang Liu[2]

[1]Department of Pharmacology, Xiamen Medical College, Xiamen 361008, China; [2]State Key Laboratory of Molecular Vaccinology and Molecular Diagnostics & Center for Molecular Imaging and Translational Medicine, School of Public Health, Xiamen University, Xiamen 361102, China; [3]Department of Imaging and Interventional Radiology, Prince of Wales Hospital, the Chinese University of Hong Kong, Shatin, Hong Kong SAR, China; [4]Departments of Microbiology, School of Life Sciences, Pondicherry University, Puducherry 605014, India; [5]Department of Biomedical and Pharmaceutical Sciences, School of Pharmacy, Chapman University, Irvine, California, USA

Correspondence to: Gang Liu. State Key Laboratory of Molecular Vaccinology and Molecular Diagnostics & Center for Molecular Imaging and Translational Medicine, School of Public Health, Xiamen University, Xiamen 361102, China. Email: gangliu.cmitm@xmu.edu.cn; Rajasekharreddy Pala. State Key Laboratory of Molecular Vaccinology and Molecular Diagnostics & Center for Molecular Imaging and Translational Medicine, School of Public Health, Xiamen University, Xiamen 361102, China; Department of Biomedical and Pharmaceutical Sciences, School of Pharmacy, Chapman University, Irvine, California, USA. Email: rrpala@chapman.edu; Yì Xiáng J. Wáng. Department of Imaging and Interventional Radiology, Prince of Wales Hospital, the Chinese University of Hong Kong, Shatin, Hong Kong SAR, China. Email: yixiang_wang@cuhk.edu.hk.

Abstract: Cardiovascular diseases (CVDs) are a severely threatening disorder and frequently cause death in industrialized countries, posing critical challenges to modern research and medicine. Molecular imaging has been heralded as the solution to many problems encountered in individuals living with CVD. The use of probes in cardiovascular molecular imaging is causing a paradigmatic shift from regular imaging techniques, to future advanced imaging technologies, which will facilitate the acquisition of vital information at the cellular and molecular level. Advanced imaging for CVDs will help early detection of disease development, allow early therapeutic intervention, and facilitate better understanding of fundamental biological processes. To promote a better understanding of cardiovascular molecular imaging, this article summarizes the current developments in the use of molecular probes, highlighting some of the recent advances in probe design, preparation, and functional modification.

Keywords: Cardiovascular disease (CVD); molecular imaging; probe

Submitted Jul 10, 2018. Accepted for publication Sep 17, 2018.
doi: 10.21037/qims.2018.09.19
View this article at: http://dx.doi.org/10.21037/qims.2018.09.19

Introduction

Cardiovascular diseases (CVDs) are considered the most threatening disorder among the global population and are a source of challenge in modern research and medicine (1). There is an urgent need to formulate sensitive and reproducible non-invasive technologies for early disease detection, more specific biomarkers and personalized treatment of CVDs. Many traditional medical imaging methodologies, such as computed tomography (CT), ultrasound, and magnetic resonance imaging (MRI), have been regularly employed to facilitate early diagnoses. These methods serve as a means to supervise early onset of CVDs. Since molecular differentiation is the basis of pathogenesis, traditional cardiovascular imaging technology has aimed at detecting a specific molecular target and fundamental biological development in CVDs (2). Accordingly, in recent years, molecular imaging technologies have been generally accepted in the role of rapid proliferating research interests that significantly promote the non-invasive diagnostic imaging for the conversion of anatomical description to detect specific tissue epitopes and monitor the fundamental biological developments at the cellular and subcellular level (3). Molecular imaging was created as a new branch

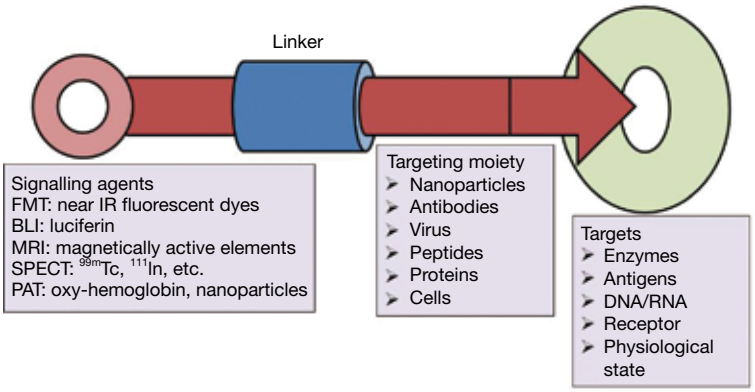

Figure 1 Schematic representation of molecular imaging probes. A molecular imaging probe is synthesized by using a linker to connect an imaging agent with a targeting moiety. FMT, fluorescence molecular tomography; BLI, bioluminescence imaging; MRI, magnetic resonance imaging; SPECT, single-photon emission computed tomography; PAT, photoacoustic tomography.

of biomedical science by merging the areas of imaging technology and probe utilization, thus enabling the direct/indirect spatio-temporal evaluation of molecular markers. In addition to this capability, molecular imaging can provide critical information for advanced diagnosis, appropriate treatment, better prognosis, improved staging, and better management—adding a significantly greater effectiveness to personalized medicine overall (4).

Cardiovascular molecular imaging technologies have been integrated with advanced scientific tools; this merger potentially allows for both morphological and functional imaging in cardiovascular pathophysiology. The emergence of cardiovascular molecular imaging provides detailed molecular and cellular level visualization that allows for early diagnostics and advanced therapeutics practices, which will additionally facilitate a greater understanding of the fundamental biological developments of CVDs. The mutual contribution among inter-disciplinary branches of science, such as molecular biology, chemistry, nanotechnology, and imaging technology, has effectively enhanced the rapid growth in the cardiovascular molecular imaging technologies and has allowed for the development of a large number of attractive new probes in the last decade. The appropriate probes should possess imaging, targeting, and therapeutic functions in order to facilitate the appropriate remedies in the battle against CVDs (2). In this section, we will first briefly describe the general working principles of molecular imaging-probe design, and then summarize the current state-of-the-art in probe-assisted cardiovascular molecular imaging.

Typical molecular imaging probes

Molecular imaging probes are agents that effectively facilitate visualization, quantification and characterization of biological processes in living systems. A molecular imaging probe typically comprises three key components: (I) an imaging agent for the corresponding imaging modality; (II) a targeting moiety that recognizes the intended molecular/cellular target; and (III) a linker connecting the imaging agent with the targeting moiety (*Figure 1*). The imaging agents used include radionuclides for positron emission tomography (PET) and single-photon emission computed tomography (SPECT), gadolinium (Gd) chelates or superparamagnetic iron oxide nanoparticles (SPIO) for MRI, fluorophores or quantum dots (QDs) for optical imaging, and microbubbles for ultrasound imaging. The targeting moiety, which specifically coordinates with the biomarker of a specific biological process, is also globally termed as a targeting ligand. The linker employed in the design of molecular imaging probes helps in merging the imaging agent with the targeting moiety, and has a significant impact on the pharmacokinetics of the molecular imaging probe. Concerning the latter point, many other distinct features are thus required to optimize the imaging quality; on the other hand, however, some probes do not even have the 3 essential components mentioned (5).

Favorable molecular imaging probes possess useful harness capabilities to gain concomitant anatomic, chemical, and physiological analytical report with high sensitivity, specificity and consistency. To diagnose the biochemical activity of CVDs, particularly at an initial stage, probes need to monitor

on the clinical change of a much lower amount of biomarker. Therefore, greater sensitivity is a critical requirement for a potential imaging probe. Amplification strategies such as augmented relaxivity of magnetic substrates or quenching of fluorochromes are the key strategies for developing sufficiently sensitive probes for clinical application. These probes can show a specific physical change that profoundly favors the signal amplification when the probes are spaced close together. In addition, due to the presence of numerous corroding enzymes and proteases in serum/tissue, maintenance of the intact structure of the imaging probes is a prerequisite to achieving high-quality images. The quantitative analysis of the image validity to assure the precession interpretation of physiological and pathological processes of the CVDs, along with the quality of molecular images, can be potentially affected by the *in vivo* stability of an imaging probe after administration (5).

Initially, the deposition of the imaging probes at the targeted site is required to allow the probes to actively interact with particular biomarkers like enzymes, receptors, and transporters, all which participate in different biological activities correlated with specific molecular/cell compartments. The specific interaction between biomarkers and imaging probes distinctly promotes the acquisition of information from the biological processes at the molecular level, which is effectively used to investigate and understand the distinct biological mechanisms underlying a specific disease. Additionally, the specificity between the imaging probe and the target site can potentially reduce the non-specific site interaction, significantly increasing the feasibility for quantification analysis of imaging output. Antibodies, peptides, aptamers and small organic molecules, have been widely and successfully employed as targeting agents for specific biomolecules in cardiovascular molecular imaging. The use of targeted imaging probes has the capacity to facilitate valuable insights into the pathophysiology of CVDs and to facilitate the development of novel therapeutic strategies (6).

Molecular imaging probes can be considered a special class of pharmaceuticals, especially some theranostics (the fusion of therapeutic and diagnostic approaches). Thus, potentiality and safety are the two most important concerns for molecular imaging probes. Generally, molecular imaging probes are administrated in low dose and their pharmacological manifestation can be negligible. However, the biological effects caused by an imaging probe still require close monitoring. The toxicity of molecular imaging probes is highly dependent on the probes' physicochemical properties, which include the size, surface charge/coating materials, probe dosage, and duration to probe exposure. In order to enhance the quality of patients' lives, there is urgent need to synthesize more biocompatible and less potentially harmful imaging probes (7,8).

Strategy for molecular imaging probes design: interdisciplinary efforts

Progress in molecular imaging highly depends on the designing of advanced probes that can effectively detect biological activities on the cellular and molecular level. The design and development of molecular imaging probes require interdisciplinary efforts from the molecular, biological, chemical, imaging and nanotechnology fields (*Figure 2*). These interdisciplinary efforts can begin with the identification of biomarkers that are applicable to human CVD. Following this, physicochemical expertise is needed to synthesize molecular imaging probes capable of interacting to the target, and to properly optimize the devices for imaging. Multifunctional imaging probes based on nanotechnology can then extend the limits of currently available molecular imaging and allow precision diagnosis, contributing greatly to the advancement of personalized medicine. However, optimism in this new technology must be tempered by consideration of its potentially harmful elements. For instance, many of the fluorophores, contrasting agents and tracers, could be toxic in nature and the right material and specific concentration needs to be first identified before a molecular imaging probe can be deemed safe to administer to patients. More specifically, a gamut of information including cytotoxicity, tissue toxicity, *in vivo* toxicity and mutagenicity, require documentation in relation to molecular imaging probes before these probes are considered suitable for biomedical application. In this regard, some fluorophores such as indocyanine green and fluorescein have had their toxicity profile's fully elucidated, and subsequently have been approved by the Food and Drug Administration (9).

Biomarker-basis of molecular imaging

Biomarkers can act as indicators of health by correlating with disease in physiological measurement, or as determiners of disease complexity, diagnosis and prognosis. In addition, biomarkers also provide signals of fundamental metabolic or pathophysiological activities, or provide pharmacological responses to interventions. The major

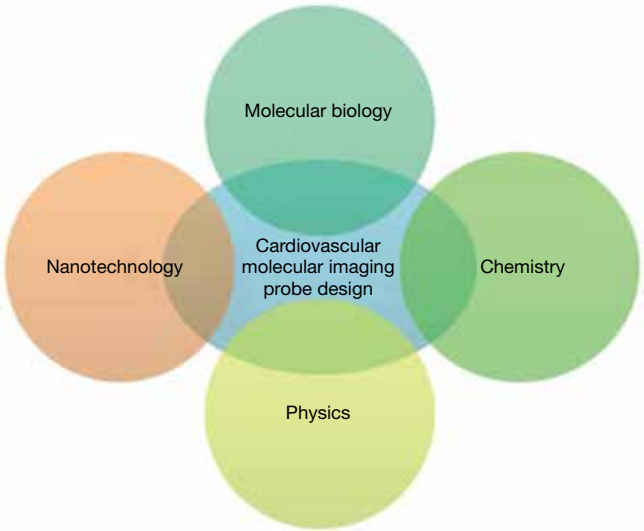

Figure 2 The designing and development of molecular imaging probes require interdisciplinary efforts from molecular, biological, chemical, physical imaging and nanotechnology sciences.

contributors to biomarker discoveries are molecular profiling studies in cardiovascular medicine, which are based on finding correlations between a molecular signature and a corresponding CVD behavior. Generally, molecular biomarkers include altered/mutant genes, proteins, lipids, and small metabolite molecules, which profiling studies then correlate with a biological behavior or a clinical consequence (10).

The selection of molecular imaging targets should meet certain criteria: They should specifically participate in the disease in question, particularly in CVD, and they should show the difference with respect to the progress and development of the disease. Biomarker determination and selection is therefore the initial, success-limiting step, in the designing of novel molecular imaging probes. As genomic and proteomic information from CVDs becomes increasingly available, databases to find new cellular/molecular biomarkers will provide a plethora of new targets for molecular imaging of CVDs (11). For example, vascular cell adhesion molecule-1, a well-validated marker of endothelial activation of atherosclerosis, could serve as a target for molecular imaging of atherosclerosis (12). Integrins such as $a_v\beta_3$, expressed by neovessels, are similarly employable for molecular imaging of atherosclerosis, and several ^{18}F-labeled affinity ligands have already been developed. The evidence above suggests that the molecular imaging of CVDs based on biomarkers is reaching beyond anatomy to encompass the assessment of aspects of molecular biology related to the pathogenesis of CVDs.

However, CVDs are highly complex and a set of biomolecules are unlikely to be able to detect most of the individual sensitivities related to developing CVD. The development of cardiovascular biomarkers then, naturally needs to overcome various obstacles. Research challenges include the development of probes for molecular imaging that will provide sensitive and robust measurement of thrombosis, infarction, angiogenesis, tissue oxygenation, activation and adhesion of immune cells. The molecular imaging probes also need a scalable synthesis using safe manufacturing processes and the necessary accompanying toxicology studies for human use. Much progress is being made in this field, and the rapidly expanding toolset of available molecular imaging probes will make it possible to non-invasively reveal the biological processes governing CVDs.

Chemistry-molecular probes synthesis

The design and development of a biologically active probe is of utmost importance to realizing the great potential of molecular imaging. By achieving the identification of select molecular biomarkers appropriate for the diagnosis of CVD, advanced chemistry has paved the way in molecular imaging probe synthesis. Specifically, click chemistry has made breakthroughs in a wide array of molecular imaging probe application developments. Within this field, it has become a routine strategy to fine-tune the synthesis of novel molecular imaging probes and to enhance their pharmacokinetic and pharmacodynamics profiles.

Generally, a 1:1 targeting moiety affinity towards the biomarker is considered suitable for molecular imaging. Biochemical amplification strategies are desirable to enhance the imaging signal in the cases where biomarker expression levels are low. The selected targeting moiety should have good affinity, particularly towards the selected biomarker. It also should possess a chemical anatomy that can transport different labels: isotopes for nuclear imaging, Gd for MRI or fluorescence, and dyes for optical imaging. For imaging technologies with intrinsic low sensitivity such as MRI, probes carrying large amounts of Gd allow for high molecular sensitivity (11).

The probe's *in vivo* pharmacokinetics, like adsorption, distribution, metabolism, and excretion, are gaining critical attention for their molecular imaging probe design potential. In general, the widely accepted factors that are believed to be significant in the probe's *in vivo* pharmacokinetics are its

particular physicochemical properties, including ionization constant, lipophilicity and stability. A molecular probe must remain stable enough in the blood circulation in order to effectively access the specifically targeted site with sufficient concentration and time for molecular imaging. Longer systemic circulation does provide greater target exposures that are highly suitable for therapeutic purposes. In cases where the molecular imaging probes are developed to image intracellular tissues, the probe needs to penetrate the cell membrane. Because ionization is a significant parameter that potentially increases/affects the solubility and membrane permeability of a molecule, most of the molecular imaging probes have been developed with ionizable groups and have different charges within the physiological pH range. Moreover, the recent developments in high-performance liquid chromatography/mass spectrometry instrumentation and procedures also provide an array of alternative techniques for determining the metabolites of the imaging probe—a capability which can amply facilitate necessary modification of the imaging probe and potentially enhance its *in vivo* stability (5,13).

Physics and advanced imaging devices

In CVDs, molecular imaging can diagnose, treat and monitor disease progress. Still, major modifications to these regular procedures need to be adopted in order to upgrade the imaging technologies in light of the concurrent development of more sophisticated molecular probes. At the time of writing, a large number of imaging modalities are under preclinical research, with some of them effectively being ready for investigation at the clinical stage. The predominant imaging modalities can be generally categorized as either anatomical imaging modalities like CT and ultrasound, or functional imaging modalities like PET, single-photon emission computed tomography (SPECT), optical imaging, molecular MRI, and magnetic resonance spectroscopy. From an engineering perspective, each imaging modality would benefit from an increased sensitivity and improved temporal and spatial resolution (2,4).

Anatomical imaging can provide anatomical information that is potentially altered by changes in the anatomy at the time of disease, while functional imaging modalities can determine biochemical activities of CVDs *in vivo* (2). Each imaging modality can be characterized by its own weaknesses and strengths. By exploiting the combined strengths of different imaging methods, a novel imaging technology might prove to be an attractive alternative to the already mentioned imaging technologies, thereby advancing the capacity to image both small animals and humans. Multimodality imaging was designed by merging different imaging techniques including anatomical, functional and molecular imaging. The sets of information of specific target sites from each imaging technique have been combined to create hybrid images that show characteristics superior to all the previously mentioned imaging technologies. Generally, multimodality imaging modalities are selected to provide synergistic, complementary, or clinically relevant data beyond that furnished by any one of the single-modality methods. For example, co-registration with MRI images provides the anatomic landscape for localizing the functional or molecular information generated by PET (14).

The ideal multimodal imaging approach should provide high precision information like the exact localization, extent, molecular change and metabolic activities of the targeted site, in addition to specifically highlighting the pathogenomic changes which eventually lead to disease. While this is still a comparatively young field, it is reasonable to expect that sometime in the future, the multimodal approach will have significantly advanced cardiovascular molecular imaging technology by formulating novel multifunctional probes. Fresh insights in hybrid imaging technology have already appreciably contributed to translational research in cardiovascular medicine with small and large animals. Nonetheless, the human anatomy's complex interlinking of organ function, (e.g., when the heart beat is affected by lung motion) yet demands further advancement be made in areas of cardiovascular imaging, such as motion detection devices (15-17).

Nanotechnology is a promising platform for multifunctional molecular imaging probe design

Nanotechnology is a multidisciplinary field and has made great strides forward in recent years. The term "nanotechnology" can generally be applied to any fabrication of new materials with a scale smaller than one hundred nanometers. Unique characteristic features like optical, electronic, magnetic, and chemical reactivity are associated with nanomaterials solely because of their nanoscale sizes, big surface area, and shapes, which can allow for various biomedical applications including molecular imaging. A wide variety of nanoparticles have been used as molecular probes with each imaging modality demanding nanoparticles with specific properties for contrast production. For example, SPIO have long

been investigated and are considered to have remarkable potential in MRI contrast enhancement. QDs, which show tunable wavelength photoluminescence from the visible region to near infrared (in accordance with their size), are among the most widely studied nanoparticles for optical imaging (18,19).

Nanoparticle imaging probes offer many advantages compared to conventional small-molecule-based imaging probes. These advantages include producing excellent contrast, lengthy circulation time, and integrating multiple properties. For example, hundreds (or more) imaging labels (fluorescence tags, radionuclides, and other biomolecules) or a group of labels for different imaging modalities, can be merged to formulate a novel single nanoparticle, thus providing drastic signal amplification. In addition, multiple and potentially different, targeting ligands (antibodies, peptides, aptamers, and small molecules) on the nanoparticle show increased binding affinity and specificity (20).

Recently, theranostics have been rapidly developing technology which can be employed as platforms for placing different functionalities not only for molecular imaging functions, but for targeted drug delivery as well. The combination of different imaging labels, targeting ligands, and therapeutics could permit the effective and controlled drug delivery to the targeted site, while providing noninvasive, quantitative monitoring in real time. Application of such multifunctional nanomaterial will potentially elevate the diagnostic validation and design of therapeutic practice, which can then in turn facilitate the prediction of clinical outcomes, realizing the hope of personalized and advance medicine (21). In recent years, the development of theranostic-based nanomedicines has gradually progressed due to the availability of better knowledge about molecular imaging technologies and the processes that occur at the basic molecular and cellular level during cell-exposure to certain therapeutic aids. The intimate understanding of mesenchymal stem cells (MSCs) and related mediated cancer therapy, has facilitated the formulation of theranostic probes which contain umbilical cord-derived MSCs conjugated with triple fusion genes containing the herpes simplex virus truncated thymidine kinase, Renilla luciferase and red fluorescent protein. By using near infrared imaging technology, the real-time activities of the cells can be monitored by bioluminescence signals provided by Renilla luciferase and red fluorescent protein. Hence, the formulated theranostic probe can effectively inhibit breast cancer progression by inducing tumor cell apoptosis and suppressing angiogenesis, in addition to facilitating the tracking of cell delivery and tumor response to MSCs and molecular and cellular activities in tumor cells (22). Similarly, other theranostic probes have been developed by conjugating MSCs with citrate-coated SPIO and investigated for their efficient labeling of human MSCs without transfection agents. The formulated theranostic probes showed no adverse effect in cell proliferation, presentation of typical cell surface marker antigen, and differentiation into the adipogenic and osteogenic lineages. Overall, the synthesized theranostic probes demonstrated very efficient capacity for intracellular magnetic labels for *in vivo* stem cell tracking by MRI (23).

The most promising applications of nanoplatform-based imaging probes appears to be in cardiovascular medicine. Imaging probes might be able to overcome the barriers of the biological system to accumulate the drug at the targeted site because certain barriers of the biological system potentially affect the drug entry and delivery (24). Still, there remains a significant concern as to the potential adverse effects of human exposure to nanoparticles. The biological distribution and circulation of nanoparticles within biological tissues, and immune responses like phagocytosis, opsonization and endocytosis of nanoparticles, are the specific considerations which seriously need to be to evaluated before the field of nanoparticles can be specialized into nanomedicine proper (19). In the design of probes for molecular imaging, several functionally active nanomaterials that have been employed have very low biocompatibility which can subsequently lead to quick excretion, instability, low circulating time, and potential toxicity. Hence, significant precaution and validation should be taken before adopting the nanomaterial in a biomedical application. PEGylation is widely known as a coating technology that is used effectively for nanoparticle formulation and can potentially enhance the blood circulation time by modulating the protein adsorption to the nanoparticle. The prolonged availability of the nanomaterial in the blood stream significantly augments the accumulation of higher concentrations of prescribed nanomaterial in the targeted site. Moreover, the surface-functionalized nanoparticles with polyethylene glycol (PEG), promote the bio-conjugation with various ligands including drug molecules. Several steps have been taken to reduce the risks posed by nanomaterials in order to enable the novel formulation of highly biocompatible and less toxic nanomedicines (e.g., silica nanoparticles) (25).

Other important questions concerning the application of nanomaterial in molecular imaging still need to be

answered before responsible clinical application is possible. These issues include a more thorough understanding of the following: the change that occurs in the association or conjugation between the nano-carrier and the drug molecules, particularly their pharmacokinetics, biodistribution and potential adverse effects of the nanotherapeutic nanomedicine; chance of change of the safety profile of the nanomaterial at the time of conjugation or surface functionalization; the possibility to reduce the toxicity of the polymeric nanoparticles which accumulate considerably at the targeted site and are made up of non-biodegradable polymer and greater than the size of the renal discharge threshold; and the adverse effects (and accompanying prevention measures), that could arise when nanomaterials cross the blood-brain barrier. The above topics are hitherto understudied; thus, clarifying them is critically significant to optimizing the selectivity, efficacy and safety of nanomaterials in clinical practice. Healthy interdisciplinary competition involving the scientific fields of physics, chemistry, biology, nanotechnology, engineering and medicine could contribute to each discipline's mutual development and the possible design of effective, cutting-edge nanomedicine for the diagnosis and treatment of clinical complications (26,27).

Potential developers of molecular imaging probes need to be aware of the specific properties of functional nanomaterials before they can be repurposed as effective nanoplatforms. The probes should be developed with optimality in features such as surface coating, targeting properties, and extent of biocompatibility, in order to create an assembly with the suitable contrast/therapeutics.

Optical imaging

Optical imaging of live tissues through photonic technology has emerged as a significant tool in advanced biomedical research. Optical imaging can be defined as a technique in which light in ultraviolet, visible or infrared ranges is used to visualize intact organisms. Certain optical imaging techniques like intracoronary optical coherence tomography, Raman spectroscopy and near infrared spectroscopy, are widely employed to inspect vascular cellular and lipid components in patients suffering from CVDs. Fluorescent probes are used to image the molecular phenotype more precisely. Near infrared fluorophores, which have an excitation and emission wavelength of 630 and 1,000 nm, have been employed in optical imaging technologies. Properties like high diffusibility, molecular targeting, and marking for angiogenesis make these fluorophores exceptional candidates for optical imaging technology (28,29). The optical imaging itself has a few advantages over rapid visualization protocols and other simpler methodologies. Fluorescence molecular tomography (FMT) and bioluminescence imaging (BLI) are the two major optical molecular imaging methods that have been employed to diagnose complications of the cardiovascular region. FMT is a recent innovation that permits greater spatial localization of the fluorescence signal, while BLI is another powerful tool for visualizing temporal and spatial development of cardiovascular complications in real time (30).

FMT

In the biomedical research area, microscopic florescence techniques are playing a major role in the study of molecular and cellular development in cell and tissue cultures. Using sophisticated labeling methods, the enhanced spatial resolution provided by florescence techniques, facilitates easy comparison between cellular dimensions and site targeted imaging. Currently, two- and three-dimensional (3D) optical imaging has been employed to investigate the biological activities in intact organisms like mammals. However, this method has come up against certain limitations such as poor light propagation in tissue, and difficulty in reconstruction of exact spatial information due the high scattering and absorbing capacity of biological tissues. As a result, the detection of the signal on the surface of the tissues will be stronger than the signal detected inside the embedded tissues because of the optical properties of the surrounding tissues. In an attempt to overcome these challenges, FMT techniques have been used to map the 3D distribution of a florescent probe or concentration of protein (31). FMT can be defined as any advanced tomographic technique which models the imaging in near infrared regions and facilitates the 3D quantitative detection of a fluorescence signal distribution in the live tissues of the small animal at any depth. Following this, nearly 50,000 to 100,000 pairs of source detectors have been used to measure the diffusion models of photon propagation in turbid media (32). The particularly high sensitivity of these optical imaging techniques potentially permits the detection in tissue of even low concentrations of targeted molecules. Furthermore, these methods are comparatively cost effective, which supports the biomedical research community by reducing their expense in research and development procedures (31). However, the effectiveness

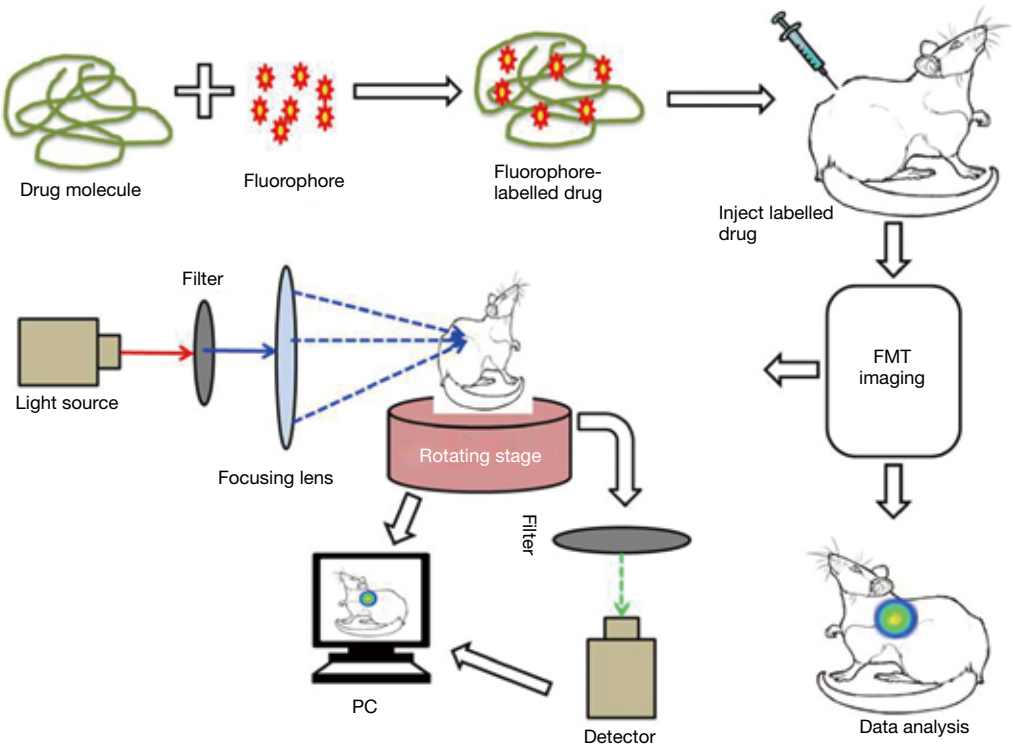

Figure 3 A schematic representation of the major components of the FMT system. FMT, fluorescence molecular tomography.

of the imaging agents in the *in vivo* condition could be highly dependent on certain factors such as probe targeting, activation, pharmacokinetics, biocompatibility and photophysics, which are all still not yet fully understood. Advancements in biomedical research have begun to investigate these variable factors as they concern the application of optical reporters for *in vivo* imaging (33).

A basic explanation of how the FMT method works is as follows. Light passes to the tissues of the animal body at different projections and signals are detected at multiple points in the tissue. The imaging prototype is generated using cylindrical geometry and charge-coupled device (CCD) detection methods. According to the recorded raw emission and excitation information, a synthetic assessment is developed and applied to the inversion code for the reconstruction of absolute fluorochrome density in the animal tissue (*Figure 3*). With the current available acquisition setup, the determination of threshold fluorochrome is approximately 200 femtomoles in the target tissues volume deep in a phantom enhances the optical properties of the tissues (34). In a separate experiment, a novel handheld device for the 3D fluorescence molecular tomography was described. The device is characterized by its bendable structure and miniaturized size (nearly 10 mm in diameter) which was particularly effective as an intraoperative tool for imaging the internal tissues and facilitating the image guide surgery (35). FMT can overcome the limitations encountered by traditional fluorescent imaging technology, such as poor images at shallow tissues depths due to scattering of signal, by increasing the number of source detectors, resulting in comparatively less background noise and high submillimeter resolution at a depth of 7.5 mm (36).

BLI

Novel approaches and technologies that facilitate the early detection of infections, even before the observation of visible clinical manifestations, result in effective diagnosis and treatment, by easing the selection of therapeutic procedures that start at these earlier stages of infection. Fluorescence molecular imaging extends several opportunities to explore the biological processes in intact organisms. Similarly, BLI is a method which works on a sensitive detection of visible light produced during the oxidation reaction between luciferase enzymes and the molecular subtract

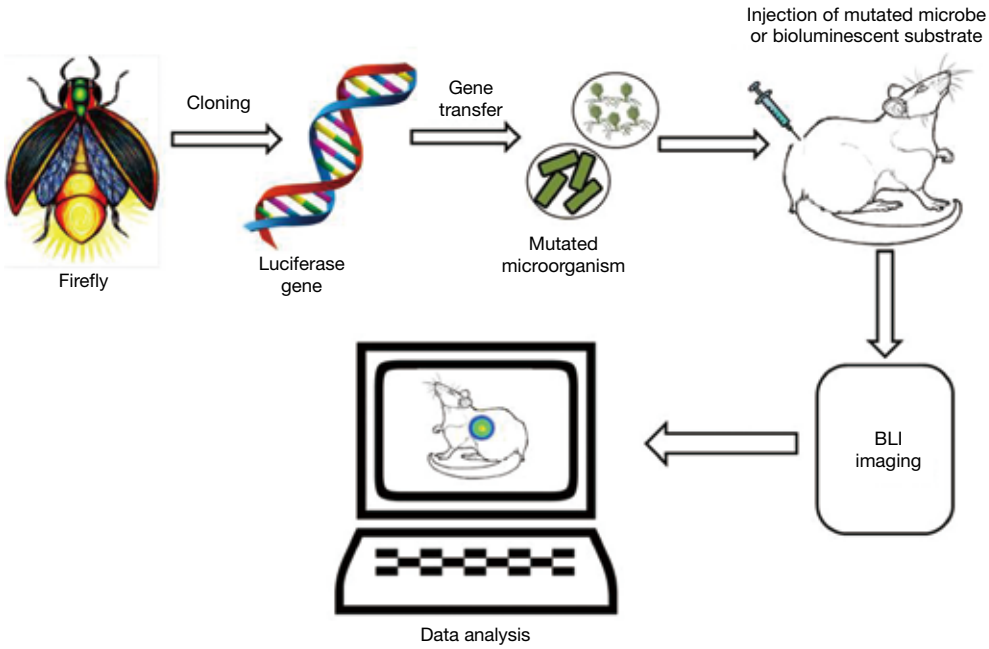

Figure 4 Schematic representation of bioluminescent imaging. BLI, bioluminescence imaging.

(30,37). Bioluminescence is the natural capacity some organisms have to convert chemical energy into light energy. Currently, biological researchers are employing this natural phenomenon to visualize intact biological tissues, using a technique called BLI. The basic principle of this technology is the detection of photons emitted from the tissues in the living organisms. In the fluorescence imaging methods, usually light absorption is required to emit light at longer wavelengths; in BLI, light absorption is not required for imaging. For the biological process of bioluminescence to occur, luciferase enzymes are required to be in the presence of luciferin (substrate) and oxygen. In some cases, the enzyme also needs other cofactors like ATP and Mg^{2+} for successful bioluminescence reactions. Most often bioluminescence emits light at a wavelength of nearly 560 nm, which allows for the imaging of deeper tissue layers with higher resolutions (*Figure 4*). This method is widely applied in the biomedical areas of monitoring transgene expression, development of infection, toxicology, progression of viral infections and gene therapies (38,39).

The major advantage of the BLI method is its relatively simple implementation which permits the monitoring of a disease with continual quantification of progression of infections, all without scarifying the experimental animal. Moreover, this method decreases the number of experimental animals required in testing because multiple measurements can be recorded within the same animal over the course of infection and treatments, which also minimizes the complication of biological variations. Recent BLI methods have used a variety of luciferase enzymes including firefly luciferase, Renilla luciferase, Gaussia luciferase, Metridia luciferase, Vargula luciferase and bacterial luciferase. Of these luciferase enzymes, firefly, Renilla and bacterial luciferases have been widely employed for optical imaging. The BLI method has gained significantly more importance than its counterpart, fluorescence molecular imaging, mostly due to FMI's lack of endogenous bioluminescent reaction in mammalian tissues to offer background free images, in addition to the prevalence of fluorescently active compounds in the biological tissues which could affect the target resolution. BLI technology also has different modalities like steady-state bioluminescent imaging, multi-reporter bioluminescent imaging, multi-component bioluminescent imaging and bioluminescence, as a supplementary imaging technique (40). The greater signal-to-noise ration due to the absence of intrinsic bioluminescence background in animal tissues, has promoted BLI as an interesting tool for monitoring biological development of a living animal in real time (41). As such, BLI has been mostly used for small animal studies to monitor and correlate the survival, engraftment and migration of a range of cell populations.

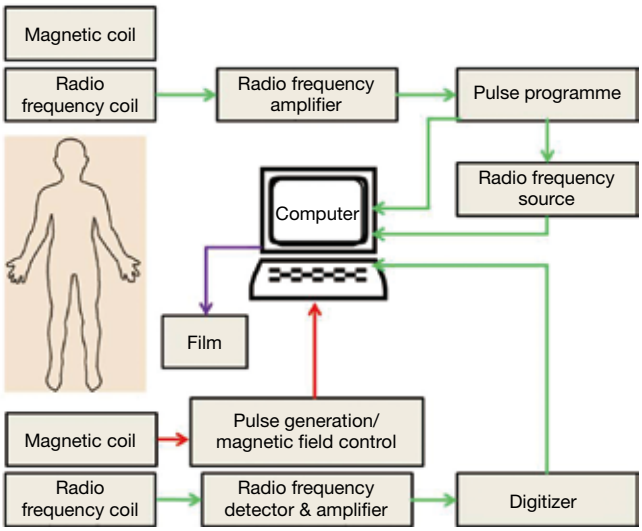

Figure 5 A schematic diagram of functional MRI scanning. MRI, magnetic resonance imaging.

MRI

The basic principle of the MRI works upon the inherent magnetic properties of tissue and the ability to employ these properties to produce tissue contrast. Single protons, which induce the magnetic movement in omni-present hydrogen atoms, produce the magnetic resonance images. As is well-known, when an electric charge in the movement that creates magnetic field, spinning protons on small magnetic field and can be conceived of as little magnet. When a patient is placed in the bore of a large magnet (MRI scanner), hydrogen protons align with the externally applied static magnetic field to generate a net magnetization vector. Most of the protons will distribute randomly on a quantum level, either with or against the scanner static magnetic fields. On the other hand, a little increase in the spins aligns protons with the field causing net tissue magnetization (*Figure 5*). The time required for this alignment is determined by the longitudinal relaxation time. This longitudinal relaxation time varies between the tissues it is employed to provide contrast for (42). MRI can provide high-spatial resolution anatomic images with intense living tissues' contrast by using the difference in relaxation times of protons in different biochemical environments. The collaboration of high spatial resolution and contrast, facilitates the anatomic responses of many disease complications to be visualized in animal tissues. MRI can be used to monitor different physiologic parameters like diffusion, permeability and change in blood oxygenation levels after neuronal activation. A recent advancement in nanotechnology is the addition of passive contrasting agents like iron-oxide nanoparticles which can further enhance the contrast (43). MRI molecular imaging data can be evaluated according to the amount of signal change, the area of the tissue displaying contrast enhancement, and the calculation of relaxation time change or direct detection of contrasting agents by multi-nuclear imaging and/or spectroscopy (44).

The MRI method of molecular imaging has certain limitations however, like lower sensitivity than that of nuclear imaging. Nevertheless, certain nanomaterials such as micelles, liposomes, iron oxide nanoparticles and emulsion can be used to deliver contrasting agents like Gd chelates in larger amounts to the targeted sites. In certain cases, iron oxide nanoparticles can be used as contrasting agent in MRI technology (45,46). The application of molecular MRI in vascular imaging is mainly focused on determining the significant components of atherosclerotic plaque, along with adhesion molecules, plaque hemorrhage, ventricular volume or blood velocity, and plaque macrophage content (47,48). MRI molecular imaging comprises a wide range of technologies like site-targeted contrasting agents, drug delivery vehicles, controllable MRI probes, and direct mapping of tissue metabolite (44). However, due to the magnetic field interference caused by devices like defibrillators and pacemakers, MRI cannot be employed on some patients with implantable devices.

SPECT

SPECT is a noninvasive technique that can facilitate 3D functional information with greater resolution, sensitivity and specificity. All nuclear-based imaging technology, including SPECT, relies on the injection of trace amounts of molecules labeled with radioactive isotopes. The decaying of radiolabeled molecules results in the emission of photons. These photons are detected by a position-sensitive detector which can give the arrival location of the photon and its energy. It cannot provide the information about the travelling path of the photons as it requires generating projections of the emitting body. A collimator, a device used to produce a parallel beam of rays or radiation, is inserted between the patient and the detector which in turn shapes the stream of emitting photons into a beam. This allows the detector to locate the photon associated to a line in space along which the decay occurred. Usually, a collimator allows to pass the photons to the detector in a certain angle rest of the photons are removed. This results in the projection

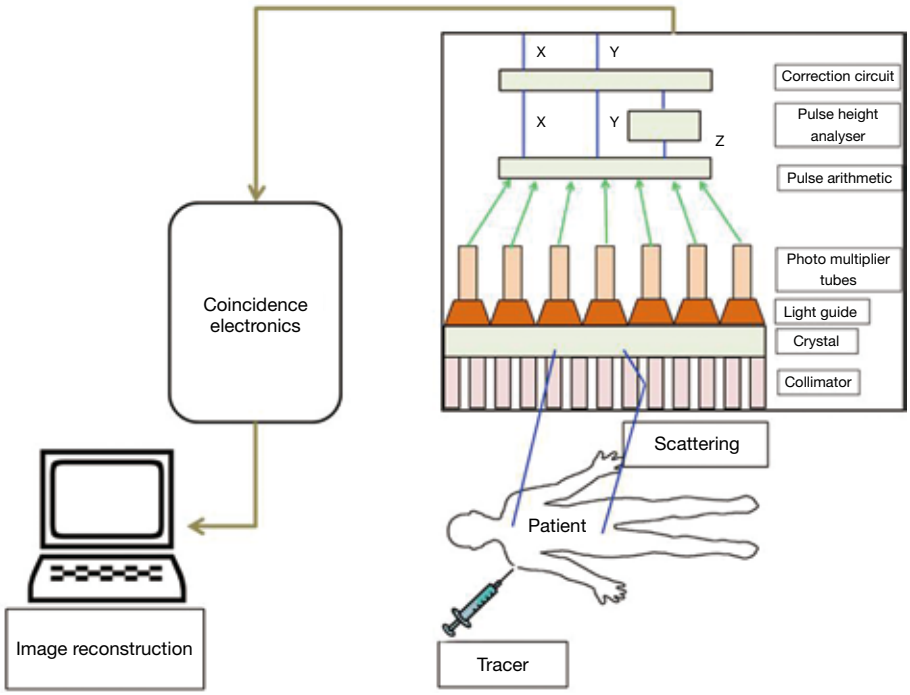

Figure 6 Image-capturing system using Single-photon emission computed tomography.

of the image at the expense of the discards of most of the photons (49). Customarily, SPECT records the 2D nuclear medicine images obtained at different positions around the patient and gives an estimated 3D radioactivity distribution by employing the tool to reconstruct from multiple projections. SPECT stands out from the other methods of medical imaging modalities due to its special features of instrumentation and image reconstruction (*Figure 6*) (50).

Generally speaking, energy resolution widely affects the quality of an image. In principle, images should be only constituted with primary photons which are emitted from a decaying radionuclide, and not the secondary scattered photons. A device possessing better energy resolution should able to discriminate the primary photons from the scattered photons and also provide the better image contrast and more precise quantification of radionuclide amount and distribution inside an animal. By using this feature of SPECT in myocardial perfusion imaging, the area of hypoperfusion can be discriminated from its neighboring normal perfusion region by enhancing image contrast (51). SPECT can also be used to detect coronary artery diseases (CAD) even at the time of asymptomatic or moderate CAD. To support this application of SPECT, research has been conducted by the American College of Cardiology Foundation and the American Society of Nuclear Cardiology to assess if SPECT could be used to rate uncertain detection and risk of CAD in asymptomatic patients at initial periods of disease complication. The experimental results demonstrated that, with a retrospectively determined group of asymptomatic patients at moderate CAD risk, SPECT had great potential in detection and risk stratification of CAD. Moreover, the test results showed that average annual mortality was 4% in patients with the high-risk scan but only showed 1.6% in patients with normal scanning. This proves that SPECT imaging can detect the complications in asymptomatic patients and can help in bypass surgery even in the nonoccurrence of symptoms (52). As can be seen, SPECT is a highly sensitive, easy and fast-labeling imaging technology with significant spatial resolution. It can facilitate convenient quantification *in vivo* and *in vitro*, provide real-time monitoring of cell viability, and enable imaging over long intervals.

Photoacoustic tomography (PAT)

PAT, also known as optoacoustic imaging, is an emerging imaging technology which holds great promise for

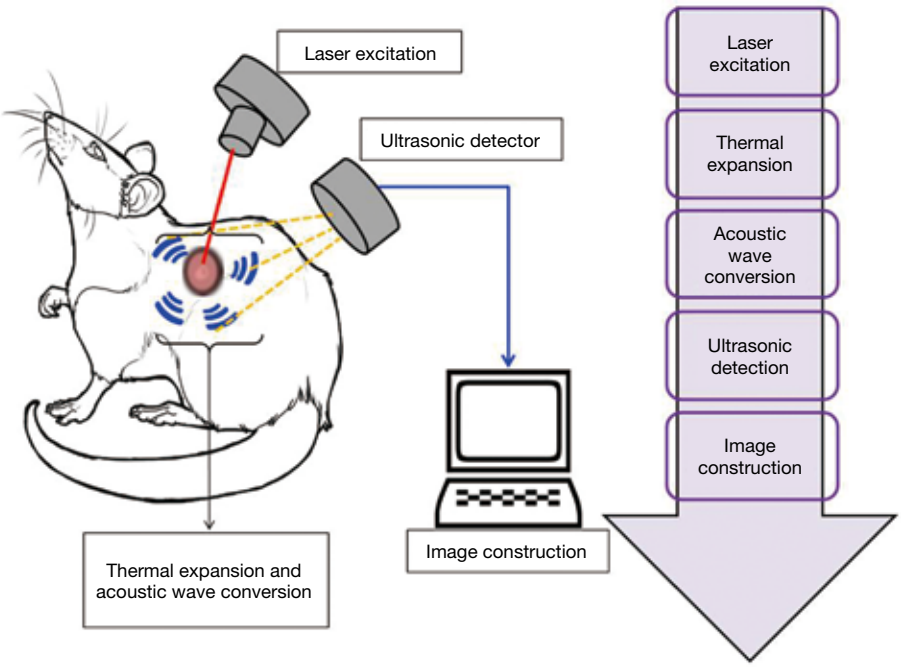

Figure 7 Schematic representation of working principle of photoacoustic imaging.

preclinical research and clinical treatment. In every imaging technology, the fundamental constraint is the limiting effect of light diffusion on spatial resolution in deep tissue. In contrast to these methods, photoacoustic imaging employs a laser light generated ultrasound, and so has emerged as a promising new technology which can potentially overcome the challenges found in traditional optical imaging. PAT works with the principle of photoacoustic effect where the absorbed optical energy is converted into acoustic energy. Biological tissues are lit by nanosecond laser pulses, raising the temperature at localized places and generating a wideband of ultrasound pulses due to thermal expansion. The light-excited ultrasound pulses spread in the biological tissues and clarify the detection boundary surrounding the biological tissues in ultrasonography (*Figure 7*) (53). The special properties of acoustic waves, which scatter much less than optical waves in tissues, are what makes PAT technology distinct from other optical imaging technologies. Interestingly, PAT is able to produce high-resolution images in both optically ballistic and diffusive regimes. Moreover, at the time of optical absorption even with single origination, PAT can readily utilize the advantages of rich endogenous and exogenous optical contrasts. For imaging vascular structures, endogenous oxy- and deoxy-hemoglobin are used as anatomical and functional contrasts. Certain dyes, nanoparticles and reporter genes are also used as exogenous contrasts for molecular imaging (33,54-56). PAT imaging has a wide range of applications like glucose metabolism imaging, deep tissue imaging of fluorescent proteins, evaluating the prolong period of biodistribution of an optical contrast agent, and video rate cross sectional imaging (57-60). Due to the advancements in science and technology, PAT has been evolving quickly towards greater spatial resolution, higher frame rates and higher sensitivity detection. Moreover, the continuous progress in PAT has also accelerated and augmented contributions from biology, chemistry and nanotechnology. In summary, PAT has several applications including performing anatomical, functional, molecular and fluid-dynamic imaging at different system levels, and plays a significant role in essential bio-research and clinical practice.

Conclusions

As a new branch of the biomedical sciences, molecular imaging was born under the merging of two areas: imaging and probe technology. Based on the probes allowing direct/indirect spatio-temporal evaluation of molecular markers, molecular imaging can provide critical information for much earlier detection of disease and is expected

to have a significant impact in personalized medicine through providing more appropriate treatment, better prognosis, improved staging and better management. This review focused on the development of probes for future applications in novel cardiovascular targeted imaging strategies. The future for probes in cardiovascular molecular imaging rests on, among other innovations, the development of targeted biological molecules, reporter gene methods to enhance gene therapy, tagging cells to track stem cell transplantation, and labeling small-molecule probes with sensitive isotopes. Realizing the potential of these promising probes is likely to play a significant role in both diagnostic and prognostic functions, and the investigation of therapeutic practices.

Acknowledgements

Funding: This work was supported by the National Natural Science Foundation of China (NSFC) (Grant Nos. 81801817, 81422023, 51273165, U1705281, and U1505221), the Major State Basic Research Development Program of China (Grant Nos. 2017YFA0205201, 2014CB744503, and 2013CB733802), and the Program for New Century Excellent Talents in University, China (NCET-13-0502).

Footnote

Conflicts of Interest: The authors have no conflicts of interest to declare.

References

1. Langer H, Schönberger T, Bigalke B, Gawaz M. Where is the trace? Molecular imaging of vulnerable atherosclerotic plaques. Semin Thromb Hemost 2007;33:151-8.
2. Liu G, Chen X, Ai H. Multifunctional Probes for Multimodality Imaging of Cancer. Molecular Imaging Probes for Cancer Research 2012:863-903.
3. Hughes M, Caruthers S, Tran T. Perfluorocarbon Nanoparticles for Molecular Imaging and Targeted Therapeutics. Proceedings of the IEEE 2008:96:397-415.
4. Chen K, Conti PS. Target-specific delivery of peptide-based probes for PET imaging. Adv Drug Deliv Rev 2010;62:1005-22.
5. Chen K, Chen X. Design and Development of Molecular Imaging Probes. Curr Top Med Chem 2010;10:1227-36.
6. Sosnovik DE, Nahrendorf M, Weissleder R. Targeted imaging of myocardial damage. Nat Clin Pract Cardiovasc Med. 2008;5 Suppl 2:S63-70.
7. Liu S, Levi J, Cheng Z. General Principles of Molecular Imaging Probe Design. Molecular Imaging Probes for Cancer Research 2012:129-47.
8. Liu G, Swierczewska M, Lee S, Chen X. Functional nanoparticles for molecular imaging guided gene delivery. Nano Today 2010;5:524-39.
9. Alford R, Simpson HM, Duberman J, Hill GC, Ogawa M, Regino C, Kobayashi H, Choyke PL. Toxicity of Organic Fluorophores Used in Molecular Imaging: Literature Review. Mol Imaging 2009;8:341-54.
10. Sajja HK, East MP, Mao H, Wang YA, Nie S, Yang L. Development of Multifunctional Nanoparticles for Targeted Drug Delivery and Noninvasive Imaging of Therapeutic Effect. Curr Drug Discov Technol 2009;6:43-51.
11. Schäfers M. The future of molecular imaging in the clinic needs a clear strategy and a multidisciplinary effort. Basic Res Cardiol 2008;103:200-2.
12. Preiss DJ, Sattar N. Vascular cell adhesion molecule-1: a viable therapeutic target for atherosclerosis? Int J Clin Pract 2007;61:697-701.
13. Alford R, Ogawa M, Choyke PL, Kobayashi H. Molecular probes for the in vivo imaging of cancer. Mol Biosyst 2009;5:1279-91.
14. Culver J, Akers W, Achilefu S. Multimodality molecular imaging with combined optical and SPECT/PET modalities. J Nucl Med 2008;49:169-72.
15. Cambria E, Pasqualini FS, Wolint P, Günter J, Steiger J, Bopp A, Hoerstrup SP, Emmert MY. Translational cardiac stem cell therapy: advancing from first-generation to next-generation cell types. NPJ Regen Med 2017;2:17.
16. Sinusas AJ, Bengel F, Nahrendorf M, Epstein FH, Wu JC, Villanueva FS, Fayad ZA, Gropler RJ. Multimodality cardiovascular molecular imaging, part I. Circ Cardiovasc Imaging 2008;1:244-56.
17. Hricak H, Choi BI, Scott AM, Sugimura K, Muellner A, von Schulthess GK, Reiser MF, Graham MM, Dunnick NR, Larson SM. Global trends in hybrid imaging. Radiology 2010;257:498-506.
18. Wang X, Liu LH, Ramström O, Yan M. Engineering nanomaterial surfaces for biomedical applications. Exp Biol Med (Maywood) 2009;234:1128-39.
19. Liu Y, Miyoshi H, Nakamura M. Nanomedicine for drug delivery and imaging: a promising avenue for cancer therapy and diagnosis using targeted functional nanoparticles. Int J Cancer 2007;120:2527-37.
20. Zhang P, Zhang L, Qin Z, Hua S, Guo Z, Chu C, Lin H,

Zhang Y, Li W, Zhang X, Chen X, Liu G. Genetically Engineered Liposome-like Nanovesicles as Active Targeted Transport Platform. Adv Mater 2018;30. doi: 10.1002/adma.201705350.
21. Idée JM, Louguet S, Ballet S, Corot C. Theranostics and contrast-agents for medical imaging: a pharmaceutical company viewpoint. Quant Imaging Med Surg 2013;3:292-7.
22. Leng L, Wang Y, He N, Wang D, Zhao Q, Feng G, Su W, Xu Y, Han Z, Kong D, Cheng Z, Xiang R, Li Z. Molecular imaging for assessment of mesenchymal stem cells mediated breast cancer therapy. Biomaterials 2014;35:5162-70.
23. Andreas K, Georgieva R, Ladwig M, Mueller S, Notter M, Sittinger M, Ringe J. Highly efficient magnetic stem cell labeling with citrate-coated superparamagnetic iron oxide nanoparticles for MRI tracking. Biomaterials 2012;33:4515-25.
24. Lin G, Mi P, Chu C, Zhang J, Liu G. Inorganic Nanocarriers Overcoming Multidrug Resistance for Cancer Theranostics. Adv Sci (Weinh) 2016;3:1600134.
25. Shamili K, Rajesh EM, Rajendran R, Madhan Shankar SR, Elango M, Abitha Devi N. Colloidal Stability and Monodispersible Magnetic Iron Oxide Nanoparticles in Biotechnology Application. Int J Nanosci 2013;12:1330002.
26. Shi Y, Pang X, Wang J, Liu G. NanoTRAIL-Oncology: A Strategic Approach in Cancer Research and Therapy. Adv Healthc Mater 2018;7:e1800053.
27. Wang J, Liu G. Imaging Nano-Bio Interactions in the Kidney: Toward a Better Understanding of Nanoparticle Clearance. Angew Chem Int Ed Engl 2018;57:3008-10.
28. Suter MJ, Nadkarni SK, Weisz G, Tanaka A, Jaffer FA, Bouma BE, Tearney GJ. Intravascular optical imaging technology for investigating the coronary artery. JACC Cardiovasc Imaging 2011;4:1022-39.
29. Lindner JR, Sinusas A. Molecular imaging in cardiovascular disease: Which methods, which diseases? J Nucl Cardiol 2013;20:990-1001.
30. Brock M. Application of bioluminescence imaging for in vivo monitoring of fungal infections. Int J Microbiol 2012;2012:956794.
31. Stuker F, Ripoll J, Rudin M. Fluorescence molecular tomography: principles and potential for pharmaceutical research. Pharmaceutics 2011;3:229-74.
32. Zilberman Y, Kallai I, Gafni Y, Pelled G, Kossodo S, Yared W, Gazit D. Fluorescence molecular tomography enables in vivo visualization and quantification of nonunion fracture repair induced by genetically engineered mesenchymal stem cells. J Orthop Res 2008;26:522-30.
33. Gao D, Liu Y, Wang Y, Yuan Z. Protein-modified ultra-small gold clusters for dual-modal in vivo fluorescence/photoacoustic imaging. Quant Imaging Med Surg 2018;8:326-32.
34. Ntziachristos V, Tung CH, Bremer C, Weissleder R. Fluorescence molecular tomography resolves protease activity in vivo. Nat Med 2002;8:757-60.
35. Yang H, He Bin, Dai X, Satpathy M, Yang L, Jiang H. FMTPen: A Miniaturized Handheld Fluorescence Molecular Tomography Probe for Image-Guided Cancer Surgery. Photonics 2015;2:279-87.
36. Ransohoff JD, Wu JC. Imaging stem cell therapy for the treatment of peripheral arterial disease. Curr Vasc Pharmacol 2012;10:361-73.
37. Jenkins DE, Oei Y, Hornig YS, Yu SF, Dusich J, Purchio T, Contag PR. Bioluminescent imaging (BLI) to improve and refine traditional murine models of tumor growth and metastasis. Clin Exp Metastasis 2003;20:733-44.
38. Sadikot RT, Blackwell TS. Bioluminescence imaging. Proc Am Thorac Soc 2005;2:537-40, 511-2.
39. Badr CE, Tannous BA. Bioluminescence imaging: progress and applications. Trends Biotechnol 2011;29:624-33.
40. Close DM, Xu T, Sayler GS, Ripp S. In vivo bioluminescent imaging (BLI): noninvasive visualization and interrogation of biological processes in living animals. Sensors (Basel) 2011;11:180-206.
41. Xu T, Close D, Handagama W, Marr E, Sayler G, Ripp S. The Expanding Toolbox of In Vivo Bioluminescent Imaging. Front Oncol 2016;6:150.
42. Duran C, Sobieszczyk PS, Rybicki FJ. Magnetic Resonance Imaging. Vascular Medicine: A Companion to Braunwald's Heart Disease (Second Edition). 2013:166-83.
43. Catana C, Procissi D, Wu Y, Judenhofer MS, Qi J, Pichler BJ, Jacobs RE, Cherry SR. Simultaneous in vivo positron emission tomography and magnetic resonance imaging. Proc Natl Acad Sci U S A 2008;105:3705-10.
44. Winter PM, Caruthers SD, Lanza GM, Wickline SA. Quantitative cardiovascular magnetic resonance for molecular imaging. J Cardiovasc Magn Reson 2010;12:62.
45. Liu H, Chu C, Liu Y, Pang X, Wu Y, Zhou Z, Zhang P, Zhang W, Liu G, Chen X. Novel Intrapolymerization Doped Manganese-Eumelanin Coordination Nanocomposites with Ultrahigh Relaxivity and Their Application in Tumor Theranostics. Adv Sci (Weinh) 2018;5:1800032.
46. Lin G, Zhang Y, Zhu C, Chu C, Shi Y, Pang X, Ren E,

Wu Y, Mi P, Xia H, Chen X, Liu G. Photo-excitable hybrid nanocomposites for image-guided photo/TRAIL synergistic cancer therapy. Biomaterials 2018;176:60-70.
47. Yang C, Tian R, Liu T, Liu G. MRI Reporter Genes for Noninvasive Molecular Imaging. Molecules 2016;21. doi: 10.3390/molecules21050580.
48. Osborn EA, Jaffer FA. The advancing clinical impact of molecular imaging in CVD. JACC Cardiovasc Imaging 2013;6:1327-41.
49. Wang J, Mi P, Lin G, Wáng YX, Liu G, Chen X. Imaging-guided delivery of RNAi for anticancer treatment. Adv Drug Deliv Rev 2016;104:44-60.
50. National Research Council. Mathematics and Physics of Emerging Biomedical Imaging. Washington, DC: The National Academies Press, 1996. Available online: https://doi.org/10.17226/5066.
51. Holly TA, Abbott BG, Al-Mallah M, Calnon DA, Cohen MC, DiFilippo FP, Ficaro EP, Freeman MR, Hendel RC, Jain D, Leonard SM, Nichols KJ, Polk DM, Soman P; American Society of Nuclear Cardiology. Single photon-emission computed tomography. J Nucl Cardiol 2010;17:941-73.
52. Khandaker MH, Miller TD, Chareonthaitawee P, Askew JW, Hodge DO, Gibbons RJ. Stress single photon emission computed tomography for detection of coronary artery disease and risk stratification of asymptomatic patients at moderate risk. J Nucl Cardiol 2009;16:516-23.
53. Sun Y, Jiang H, O'Neill BE. Photoacoustic Imaging: An Emerging Optical Modality in Diagnostic and Theranostic Medicine. J Biosens Bioelectron 2011;2:108.
54. Beard P. Biomedical photoacoustic imaging. Interface Focus 2011;1:602-31.
55. Xia J, Yao J, Wang LV. Photoacoustic tomography: principles and advances (invited review). Progress In Electromagnetics Research 2014;147:1-22.
56. Xia J, Wang LV. Small-Animal Whole-Body Photoacoustic Tomography: A Review. IEEE Transactions on Biomedical Engineering 2014;61:1380-9.
57. Li L, Pang X, Liu G. Near-Infrared Light-Triggered Polymeric Nanomicelles for Cancer Therapy and Imaging. ACS Biomater Sci Eng 2018;4:1928-41.
58. Chu C, Lin H, Liu H, Wang X, Wang J, Zhang P, Gao H, Huang C, Zeng Y, Tan Y, Liu G, Chen X. Tumor Microenvironment-Triggered Supramolecular System as an In Situ Nanotheranostic Generator for Cancer Phototherapy. Adv Mater 2017;29. doi: 10.1002/adma.201605928.
59. Cai W, Gao H, Chu C, Wang X, Wang J, Zhang P, Lin G, Li W, Liu G, Chen X. Engineering Phototheranostic Nanoscale Metal–Organic Frameworks for Multimodal Imaging-Guided Cancer Therapy. ACS Appl Mater Interfaces 2017;9:2040-51.
60. Wang X, Zhang L, Wang J, Liu X, Lv P, Zeng J, Liu G. Size-Controlled Biocompatible Silver Nanoplates for Contrast-Enhanced Intravital Photoacoustic Mapping of Tumor Vasculature. J Biomed Nanotechnol 2018;14:1448-57.

Cite this article as: Zeng Y, Zhu J, Wang J, Parasuraman P, Busi S, Nauli SM, Wáng YX, Pala R, Liu G. Functional probes for cardiovascular molecular imaging. Quant Imaging Med Surg 2018;8(8):838-852. doi: 10.21037/qims.2018.09.19

Review Article

CT and MRI of adrenal gland pathologies

Fuqin Wang[1#], Junwei Liu[1#], Ruoxi Zhang[1], Yonghua Bai[2], Cailin Li[1], Bangguo Li[1], Heng Liu[1], Tijiang Zhang[1]

[1]Department of Radiology, [2]Department of Pathology, Affiliated Hospital of Zunyi Medical University, Zunyi 563000, China

[#]These authors contributed equally to this work.

Correspondence to: Dr. Tijiang Zhang. Department of Radiology, Affiliated Hospital of Zunyi Medical University, 149 Dalian Road, Zunyi 563000, China. Email: tijzhang@163.com; Dr. Heng Liu, Department of Radiology, Affiliated Hospital of Zunyi Medical University, 149 Dalian Road, Zunyi 563000, China. Email: zmcliuh@163.com.

Abstract: Besides ultrasound and nuclear medicine techniques, computed tomography (CT) and magnetic resonance imaging (MRI) are commonly used to examine adrenal lesions in both symptomatic and asymptomatic patients. Some adrenal lesions have characteristic radiological features. If an adrenal nodule is discovered incidentally, determining whether the lesion is benign or malignant is of great importance. According to their biological behavior, lesions can be divided into benign (mainly: adenoma, hyperplasia, pheochromocytoma, cyst, hemorrhage, cystic lymphangioma, myelolipoma, hemangioma, ganglioneuroma, teratoma) and malignant (mainly: metastases, adrenal cortical carcinoma, neuroblastoma, lymphoma) conditions. In this paper, we review CT/MRI findings of common adrenal gland lesions.

Keywords: Adrenal gland; adrenal lesions; computed tomography (CT); magnetic resonance imaging (MRI)

Submitted Jul 28, 2018. Accepted for publication Sep 14, 2018.
doi: 10.21037/qims.2018.09.13
View this article at: http://dx.doi.org/10.21037/qims.2018.09.13

Introduction

According to their biological behavior, lesions of the adrenal grands can be classified into being benign or being malignant (including primary or metastatic) (*Table 1*). Different lesions have different treatment options and clinical prognoses, so it is of great clinical value to make a differential diagnosis based on computed tomography (CT) and magnetic resonance imaging (MRI) findings. Thought ultrasound and Nuclear medicine tests are commonly used for adrenal lesion assessment. This article is focused on CT and MRI.

Adrenal lesions can be classified into two types: symptomatic and asymptomatic. It has been reported that only a small number of adrenal tumors are functional and an even smaller number are malignant (1). Some adrenal lesions can secrete hormones that cause endocrine syndromes, and patients further develop clinical symptoms, such as Conn syndrome and Cushing syndrome (CS) (*Table 2*).

CS or hypercortisolism is classically described as the signs and symptoms associated with prolonged exposure to pathologically elevated cortisol levels (2), which represents hypercortisolism stemming from various causes other than a pituitary adenoma (3). CS can result from exogenous administration of glucocorticoids or endogenous overproduction of cortisol (4). The triggering pathways of CS can be divided into pituitary-dependent and pituitary-independent. Females are more likely to have CS than males. CS is most commonly caused by adrenal adenomas; other causes include adrenocortical carcinoma (ACC), pheochromocytomas.

CS is characterized by symptoms such as central obesity, buffalo hump, a rounded face, chromatosis, muscle weakness, hypertension, acne, hirsutism, menstrual irregularities, diabetes mellitus, osteoporosis, immune suppression, gonadal dysfunction, and mood changes (1-3,5). The clinical manifestations of CS are related to the patient's age and the duration and degree of the hypercortisolism (5).

Conn syndrome, or primary aldosteronism, which is characterized by excessive spontaneous secretion of aldosterone from the adrenal glands, affects 6% of people

Table 1 Classification of adrenal benign and malignant lesions

Location	Benign lesions	Malignant lesions
Cortex	Adenoma	Adenocarcinoma
Medulla	Pheochromocytoma, ganglioneuroma	Neuroblastoma
Cortex & medulla	Hyperplasia, hemorrhage	Metastases
Interstitial	Myelolipoma, cystic lymphangioma, hemangioma, cyst, teratoma	Lymphoma

Table 2 The causes of Conn syndrome and Cushing syndrome in adrenal glands

Endocrine syndromes	Factors of adrenal glands
Cushing syndrome	Adrenal adenoma
	Adrenocortical carcinoma
	Pheochromocytomas
	Primary pigmented nodular adrenocortical disease (PPNAD)
	Macronodular hyperplasia with marked adrenal enlargement (MHMAE)
Conn syndrome	Adrenal adenoma (50–60%)
	Adrenocortical carcinoma (1%)
	Adrenal hyperplasia (bilateral idiopathic hyperplasia, primary adrenal hyperplasia)

with high blood pressure and can be either sporadic or familial (6,7). Conn syndrome is related to autonomous aldosterone production causing sodium retention, plasma renin suppression, hypertension, cardiovascular damage, and increased potassium excretion, leading to variable degrees of hypokalemia (8). The prevalence of cardiovascular disease in Conn syndrome patients is higher than that in normal individuals in the same age group. Often, patients are usually asymptomatic, but there may be symptoms of fatigue, muscle weakness, cramping, headaches, and palpitations. Patients may also have symptoms of polydipsia and polyuria due to hypokalemia caused by renal diabetes insipidus.

Addison disease, or primary adrenal insufficiency, is a systemic disease caused by hypoadrenocortical hypofunction. Addison disease has many causes, the most common of which is autoimmune adrenalitis, and other causes include tuberculosis, malignant tumor, infection, hemorrhage, HIV and certain genetic conditions. The incidence of Addison disease is 0.6/100,000 of population per year (9). Patients may experience weight loss, weakness, fatigue, gastrointestinal upset, orthostatic hypotension and pigmentation of skin (10). Dehydration, shock, hyperkalemia, and hyponatremia occurred in patients with adrenal crisis. Different causes of Addison's disease have different CT and MRI findings. CT study of the morphological changes of adrenal glands on patients with Addison's disease might help to define the etiology of the disease and contribute to treatment planning (11). Treatments for Addison disease include etiological treatment, hormone therapy (including glucocorticoids and mineralocorticoids) and treatment of adrenal crisis. When patients develop adrenal crisis, they need a stress dose of hydrocortisone and a large amount of fluid infusion. The treatment corticosteroid replacement and the prognosis following the treatment is the same as the normal population (12).

Normal anatomy of the adrenals

The adrenal glands are situated in the retroperitoneal space, close to the upper pole of the kidney (13). The normal adrenal gland has a linear, inverted V or Y, triangular shape (14). Each adrenal gland consists of two parts: the cortex and medulla, which have different embryological origins, distinct macroscopic and microscopic structures, as well as different functions and properties (15). The cortex derives from the mesoderm and it can be further divided into three areas: the lateral glomerular zone, the middle fascicular

Figure 1 Adrenocortical adenoma confirmed with pathology in a 35-year-old man with lumbago. (A) Axial precontrast CT image shows a 53 mm × 45 mm × 45 mm, well-defined, heterogeneous cystic and solid mass (arrows); (B) axial postcontrast CT image shows marked enhancement in substantial parts of areas; (C) coronal reformatted image shows the lesion locates in the anterosuperior of the left kidney, which seems to be connected with the internal branch of the left adrenal gland.

zone, and the medial reticulate zone, while the medulla consists of pheochromocytes.

The adrenal glands are highly vascularized. The adrenal artery has three sources: the middle adrenal artery originates from the abdominal aorta; the upper adrenal artery originates from the inferior phrenic artery; and the inferior adrenal artery originates from the renal artery (1,13,16). The branches of these arteries are anastomosed to each other. Venous return is different, the right adrenal vein enters the inferior vena cava, and the left adrenal vein converges with the left renal vein.

The lateral glomerular zone cells secrete mineralocorticoids (mainly aldosterone), the middle fascicular zone cells secrete glucocorticoids (mainly cortisol), and the medial reticulate zone cells produce sex hormones, such as dehydroepiandrosterone and estradiol.

Benign conditions

Adrenocortical adenoma

With benign nature, adrenocortical adenomas are the most common adrenal tumors (17). In addition, most incidentally discovered adrenal lesions are also benign adrenal adenomas (18,19).The incidence of adenomas is 3% at autopsy. It has been reported that the prevalence of adrenocortical adenomas is associated with age. The proportion of adenomas in men and women is about 1:2. Adrenocortical adenomas include functional and nonfunctioning adenomas. Functional adenomas can be accompanied by hypercortisolism (or CS) and primary hyperaldosteronism (or Conn's syndrome). However, most lesions are nonfunctional (20). Nonfunctioning adenomas occur in the cortex, accounting for 25% of adrenal nonfunctioning tumors. Although CT cannot differentiate functional and nonfunctional adenomas, it can suggest a functioning adenoma when the contralateral adrenal gland atrophies.

The gross appearance of an adenoma is a solid tumor with hemorrhagic or cystic changes (*Figure 1*), and occasionally calcification. Under a light microscope, the tumor cells are similar to normal cortical cells, with small nuclei, pale-staining cytoplasm, and arrangement in clusters, and some cells contained large amounts of fat. In addition, the mesenchyme separating the blood vessels is visible.

Adenomas are typically smaller in size, well-defined and homogeneous in attenuation. Generally, adenomas are homogeneous on unenhanced and contrast-enhanced CT images, and its density is equal to or slightly lower than that of normal adrenal gland tissue. When the tumor is necrotic and/or cystic, the density is uneven (*Figures 2,3*). Adenomas can be divided into two types: lipid-rich adenomas (70%, density less than 10 Hounsfield units (HUs) on pre-contrast-enhanced CT scan images) and lipid- poor adenomas (30%, with a density between 10–30 HU). On unenhanced CT scans, the decrease in the density of the lesion due to an increase in the amount of fat (21), and higher density is measured in lipid-poor adenomas than in lipid-rich adenomas.

Adenomas are usually characterized by homogeneity and mild enhancement. Caoili *et al*. reported that benign adenomas typically demonstrate an absolute percentage washout (APW) ≥60% and a relative percentage washout (RPW) of ≥40%, which can be computed in 10 to 15 minutes on delayed images .If the APW is 60% and/or the RPW 40%, the lesion is characterized as an adenoma (22). The density of the tumor changes with the size of the lesion.

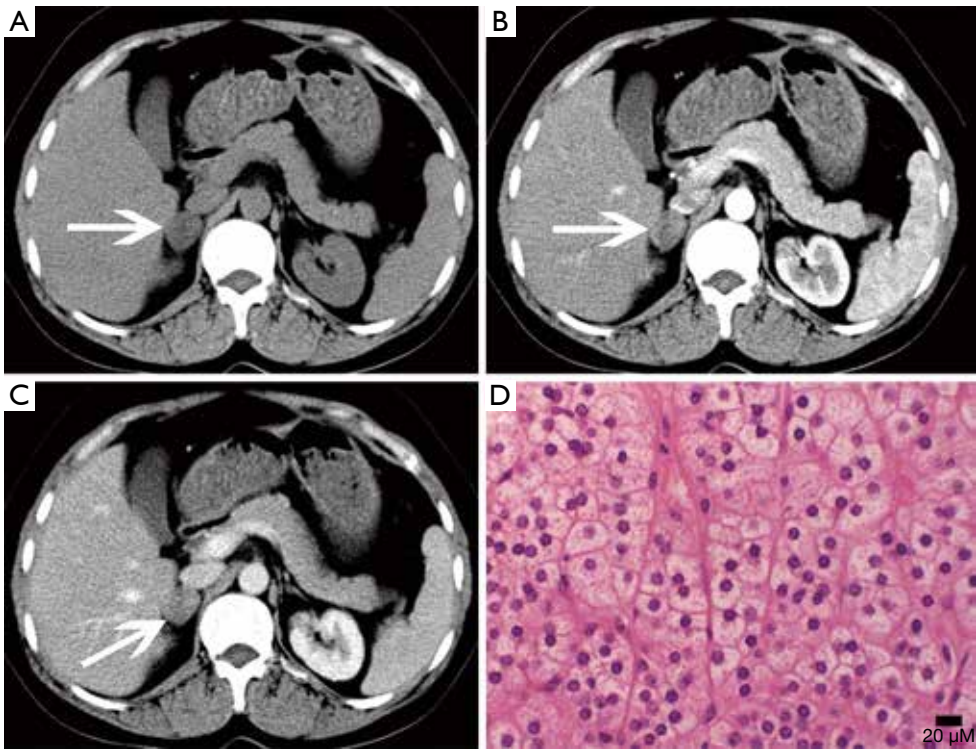

Figure 2 Adrenocortical adenoma confirmed with pathology in a 43-year-old woman who presented with right adrenal mass for 4 years. (A) Axial pre-contrast CT image shows a 21 mm × 20 mm mass with clear margin and heterogeneous density (arrows); (B) axial arterial and (C) venous phase images show moderate enhancement; (D) photomicrograph (original magnification, ×400; H-E stain) shows the tumor cells are similar to normal cortical cells, with pale-staining cytoplasm.

Figure 3 Adrenocortical adenoma in a 14-year-old boy presented with Cushing syndrome. (A) Axial pre-contrast CT image shows a 59 mm × 60 mm soft tissue density mass (arrows); (B) axial arterial and (C) venous phase images show inhomogeneous marked enhancement.

The larger and more heterogenous the tumor is, the greater the possibility of cystic and necrotic areas.

On MRI, lipid-rich adrenocortical adenomas have high intensity signal on T1- and T2-weighted images. Chemical shift imaging can detect a large amount of fat in the cytoplasm according to its special principles. Because of the different precession frequencies of protons in water molecules and fat, many adenomas show high signal on in-phase imaging and the signal decreases in the out-of-phase imaging.

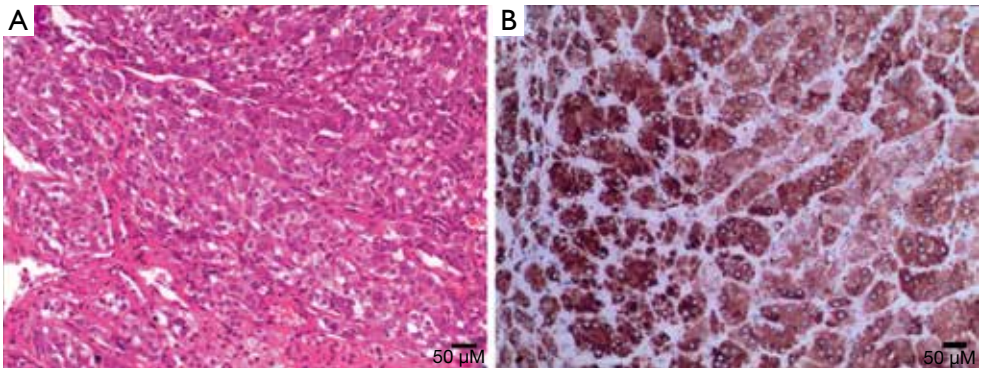

Figure 4 (A) Photomicrograph (original magnification, ×200; H-E stain) shows rare unilateral nodular cortical hyperplasia. (B) Photomicrograph (original magnification, ×200; immunohistochemical staining): melan-A (+).

Hyperplasia

Hyperplasia can be seen as a diffuse process, that may involve the entire adrenal gland, or nodular hyperplasia, and it is typically bilateral (13,23). Diffuse hyperplasia is usually characterized by homogeneous thickening of the entire adrenal gland, maintaining its overall normal inverted-V or inverted-Y appearance (1). As nodular hyperplasia, if the nodules are large enough, they can be identified at cross-sectional imaging.

Most hyperplasia occurs in women, and the proportion in men and women is approximately 1:4, with a prevalence that increases with age and is estimated to be 0.51% (24). Once the hyperplastic adrenal cortex actively produces hormones, hormonal abnormalities in the blood can result, and ultimately CS and Conn syndrome may occur. The treatment of hyperplasia is associated with clinical manifestations. There is no need for treatment when no clinical and biological evidence indicates that hyperplasia is accompanied by adrenal cortical hyperfunction (24). When the patient has symptoms, sampling of the adrenal vein is essential for determining the next step of treatment.

Nodular hyperplasia is evidenced by multiple nodules in the adrenal glands, and the cells in the nodules are the same as those in the surrounding normal tissue (*Figure 4*). Diffuse hyperplasia shows enlarged cell volume and increased lipid content in the cytoplasm.

The density and signal of hyperplasia on CT and MRI is the same as that of the normal adrenal gland, but the density of some patients may be lower than that of the normal adrenal gland on unenhanced imaging (24).

Pheochromocytoma

Pheochromocytomas are neural crest cell tumors occurring in the adrenal medulla. Pheochromocytomas are also a rare neuroendocrine tumor that secretes catecholamine, which are potent vasoactive hormones. It is known as the 10% tumor: 10% of these tumors are non-functioning, 10% occur in children, 10% are located outside the adrenal glands, and 10% are bilateral. Goffredo *et al.* (25) reported that although most cases of pheochromocytoma are benign, approximately 10% to 15% are malignant. Pathologically, there are multi-angle chromaffin cells under the electron microscopy. Under light microscopy, dense chromaffin granules can be seen around the nucleus (*Figure 5*).

The incidence of pheochromocytoma is 0.1–0.2%, and has no sex difference. The clinical manifestation of these tumors is different from person to person and associated with the excess hormone produced by the tumor. Approximately 10% of pheochromocytomas are asymptomatic (14). Symptomatic patients may experience a feeling of flushing, hypermetabolism, hyperglycemia, hyperhidrosis, headache, palpitations and panic attacks or anxiety. The most common symptom is new onset, malignant, secondary hypertension.

The size of pheochromocytomas is diverse; they are usually larger than adenomas, but smaller than metastatic tumors. A functional lesion is often not as large as a nonfunctional lesion. Pheochromocytoma may be visible as a well-defined mass, which may be solid or cystic to variable degrees (26). CT and MRI can clearly characterize and localize suspected pheochromocytomas. CT is associated with a certain amount of radiation damage; therefore, MRI

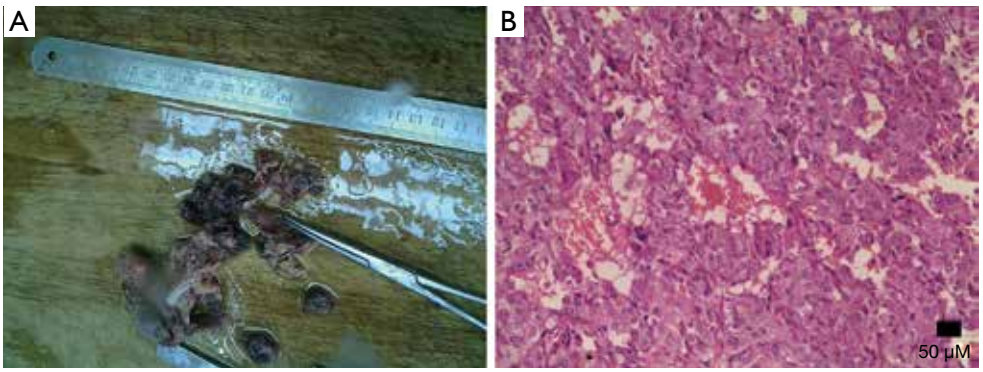

Figure 5 (A) Gross specimen picture shows dark red broken tissue and pinky-grey in section. (B) Photomicrograph (original magnification, ×200; H-E stain) shows the tumor cells are irregular polygons, and some cells have multiple nuclei.

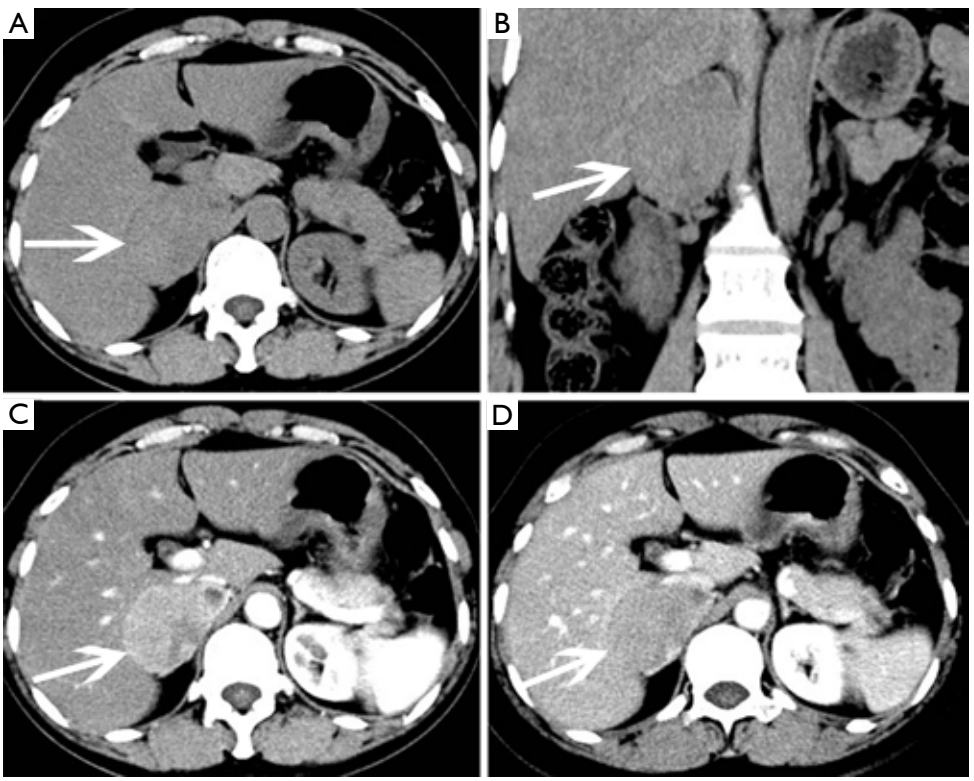

Figure 6 Pheochromocytoma in a 45-year-old woman presented with hypertension. (A) Axial and (B) coronal pre-contrast CT images show a 59 mm × 40 mm × 63 mm soft tissue density mass at the right adrenal area (arrows). (C) Axial arterial and (D) venous phase images show heterogeneous enhancement.

is the first choice imaging method for children, pregnant women, young people and breast-feeding mothers (22). Attenuation values of pheochromocytomas are often similar to those of muscle tissue, and are significantly higher than those of adrenal adenomas. On CT and MRI, lesions with hemorrhage and necrosis can be heterogeneous (*Figures 6*,7). Pheochromocytomas are hyperintense on T2-weighted images (light bulb sign) (1,9), however, there is no such characteristic appearance in some pheochromocytomas (*Figure 8*).

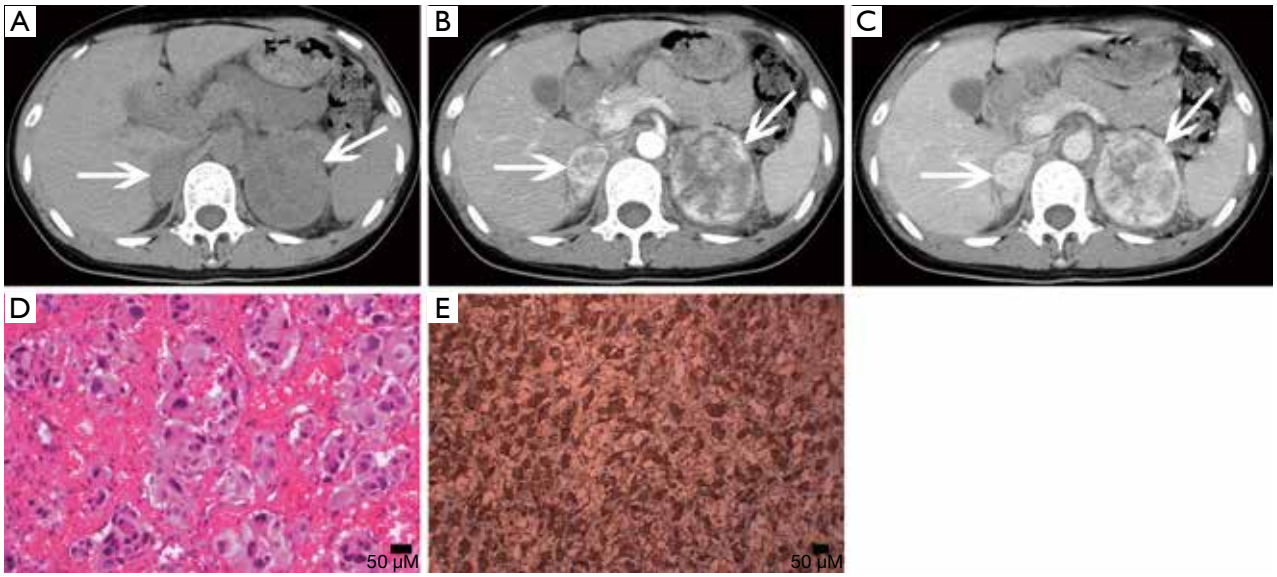

Figure 7 Pheochromocytoma in a 42-year-old woman presented with hypertension and lumbago. (A) Axial pre-contrast CT image shows clear margin and heterogeneous density mass at bilateral adrenal gland areas (arrows). The larger one is located in the left adrenal gland, about 60 mm × 54 mm. (B) Axial arterial and (C) venous phase images show they are obviously and heterogeneously enhanced. (D) Photomicrograph (original magnification, ×200; H-E stain) and (E) Photomicrograph (original magnification, ×100; immunohistochemical staining): CgA (+++).

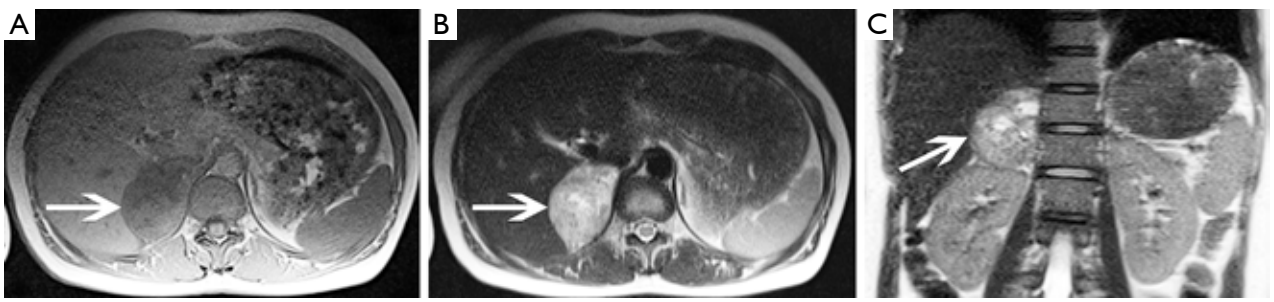

Figure 8 Pheochromocytoma in a 38-year-old woman. (A) Axial T1-weighted image, (B) axial T2-weighted image and (C) coronal T2-weighted image show a 66 mm × 57 mm × 41 mm mass located in the right adrenal (arrows) and show heterogeneity with hyperintense on T2-weighted image and hypointense on T1-weighted image.

Myelolipoma

Adrenal myelolipomas are rare benign tumors consisting of hematopoietic tissue and fat. These tumors are hormonally silent and clinically asymptomatic and are usually detected incidentally on CT (27). Patients may feel pain only with large myelolipomas (more than 10 cm) or those with intratumoral hemorrhage. Myelolipomas grow slowly, and there is usually no need for treatment. Surgical removal is necessary when the lesion is large and accompanied by clinical symptoms. It has been reported that congenital adrenal hyperplasia may be related to the occurrence of bilateral myelolipomas (1).

The composition of fat and bone marrow is visible under microscopy (*Figure 9*). Furthermore, there is internal hemorrhage in some lesions. It has been reported that other lesions can also contain fat, including adenomas, ACCs, pheochromocytomas, adrenal lipomas, or adrenal teratomas. In adrenal nodules containing >50% gross (mature) fat, the diagnosis of adrenal myelolipoma can be reasonably considered (19,28).

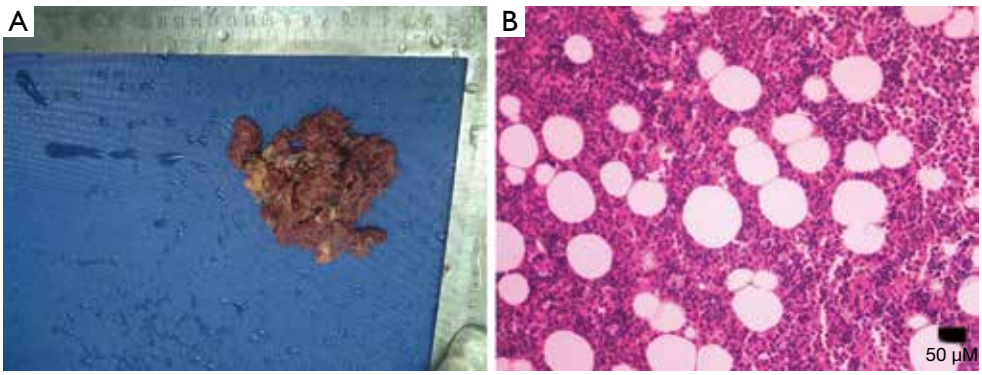

Figure 9 (A) Gross specimen picture shows greyish white and greyish yellow cystic wall tissue, 11 cm × 5 cm, with thickness of the wall, 0.3–0.5 cm, and grayish yellow matter attached to the cystic wall. (B) Photomicrograph (original magnification, ×100; H-E stain) shows the tumor consists of mature adipocytes and bone marrow hematopoietic cells.

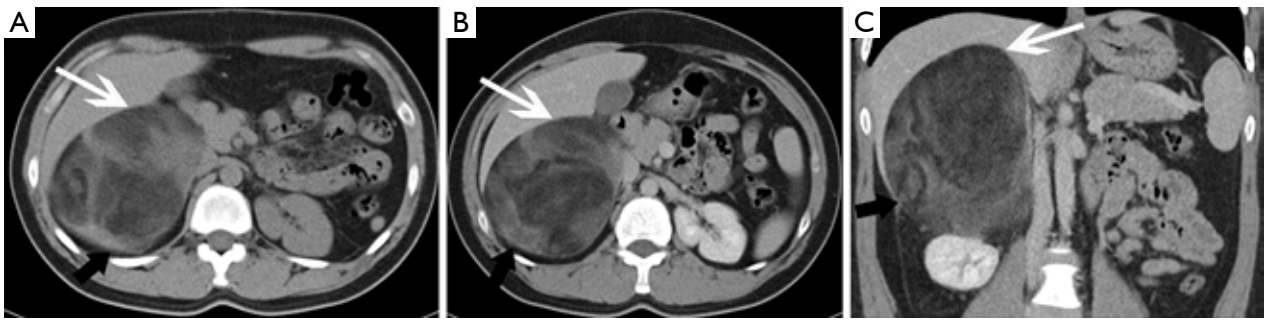

Figure 10 Adrenal myelolipoma in a 24-year-old man complained of right flank malaise. (A) Axial pre-contrast-enhanced CT scan image demonstrates a 103 mm × 103 mm × 132 mm, large heterogeneous fat lesion (white arrows) with high attenuation content (black arrows). (B) Post-contrast-enhanced axial CT scan image and (C) coronal reformatted image show soft tissue components slightly intensified and fat component not enhanced.

Owing to their lipid content, myelolipomas present with specific imaging characteristics with the attenuation less than 0 HU, sometimes less than –50 HU on pre-contrast CT images. Due to the appearance of hematopoietic tissue, the attenuation of myelolipomas is mildly higher than that of ambient fat space (16) (*Figure 10*). On contrast-enhanced CT images,the hematopoietic tissue shows contrasted enhancement. On MRI, it shows high signal on both T1- and T2-weighted images and there is a loss of signal on fat-saturated MRI (*Figure 11*).

Cysts

Adrenal cysts are relatively rare, and often occur unilaterally. This is an unusual disease that is usually caused by epithelial or endothelial proliferation, hemorrhage, or parasitic disease. Currently, there are four classifications for cysts: endothelial (more than 80%), epithelial, parasitic, and pseudocysts (24,26). The prevalence of adrenal cyst is 0.064–0.18% and shows a 3:1 female predilection. They are often detected incidentally because adrenal cysts are nonfunctional. For symptomatic patients, the main symptoms include an abdominal mass, hypertension, waist and abdominal pain. When lesions are large or functional, malignancy should be considered.

Adrenal cysts are reasonably simple to characterize radiologically. A cyst appears as a round mass with a clear border and a density close to water (*Figure 12*), and often have thin walls less than 3 mm as well as internal septa, and both the walls and septa may enhance or contain calcifications (16,29) (*Figure 13*). Adrenal cysts have features with high signal on T2-weighted images and low signal on T1-weighted

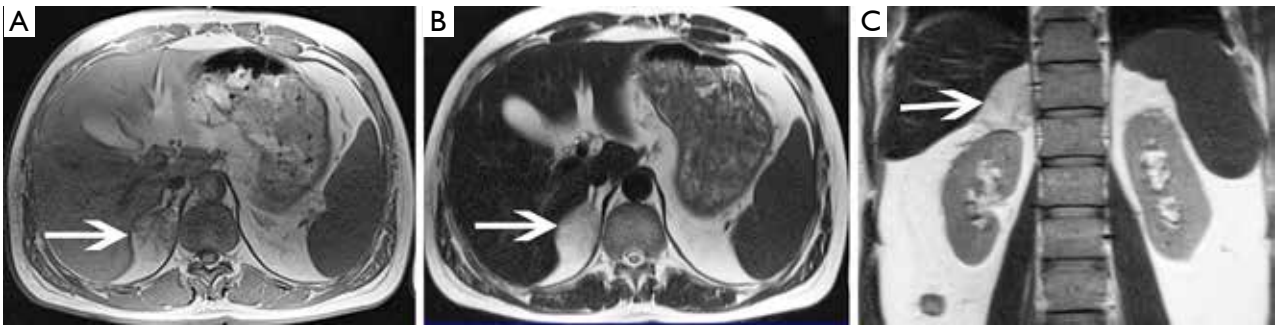

Figure 11 Adrenal myelolipoma in a 42-year-old man detected in health check. (A) Axial T1-weighted image, (B) axial T2-weighted image and (C) coronal T2-weighted image show a right adrenal mass of heterogeneous, slightly high signal (fatty signal) with strips of iso-intensity (myeloid signal, arrows).

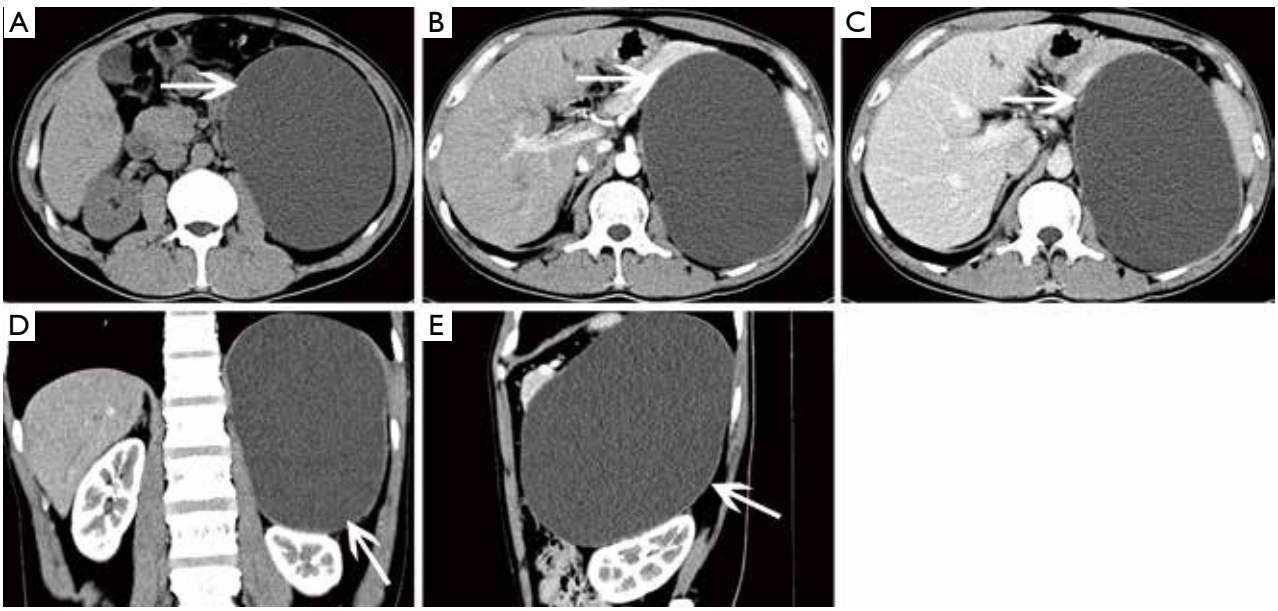

Figure 12 Cyst in a 38-year-old man confirmed with pathology complained of flank malaise. (A) Axial pre-contrast CT image shows a big (118 mm × 158 mm × 184 mm), homogeneous, low density left adrenal mass (arrows). (B,C) Axial, (D) coronal, (E) sagittal postcontrast CT images show non-enhancing contents and compressing displacement of the left kidney.

images, without contrast enhancement (*Figure 14*).

When nodular non-enhancement occurs, a cystic adrenal tumor which is prone to cystic changes, especially pheochromocytoma and cortical adenocarcinoma should be considered (17,20).

Cystic lymphangioma

Adrenal cystic lymphangioma is a type of adrenal endothelial cyst (30). It is a congenital developmental malformation formed by the benign proliferation of primitive lymphatic vessels. Briefly speaking, it is a lesion which composed of dilated lymphatic vessels. The incidence of adrenal cystic lymphangioma is reported to be approximately 0.06% (1), and occur at all ages, with the peak incidence between the third and sixth decades of life (31,32). Some researchers have found that these tumors occur distinctly in females. Like most cysts, adrenal cystic lymphangiomas are commonly asymptomatic and incidentally detected (33). However, if the lesion is large enough to compress surrounding tissues and organs, there are corresponding clinical symptoms, such as a palpable abdominal mass,

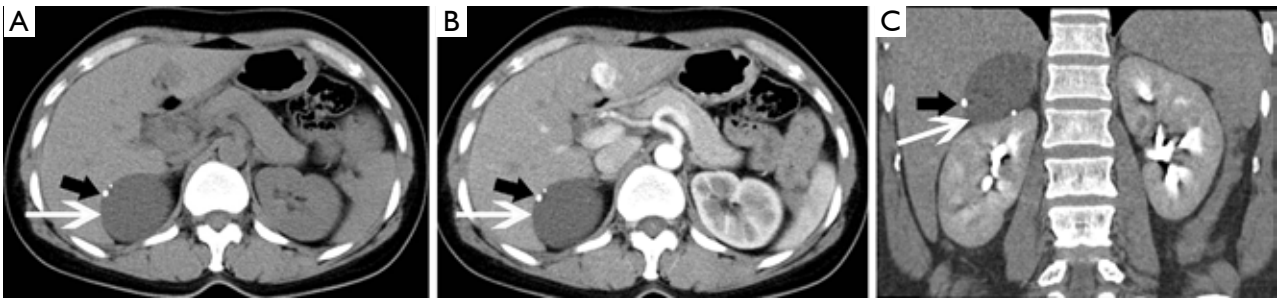

Figure 13 Cyst in a 42-year-old woman with left lumbago. (A) Axial unenhanced CT image shows a well-defined homogeneous round masse of near-water attenuation (white arrows) with punctate calcifications (black arrows) on its thin wall. (B) Axial postcontrast CT image shows the mass does not enhance. (C) There is no contrast enhancement in the cystic cavity on coronal multiplanar reformation image from contrast-enhanced CT.

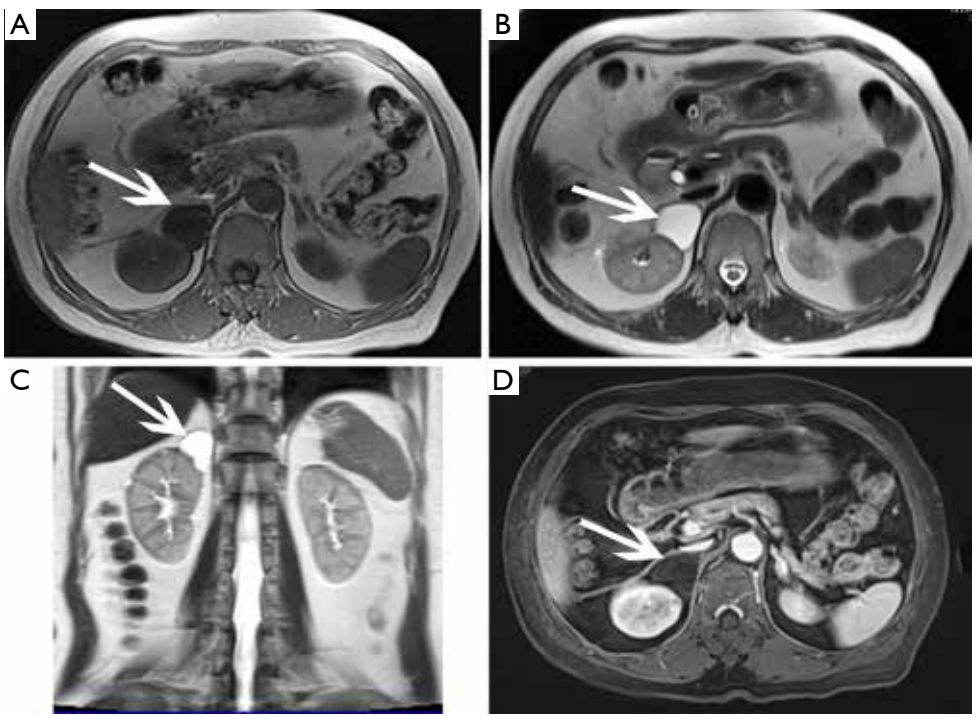

Figure 14 Cyst in a 78-year-old woman. (A) Axial T1-weighted image shows a 38 mm × 27 mm × 36 mm, round, low signal mass (arrows) in the right adrenal gland. (B,C) Axial, coronal T2-weighted images show the lesion of homogeneous high signal. (D) No contrast enhancement in axial postcontrast T1-weighted image.

gastrointestinal symptoms and abdominal pain.

Histologically, almost all of these tumors have polycystic changes of different sizes. The endothelial cells in the inner area can be observed under microscopy (*Figure 15*). CD31, CD34 (endothelial specific markers) (34) and D2-40 (lymphatic markers) (32) can help diagnose this disease.

On CT, cystic Lymphangioma shows as sharply demarcated, uniform low-density lumps without enhancement (*Figures 16-18*). Lymphangiomas usually have smooth thin walls, and calcification may occur (*Figures 19,20*). On MRI, adrenal lymphangioma are typically T1 hypointense and T2 hyperintense. Therefore, imaging examinations can only prove that adrenal lymphangioma lesion originates from the adrenal gland, but it cannot

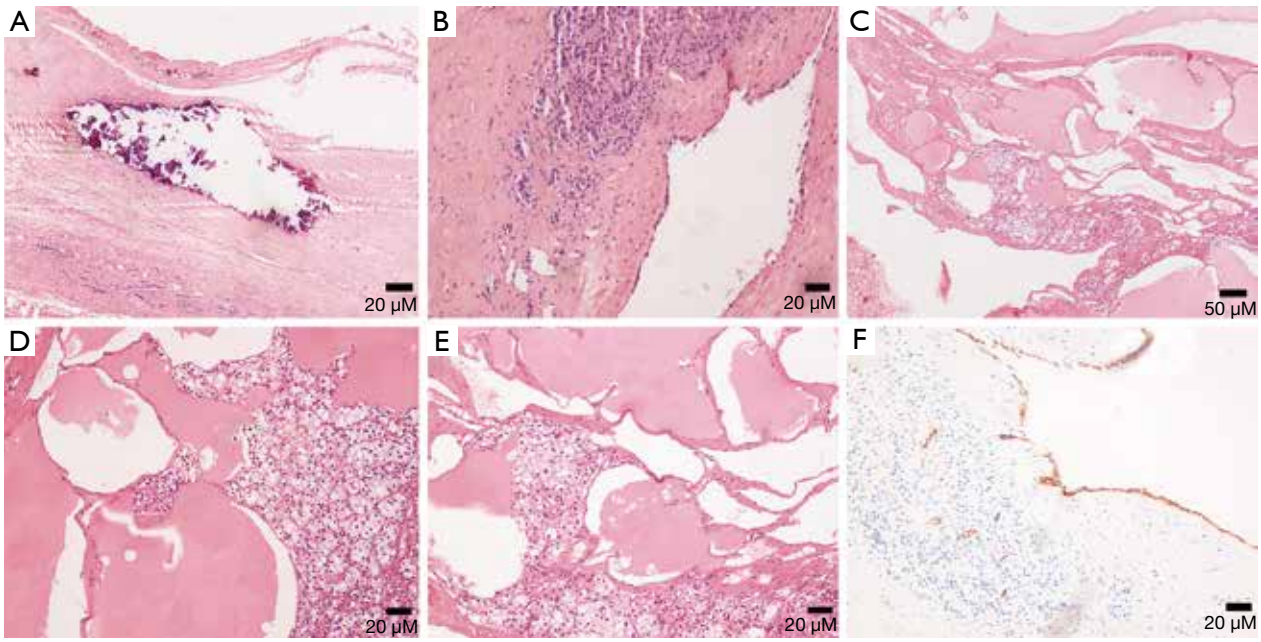

Figure 15 (A-E) Photomicrographs (original magnification, A,B: ×100; C: ×40; D,E: ×100; H-E stain) show calcification in (A) lymphangiomas lined by flattened endothelial cells with no significant atypia in (B) and lymphatic fluid and dilated lymphatic ducts are found in (C-E). (F) Photomicrograph (original magnification, ×100; D2-40 IHC stain) presents positive result.

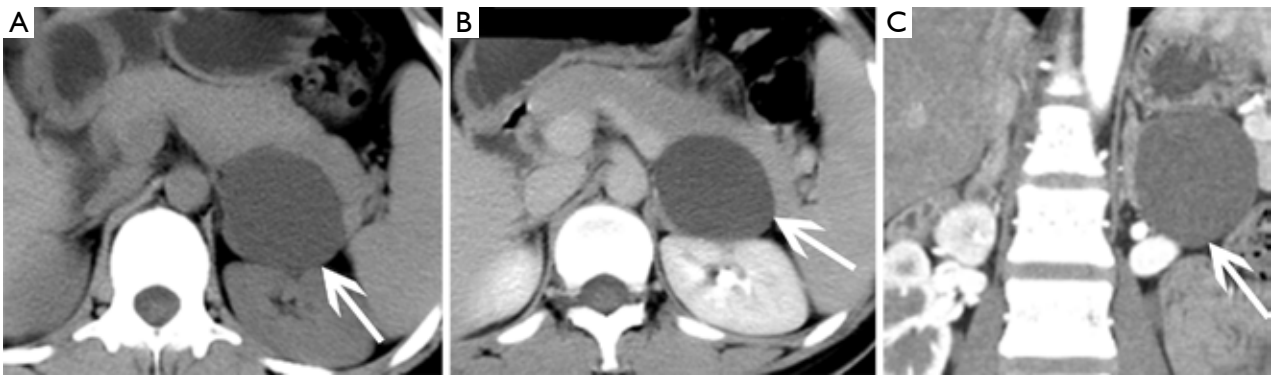

Figure 16 Cystic lymphangioma in a 35-year-old man detected in health check. (A) Axial pre-contrast CT image shows an ovoid, well-circumscribed, low density left adrenal mass (arrows) without contrast enhancement. (B) Axial and (C) coronal postcontrast CT images show non-enhancing contents.

distinguish cystic lymphangiomas from other cysts.

Teratoma

Teratomas are solid neoplasms originating from germ cells and have the potential to differentiate into somatic cells. These tumors often contain 2 or 3 germ layer tissues, and are most commonly seen in gonads and the sacrococcygeal, mediastinal, retroperitoneal and pineal regions. The biological characteristics of these tumors range from benign to borderline and malignant mature teratomas with malignant transformation, which most often manifest as the development of solid components superimposed on pre-existing cystic components (35). Mature teratomas are usually benign, but there is a possibility of malignancy, the chances of which are greater in adults than in children (36).

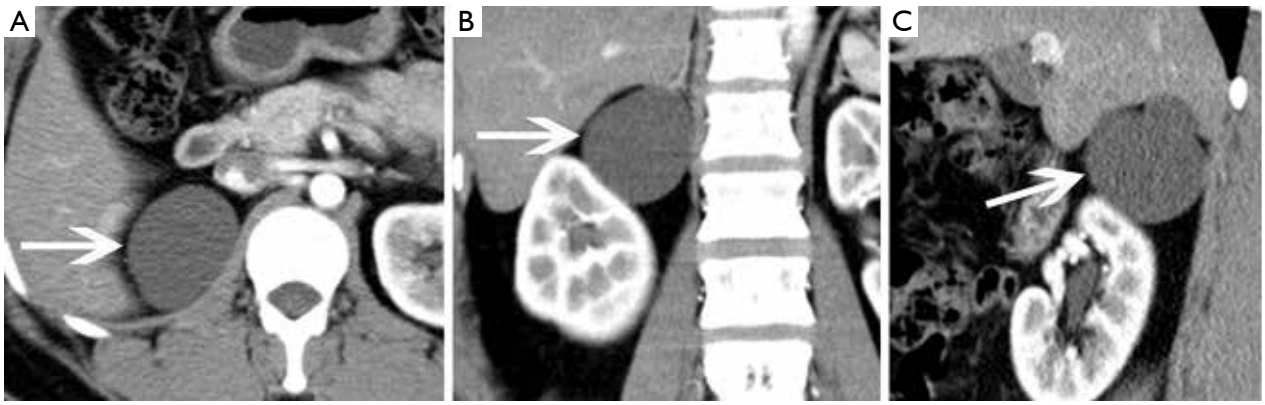

Figure 17 Cystic lymphangioma in a 35-year-old woman detected in health check and confirmed with pathology. (A) Axial, (B) coronal and (C) sagittal postcontrast CT images show a 43 mm × 51 mm × 47 mm, well-demarcated, low density mass (arrows) of the right adrenal gland with non-enhancing contents.

Figure 18 Cystic lymphangioma in a 50-year-old woman complained left loin pain with no obvious cause. (A) Axial pre-contrast CT image shows 25 mm × 35 mm × 60 mm low density mass (arrows) with thin wall. (B) Axial and (C) coronal postcontrast CT images show no enhancement of this lesion.

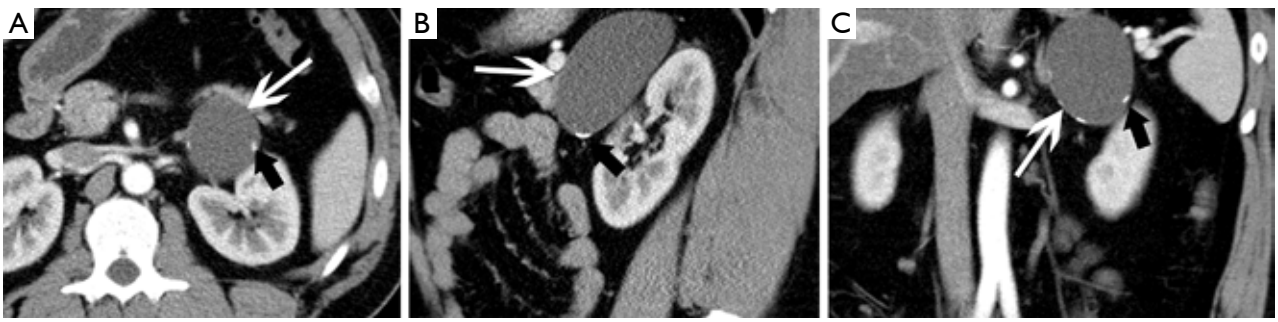

Figure 19 Cystic lymphangioma confirmed with pathology in a 27-year-old man presented with hypertension. (A) Axial, (B) sagittal and (C) coronal postcontrast CT images show an elliptical, low density left adrenal mass (white arrows) with scattered peripheral calcifications (black arrows).

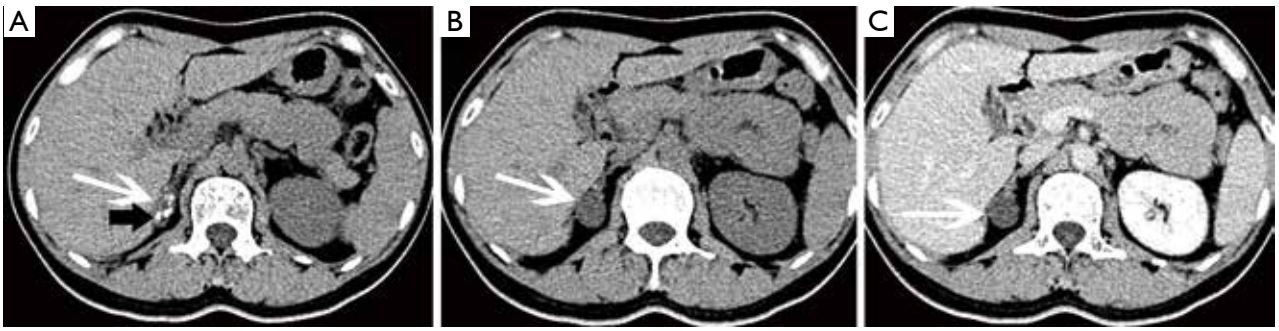

Figure 20 Cystic lymphangioma in a 40-year-old woman detected in health check. (A,B) Axial precontrast CT scan images show a low density lesion (white arrows) with punctate and nodular peripheral calcifications (black arrows). (C) Axial post-contrast CT image shows this lesion with non-enhancing contents.

Primary retroperitoneal teratomas of the adrenal gland are very uncommon (4% of all primary teratomas) (37). The typical gross appearance of teratomas includes hair, teeth, bone, calcification, soft tissue, and fat. Microscopically, muscle cells, glandular epithelium, squamous epithelium and osteocytes can be observed.

Unenhanced CT reveals a well-defined mixed density mass with low-density cystic and fatty areas and high density calcifications. Septations are visible in the mass. Egg-shell calcification is a characteristic manifestation of an adrenal teratoma. On MRI, both T1- and T2-weighted images show mixed signals, on which fat is hyperintense. On enhanced CT and MRI, slight enhancement of the substantial part and a hyperdense peripheral rim and internal septations with significant enhancement are visible (*Figure 21*).

Hemorrhage

Adrenal hemorrhage most commonly appears during the neonatal period and is rarely seen in adults (16), and can be divided into traumatic causes and nontraumatic causes with a prevalence of 1.9–5.5‰. Blunt trauma is the most common causative factor for all adrenal hemorrhage. Traumatic adrenal hemorrhage is usually bilateral, but the right side is more commonly affected (16,24). Non traumatic bleeding is also common on both sides. Coagulation disorders, hemorrhagic diseases or stress can give rise to hemorrhage. Common stress events include surgery, sepsis, as well as severe burns (1). Adrenal hemorrhage can also be a complication of adrenal venous sampling (16,24). On histopathology, bleeding often affects the medulla, accompanied by different degrees of cortical involvement.

Symptoms depend on the degree of hemorrhage, and the patient may have symptoms ranging from mild back pain change to shock. Nevertheless, hemorrhage may appear in both benign and malignant lesions, such as adenomas, myelolipomas, pheochromocytomas, metastases and adrenal cortical carcinomas.

On CT and MRI, adrenal hemorrhage has a round or oval appearance, and the density and signal change according to the different stages of the disease. Acute hemorrhage presents with high density on non-contrast-enhanced CT, and the density decreases along with the size of the lesion (29,38). If the normal abdominal CT manifestations of the abdomen cannot exclude the possibility of hemorrhage, follow-up imaging is necessary.

Adrenal hemorrhage has a different image performance on T1- and T2-weighted imaging during different periods, based on the stage of bleeding and its components. Early hemorrhage is isointense on T1-weighted imaging and shows low signal on T2-weighted imaging. At medium term, lesions show high signal on both T1- and T2-weighted images. Late hemorrhage is hypointense on T1- and T2-weighted images.

Hemangioma

Adrenal hemangiomas are extraordinarily scarce, nonfunctional, benign tumors composed of angioblastic cells. Hemangiomas consist of four types: cavernous hemangioma, venous hemangioma, capillary type hemangioma and mixed hemangioma (33). Capillary and cavernous hemangiomas are the main types, with the latter type being more frequent. The prevalence of adrenal

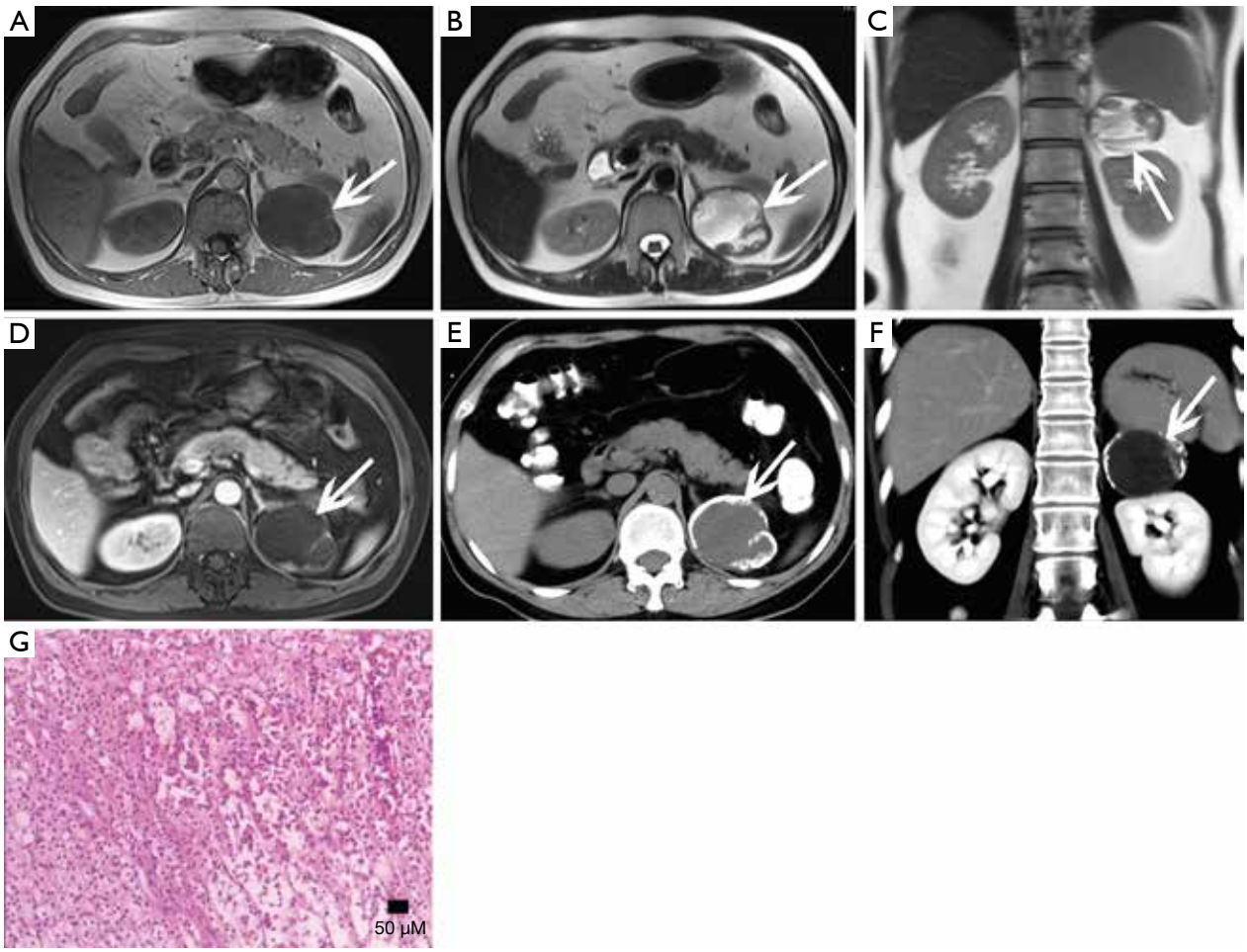

Figure 21 Teratoma in a 47-year-old woman detected in health check. (A) Axial T1-weighted image, (B) axial T2-weighted image; (C) coronal T2-weighted image. (D) Axial in-phase T1-weighted image. A 59 mm × 47 mm × 45 mm mass locates in the left adrenal (arrows) and shows heterogeneity with low signal intensity at T1-weighted image and high signal intensity at T2-weighted image with strip enhancement on enhanced scan. (E) Axial pre-contrast-enhanced CT scan image and (F) coronal reformatted image show egg-shell calcifications. (G) Photomicrograph (original magnification, ×100; H-E stain) shows fibrous tissue, adipose tissue and muscle fibers are found in tumor tissues, and necrosis and calcification are noted.

hemangiomas is 1 per 10,000 autopsies (1). Although they are generally asymptomatic and detected by chance, these neoplasms are mainly composed of blood vessels and are inclined to be incredibly vascularized (1), which makes these tumors associated with a high risk of hemorrhage. Therefore, it is important for further management to make the correct pretreatment diagnosis.

Pre-contrast CT scan shows these neoplasms to be well-circumscribed and homogenous with low density. Post-contrast CT scans show nodular enhancement during the arterial phase, and progressive enhancement in venous phase and delayed phases (*Figure 22*). Some these masses are low density and difficult to distinguish from cysts (*Figure 23*). Calcifications may also be present. Phleboliths are characteristic. On MRI, these tumors typically have low signal intensity on T1-weighted imaging and high signal intensity on T2-weighted imaging.

Ganglioneuroma

Ganglioneuromas are a rare benign neurogenic tumor originating from the adrenal medulla, and account for approximately 0.3–2% of all adrenal incidentalomas (39). Only rarely are they hormonally active. These tumors can

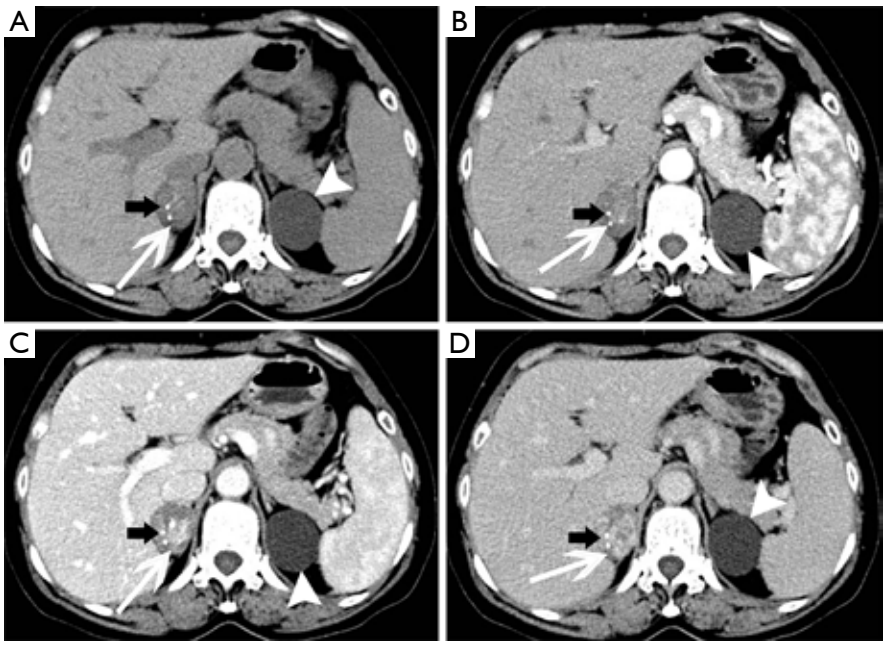

Figure 22 Right adrenal hemangioma and left adrenal cyst in a 64-year-old woman. (A) Axial unenhanced CT image shows a 31 mm × 28 mm, well-demarcated round mass (white arrows) with stippled calcifications (black arrows) in the right adrenal, and a low density lesion of the left adrenal gland (arrowheads). (B-D) Axial arterial phase, venous phase and delayed phase CT images show the right lesion is heterogeneous and with marked enhancement, and also progressive enhancement in venous phase and delayed phase, the left one has no enhancement.

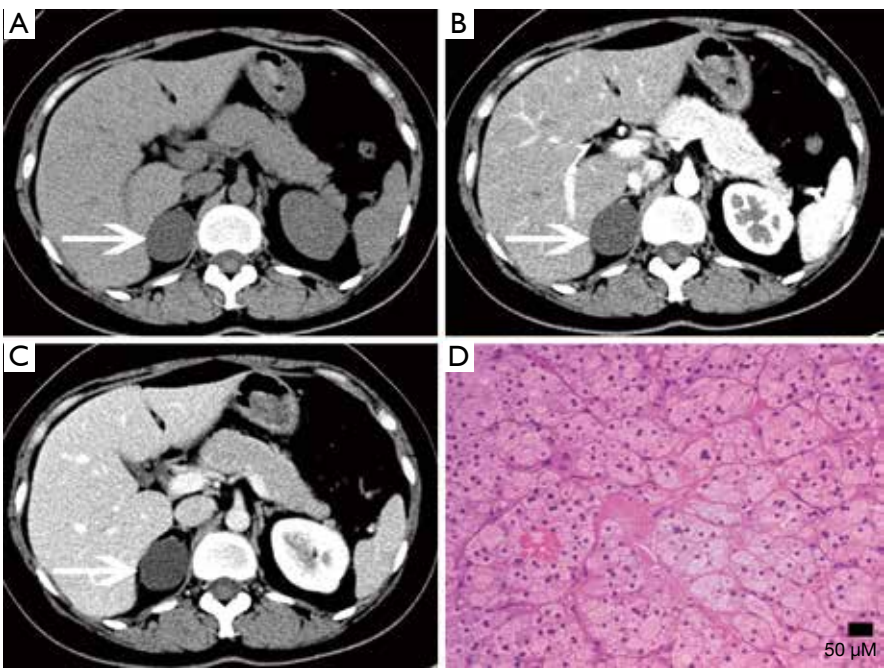

Figure 23 Hemangioma in a 35-year-old woman detected in health check. (A) Axial pre-contrast CT image shows a round, low density right adrenal mass (arrows). (B) Axial arterial phase and (C) axial venous phase CT images show no enhancement of this lesion. (D) Photomicrograph (original magnification, ×100; H-E stain) shows vines vascular hyperplasia in full field, and no specific cells are noted.

Figure 24 Ganglioneuroma in a 29-year-old man detected in health check. (A) Axial pre-contrast CT image demonstrates a well-circumscribed, homogeneous oval mass with low density (arrows). (B-C) Axial arterial phase and axial venous phase CT images show mild homogeneous enhancement.

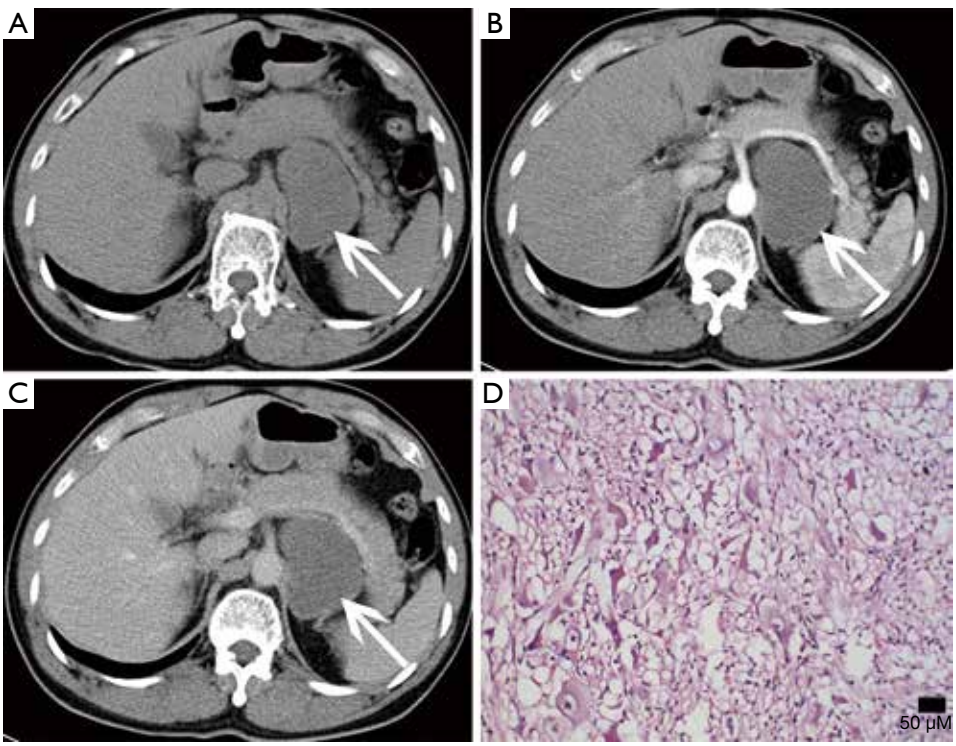

Figure 25 Ganglioneuroma in a 45-year-old man detected in health check. (A) Axial pre-contrast CT image shows a 40 mm × 72 mm, crescent homogeneous, low density lesion in the left adrenal area (arrows) with thin wall. (B) Axial arterial phase and (C) axial venous phase CT images show slight enhancement of the tumor and wall. (D) Photomicrograph (original magnification, ×200; H-E stain) shows spindle shaped tumor cells proliferate and more ganglion cells.

occur at any age and are more common in young people and adults, and are more common in women than men. Ganglioneuromas are usually detected incidentally and even with large lesions, patients usually do not develop symptoms.

These lesions are usually solid masses with clear boundaries and can be a shape of casting mold. Microscopically, they are composed of mature ganglion cells, Schwann cells, mucous matrix and nerve fibers (40).

CT can reveal a well-circumscribed, homogeneous solid tumor with clear boundaries (*Figures 24,25*), which may be companied by punctate or discrete calcifications (in 20% of

Figure 26 Left adrenal neuroblastoma in 6-year-old girl. (A) Axial pre-contrast CT scan shows a 27 mm × 35 mm left adrenal mass (white arrows) with soft tissue attenuation and amorphous calcification (black arrows). (B-C), Contrast-enhanced axial CT scan images show tumor inhomogeneous enhancement.

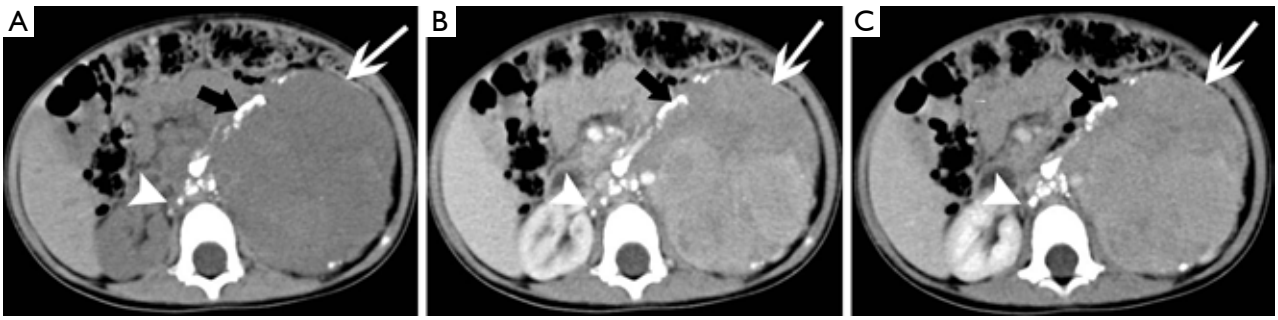

Figure 27 Neuroblastoma in 1-year-old girl presented with left abdominal mass. (A) Axial pre-contrast CT image shows a 78 mm × 89 mm, round mass above the left kidney (white arrows), extending across the midline with patchy calcifications (black arrows). Abdominal aorta is embedded by the mass. Nodules of soft tissue density with calcifications can be detected near the spine (arrowheads). (B) Axial arterial and (C) venous phase images show the big lesion markedly and heterogeneously enhanced.

ganglioneuromas). Enhancement varies and lesions often encircle blood vessels, rather than directly encroaching or occluding them. On MRI, these lesions show hypointense on T1-weighted images and have varied signal on T2-weighted images.

Malignant conditions

Neuroblastoma

Pheochromocytoma and other adrenal benign or malignant tumors can also occur in children, but neuroblastoma is the second most common abdominal mass in children besides Wilms' tumor. Neuroblastomas originate from the neural crest of the embryo with malignant nature, and usually occur in the adrenal medulla (40). Generally, neuroblastomas have no clinical symptoms unless they invade surrounding organs or metastasize. Sometimes, patients may have symptoms of flushing, tachycardia or high blood pressure due to excessive catecholamine production. The prognosis of neuroblastoma varies depending on whether the tumor has spread or metastasized (such as to liver or bone).

Under microscopy, tumor cells are blue stained small round cells, arrayed around the neuropil and have an appearance similar to that of a chrysanthemum.

Lesions always present with calcifications, necrotic, hemorrhagic and cystic changes, which lead to density/signal inhomogeneity (*Figure 26*). CT shows a large mass extending across the midline, engulfing abdominal vessels and dislocating surrounding structures (*Figure 27*). On MRI, these tumors are nonhomogeneous and hyperintense on T2-weighted images and hypointense on T1-weighted images (*Figure 28*). Heterogeneous enhancement on post-contrast imaging may occur. Hemorrhagic areas

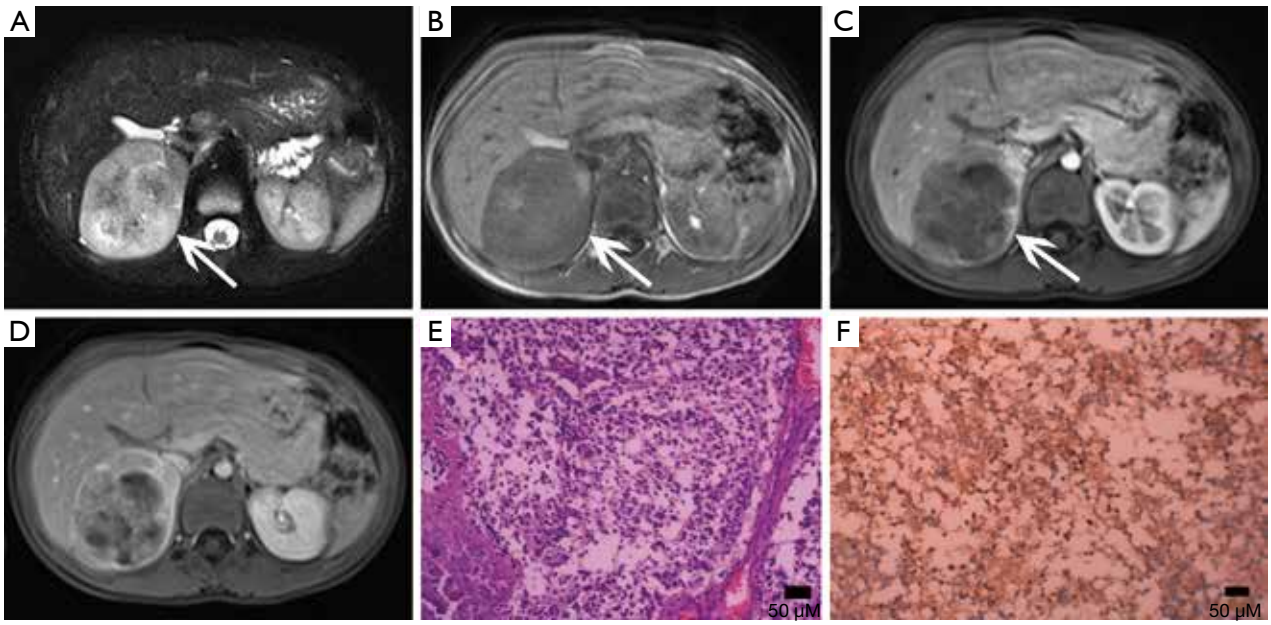

Figure 28 Neuroblastoma confirmed with pathology in 4-year-old boy. (A) Axial T2-weighted image, (B) axial T1-weighted image show a 62 mm × 54 mm oval mass with mixed signal (arrows). (C-D) Enhanced MR imaging demonstrates marked heterogeneous enhancement. (E) Photomicrograph (original magnification, ×400; H-E stain) shows the tumor consists of ganglion cells and ensheathing cells. (F) Photomicrograph (original magnification, ×200; immunohistochemical staining): NSE (+).

are hyperintense on T1-weighted images, and cystic and necrotic areas are hyperintense on T2-weighted images.

Metastases

The adrenal blood supply is plentiful, and accordingly, it is a common organ for hematogenous metastasis of malignant tumors (41,42). While all malignant tumors have the possibility of metastasizing to the adrenal gland, the most common primary malignancies that affect the adrenal gland include lung cancer, breast cancer, gastric cancer, liver cancer and pancreatic cancer. The bilateral adrenal glands are usually involved, but unilateral involvement may occur. Metastases occur more commonly in the left gland than in the right gland. On autopsy, about 27% of malignant tumors cause adrenal metastasis.

Adrenal metastasis has no specific imaging findings in routine CT or MRI. On pre-contrast CT scan, the attenuation of metastatic tumors is usually greater than 10 HU. There may be calcification and areas of hemorrhage. There is irregular peripheral enhancement following contrast administration (*Figure 29*), but most lesions usually display obviously enhanced on enhanced CT scan (*Figures 30,31*). On MRI, adrenal metastases show low signal on T1-weighed imaging and high signal on T2-weighed imaging; sometimes, it may be isointense on T1- and T2-weighed imaging with ring or uneven enhancement after contrast administration (*Figure 32*).

ACC

ACC is a malignant tumor occurring in the adrenal cortex. The incidence of the disease is low, approximately 1–2 out of every one million people (43) and occurs slightly more in females than males and can occur at any age but has distinct bimodal characteristics. The majority of ACCs have endocrine function, so it is typically detected early. The mass may lead to CS or primary aldosteronism or abnormal sexuality. Other symptoms include weight loss, upper abdominal pain, or gastrointestinal complaints. ACCs are typically large masses, usually >6 cm and people often present with palpable mass.

Macroscopically, necrosis and cystic degeneration often occur in ACC. Under microscopy, the cells are heteromorphic, and there are a large number of multinucleated giant cells and nuclear division.

On pre-contrast-enhanced CT, ACC is usually

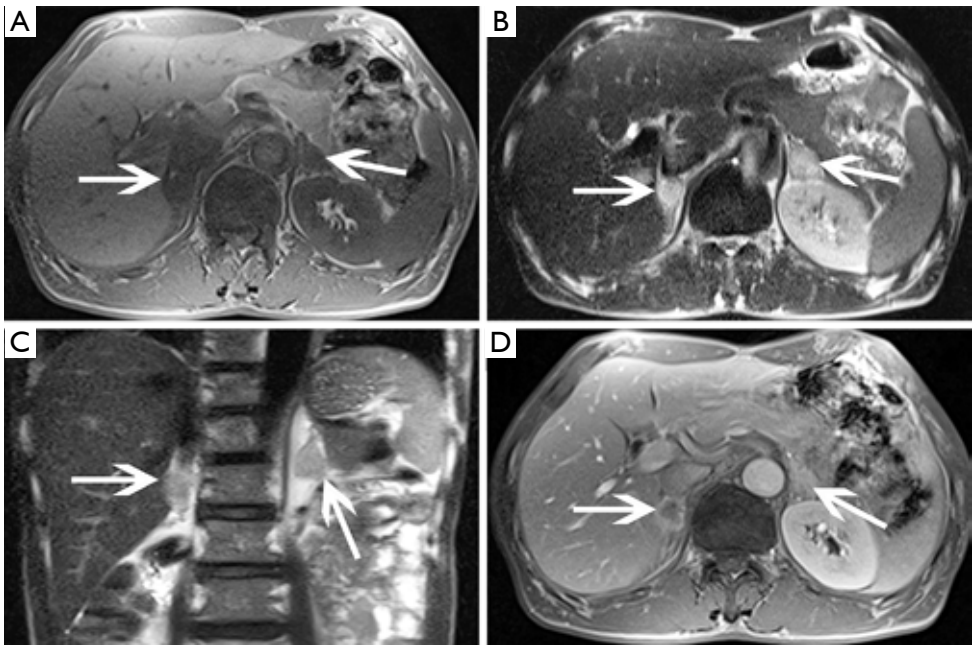

Figure 29 Bilateral adrenal metastases in a 58-year-old man with right peripheral lung carcinoma. (A) Axial T1-weighted image, (B) axial T2-weighted image, (C) coronal T2-weighted image and (D) axial contrast enhanced T1-weighted image show bilateral adrenal masses (arrows) which show heterogeneous with low signal intensity at T1-weighted imaging and high signal intensity at T2-weighted imaging with the right one irregular, thick-wall peripheral enhancement and the left one heterogeneous enhancement.

Figure 30 Metastases in a 59-year-old woman with small cell lung cancer. (A) Axial pre-contrast CT image shows a 21 mm × 17 mm round nodule with CT attenuation value about 41 HU (arrows). (B) Axial arterial and (C) venous phase images show obvious enhancement.

characterized by a well-demarcated heterogeneous mass with the attenuation greater than 10 HU (1,18). On post-contrast-enhanced CT, ACCs show heterogeneous enhancement. Necrosis and cyst formation are common, particularly in the central part of the lesion (*Figure 33*).

The MRI manifestations of ACC are characterized heterogenous hyperintensity on T2-weighted images and hypointensity on T1-weighted images. As a result, necrosis and hemorrhage, both T1- and T2-weighted images may appear heterogeneous. Areas of hemorrhage may appear hyperintense on T1-weighted images and necrosis may demonstrate high signal intensity on T2-weighted images. One study suggested that invasion of the inferior vena cava is a common complication of ACC.

Lymphoma

Lymphoma is a malignant tumor originating from lymphohematopoietic system that infrequently involves of the adrenal gland. The incidence of non-

Figure 31 Metastases in a 53-year-old man with left small cell lung cancer. (A) Axial pre-contrast CT image shows a 15 mm × 18 mm, well-circumscribed nodule at left adrenal gland area (arrows). (B) Axial arterial and (C) venous phase images show marked enhancement.

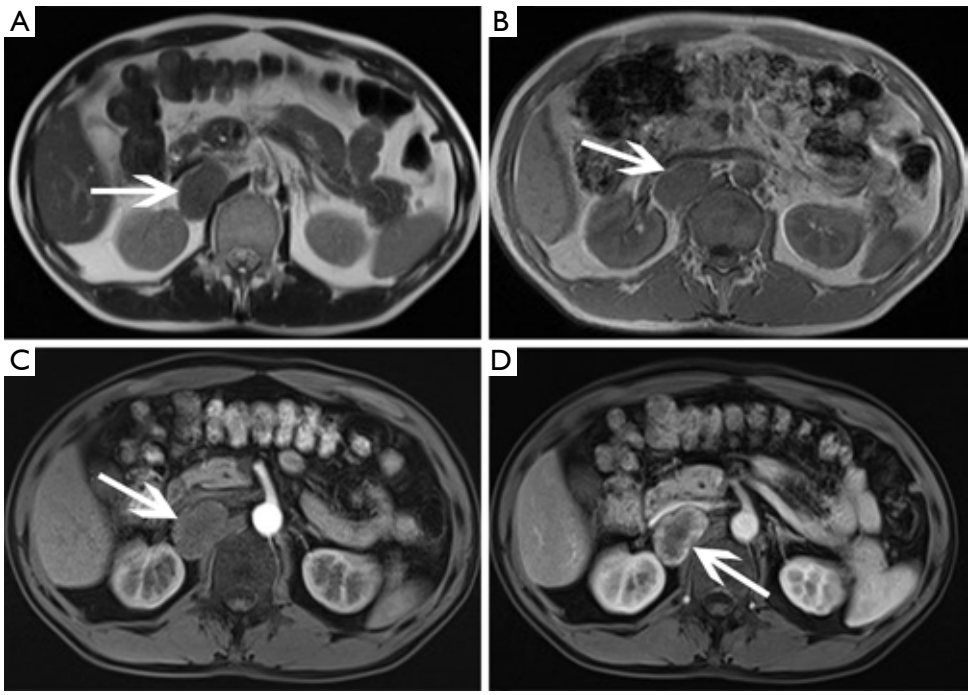

Figure 32 Metastases in a 53-year-old man with liver cancer. (A) Axial T2-weighted image and (B) axial T1-weighted image show a 38 mm × 21 mm, well-circumscribed isointense nodule at right adrenal gland area (arrows). (C-D) Axial in-phase T1-weighted image show progressive and heterogeneous enhancement.

Hodgkin's lymphoma (NHL) is higher than that of Hodgkin's lymphoma (HL) (18). There are two types of this condition: primary lymphoma and secondary lymphoma. Primary adrenal lymphoma is extremely rare, and is defined as malignant neoplastic proliferation of the lymphoid cells exclusively in the adrenal glands. Furthermore, primary lymphoma is confined to a single organ but may involve the neighboring lymph nodes. If not, it is thought to be secondary. If invasion by lymphoma is suspected, other nodal stations should be scanned and commonly affected organs (spleen, liver) should be closely scrutinized (25). Patients may present with fever, night sweats, emaciation, itching, adrenal insufficiency and other systemic symptoms.

The pathological characteristics of NHL and HL are different. NHL shows mainly lymphocytes, tissue cells or reticular cells with different degrees of differentiation. However, the tumor tissues of HL contain lymphocytes, eosinophils, plasma cells and specific Reed-Steinberg cells.

Lymphoma lesions are typically large and homogeneous.

Figure 33 Adrenocortical carcinoma in a 52-year-old man complained abdominal pain and abdominal mass. (A) Axial pre-contrast CT scan shows a large left suprarenal mass with soft tissue attenuation and lower density zone in the center (white arrows). The liver, abdominal and retroperitoneal showed multiple round low density nodules with multiple sizes (black arrows). (B) Axial arterial phase and (C) venous phase volume-rendered CT images show the substantial part of the tumor rapidly enhanced in arterial phase and consistently enhanced in venous phase with progressive enhancement. The liver, abdominal and retroperitoneal nodules show heterogeneous enhancement. Partial filling defect of inferior vena cava caused by tumorous embolus.

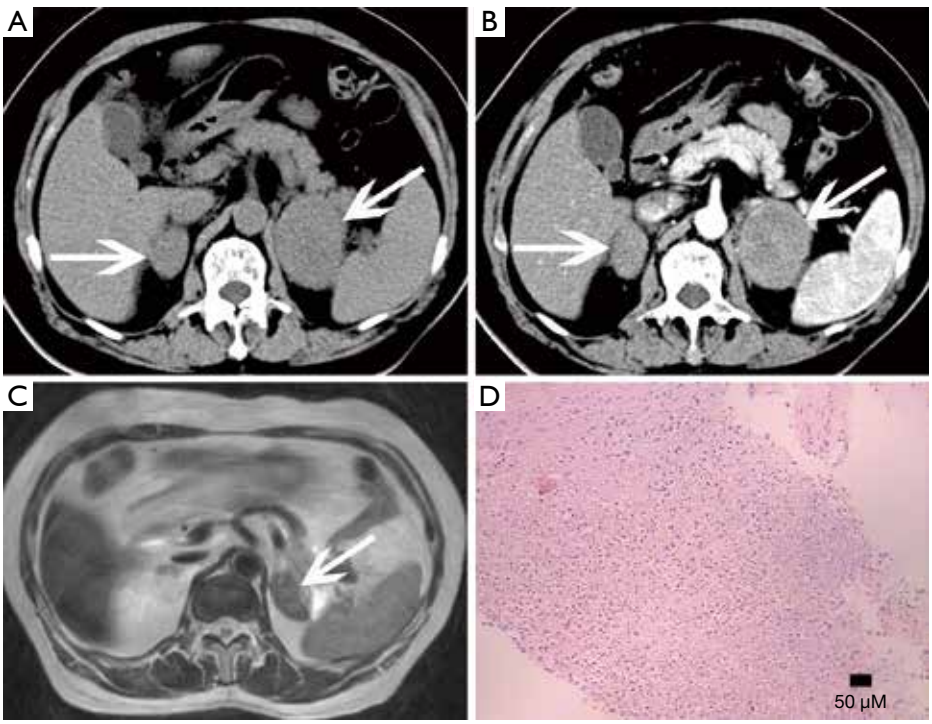

Figure 34 Bilateral adrenal lymphomas in a 76-year-old man. (A) Axial pre-contrast CT scan and (B) contrast-enhanced axial CT scan images show bilateral adrenal round masses (arrows) with CT attenuation value about 35 HU and slightly enhanced. (C) Axial T2-weighted image after two courses of chemotherapy, the mass decreased significantly, showing low signal intensity at T2-weighted imaging. (D) Photomicrograph (original magnification, ×100; H-E stain) shows tumor cells were large, diffuse, infiltrated, and had significant heteromorphism and the mitotic figures.

Like neuroblastomas and cortical cancer, the density of adrenal lymphoma is heterogeneous because of hemorrhagic, necrotic and cystic changes. The enlargement of the retroperitoneal lymph nodes is also common. On MRI, the typical manifestation of adrenal lymphoma is low intensity on T1-weighted images and high-intensity on T2. A mild to moderate enhancement can be seen on enhanced scan (*Figure 34*).

Conclusions

Lesions in the adrenal glands can secrete hormones and cause corresponding endocrine syndrome. CS and Conn syndrome are two of them. We summarize the adrenal lesions associated with Cushing's syndrome and conn syndrome in this article. In symptom patients, imaging examination is performed to search for lesions. However, most adrenal lesions are hormonally silent and clinically asymptomatic and are usually detected incidentally in routine health check care or tests for other purposes. Radiologists should be familiar with imaging characteristics of adrenal incidentaloma.

Acknowledgements

Funding: This work was supported by the National Natural Science Foundation of China (grant No. 81760309), Science and Technology Foundation of Health and Family Planning Commission of Guizhou Province (grant No. gzwjkj2017-1-013), and innovation team of medical imaging center of education department of Guizhou province [Talent team of Guizhou Education (2014) 37].

Footnote

Conflicts of Interest: The authors have no conflicts of interest to declare.

References

1. Lattin GE Jr, Sturgill ED, Tujo CA, Marko J, Sanchez-Maldonado KW, Craig WD, Lack EE. From the radiologic pathology archives: Adrenal tumors and tumor-like conditions in the adult: radiologic-pathologic correlation. Radiographics 2014;34:805-29.
2. Lau D, Rutledge C, Aghi MK. Cushing's disease: current medical therapies and molecular insights guiding future therapies. Neurosurg Focus 2015;38:E11.
3. Wagner-Bartak NA, Baiomy A, Habra MA, Mukhi SV, Morani AC, Korivi BR, Waguespack SG, Elsayes KM. Cushing Syndrome: Diagnostic Workup and Imaging Features, With Clinical and Pathologic Correlation. AJR Am J Roentgenol 2017;209:19-32.
4. Bansal V, El Asmar N, Selman WR, Arafah BM. Pitfalls in the diagnosis and management of Cushing's syndrome. Neurosurg Focus 2015;38:E4.
5. Eckstein N, Haas B, Hass MD, Pfeifer V. Systemic therapy of Cushing's syndrome. Orphanet J Rare Dis 2014;9:122.
6. Monticone S, Buffolo F, Tetti M, Veglio F, Pasini B, Mulatero P. Genetics in endocrinology: The expanding genetic horizon of primary aldosteronism. Eur J Endocrinol 2018;178:R101-11.
7. Aristizabal Prada ET, Castellano I, Susnik E, Yang Y, Meyer LS, Tetti M, Beuschlein F, Reincke M, Williams TA. Comparative Genomics and Transcriptome Profiling in Primary Aldosteronism. Int J Mol Sci 2018;19(4).
8. Vilela LAP, Almeida MQ. Diagnosis and management of primary aldosteronism. Arch Endocrinol Metab 2017;61:305-12.
9. Munir S, Waseem M. Addison Disease. StatPearls. Treasure Island (FL): StatPearls Publishing StatPearls Publishing LLC., 2018.
10. Michels A, Michels N. Addison disease: early detection and treatment principles. Am Fam Physician 2014;89:563-8.
11. Wang YX, Chen CR, He GX, Tang AR. CT findings of adrenal glands in patients with tuberculous Addison's disease. J Belge Radiol 1998;81:226-8.
12. Brandão Neto RA, de Carvalho JF.Diagnosis and classification of Addison's disease (autoimmune adrenalitis). Autoimmun Rev 2014;13:408-11.
13. Elsayes KM, Mukundan G, Narra VR, Lewis JS Jr, Shirkhoda A, Farooki A, Brown JJ. Adrenal masses: mr imaging features with pathologic correlation. Radiographics 2004;24 Suppl 1:S73-86.
14. Korivi BR, Elsayes KM, de Castro SF, Garg N, Qayyum A. An Update of Practical CT Adrenal Imaging: What Physicians Need to Know. Current Radiology Reports 2015;3:12.
15. Michalopoulos N, Pazaitou-Panayiotou K, Boudina M, Papavramidis T, Karayannopoulou G, Papavramidis S. Mixed corticomedullary adrenal carcinoma. Surg Today 2013;43:1232-9.
16. Song JH, Mayo-Smith WW. Current status of imaging for adrenal gland tumors. Surg Oncol Clin N Am 2014;23:847-61.
17. Ctvrtlik F, Koranda P, Tichy T. Adrenal disease: a clinical update and overview of imaging. A review. Biomed Pap Med Fac Univ Palacky Olomouc Czech Repub 2014;158:23-34.
18. Song JH, Chaudhry FS, Mayo-Smith WW. The incidental adrenal mass on CT: prevalence of adrenal disease in 1,049 consecutive adrenal masses in patients with no known malignancy. AJR Am J Roentgenol 2008;190:1163-8.
19. Schieda N, Siegelman ES. Update on CT and MRI of Adrenal Nodules. AJR Am J Roentgenol 2017;208:1206-17.

20. Johnson PT, Horton KM, Fishman EK. Adrenal mass imaging with multidetector CT: pathologic conditions, pearls, and pitfalls. Radiographics 2009;29:1333-51.
21. Park JJ, Park BK, Kim CK. Adrenal imaging for adenoma characterization: imaging features, diagnostic accuracies and differential diagnoses. Br J Radiol 2016;89:20151018.
22. Caoili EM, Korobkin M, Francis IR, Cohan RH, Dunnick NR. Delayed enhanced CT of lipid-poor adrenal adenomas. AJR Am J Roentgenol 2000;175:1411-5.
23. Wang YX, He GX, Du LJ, Jiang H, Tang AR. CT findings in congenital adrenal hyperplasia due to 11 beta hydroxylase deficiency at puberty age. JBR-BTR 1999;82:11-2.
24. Liu H, Wang AP, Bo YH, Li YR, Tang ZM, Zhang TJ. CT and MRI Findings of Adrenal Cystic Lesions. J Clin Radiol 2015;34:591-5.
25. Goffredo P, Sosa JA, Roman SA. Malignant pheochromocytoma and paraganglioma: a population level analysis of long-term survival over two decades. J Surg Oncol 2013;107:659-64.
26. Farrugia FA, Martikos G, Surgeon C, Tzanetis P, Misiakos E, Zavras N, Charalampopoulos A. Radiology of the adrenal incidentalomas. Review of the literature. Endocr Regul 2017;51:35-51.
27. Wang YX, Wu JT, He GX, Pan ZL.CT of adrenal myelolipoma: report of 7 cases. JBR-BTR 1999;82:231-3.
28. Schieda N, Al Dandan O, Kielar AZ, Flood TA, McInnes MD, Siegelman ES. Pitfalls of adrenal imaging with chemical shift MRI. Clin Radiol 2014;69:1186-97.
29. Boland GW, Blake MA, Hahn PF, Mayo-Smith WW. Incidental adrenal lesions: principles, techniques, and algorithms for imaging characterization. Radiology 2008;249:756-75.
30. Rowe SP, Bishop JA, Prescott JD, Salvatori R, Fishman EK. CT Appearance of Adrenal Cystic Lymphangioma: Radiologic-Pathologic Correlation. AJR Am J Roentgenol 2016;206:81-5.
31. Kim KH, Lee JI, Bae JM. Significant growth of adrenal lymphangioma: A case report and review of the literature. Int J Surg Case Rep 2015;17:48-50.
32. Ellis CL, Banerjee P, Carney E, Sharma R, Netto GJ. Adrenal lymphangioma: clinicopathologic and immunohistochemical characteristics of a rare lesion. Hum Pathol 2011;42:1013-8.
33. Secil M, Demir O, Yorukoglu K. MRI of adrenal lymphangioma: a case report. Quant Imaging Med Surg 2013;3:347-8.
34. Liu B, Li Y, Wang S. Adrenal lymphangioma removed by a retroperitoneoscopic procedure. Oncol Lett 2013;5:539-40.
35. Niu M, Liu A, Zhao Y, Feng L. Malignant transformation of a mature teratoma of the adrenal gland: A rare case report and literature review. Medicine 2017;96:e8333.
36. Ramakant P, Rana C, Singh KR, Mishra A. Primary adrenal teratoma: An unusual tumor - Challenges in diagnosis and surgical management. J Postgrad Med 2018;64:112-4.
37. Narla SL, Jacob S, Kurian A, Parameswaran A. Primary mature cystic teratoma with carcinoid mimicking an adrenal tumor: Report of a rare association and review of literature. Indian J Pathol Microbiol 2016;59:200-2.
38. Mazzaglia PJ. Radiographic evaluation of nonfunctioning adrenal neoplasms. Surg Clin North Am 2014;94:625-42.
39. Mylonas KS, Schizas D, Economopoulos KP. Adrenal ganglioneuroma: What you need to know. World J Clin Cases 2017;5:373-7.
40. Herr K, Muglia VF, Koff WJ, Westphalen AC. Imaging of the adrenal gland lesions. Radiol Bras 2014;47:228-39.
41. Lim W, Ridge CA, Nicholson AG, Mirsadraee S. The 8th lung cancer TNM classification and clinical staging system: review of the changes and clinical implications. Quant Imaging Med Surg 2018;8:709-18.
42. Wang YX, Gong JS, Suzuki K, Morcos SK. Evidence based imaging strategies for solitary pulmonary nodule. J Thorac Dis 2014;6:872-87.
43. Kerkhofs TM, Verhoeven RH, Van der Zwan JM, Dieleman J, Kerstens MN, Links TP, Van de Poll-Franse LV, Haak HR. Adrenocortical carcinoma: a population-based study on incidence and survival in the Netherlands since 1993. Eur J Cancer 2013;49:2579-86.

Cite this article as: Wang F, Liu J, Zhang R, Bai Y, Li C, Li B, Liu H, Zhang T. CT and MRI of adrenal gland pathologies. Quant Imaging Med Surg 2018;8(8):853-875. doi: 10.21037/qims.2018.09.13

Letter to the Editor

Informed communication with study subjects of radiographically detected osteoporotic vertebral deformity

Yì Xiáng J. Wáng, Nazmi Che-Nordin

Department of Imaging and Interventional Radiology, the Chinese University of Hong Kong, Prince of Wales Hospital, Shatin, New Territories, Hong Kong SAR, China

Correspondence to: Dr. Yì Xiáng J. Wáng. Department of Imaging and Interventional Radiology, the Chinese University of Hong Kong, Prince of Wales Hospital, Shatin, New Territories, Hong Kong SAR, China. Email: yixiang_wang@cuhk.edu.hk.

Submitted Sep 01, 2018. Accepted for publication Sep 11, 2018.
doi: 10.21037/qims.2018.09.06
View this article at: http://dx.doi.org/10.21037/qims.2018.09.06

We read with interests the article of Li *et al.* (1). This article details the plan of the Prospective Urban Rural Epidemiology (PURE) China Action on Spine and Hip status (CASH) study. It is a prospective large-scale population study with a community-based sampling and recruitment strategy. The aim of PURE CASH study is to determine the prevalence of osteoporosis and spinal fracture, and explore the potential relationship between spinal fracture and bone mineral density (BMD) with QCT measurement. Participants in the PURE CASH study are recruited from 12 centers in seven provinces in China. These data may have great significance for future policy-making and the prevention of osteoporosis and osteoporotic fractures in China (1).

On the aspect of radiological assessment of spine, in the PURE CASH study plan it is noted that '*the lateral scout view images from the QCT are used to detect vertebral body fractures according to Genant's semiquantitative (SQ) method. Each vertebral body is classified as normal (grade 0), mild (grade 1, approximately 20–25% depression in height and a reduction in area 10–20%), moderate (grade 2, approximately 25–40% depression in height and a reduction in area 20–40%), or severe (grade 3, more than 40% reduction in height and area) fracture… A subject is considered to have a spinal osteoporotic fracture if any one of the T4–L4 vertebral bodies had a VFA (vertebral fracture assessment) score ≥ grade 1... The vBMD (volumetric bone mineral density) results along with any abnormal CT scan findings will be provided to the participants*' (1). Hereby we like to elaborate our experience using Genant's semiquantitative (SQ) method (2), as well as the possibility of 'overcall' if we describe SQ grade-1 vertebral deformity (VD) as 'vertebral fracture' and if investigators communicate to the study subjects as such.

The SQ criteria proposed by Genant *et al.* (2) are now being widely applied in research setting. Note the initial description of SQ criteria also stressed the importance of qualitative/radiological evaluation. It was noted that '*aside from morphometric features, most vertebral fractures are readily distinguished by the presence of endplate deformities and buckling of cortices, by the lack of parallelism of end plates, and by the loss of vertical continuity of vertebral morphology… Subtle distinctions between a fractured end plate and the deformity of Schmorl's nodes or the remodeling of the vertebral bodies due to degenerative disk disease and scoliosis can frequently be made qualitatively by an experienced or trained observer*' (2). These points have been emphasized many times later. Genant and Jergas described that '*in addition to height reductions, the reader pays careful attention to alterations in the shape and configuration of the vertebrae relative to adjacent vertebrae and expected normal appearances. These features add a strong qualitative, sometimes subjective aspect to the interpretation*' (3). Genant also communicated that '*the first step in the process is to visually determine whether a fracture or a non-fracture deformity exists. The next steps include determining whether endplate deformities (horizontal edges) are present; lack of parallelism of endplates exists, buckling of cortices (on the vertical edges) and, finally, whether there is loss of vertical continuity with adjacent vertebrae*' (4). Appropriate use of Genant's criteria requires knowledge of developmental deformities [e.g., Scheuermann's disease (osteochondrosis of vertebral

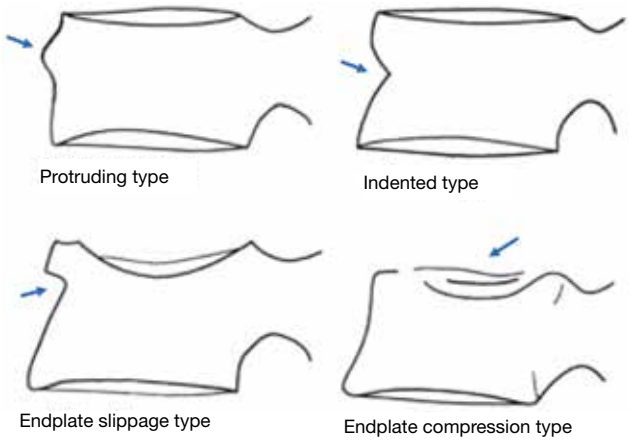

Figure 1 The vertebral fracture morphological classifications proposed by Yoshida *et al.* Modified from reference (8) with permission.

end plates)] and acquired deformities (e.g., osteoarthritis) that do not represent fractures and recognition of features that suggest causes of fractures other than osteoporosis. The common developmental wedge deformities of the mid-thoracic and thoracolumbar regions, the reverse wedging of lower lumbar vertebrae, and the common mild endplate bowing of the lower lumbar vertebrae should be recognized. Nonfractural changes of the vertebrae shape should be evaluated to exclude deformities including developmental short vertebral height, Cupid's bow deformity, Scheuermann's disease, and Schmorl's nodes, and degenerative remodeling (5). An isolated anterior wedging of vertebral body between vertebrae of normal shape may suggest osteoporotic vertebral deformity (oVD), rather than if wedged or biconcave vertebrae are evident throughout much of the thoracic or lumbar spine (6,7). It is understood in the PURE CASH study spine radiograph will be read by experienced radiologists (1), and they will likely read SQ criteria appropriately. However it will be helpful to include Genant *et al.*'s description of SQ criteria's qualitative/radiological assessment requirement in the formal study protocol. As the PURE CASH study involves 12 centers in seven provinces in China, without such formal documentation, there could be chances that miscommunication and misinterpretation may occur locally at individual research sites.

Furthermore, we felt it is very difficult to precisely estimate vertebral lateral area reduction. Increasingly, this percentage area reduction requirement has been dropped by users of SQ criteria; instead, only the percentage vertebral height reduction is estimated (4). In addition, according to Genant *et al.*'s description, oVDs are estimated visually (2). However, without quantitative measurement, we also found it could be difficult to accurately and consistently estimate vertebral height loss. In our experience, the main discord for inter-reader grading disagreement relates to the borderline cases, for example, a perceived reduction in vertebral height of approximately 20% can be categorized as normal by one reader and grade-1 VD by another reader. Similarly, a perceived reduction in vertebral body height of approximately 25% can be categorized as grade-1 or grade-2 VD. Therefore in our practice while we reply on qualitative/radiological approach to define an oVD, to improve consistency we use quantitative measurement for grading. The important component of assessment is that a vertebra should be carefully compared with its neighbors, for their morphology as well as height estimation. The anterior osteophyte and posterior uncinate should be excluded during the measurement. Note where to start to place the cursor for measurement has notable influence for the measured ratio. Again the placing of cursors requires radiological assessment, particularly when multiple neighboring vertebral bodies are involved with deformity. To measure a few times and take the mean may be applied for borderline cases.

Recent work further emphasized the importance of identifying osteoporotic vertebral endplate/cortex fracture (*Figures 1,2*) [ECF, or ABQ fracture as defined by Jiang *et al.* (9)]. In addition to vertebral height, particularly attention should be paid to the endplate and vertebral anterior cortex (2,3,8-10). Lentle *et al.* (11) showed ECF grade-1 vertebral fracture (VF) was associated with higher risk of VFs as well as nonvertebral major osteoporotic fracture, while grade-1 SQ-VD deformity was not associated with higher risk of non-vertebral fracture. We showed subjects with grade-1 SQ-vertebral deformity had a similar BMD compared with subjects without fracture, while subjects with grade-1 ECF VF had lower BMD (12). Our unpublished data shows that within the same mild/moderate VD grades, compared with the subjects without ECF, the subjects with ECF are associated with a higher short term (4-years) future risk of VD progression and new incident VD. Whether scout view images from the QCT are of sufficient image quality to detect subtle changes associated with ECF remains to be validated. It has noted that '*relative reductions in vertebral height may not be a necessary nor sufficient criterion by which to diagnose a fracture*' (13).

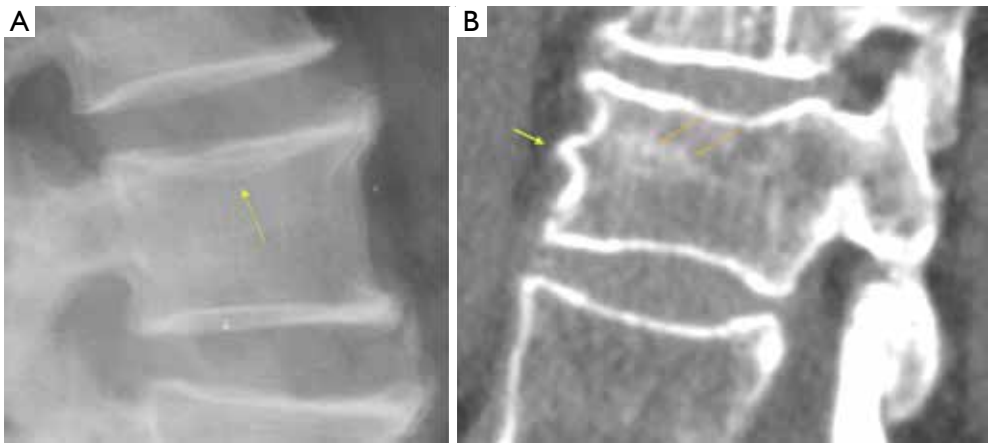

Figure 2 Examples of endplate/cortex fracture (ECF) without apparent height loss. (A) A vertebral upper endplate fracture (yellow arrow) without apparent height loss; (B) a sagittally reconstructed CT image shows anterior cortex fracture (yellow arrow) associated with a low energy trauma. Note a fracture line can be identified horizontally (orange arrows) with condensed trabecula or trabecula repairing [reproduced from reference (5) with permission].

In terms of terminology, as Genant's criteria do not require a conventional 'fracture' sign, we feel radiographical osteoporotic vertebral deformity (roVD) may be the appropriate term for radiographically detected deformity, especially for mild oVD. Different imaging technologies have difference sensitivity and specificity for detecting and classifying vertebral fracture. It is understood that if an endplate/cortex fracture exists, then it will be reasonable to call the involved vertebra as having a 'fracture'. It has been recently noted that VDs with >34% height loss is usually associated with radiographically identifiable vertebra fracture signs (14), therefore the term vertebral fracture may be appropriate for these roVDs.

Additionally, oVDs of elderly men and elderly women's are likely to have distinctly different features. For example, while it is generally accepted that osteoporotic VF is much more common in elderly women than elderly men, the difference in prevalence of roVD between elderly men and elderly women is small (12) (*Figure 3*). According to some reports, the prevalence of roVD is more common in elderly men than elderly women (15). On the other hand, roVDs in elderly women are more likely to have ECF than elderly men (*Figure 3*) (12). roVDs with 25–34% height loss can be with or without ECF in women, while roVD with 25–34% height loss usually do not have ECF in men (14). Our unpublished data also shows lower endplate in elderly men is much less likely to fracture than lower endplate in elderly women. These evidences suggest that the Genant's SQ criteria may not be most suitable for assessing roVD in men. Indeed, Szulc *et al.* (16) suggested that a cut-off of 30% for wedge deformities from T6 to T9 (thoracic kyphosis site) and that 25% for deformities at other levels may have a high specificity and a moderate sensitivity for identifying VDs related to low BMD in men. A recent Swedish study reported that, if low threshold for oVD (i.e., 10% estimated vertebral height loss in that study) is used, then a clinical relevance of prevalent vertebral fracture in elderly men is low (17).

Despite years' research, the radiographic criteria for osteoporotic VF and its grading remain debated (6,13,18-20). To communicate with study subjects of mild roVD, appropriate terminology should be used, so to avoid both 'over-call' and 'under-call'. Though group-wise and statistically, even mild oVDs are associated with greater future osteoporotic VF (21), the importance of mild roVD remain unclear at individual subject's level, and this is particularly the case for males. Indeed, it has been emphasized that Genant's criteria is developed for epidemiological and large clinical trial usage. It is acknowledged that osteoporosis pharmacotherapy should be strongly considered for patients with an osteoporotic VF of more recent, higher grade, or multiple fractures (22). A grade 1, solitary, asymptomatic, incidentally discovered vertebral fracture is of questionable clinical significance. The clinical prevalence and appropriate management of these silent VDs remain unknown (13,19,20,22).

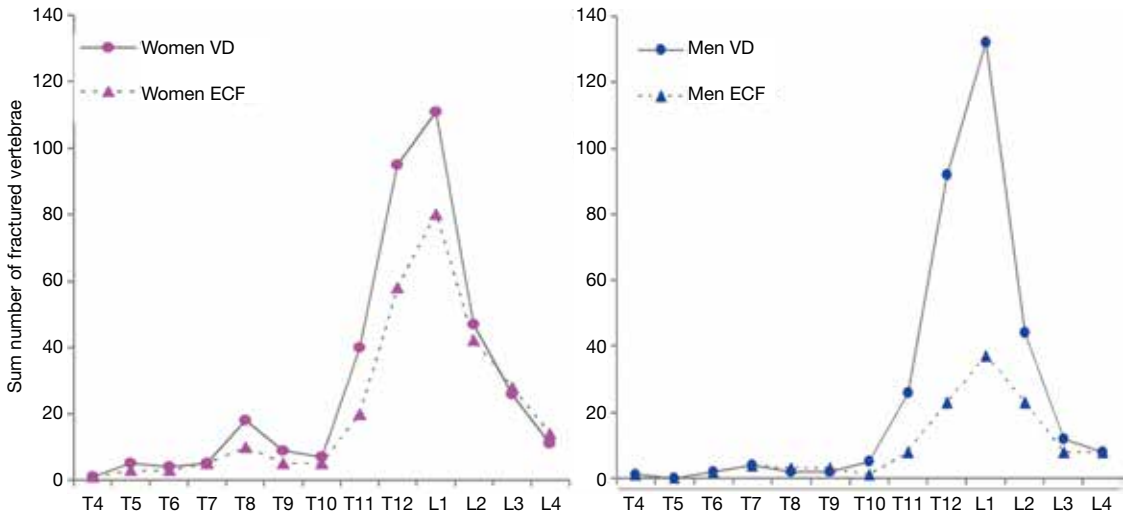

Figure 3 Osteoporotic vertebral deformity distribution from MrOS (Hong Kong) and MsOS (Hong Kong) studies, involving 1,954 elderly Chinese men (mean: 72.3 years) and 1,953 elderly Chinese women (mean: 72.5 years). Endplate/cortex fracture (ECF) is substantially more common in women than in men, while the difference in vertebral deformity (VD) prevalence according to Genant's criteria is smaller [Reproduced from reference (12) with permission]. MrOS, Osteoporotic Fractures in Men; MsOS, Osteoporotic Fractures in Women.

Acknowledgements

None.

Footnote

Conflicts of Interest: The authors have no conflicts of interest to declare.

References

1. Li K, Zhang Y, Wang L, Duanmu YY, Tian W, Chen H, Yin L, Bo J, Wang Y, Li W, He L, Zhao WH, Xu SQ, Zhao LF, Zhou J, Wang FZ, Liu Y, Zhu L, Chen YZ, Zhang XL, Hao XG, Shi ZW, Wang JY, Shao JM, Chen ZJ, Lei RS, Ning G, Zhao Q, Jiang YH, Zhi YH, Li BQ, Chen X, Xiang QY, Wang L, Ma YZ, Liu SW, Cheng XG. The protocol for the Prospective Urban Rural Epidemiology China Action on Spine and Hip status study. Quant Imaging Med Surg 2018;8:667-72.
2. Genant HK, Wu CY, van Kuijk C, Nevitt MC. Vertebral fracture assessment using a semiquantitative technique. J Bone Miner Res 1993;8:1137-48.
3. Genant HK, Jergas M. Assessment of prevalent and incident vertebral fractures in osteoporosis research. Osteoporos Int 2003;14 Suppl 3:S43-55.
4. Schwartz EN, Steinberg D. Detection of vertebral fractures. Curr Osteoporos Rep 2005;3:126-35.
5. Wáng YX, Santiago RF, Deng M, Nogueira-Barbosa MH. Identifying osteoporotic vertebral endplate and cortex fractures. Quant Imaging Med Surg 2017;7:555-91.
6. Szulc P. Vertebral Fracture: Diagnostic Difficulties of a Major Medical Problem. J Bone Miner Res 2018;33:553-9.
7. Wáng YX, Deng M, He LC, Che-Nordin MN Santiago RF. Osteoporotic vertebral endplate and cortex fractures: A pictorial review. J Orthop Translat 2018. https://doi.org/10.1016/j.jot.2018.08.004
8. Yoshida T, Nanba H, Mimatsu K, Kasai T. Treatment of osteoporotic spinal compression fractures. Conservative therapy and its limitation. Clin Calcium 2000;10:53-8.
9. Jiang G, Eastell R, Barrington NA, Ferrar L. Comparison of methods for the visual identification of prevalent vertebral fracture in osteoporosis. Osteoporos Int 2004;15:887-96.
10. Ito Z, Harada A, Matsui Y, Takemura M, Wakao N, Suzuki T, Nihashi T, Kawatsu S, Shimokata H, Ishiguro N. Can you diagnose for vertebral fracture correctly by plain X-ray? Osteoporos Int 2006;17:1584-91.
11. Lentle BC, Berger C, Probyn L, et al. for the CaMos Research Group. Comparative Analysis of the radiology of osteoporotic vertebral fractures in women and men: cross-sectional and longitudinal observations from the Canadian

Multicentre Osteoporosis Study (CaMos). J Bone Miner Res 2018;33:569-79.
12. Deng M, Zeng XJ, He LC, Leung JCS, Kwok AWL, Griffith JF, Kwok T, Leung PC, Wáng YXJ. Osteoporotic Vertebral Fracture Prevalence in Elderly Chinese Men and Women: A Comparison of Endplate/Cortex Fracture-Based and Morphometrical Deformity-Based Methods. J Clin Densitom 2017. [Epub ahead of print]. doi: 10.1016/j.jocd.2017.11.004.
13. Lentle B, Trollip J, Lian K. The Radiology of Osteoporotic Vertebral Fractures Redux. J Clin Densitom. 2016;19:40-7.
14. Deng M, Kwok TCY, Leung JCS, Leung PC, Wang YX. All osteoporotically deformed vertebrae with >34% height loss have radiographically identifiable endplate/cortex fracture. J Orthop Translat 2018;14:63-6.
15. Waterloo S, Søgaard AJ, Ahmed LA, Damsgård E, Morseth B, Emaus N. Vertebral fractures and self-perceived health in elderly women and men in a population-based cross-sectional study: the Tromsø Study 2007-08. BMC Geriatr 2013;13:102.
16. Szulc P, Munoz F, Marchand F, Delmas PD. Semiquantitative evaluation of prevalent vertebral deformities in men and their relationship with osteoporosis: the MINOS study. Osteoporos Int 2001;12:302-10.
17. Kherad M, Rosengren BE, Hasserius R, Nilsson JA, Redlund-Johnell I, Ohlsson C, Lorentzon M, Mellstrom D, Karlsson MK. Low clinical relevance of a prevalent vertebral fracture in elderly men--the MrOs Sweden study. Spine J 2015;15:281-9.
18. Oei L, Koromani F, Rivadeneira F, Zillikens MC, Oei EH. Quantitative imaging methods in osteoporosis. Quant Imaging Med Surg 2016;6:680-98.
19. McKiernan FE. Violet Fox: A Clinical View of Vertebral Fractures. J Clin Densitom. 2016;19:35-9.
20. Lentle BC, Hg Oei E, Goltzman D, Rivadeneira F, Hammond I, Oei L, Kovacs CS, Hanley DA, Prior JC, Leslie WD, Kaiser SM, Adachi JD, Probyn L, Brown J, Cheung AM, Towheed T. Vertebral Fractures and Morphometric Deformities. J Bone Miner Res. 2018;33:1544-1545.
21. Roux C, Fechtenbaum J, Kolta S, Briot K, Girard M. Mild prevalent and incident vertebral fractures are risk factors for new fractures. Osteoporos Int 2007;18:1617-24.
22. Kendler DL, Bauer DC, Davison KS, Dian L, Hanley DA, Harris ST, McClung MR, Miller PD, Schousboe JT, Yuen CK, Lewiecki EM. Vertebral Fractures: Clinical Importance and Management. Am J Med 2016;129:221.e1-10.

Cite this article as: Wáng YX, Che-Nordin N. Informed communication with study subjects of radiographically detected osteoporotic vertebral deformity. Quant Imaging Med Surg 2018;8(8):876-880. doi: 10.21037/qims.2018.09.06

Letter to the Editor

Incidental abnormal bone marrow signal on magnetic resonance imaging and reflexive testing for the *JAK2* V617F mutation

Stephen E. Langabeer

Cancer Molecular Diagnostics, St. James's Hospital, Dublin, Ireland

Correspondence to: Stephen E. Langabeer, PhD, FRCPath. Cancer Molecular Diagnostics, Central Pathology Laboratory, St. James's Hospital, Dublin, D08 E9P6, Ireland. Email: slangabeer@stjames.ie.

Submitted May 31, 2018. Accepted for publication Aug 21, 2018.
doi: 10.21037/qims.2018.08.11
View this article at: http://dx.doi.org/10.21037/qims.2018.08.11

With the increasing employment of imaging modalities in the diagnostic work up of patients comes an increase in the number of incidental cases with an abnormal bone marrow signal. Hematological malignancy can be visualized in the bone marrow by several imaging procedures but interpretation must also consider the variation in marrow appearances due to compositional changes associated with normal aging and hematological demand (1). While sporadic cases of acute leukemia, lymphoma, myeloma, metastatic carcinoma and myeloproliferative neoplasms (MPN) have been diagnosed from this initial finding by subsequent bone marrow biopsy and hematological work up (2,3), the utility of up-front reflexive screening for hematological malignancy-associated mutations in such incidental cases has not been assessed. The classical Philadelphia chromosome-negative MPN are clinically related, stem cell neoplasms characterised by hyper-expansion of mature hematopoietic cell lineages primarily in the bone marrow. The most common driver mutation of these MPN is the acquired *JAK2* V617F which results in constitutive activation of hematopoietic growth factor signalling and which is present in greater than 95% of patients with polycythemia vera and in 50–60% of patients with essential thrombocythemia and primary myelofibrosis (4). It is therefore of interest to note that from a cancer molecular diagnostics perspective, an isolated, atypical bone marrow magnetic resonance imaging (MRI) signal has become an infrequent but recurring trigger for requesting molecular analysis of the *JAK2* V617F.

In order to address the laboratory impact and clinical value of such requests, a retrospective audit was performed on all *JAK2* V617F requests received at a molecular diagnostics centre for hematological malignancies. From January 2006 to December 2017 inclusive, 15,562 diagnostic requests for *JAK2* V617F mutation analysis were received. Of these, 29 requests (0.2%) were received with the only clinical details provided on the request form of an abnormal BM signal upon MRI. The median age was 52 years and comprised 12 females and 17 males. Using a standardised allele-specific PCR screening assay capable of detecting a 2% mutant allele burden (5) and unchanged throughout the audit period, the *JAK2* V617F mutation was not detected in any of these 29 patients.

Diagnosis and classification of an MPN not only requires molecular detection of typical somatic events such as the *JAK2* V617F, *JAK2* exon 12, *CALR* exon 9 and *MPL* exon 10 mutations, but is also reliant on other clinical and hematological criteria (6). Selecting which patients to screen for the presence of the MPN driver mutations of *JAK2*, *CALR* and *MPL* requires careful consideration in order to optimize laboratory resources (7,8). While further hematological follow up in patients with an abnormal bone marrow signal on MRI is advocated and despite this molecular diagnostic analysis not appreciably impacting on the overall laboratory workload, reflexive testing for the *JAK2* V617F mutation in such cases without overt hematological evidence of an MPN appears inappropriate.

Acknowledgements

None.

Footnote

Conflicts of Interest: The author has no conflicts of interest to declare.

References

1. Navarro SM, Matcuk GR, Patel DB, Skalski M, White EA, Tomasian A, Schein AJ. Musculoskeletal Imaging Findings of Hematologic Malignancies. Radiographics 2017;37:881-900.
2. Shah GL, Rosenberg AS, Jarboe J, Klein A, Cossor F. Incidence and evaluation of incidental abnormal bone marrow signal on magnetic resonance imaging. ScientificWorldJournal 2014;2014:380814.
3. Spierings J, van der Linden AN, Kuijper PH, Tick LW, Nijziel MR. Incidentally detected diffuse signal alterations of bone marrow on MRI: is bone marrow biopsy indicated? Neth J Med 2014;72:345-8.
4. Vainchenker W, Kralovics R. Genetic basis and molecular pathophysiology of classical myeloproliferative neoplasms. Blood 2017;129:667-679.
5. Bench AJ, White HE, Foroni L, Godfrey AL, Gerrard G, Akiki S, Awan A, Carter I, Goday-Fernandez A, Langabeer SE, Clench T, Clark J, Evans PA, Grimwade D, Schuh A, McMullin MF, Green AR, Harrison CN, Cross NC; British Committee for Standards in Haematology. Molecular diagnosis of the myeloproliferative neoplasms: UK guidelines for the detection of JAK2 V617F and other relevant mutations. Br J Haematol 2013;160:25-34.
6. Arber DA, Orazi A, Hasserjian R, Thiele J, Borowitz MJ, Le Beau MM, Bloomfield CD, Cazzola M, Vardiman JW. The 2016 revision to the World Health Organization classification of myeloid neoplasms and acute leukemia. Blood 2016;127:2391-405.
7. Tefferi A, Noel P, Hanson CA. Uses and abuses of JAK2 and MPL mutation tests in myeloproliferative neoplasms a paper from the 2010 William Beaumont hospital symposium on molecular pathology. J Mol Diagn 2011;13:461-6.
8. Haslam K, Langabeer SE. Who to screen for calreticulin mutations? An audit of real-life practice and review of current evidence. Eur J Intern Med 2017;40:e22-e23.

Cite this article as: Langabeer SE. Incidental abnormal bone marrow signal on magnetic resonance imaging and reflexive testing for the *JAK2* V617F mutation. Quant Imaging Med Surg 2018;8(8):881-882. doi: 10.21037/qims.2018.08.11

In memoriam: Dr. Juergen Karl Willmann

We are extremely saddened by the passing of Professor Juergen Karl Willmann (*Figure 1*). Professor Willmann died in a car accident on Jan 8 this year at the rather young age of 45 years old. Dr. Juergen Karl Willmann served as an associate editor of our journal shortly after this journal was founded in late 2011 and made significant contributions to the development of this journal. His passing is a tremendous loss to everyone.

Dr. Juergen Karl Willmann was superb clinician and brilliant scientist. Dr Willmann was a Professor of Radiology and Chief of Body Imaging at Stanford University School of Medicine and Vice chair for strategy, outreach and clinical trials. Dr. Willmann was an elected fellow of the Society of Abdominal Radiology and of the American Institute for Medical and Biological Engineering. Before his career at Stanford, Dr. Willmann was educated in Germany and Switzerland. He attended Albert Ludwig University of Freiburg in Germany and completed his medical internship at the University Medical Center Freiburg and his residency at University Hospital Zurich in Switzerland. Dr. Willmann is described by his colleagues as "*exceptionally intelligent, highly driven, supremely organized and a wonderful leader, mentor, father and husband.*"

Dr. Willmann and his lab worked on targeted contrast microbubbles for early detection of tumors and to direct drugs for treatment. His team was the first to use the microbubble technology in human clinical imaging trials, leveraging them to identify ovarian cancer and breast cancer. Dr. Willmann's investigation into cancer detection and imaging technologies earned him the 2017 Distinguished Investigator Award from the Academy for Radiology & Biomedical Imaging Research.

Dr. Willmann is survived by his wife Amelie Lutz, and their two children, Alexander and Juliana Willmann; his parents, Elisabeth and Karl Willmann; and sister Sabine Willmann.

Figure 1 Professor Juergen Karl Willmann.

Quant Imaging Med Surg **Editorial Office**
AME Publishing Company, Hong Kong, China. (Email: qims@amegroups.com)
doi: 10.21037/qims.2018.09.20
Conflicts of Interest: The authors have no conflicts of interest to declare.
View this article at: http://dx.doi.org/10.21037/qims.2018.09.20

Cite this article as: In memoriam: Dr. Juergen Karl Willmann. Quant Imaging Med Surg 2018;8(8):883. doi: 10.21037/qims.2018.09.20